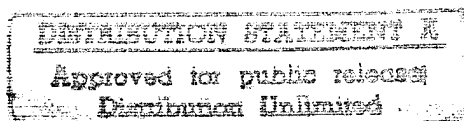




# **Large Deformation Analysis of Nonlinear Homogeneous and Heterogeneous Media Using an Adaptive Arbitrary Lagrangian- Eulerian Finite Element Method**

Somnath Ghosh  
Applied Mechanics



DTIC QUALITY INSPECTED 4

**U.S. Army Research Office**  
Research Triangle Park, North Carolina 27709-2211

Grant No. DAAL03-91-G-0168  
**Final**  
For the Period August 16, 1991 - September 30, 1995  
RF Project No. 769182/724944

November, 1995

19960212 093

# REPORT DOCUMENTATION PAGE

Form Approved  
OMB No. 0704-0188

Public reporting burden for this collection of information is estimated to average 1 hour per response, including the time for reviewing instructions, searching existing data sources, gathering and maintaining the data needed, and completing and reviewing the collection of information. Send comments regarding this burden estimate or any other aspect of this collection of information, including suggestions for reducing this burden, to Washington Headquarters Services, Directorate for Information Operations and Reports, 1215 Jefferson Davis Highway, Suite 1204, Arlington, VA 22202-4302, and to the Office of Management and Budget, Paperwork Reduction Project (0704-0188), Washington, DC 20503.

1. AGENCY USE ONLY (Leave blank)		2. REPORT DATE November 1995	3. REPORT TYPE AND DATES COVERED
4. TITLE AND SUBTITLE Large Deformation Analysis Of Nonlinear Homogeneous And Heterogeneous Materials Using An Adaptive Arbitrary Lagrangian-Eulerian Finite Element Method		5. FUNDING NUMBERS DAAL03-91-G-0168	
6. AUTHOR(S) Somnath Ghosh, P.I.		8. PERFORMING ORGANIZATION REPORT NUMBER	
7. PERFORMING ORGANIZATION NAME(S) AND ADDRESS(ES) Department of Engineering Mechanics The Ohio State University 323 Boyd Laboratory 155 W. Woodruff Avenue		10. SPONSORING / MONITORING AGENCY REPORT NUMBER ARO 29040.16-EG	
9. SPONSORING / MONITORING AGENCY NAME(S) AND ADDRESS(ES) U. S. Army Research Office P. O. Box 12211 Research Triangle Park, NC 27709-2211		11. SUPPLEMENTARY NOTES The view, opinions and/or findings contained in this report are those of the author(s) and should not be construed as an official Department of the Army position, policy, or decision, unless so designated by other documentation.	
12a. DISTRIBUTION / AVAILABILITY STATEMENT Approved for public release; distribution unlimited.		12b. DISTRIBUTION CODE	
13. ABSTRACT (Maximum 200 words)  Research has been conducted to advance the state of the art in (a) multiple scale modeling of advanced heterogeneous materials, (b) in large deformation analysis of solids with applications in metal forming, and also (c) in solidification modeling. For modeling heterogeneous materials (a), a new Voronoi Cell finite element model has been developed which naturally evolves from the microstructure. Formulations have been developed for thermo-elasticity, elasto-plasticity and heat conduction. This is then cast in multiple scale modeling of heterogeneous (porous and composite) materials by combining with asymptotic homogenization theory. In (b), an adaptive arbitrary Lagrangian-Eulerian (ALE) finite element method has been developed for solving metal forming problems with strain localization. The ALE mesh movement is coupled with r-adaptation to minimize element distortion, and with s-adaptation to achieve local enrichment. Finally heat transfer analysis for solidification problems has been conducted to evaluate the temperature field and location of the phase change interface using the ALE description.			
14. SUBJECT TERMS Voronoi Cell Finite Element Method Arbitrary Lagrangian-Eulerian Method Composite Materials, Metal Forming		15. NUMBER OF PAGES 169	
		16. PRICE CODE	
17. SECURITY CLASSIFICATION OF REPORT UNCLASSIFIED	18. SECURITY CLASSIFICATION OF THIS PAGE UNCLASSIFIED	19. SECURITY CLASSIFICATION OF ABSTRACT UNCLASSIFIED	20. LIMITATION OF ABSTRACT UL

**Large Deformation Analysis of Nonlinear Homogeneous and  
Heterogeneous Media Using an Adaptive Arbitrary  
Lagrangian-Eulerian Finite Element Method**

Final Report to

**Engineering and Environmental Sciences Division**

**Solid Mechanics Program**

**Dr. K. R. Iyer, Program Manager**

**Department Of The Army  
ARMY RESEARCH OFFICE  
P.O. Box 12211  
Research Triangle Park  
NC 27709-2211**

for

**Grant # DAAL03-91-G-0168  
to The Ohio State University**

by

**Somnath Ghosh, Principal Investigator  
Associate Professor of Applied Mechanics  
Department of Aerospace Engineering, Applied Mechanics and Aviation  
323 Boyd Laboratory, 155 W. Woodruff Ave.  
The Ohio State University, Columbus, OH 43210**

November 1995

# Contents

<b>1</b>	<b>Introduction</b>	<b>1</b>
<b>2</b>	<b>List of Publications</b>	<b>3</b>
2.1	Theses Acknowledging this Grant . . . . .	3
2.2	Publications Acknowledging this Grant . . . . .	3
<b>3</b>	<b>The Voronoi Cell Finite Element Method for Heterogeneous Microstructures</b>	<b>5</b>
3.1	Introduction . . . . .	5
3.2	The Voronoi Cell Finite Element Model for Heterogeneous Microstructures . . . . .	7
3.2.1	Variational principle with assumed stress hybrid method . . . . .	8
3.2.2	Element formulations and assumptions . . . . .	9
3.2.3	Constitutive Relations . . . . .	11
3.2.4	Solution Method for the Weak Form . . . . .	12
3.2.5	Numerical Aspects of Voronoi Cell FEM . . . . .	13
3.3	Shape Based Stress Representations . . . . .	14
3.3.1	Numerical Implementation of Reciprocal Stress Functions . . . . .	18
3.3.2	A Simple Convergence Study . . . . .	20
3.4	VCFEM for Porous Microstructures . . . . .	21
3.4.1	Numerical Validation . . . . .	21
3.4.2	Effect Of Microstructural Morphology On Yield Surfaces . . . . .	23
3.5	VCFEM for Composite Microstructures . . . . .	38
3.6	Conclusions . . . . .	41
<b>4</b>	<b>Multiple Scale Modeling of Heterogeneous Materials Using Asymptotic Homogenization and the Voronoi Cell FEM</b>	<b>46</b>
4.1	Introduction . . . . .	46
4.2	Asymptotic Homogenization for Multiple Scale Analysis . . . . .	49
4.2.1	Microscopic Equilibrium Equation and Homogenized Constitutive Relation .	53
4.2.2	Macroscopic Equations . . . . .	54
4.3	Microstructural Analysis with VCFEM . . . . .	54
4.3.1	Variational Principles in VCFEM . . . . .	55
4.4	Elastic-plastic Homogenization with VCFEM . . . . .	57
4.4.1	Calculation of Microscopic Stresses . . . . .	58
4.4.2	Calculation of Homogenized Tangent Modulus . . . . .	59
4.5	Numerical Implementation . . . . .	59

4.5.1	Incorporation in the Macroscopic Analysis Module . . . . .	59
4.5.2	Implementing Periodicity Boundary Condition . . . . .	60
4.6	Numerical Examples . . . . .	62
4.6.1	Validation of the Homogenization Model . . . . .	62
4.6.2	Multiple Scale Analysis . . . . .	75
4.7	Conclusions . . . . .	100
<b>5</b>	<b>R-S Adapted Arbitrary Lagrangian-Eulerian Finite Element Method for Metal Forming Problems with Strain Localization</b>	<b>108</b>
5.1	Introduction . . . . .	108
5.2	Governing Equations . . . . .	110
5.2.1	Basic equations in the ALE model . . . . .	110
5.2.2	Constitutive Model . . . . .	110
5.2.3	Contact Formulation . . . . .	112
5.3	Node Relocation (R-Adaptation) . . . . .	113
5.4	Adaptive Mesh Superposition With S-Method . . . . .	114
5.4.1	Finite element formulations for global local analysis . . . . .	116
5.4.2	Construction of superimposed domains . . . . .	119
5.4.3	Aspects of Numerical Integration . . . . .	120
5.5	Numerical Examples . . . . .	120
5.5.1	Plane strain tension test with surface imperfection . . . . .	121
5.5.2	Tension test of a notched specimen . . . . .	122
5.5.3	Metal forming examples . . . . .	126
5.6	Conclusions . . . . .	132
<b>6</b>	<b>An Arbitrary Lagrangian-Eulerian Finite Element Model for Heat Transfer Analysis of Solidification Processes</b>	<b>144</b>
6.1	Introduction . . . . .	144
6.2	Governing Equations In Arbitrary Lagrangian-Eulerian Description . . . . .	147
6.3	Finite Element Formulations For Heat Transfer Analysis . . . . .	149
6.3.1	Movement of the phase change interface . . . . .	151
6.4	Numerical Implementation . . . . .	152
6.4.1	Iteration Scheme . . . . .	152
6.4.2	Evaluation of Normals to the Interface . . . . .	153
6.4.3	Introduction of a Pseudo Domain for Discretization . . . . .	154
6.5	Numerical Examples . . . . .	155
6.5.1	An one-dimensional problem . . . . .	156
6.5.2	Solidification of a Cylindrical Body . . . . .	156
6.5.3	Solidification of a Square Region . . . . .	159
6.5.4	Simplified Example of a Continuous Casting Process . . . . .	161
6.6	Conclusions . . . . .	163
<b>7</b>	<b>List of Participating Scientific Personnel</b>	<b>169</b>

# Chapter 1

## Introduction

The project entitled “*Large Deformation Analysis of Nonlinear Homogeneous and Heterogeneous Media Using an Adaptive Arbitrary Lagrangian-Eulerian Finite Element Method*” at the University of Alabama in March 1991, where the PI was then an Assistant Professor of Engineering Mechanics. It was subsequently transferred to the Ohio State University, where the PI relocated beginning September 1991. A no-cost extension was granted to continue this project till September 30, 1995. During the four year period of this grant, substantial progress has been made in advancing the state of the art in multiple scale modeling of advanced heterogeneous materials, in large deformation analysis of solids with applications in metal forming, and also in solidification modeling. Research has been conducted in a few distinct areas that are delineated below. A list of publications, acknowledging this grant is provided in chapter 2.

### **I. The Voronoi Cell Finite Element Model for Heterogeneous Microstructures**

(Details in: Chapter 3)

A new finite element model has been developed for analysis of heterogeneous media, in which the second phase is randomly dispersed within the matrix. A mesh generator based on Dirichlet tessellation discretizes the domain, accounting for arbitrariness in location, shape and size of the second phase. This results in a network of convex “Voronoi polygons”, which forms the elements in a finite element mesh. An assumed stress hybrid formulation has been implemented for accommodating arbitrary multi-sided elements in the finite element model. Composite element formulations have been developed to incorporate the effect of second phase within each element. Formulations have been developed for elasticity, thermo-elasticity, elasto-plasticity and heat conduction.

### **II. Multiple Scale Modeling of Heterogeneous Materials Using Asymptotic Homogenization and the Voronoi Cell FEM**

(Details in: Chapter 4)

In this work, a multiple scale finite element model (VCFEM-HOMO) has been developed for elastic-plastic analysis of heterogeneous (porous and composite) materials by combining asymptotic homogenization theory with the Voronoi Cell finite element model (VCFEM). VCFEM for

microstructural modeling originates from Dirichlet tessellation of representative material elements at sampling points in the structure. Structural modeling is done by the general purpose finite element code ABAQUS, and interfacing with the microscale VCFEM analysis is done through the user subroutine in ABAQUS for material constitutive relation, UMAT. Asymptotic homogenization in UMAT generates macroscopic material parameters for ABAQUS. Following the macroscopic analysis, a local VCFEM analysis is invoked to depict the true evolution of microstructural state variables. Various numerical examples are executed for validating the effectiveness of VCFEM-HOMO, and the effect of size, shape and distribution of heterogeneities on local and global response is examined.

### **III. R-S Adapted Arbitrary Lagrangian-Eulerian Finite Element Method For Metal Forming Problems with Strain Localization**

(Details in: Chapter 5)

In this work, an adaptive arbitrary Lagrangian-Eulerian (ALE) finite element method is developed for solving large deformation problems, with applications in metal forming simulation. The ALE mesh movement is coupled with *r-adaptation* of automatic node relocation, to minimize element distortion during the process of deformation. Strain localization is considered in this study through the constitutive relations for ductile porous materials, proposed by Gurson and Tvergaard. Prediction of localized deformation is achieved through a multi-level mesh superimposition method, termed as *s-adaptation*. The model is validated by comparison with established results and codes, and a few metal forming problems are simulated to test its effectiveness.

### **IV. Arbitrary Lagrangian-Eulerian Finite Element Method in Solidification Modeling**

(Details in: Chapter 6)

A heat transfer analysis for solidification problems has been conducted to evaluate the temperature-field and the location of the phase change interface. The arbitrary Lagrangian-Eulerian kinematic description has been utilized in the finite element formulation for imparting flexibility to the motion of the nodes in model. By detaching the nodal points from the underlying material, nodes can be monitored to follow the evolving front while maintaining shapes of the elements. Special numerical techniques to smoothen the deforming front and to avoid continuous remeshing are introduced. Numerical examples have been solved to establish the validity of the present model and its strength.

## Chapter 2

# List of Publications

### 2.1 Theses Acknowledging this Grant

1. "Voronoi Cell Finite Element Method for Micropolar Thermoelastic Heterogeneous Materials", Y.S. Liu, M.S. Thesis, The Ohio State University, 1994.
2. "R-S Adapted Arbitrary Lagrangian Eulerian Finite Element Method For Metal Forming Analysis With Strain Localization", S. Raju, M.S. Thesis, The Ohio State University, 1995.

### 2.2 Publications Acknowledging this Grant

#### I. Voronoi Cell Finite Element Model for Heterogeneous Microstructures

1. **S. Ghosh** and S. Moorthy, "A Model for Analysis of Arbitrary Composite and Porous Microstructures with Voronoi Cell Finite Elements," (in review).
2. S. Moorthy and **S. Ghosh**, " Mesoscopic Analysis of Small Deformation in Heterogeneous Materials using Voronoi Cell Finite Element Model," **Computational Mechanics' 95 Theory and Applications**, S. N. Atluri, G. Yagawa, and T. Cruse eds., pp 1916-1921, 1995.
3. **S. Ghosh** and Y. Liu, "Voronoi Cell Finite Element Model Based on Micropolar Theory of Thermoelasticity for Heterogeneous Materials," **International Journal for Numerical Methods in Engineering**, Vol. 38, pp 1361-1398, 1995.
4. **S. Ghosh** and S. Moorthy, "Elastic-Plastic Analysis of Heterogeneous Microstructures Using the Voronoi Cell Finite Element Method," **Computer Methods in Applied Mechanics and Engineering**, Vol. 121, pp 373-409, 1995.
5. **S. Ghosh** and R. L. Mallett, " Voronoi Cell Finite Elements," **Computers and Structures**, Vol. 50, No.1, pp 33-46, 1994.
6. S. Moorthy, **S. Ghosh** and Y.S. Liu, , " Voronoi Cell Finite Element Model for Thermo-Elastoplastic Deformation in Random Heterogeneous Media," **Applied Mechanics Reviews**, Vol. 47, No. 1, Part 2, pp 207-221, 1994.

7. S. Moorthy, S. Ghosh and Y.S. Liu, " Voronoi Cell Finite Element Model for Random Micropolar Elastic-Plastic Heterogeneous Media," *Proceedings of 13th Army Symposium on Solid Mechanics*, S.C. Chou, F. D. Bartlett, T. W. Wright and K. Iyer eds., pp 527-538, 1994.
8. S. Ghosh and S. Moorthy, " A Voronoi Cell Finite Element Model for Random Heterogeneous Media," *Probabilities and Materials, Tests, Models and Applications, Proceedings of NATO Workshop PROBAMAT*, NATO ASI Series, Vol. 269, pp 273-284, 1994.
9. S. Ghosh and S. N. Mukhopadhyay, " A Material Based Finite Element Analysis of Heterogeneous Media Involving Dirichlet Tessellations , " *Computer Methods in Applied Mechanics and Engineering*, Vol. 104, pp 211-247, 1993.

## II. Multiple Scale Modeling of Heterogeneous Materials Using Asymptotic Homogenization and the Voronoi Cell FEM

10. S. Ghosh, K. Lee and S. Moorthy, "Two Scale Analysis of Heterogeneous Elastic-Plastic Materials with Asymptotic Homogenization and Voronoi Cell Finite Element Model," (in review)
11. S. Ghosh, K. Lee and S. Moorthy, "Multiple Scale Analysis of Heterogeneous Elastic Structures Using Homogenization Theory and Voronoi Cell Finite Element Method," *International Journal of Solids and Structures*, Vol. 32, No. 1, pp 27-62, 1995.

## III. R-S Adapted Arbitrary Lagrangian-Eulerian Finite Element Method for Metal Forming Problems with Strain Localization

12. S. Ghosh and S. Raju, "R-S adapted arbitrary Lagrangian Eulerian finite element method for metal forming analysis with strain localization," (in review)
13. S. Raju and S. Ghosh, " Adaptive Arbitrary Lagrangian-Eulerian Finite Element Method for Metal Forming Problems," *Computational Mechanics' 95 Theory and Applications*, S. N. Atluri, G. Yagawa, and T. Cruse eds., pp 1414-1419, 1995.
14. Ghosh, S. and Manna, S.K., " R-Adapted Arbitrary Lagrangian-Eulerian Finite Element Simulation of Metal Forming Processes", *ASM Journal of Materials Engineering and Performance*, Vol. 2(2), pp 271-282, 1993.

## IV. ALE Finite Element Method in Solidification Modeling

15. Ghosh, S. and Moorthy, S., " An Arbitrary Lagrangian-Eulerian Finite Element Model for Heat Transfer Analysis of Solidification Processes ", *Numerical Heat Transfer Part A*, Vol. 23, pp 327-350, 1993.
16. Ghosh, S., " Heat Transfer Analysis of Solidification Processes by the Arbitrary Lagrangian-Eulerian Finite Element Method ", *Computational Methods in Materials Processing*, MD- Vol. 39, ASME, pp 159-170, 1992.  
• Paper presented at *ASME Winter Annual Meeting*, Anaheim, CA, November 1992.

## Chapter 3

# The Voronoi Cell Finite Element Method for Heterogeneous Microstructures

### Summary

The Voronoi Cell finite element model (VCFEM) has been successfully developed for materials with arbitrary microstructural distribution. In this method, the finite element mesh evolves naturally by *Dirichlet Tessellation* of the microstructure. Composite VCFEM for small deformation plasticity has been developed by expressing the element stresses in terms of polynomial expansions of location coordinates. Though this works well for discrete composites with inclusions, its effectiveness diminishes sharply for porous materials with voids. The effect worsens sharply with voids of arbitrary shapes. To overcome this limitation, a new way of defining stress functions is introduced in this work. Based on a transformation method similar to the Schwarz-Christoffel conformal mapping, it introduces reciprocal stress functions that are derived to incorporate shape effects. Several numerical experiments are conducted to establish the strength of this formulation. The effect of various microstructural morphologies on the overall response and local variables are studied.

### 3.1 Introduction

Increased use of many advanced heterogeneous materials in the aerospace, automotive and electronics industries, has prompted widespread research for understanding their deformation and failure mechanisms in the recent years. Important classes of materials among them are metal/alloy systems with microscopic precipitates and pores, and composites containing a dispersion of fibers, whiskers or particulates in the matrix. The influence of microscopic heterogeneities on the overall behavior, depends on morphological characteristics like size, shape, orientation and spatial distribution of constituent phases, as well as on their properties. For example, ductility is reduced with increasing volume fraction of reinforcements in

metal-matrix composites. Christman et. al. [1] have shown that local plastic flow, which yields weaker areas of inhomogeneous deformation, is highly sensitive to shape of the reinforcements for identical global stresses. Studies reflecting the details of actual (not idealized) microstructure, are indispensable for establishing microstructure-property relationships. It is through these studies, that the effect of morphology on evolving state variables like stresses, plastic strains, void growth, and material variables like strain hardening and flow stress, can be established.

A number of micromechanical theories have been developed to predict overall constitutive response by employing continuum mechanics principles at the microscopic level. Notable among various analytical micromechanical models are those based on variational approach using extremum principles [2], probabilistic approaches [3], self-consistent schemes [4, 5] and the generalized self consistent models [6]. Though analytical micro-mechanical models are reasonably effective in predicting equivalent material properties for simple geometries and low second phase volume fractions, arbitrary distribution of shapes, sizes and location in real materials, cannot be deterministically treated. Constitutive response of the constituent phases are also restricted, and predictions with large property mismatches are not reliable. Despite the progress in analytical modeling of brittle heterogeneous materials, relatively little has been done for ductile materials. Important contributions have been made by Tandon and Weng [7], who have used the Mori-Tanaka mean-stress theory in conjunction with small strain elastic-plastic deformation theory, and by Dvorak and Bahei-El-Din [8] using a “vanishing fiber diameter” model, for rate-independent plastic matrix with elastic fibers. More recently, Dvorak and Bahei-El-Din [9] have developed the bimodal plasticity theory for nonhardening matrices. Aboudi [10] has predicted the response of composites with viscoplastic matrices and elastic inclusions and voids. Nemat-Nasser and coworkers [11] have used Fourier series expansions for periodic microstructures to develop elastic-plastic and creep models. The appropriateness of these models for many real materials is however questionable. This is because when plastic flow occurs in the ductile phase, the deformation is no longer homogeneous. Local properties become stress dependent and the overall constitutive response is influenced by the distributions and shapes of second phase.

Intractability of analytical models have necessitated the introduction of *Unit Cell* formulations [1, 13, 14] using computational techniques like the finite element method. These models generate overall material response through detailed discretization of a representative material element (RME). A majority of these models make assumptions of “perfect” local periodicity and uniform second phase distribution. Effectively, the local periodicity assumption can reduce the RME to a basic structural element (BSE), thereby making the unit cells very simple. A basic structural element is defined as the smallest element of the microstructure reflecting the basic geometrical features (see figure 1(b)). It is generally observed though, that real microstructures rarely possess such ordered structures as are necessary for this idealization. For accurate depiction of the microstructural evolution, the size of conventional FEM elements should be one to two orders of magnitude smaller than the BSE size. This results in the creation of very large meshes and enormous computations, for predictions on morphological changes and their effects on microstructural failure. This

limitation of conventional finite element methods necessitate novel computational methods for increased effectiveness in micro-mechanics studies.

To overcome the shortcomings of conventional Unit Cell models for arbitrary microstructural distribution, Ghosh and coworkers have innovated a material based *Voronoi Cell Finite Element Method (VCFEM)* [26, 27, 28, 29, 30, 19, 20]. In this method, the finite element mesh evolves by *Dirichlet Tessellation* of the microstructure (see [19], resulting in a network of multi-sided “Voronoi” polygons or cells containing one heterogeneity at most (figure 3.1). Effectively, each Voronoi cell element may be identified as a basic structural element of the microstructure. In VCFEM formulations, each cell with the embedded heterogeneity is treated as an element without any further discretization. It can thus drastically reduce preprocessing efforts as well as actual computations expended for complex RME’s. Additionally, it has been demonstrated by Richmond and coworkers [22] tessellation methods can be used very effectively in quantitative characterization of micrographs. Thus VCFEM can be used effectively to provide a direct link between quantitative metallography and mechanical response. In the VCFEM fomulations for small deformation plasticity [26, 27], the stress field within each element is expanded as polynomials of position coordinates. Though this works well for discrete composites with inclusions, its effectiveness diminishes sharply for porous materials with voids. Large number of terms are required in the stress expressions to yield acceptable accuracy. The accuracy drops sharply with voids of arbitrary shapes. This is because the stress functions are required to meet the zero traction condition at the void boundary and undergo very large gradients near the interface. For composites, this is less drastic and a reasonable number of terms can accommodate the traction discontinuity.

In this work, a new method of defining stress functions is introduced as a remedy. Based on a transformation, similar to the Schwarz-Christoffel conformal mapping, reciprocal stress functions are derived to incorporate shape effects. These modifications make it very suitable for application to a wide variety of heterogeneous materials. The chapter begins with a brief overview of the VCFEM formulation and elucidates the limitations of pure polynomial based stress expansions. It then introduces shape based stress interpolations and solves several numerical experiments to establish the strength of this formulation. Finally, the effect of various microstructural morphologies on overall response and local evolution are qualitatively studied.

### 3.2 The Voronoi Cell Finite Element Model for Heterogeneous Microstructures

Voronoi cells resulting from Dirichlet tessellation of a heterogeneous microstructure make rather unconventional elements, due to the arbitrariness in the number of edges. The application of conventional displacement-based finite element methods to these elements, suffer from difficulties associated with interelement displacement compatibility and rank deficiencies of the stiffness matrix. The Voronoi Cell finite element model developed by Ghosh and coworkers [26, 27, 28, 29, 30] avoids these difficulties by invoking the assumed stress hybrid

method introduced by Pian [33]. In this formulation, independent assumptions are made on an equilibrated stress field in the interior of each element and a compatible displacement field on the element boundary. Small deformation, elastic-plastic analysis of materials, embedded with second phase inclusions, has shown significant promise with this method [26, 27]. The developments use an assumed stress hybrid formulation for rate independent  $J_2$  flow theory, based on a generalized Hu-Washizu principle, originally proposed by Atluri [34, 35]). Though the details of this method are available in [26, 27], a brief overview of the formulation essentials is presented here for completeness.

### 3.2.1 Variational principle with assumed stress hybrid method

Consider a typical representative material element (RME)  $\Omega$ , as shown in figure 1. The heterogeneous domain  $\Omega$  is tessellated into  $N$  Voronoi cells based on the location, shape and size of  $N$  heterogeneities as explained in [19]. The matrix phase in each Voronoi cell is denoted by  $\Omega_m$  and the heterogeneity (void or inclusion) is denoted by  $\Omega_c$ . Each element boundary  $\partial\Omega_e$  is assumed to be comprised of three mutually disjoint parts, viz. (a) prescribed traction boundary  $\Gamma_{tm}$ , (b) prescribed displacement boundary  $\Gamma_{um}$ , and (c) interelement boundary  $\Gamma_m$ , i.e.  $\partial\Omega_e = \Gamma_{tm} \cup \Gamma_{um} \cup \Gamma_m$ . The matrix-second phase interface  $\partial\Omega_c$  has an outward normal  $\mathbf{n}^c$ , while  $\mathbf{n}^e$  is the outward normal to  $\partial\Omega_e$ . An incremental finite element formulation is invoked to account for the evolutionary constitutive equations in rate independent plasticity. At the beginning of the  $p$ -th increment, let  $\boldsymbol{\sigma}$  be an equilibrated stress field with a strain field  $\boldsymbol{\epsilon}(\boldsymbol{\sigma}, \text{load history})$ , and  $\mathbf{u}$  be a compatible displacement field on the element boundary. Also let  $\Delta\boldsymbol{\sigma}$  correspond to an equilibrated stress increment in  $\Omega_e$ ,  $\Delta\mathbf{u}$  to a compatible displacement increment on  $\partial\Omega_e$ , and  $\Delta\mathbf{t}$  to a traction increment on  $\Gamma_{tm}$ . The incremental problem is solved by using a two field assumed stress hybrid variational principle, derived from an element energy functional as:

$$\begin{aligned} \Pi_e(\Delta\boldsymbol{\sigma}, \Delta\mathbf{u}) = & - \int_{\Omega_e} \Delta B(\boldsymbol{\sigma}, \Delta\boldsymbol{\sigma}) \, d\Omega - \int_{\Omega_e} \boldsymbol{\epsilon} : \Delta\boldsymbol{\sigma} \, d\Omega \\ & + \int_{\partial\Omega_e} (\boldsymbol{\sigma} + \Delta\boldsymbol{\sigma}) \cdot \mathbf{n}^e \cdot (\mathbf{u} + \Delta\mathbf{u}) \, \partial\Omega - \int_{\Gamma_{tm}} (\bar{\mathbf{t}} + \Delta\bar{\mathbf{t}}) \cdot (\mathbf{u} + \Delta\mathbf{u}) \, d\Gamma \\ & - \int_{\partial\Omega_c} (\boldsymbol{\sigma}^m + \Delta\boldsymbol{\sigma}^m - \boldsymbol{\sigma}^c - \Delta\boldsymbol{\sigma}^c) \cdot \mathbf{n}^c \cdot (\mathbf{u}' + \Delta\mathbf{u}') \, \partial\Omega \end{aligned} \quad (3.1)$$

where  $\Delta\mathbf{u}'$  the displacement of the interface and  $\Delta\mathbf{B}$  is the increment in element complementary energy. Superscripts  $m$  and  $c$  represent respectively the matrix and second phase parts of the Voronoi cell element. The energy functional for the entire domain is obtained by adding each element functional as

$$\Pi = \sum_{e=1}^N \Pi_e \quad (3.2)$$

The first variation of  $\Pi_e$  with respect to the stress increments  $\Delta\boldsymbol{\sigma}$ , results in the kinematic relations as the Euler equation,

$$\nabla \Delta\mathbf{u} = \Delta\boldsymbol{\epsilon} \text{ in } \Omega_e \quad (3.3)$$

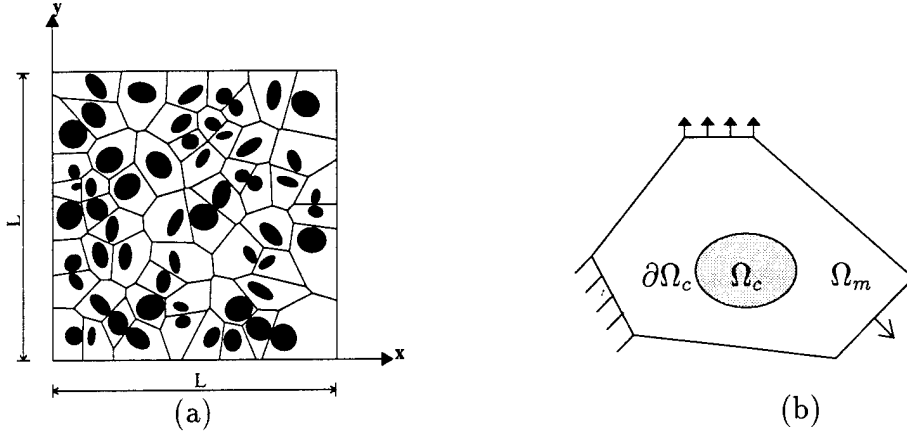


Figure 3.1: (a) Representative material element (b) Voronoi cell finite element

while the first variation of  $\Pi$  with respect to boundary displacement increments  $\Delta\mathbf{u}$  yields traction conditions as Euler equations,

$$\begin{aligned} (\boldsymbol{\sigma} + \Delta\boldsymbol{\sigma}) \cdot \mathbf{n}^{e+} &= -(\boldsymbol{\sigma} + \Delta\boldsymbol{\sigma}) \cdot \mathbf{n}^{e-} \quad \text{on } \Gamma_m \quad \text{Interelement traction reciprocity} \\ (\boldsymbol{\sigma} + \Delta\boldsymbol{\sigma}) \cdot \mathbf{n}^e &= \bar{\mathbf{t}} + \bar{\Delta}\mathbf{t} \quad \text{on } \Gamma_{tm} \quad \text{Traction boundary conditions} \\ (\boldsymbol{\sigma}^c + \Delta\boldsymbol{\sigma}^c) \cdot \mathbf{n}^c &= (\boldsymbol{\sigma}^m + \Delta\boldsymbol{\sigma}^m) \cdot \mathbf{n}^c \quad \text{on } \partial\Omega_c \quad \text{Interface traction reciprocity} \end{aligned} \quad (3.4)$$

Equilibrated stress increments  $\Delta\boldsymbol{\sigma}$ , constitutive relations, along with the incremented form of the energy functional completely define the  $p$ -th increment problem.

### 3.2.2 Element formulations and assumptions

In the Voronoi cell finite element model (VCFEM) formulation, independent assumptions on the equilibrated incremental stress field in  $\Omega_e$  and on the compatible incremental displacement field on  $\partial\Omega$  are made. Furthermore, independent assumptions on stress increments  $\Delta\boldsymbol{\sigma}$  are made in the matrix and heterogeneity phases to accommodate stress jumps across the interface. Use of Airy's stress functions  $\Phi(x, y)$  is a convenient method of deriving polynomial forms of stress increments in two-dimensional analysis, and is expressed as:

$$\Delta\sigma_{xx} = \frac{\partial^2\Phi}{\partial y^2}, \quad \Delta\sigma_{yy} = \frac{\partial^2\Phi}{\partial x^2}, \quad \Delta\sigma_{xy} = -\frac{\partial^2\Phi}{\partial x\partial y} \quad (3.5)$$

Different expressions may be assumed for  $\Phi$  in the matrix and inclusion phases. For example, a third order complete polynomial expansion of  $\Phi^m$  may be assumed to give the stress increments in the matrix phase as

$$\begin{Bmatrix} \Delta\sigma_{xx}^m \\ \Delta\sigma_{yy}^m \\ \Delta\sigma_{xy}^m \end{Bmatrix} = \begin{bmatrix} 1 & y & 0 & 0 & 0 & x & 0 \\ 0 & 0 & 1 & x & 0 & 0 & y \\ 0 & 0 & 0 & 0 & 1 & -y & -x \end{bmatrix} \begin{Bmatrix} \Delta\beta_1^m \\ \vdots \\ \Delta\beta_7^m \end{Bmatrix} \quad (3.6)$$

where  $\{\Delta\beta^m\}$ 's correspond to a set of yet undetermined stress coefficients. In general, the stress functions can be arbitrary functions of location, yielding stress increments in the form

$$\begin{aligned}\{\Delta\sigma^m\} &= [\mathbf{P}^m(x, y)]\{\Delta\beta^m\} \\ \{\Delta\sigma^c\} &= [\mathbf{P}^c(x, y)]\{\Delta\beta^c\}\end{aligned}\quad (3.7)$$

Compatible displacement increments may be generated by interpolation in terms of generalized nodal values on the element boundary  $\partial\Omega_e$  as well as on the interface  $\partial\Omega_c$ . Note that compatible displacement fields on  $\partial\Omega_c$  imply perfect bonding in the case of composite materials. A linear interpolation of displacement increments on the  $i$ th and  $(i+1)$ th boundary nodal points, for example may be expressed as,

$$\{\Delta\mathbf{u}\} = \begin{Bmatrix} \Delta u_x \\ \Delta u_y \end{Bmatrix} = \begin{bmatrix} 1 - s/l_i & 0 & s/l_i & 0 \\ 0 & 1 - s/l_i & 0 & s/l_i \end{bmatrix} \begin{Bmatrix} \Delta q_{2i-1} \\ \Delta q_{2i} \\ \Delta q_{2i+1} \\ \Delta q_{2i+2} \end{Bmatrix} \quad (3.8)$$

where  $l_i$  is the length of segment and  $s$  is the distance from the  $i$ -th node. The displacement increments on the element boundary and interface may be written as,

$$\begin{aligned}\{\Delta\mathbf{u}\} &= [\mathbf{L}^e]\{\Delta\mathbf{q}\} \\ \{\Delta\mathbf{u}'\} &= [\mathbf{L}^c]\{\Delta\mathbf{q}'\}\end{aligned}\quad (3.9)$$

where  $\{\Delta\mathbf{q}\}$  and  $\{\Delta\mathbf{q}'\}$  are generalized displacement increment vectors. Substituting element approximations for stresses (3.7), and displacements (3.9), in the energy functional (3.1), and setting the first variations with respect to the stress parameters  $\Delta\beta^m$  and  $\Delta\beta^c$  respectively to zero, results in the following two weak forms of the kinematic relations (3.3),

$$\begin{aligned}\int_{\Omega_m} [\mathbf{P}^m]^T \{\epsilon + \Delta\epsilon\} d\Omega &= \int_{\partial\Omega_e} [\mathbf{P}^m]^T [\mathbf{n}^e] [\mathbf{L}^e] d\Omega \{\Delta\mathbf{q}\} - \int_{\partial\Omega_c} [\mathbf{P}^m]^T [\mathbf{n}^c] [\mathbf{L}^c] d\Omega \{\Delta\mathbf{q}'\} \\ \int_{\Omega_c} [\mathbf{P}^c]^T \{\epsilon + \Delta\epsilon\} d\Omega &= \int_{\partial\Omega_c} [\mathbf{P}^c]^T [\mathbf{n}^c] [\mathbf{L}^e] d\Omega \{\Delta\mathbf{q}'\}\end{aligned}\quad (3.10)$$

For two-dimensional problems  $[\mathbf{n}^e]$  and  $[\mathbf{n}^c]$  are  $(3 \times 2)$  matrices, consisting of the normal components in the form:

$$[\mathbf{n}(\mathbf{x})] = \begin{bmatrix} n_x(\mathbf{x}) & 0 \\ 0 & n_y(\mathbf{x}) \\ n_y(\mathbf{x}) & n_x(\mathbf{x}) \end{bmatrix}$$

Setting the first variation of the total energy functional (3.2) with respect to  $\Delta\mathbf{q}$  and  $\Delta\mathbf{q}'$  to zero results in the weak form of the traction reciprocity conditions as

$$\sum_{e=1}^N \begin{bmatrix} \int_{\partial\Omega_e} [\mathbf{L}^e]^T [\mathbf{n}^e]^T [\mathbf{P}^m] d\Omega & \mathbf{0} \\ -\int_{\partial\Omega_e} [\mathbf{L}^c]^T [\mathbf{n}^c]^T [\mathbf{P}^m] d\Omega & \int_{\partial\Omega_c} [\mathbf{L}^c]^T [\mathbf{n}^c]^T [\mathbf{P}^c] d\Omega \end{bmatrix} \begin{Bmatrix} \beta^m + \Delta\beta^m \\ \beta^c + \Delta\beta^c \end{Bmatrix} =$$

$$\sum_{e=1}^N \left\{ \begin{array}{l} \int_{\Gamma_{tm}} [\mathbf{L}^e]^T \{ \bar{\mathbf{t}} + \bar{\Delta t} \} d\Omega \\ \{ \mathbf{0} \} \end{array} \right\} \quad (3.11)$$

For an elastic-plastic material, the strain increments  $\Delta\epsilon$  in equation (3.10) are non-linear functions of the current state of stress  $\sigma$  as well as of their increments  $\Delta\sigma$ . The non-linear finite element equations (3.10) and (3.11) are solved for the stress parameters  $(\Delta\beta^m, \Delta\beta^c)$  and the nodal displacement increments  $(\Delta\mathbf{q}, \Delta\mathbf{q}')$  at the  $p$ -th increment.

### 3.2.3 Constitutive Relations

A rate independent small deformation elasto-plastic constitutive relation, following  $J_2$  flow theory with isotropic hardening, is considered in this work. A brief account of the numerical integration of the constitutive relations is presented here. More details are given in [27] and a similar method is also presented in [26]. An additive decomposition of the strain increments  $\Delta\epsilon$  into an elastic part  $\Delta\epsilon^e$  and a plastic part  $\Delta\epsilon^{pl}$  is assumed, i.e.

$$\Delta\epsilon = \Delta\epsilon^e + \Delta\epsilon^{pl} \quad (3.12)$$

The elastic part of the strain increment tensor is obtained by the inner product of the compliance tensor with the stress increment tensor. The yield surface in stress-space at the beginning of the  $p$ -th increment is expressed as,

$$Y^p(\epsilon, \Delta\epsilon) = \sqrt{\frac{3}{2} \sigma' : \sigma'} \quad (3.13)$$

where  $\sigma'$  is the stress deviator and  $Y(\epsilon, \Delta\epsilon)$  is the radius of the flow surface. The plastic strain increment  $\Delta\epsilon^{pl}$  is obtained by numerically integrating the flow rule by the backward Euler method to yield :

$$\Delta\epsilon^{pl} = \Delta\lambda(\sigma + \Delta\sigma)' \quad (3.14)$$

where  $\Delta\lambda$  is a non-negative incremental flow parameter. Since  $\Delta\epsilon$  is in general a function of  $\Delta\lambda$ ,  $\sigma$  and  $\Delta\sigma$ , the flow surface radius can be expressed in the form,

$$Y^{p+1} = Y^{p+1}(\Delta\lambda, \sigma, \Delta\sigma)$$

and the flow parameter  $\Delta\lambda$  can be evaluated from the following relations.

$$\Delta\lambda = 0 \text{ if } \sigma_{eff}^{p+1} < Y^p \text{ (elastic unloading)} \quad (3.15)$$

$$\sigma_{eff}^{p+1} = Y^{p+1} \text{ if } \sigma_{eff}^{p+1} \geq Y^p \text{ (neutral and plastic loading)} \quad (3.16)$$

Numerical implementation requires computation of tangent operators through linearized forms of the constitutive relations. If  $d\epsilon$  is the first order correction to the current strain increment  $\Delta\epsilon$ , and  $d\sigma$  is the corresponding stress increment  $\Delta\sigma$  correction, the fourth order elastic-plastic compliance tensor (or tangent operator)  $\mathbf{S}$  is given by the relation

$$d\epsilon = \mathbf{S} : d\sigma$$

The elastic part of this equation expressed as

$$d\boldsymbol{\epsilon}^e = \mathbf{S}_e : d\boldsymbol{\sigma} \quad (3.17)$$

The plastic part of the strain correction  $d\boldsymbol{\epsilon}^{pl}$  however requires a first order correction  $d\lambda$  to the current flow parameter  $\Delta\lambda$ , which by the  $J_2$  flow theory, takes the form

$$d\boldsymbol{\epsilon}^{pl} = \frac{9}{4H} \frac{(\boldsymbol{\sigma} + \Delta\boldsymbol{\sigma})' \otimes (\boldsymbol{\sigma} + \Delta\boldsymbol{\sigma})'}{(\sigma_{eff}^{p+1})^2} : d\boldsymbol{\sigma} = \mathbf{S}_{pl} : d\boldsymbol{\sigma} \quad (3.18)$$

where  $H$  is a linearized hardening modulus. The elasto-plastic tangent operator  $\mathbf{S}$  is obtained by adding equations (3.17) and (3.18) as

$$\mathbf{S} = \mathbf{S}_e + \mathbf{S}_{pl} \quad (3.19)$$

A linearized form of the incremental complementary energy functional  $\Delta B$  in equation (3.1) can now be expressed in terms of the tangent operator as

$$dB(\boldsymbol{\sigma}, d\boldsymbol{\sigma}) = \frac{1}{2} d\boldsymbol{\sigma} : \mathbf{S} : d\boldsymbol{\sigma} \quad (3.20)$$

Note that the elastic-plastic tangent operator  $\mathbf{S}$  in equation (3.19) is positive definite since its components are individually positive definite. Both plane stress and plane strain conditions have been solved in an iterative manner by this basic algorithms. Details are provided in [27].

### 3.2.4 Solution Method for the Weak Form

For rate independent plasticity, the strain increments  $\Delta\boldsymbol{\epsilon}(\Delta\boldsymbol{\sigma}, \boldsymbol{\sigma})$  are nonlinear functions of the stress parameters  $\Delta\boldsymbol{\beta}^m$  and  $\Delta\boldsymbol{\beta}^c$ . An iterative solution process is therefore invoked for equation (3.10) to evaluate the stresses, given the nodal displacement increments  $\{\Delta\mathbf{q}\}$  and  $\{\Delta\mathbf{q}'\}$ . Let  $\{d\boldsymbol{\beta}\}^i$  correspond to the correction to the value of  $\Delta\boldsymbol{\beta}$  in the  $i$ -th iteration, i.e.

$$\begin{aligned} \{\Delta\boldsymbol{\beta}^m\} &= \{\Delta\boldsymbol{\beta}^m\}^i + \{d\boldsymbol{\beta}^m\}^i \\ \{\Delta\boldsymbol{\beta}^c\} &= \{\Delta\boldsymbol{\beta}^c\}^i + \{d\boldsymbol{\beta}^c\}^i \end{aligned}$$

The kinematic equation (3.10) may then be linearized with respect to  $\Delta\boldsymbol{\beta}$  to yield:

$$\begin{bmatrix} \mathbf{H}_m & \mathbf{0} \\ \mathbf{0} & \mathbf{H}_c \end{bmatrix} \begin{Bmatrix} d\boldsymbol{\beta}^m \\ d\boldsymbol{\beta}^c \end{Bmatrix}^i = \begin{bmatrix} \mathbf{G}_e & -\mathbf{G}_{cm} \\ \mathbf{0} & \mathbf{G}_{cc} \end{bmatrix} \begin{Bmatrix} \mathbf{q} + \Delta\mathbf{q} \\ \mathbf{q}' + \Delta\mathbf{q}' \end{Bmatrix} - \begin{Bmatrix} \int_{\Omega_m} [\mathbf{P}^m]^t \{\boldsymbol{\epsilon} + \Delta\boldsymbol{\epsilon}\}^i d\Omega \\ \int_{\Omega_c} [\mathbf{P}^c]^t \{\boldsymbol{\epsilon} + \Delta\boldsymbol{\epsilon}\}^i d\Omega \end{Bmatrix} \quad (3.21)$$

In a condensed form this can be restated as:

$$[\mathbf{H}] \{d\boldsymbol{\beta}\}^i = [\mathbf{G}] \{\Delta\mathbf{u}\} - \begin{Bmatrix} \int_{\Omega_m} [\mathbf{P}^m]^t \{\boldsymbol{\epsilon} + \Delta\boldsymbol{\epsilon}\}^i d\Omega \\ \int_{\Omega_c} [\mathbf{P}^c]^t \{\boldsymbol{\epsilon} + \Delta\boldsymbol{\epsilon}\}^i d\Omega \end{Bmatrix} \quad \forall e = 1 \dots N \quad (3.22)$$

where,

$$[\mathbf{H}_m] = \int_{\Omega_m} [\mathbf{P}^m]^T [\mathbf{S}] [\mathbf{P}^m] d\Omega, \quad [\mathbf{H}_c] = \int_{\Omega_c} [\mathbf{P}^c]^T [\mathbf{S}] [\mathbf{P}^c] d\Omega$$

$$[\mathbf{G}_e] = \int_{\partial\Omega_e} [\mathbf{P}^m]^T [\mathbf{n}^e] [\mathbf{L}^e] d\Omega, \quad [\mathbf{G}_{cm}] = \int_{\partial\Omega_c} [\mathbf{P}^m]^T [\mathbf{n}^c] [\mathbf{L}^c] d\Omega, \quad [\mathbf{G}_{cc}] = \int_{\partial\Omega_c} [\mathbf{P}^c]^T [\mathbf{n}^c] [\mathbf{L}^c] d\Omega$$

$[\mathbf{S}(x, y)]$  is the instantaneous elastic-plastic tangent compliance tensor as derived in equation (3.19). A quasi-Newton iterative solution procedure is used to solve equation (3.22). Details of numerical integration schemes for plane stress and plane strain conditions are presented in [26, 27].

The above procedure of solving for the stresses take place within an iterative loop, in which the traction reciprocity conditions (3.11) are solved for the nodal displacement increments  $\{\Delta\mathbf{q}\}$  and  $\{\Delta\mathbf{q}'\}$ . Proceeding in the same way as for stresses, let  $\{d\mathbf{q}\}^j$  correspond to the correction in  $\{\Delta\mathbf{q}\}$  in the  $j$ -th iteration of (3.11), i.e.

$$\{\Delta\mathbf{q}\} = \{\Delta\mathbf{q}\}^j + \{d\mathbf{q}\}^j$$

$$\{\Delta\mathbf{q}'\} = \{\Delta\mathbf{q}'\}^j + \{d\mathbf{q}'\}^j$$

Substituting equation (3.22) in the linearized global traction reciprocity equation (3.11), with respect to  $\{\Delta\mathbf{q}\}$ , yields the matrix equation:

$$\sum_{e=1}^N [\mathbf{G}]^T [\mathbf{H}]^{-1} [\mathbf{G}] \begin{Bmatrix} d\mathbf{q} \\ d\mathbf{q}' \end{Bmatrix}^j = \sum_{e=1}^N \begin{Bmatrix} \int_{\Gamma_{tm}} [\mathbf{L}^m]^T \{\bar{\mathbf{t}} + \Delta\mathbf{t}\} d\Omega \\ \mathbf{0} \end{Bmatrix} -$$

$$\sum_{e=1}^N \begin{bmatrix} \int_{\partial\Omega_e} [\mathbf{L}^e]^T [\mathbf{n}^e]^T [\mathbf{P}^m] d\Omega & \mathbf{0} \\ -\int_{\partial\Omega_c} [\mathbf{L}^c]^T [\mathbf{n}^c]^T [\mathbf{P}^m] d\Omega & \int_{\partial\Omega_c} [\mathbf{L}^c]^T [\mathbf{n}^c]^T [\mathbf{P}^c] d\Omega \end{bmatrix} \begin{Bmatrix} \beta^m + \Delta\beta^m \\ \beta^c + \Delta\beta^c \end{Bmatrix}^j$$

or, in standard finite element notation

$$\sum_{e=1}^N [\mathbf{K}_e] \{d\mathbf{u}\}^j = \sum_{e=1}^N \{\mathbf{f}_e\} -$$

$$\sum_{e=1}^N \begin{bmatrix} \int_{\partial\Omega_e} [\mathbf{L}^e]^T [\mathbf{n}^e]^T [\mathbf{P}^m] d\Omega & \mathbf{0} \\ -\int_{\partial\Omega_c} [\mathbf{L}^c]^T [\mathbf{n}^c]^T [\mathbf{P}^m] d\Omega & \int_{\partial\Omega_c} [\mathbf{L}^c]^T [\mathbf{n}^c]^T [\mathbf{P}^c] d\Omega \end{bmatrix} \begin{Bmatrix} \beta^m + \Delta\beta^m \\ \beta^c + \Delta\beta^c \end{Bmatrix}^j \quad (3.23)$$

With known traction increments on  $\Gamma_{tm}$  and displacement increments on  $\Gamma_{um}$ , the linearized global traction reciprocity condition (3.23) is solved iteratively using the quasi-Newton method for nodal displacement increments.

### 3.2.5 Numerical Aspects of Voronoi Cell FEM

Matrices  $[\mathbf{H}_m]$  and  $[\mathbf{H}_c]$  need to be inverted for evaluating the element stiffness matrix  $[\mathbf{K}_e]$ . However, Airy's stress functions represented by simple polynomial expressions of Cartesian coordinates can sometimes lead to a bad conditioning number for  $[\mathbf{H}_m]$  and  $[\mathbf{H}_c]$ . This can lead to considerable numerical inaccuracy in the resulting stiffness matrix. To circumvent

this problem, Ghosh et.al. [26, 27] have used scaled polynomial stress functions in terms local element coordinates  $(\xi, \eta)$ . The mapping from the  $(x, y)$  coordinate system is expressed as:

$$\begin{aligned}\xi &= (x - x_c)/l \\ \eta &= (y - y_c)/l\end{aligned}\quad (3.24)$$

where  $(x_c, y_c)$  are the centroidal coordinates of a Voronoi cell element and  $l$  is a scaling parameter given as:

$$l = \sqrt{\max(x - x_c) \max(y - y_c)} \quad \forall (x, y) \in \partial\Omega_e$$

The scaling to  $(\xi, \eta)$ , leads to an approximate range of variation  $-1 \leq \xi \leq 1$  and  $-1 \leq \eta \leq 1$  in most Voronoi cell elements. Note that this range is exactly true for square elements. As an example, a third order complete polynomial Airy's function in terms of  $(\xi, \eta)$  gives rise to:

$$[\mathbf{P}] = \begin{bmatrix} 1 & \eta & 0 & 0 & 0 & \xi & 0 \\ 0 & 0 & 1 & \xi & 0 & 0 & \eta \\ 0 & 0 & 0 & 0 & 1 & -\eta & -\xi \end{bmatrix}$$

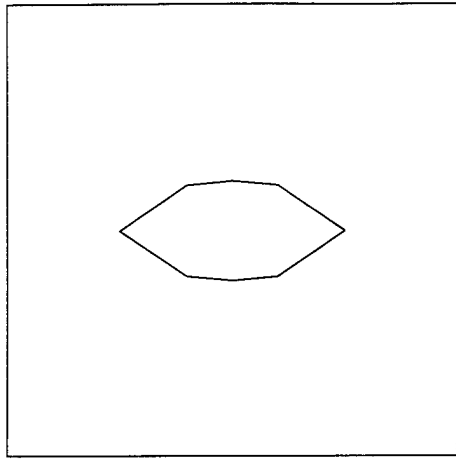
Another factor that contributes to the convergence of the method is accurate domain integration to evaluate  $[\mathbf{H}_m]$  and  $[\mathbf{H}_c]$ . For polynomial stress functions, the matrices are also polynomial functions of scaled coordinates  $(\xi, \eta)$ . For numerical domain integration of these functions, the Voronoi cells are subdivided into quadrilaterals (see figure 3.4(a)) to be mapped into square master domains. Integration is then performed by Gaussian quadrature rule, with number of Gauss points determined from the order of terms in  $[\mathbf{P}]$ .

### 3.3 Shape Based Stress Representations

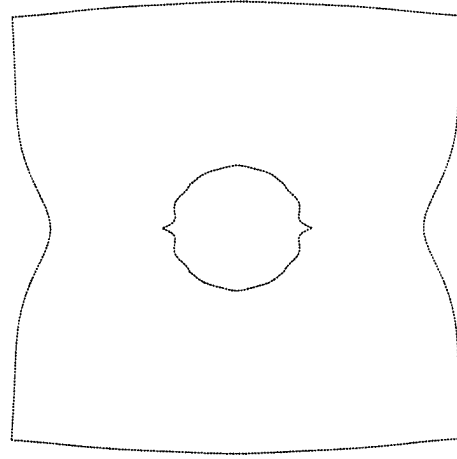
An important criterion, affecting the convergence of multiple phase Voronoi cell elements, is the proper representation of stress fields in each of the constituent phases. In general, choosing matrix stress functions from micromechanics considerations, adds considerably to the element efficiency. Three different conditions that are indispensable in this regard are:

1. Stress functions should, in some way, account for the shape of the heterogeneity.
2. Effects of the heterogeneity shape should vanish at large distances from the interface, for matrix stress functions .
3. Shape effects in matrix stress functions should facilitate traction reciprocity at the interface.

For both composite and porous materials, the first two considerations imply that the shape effect should be dominant near the interface, but vanish in the far-field. The third condition is intended to counteract interface tractions caused by the inclusion for composites, while



(a)



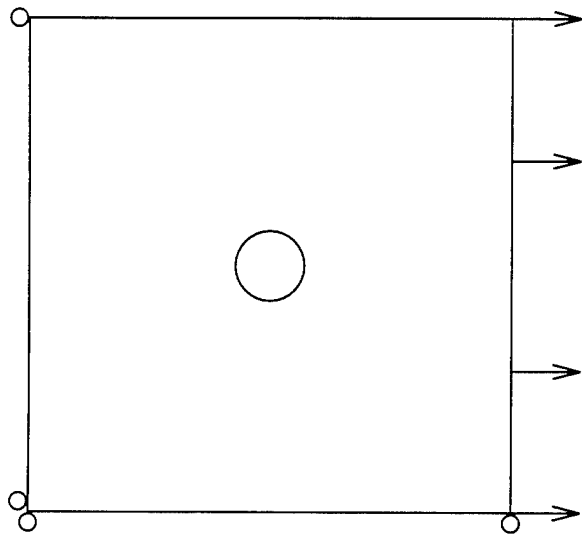
(b)

Figure 3.2: (a) Actual shape of a Voronoi Cell with embedded heterogeneity (b) Transformed shape of the VCE by approximate Schwarz Christoffel transformation

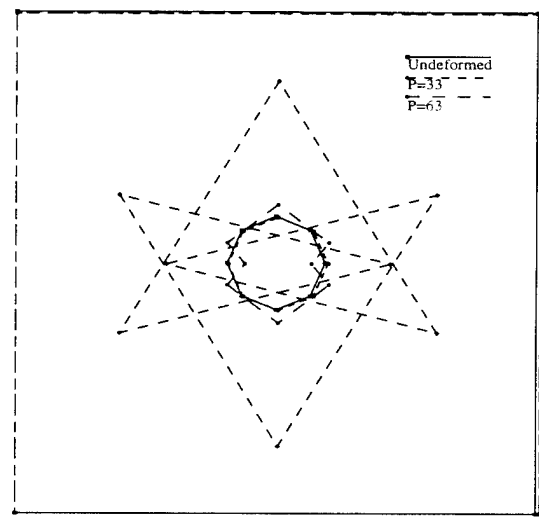
reduce to zero interface tractions for porous materials.

Pure polynomial forms Airy's stress functions do not explicitly account for the shape of the heterogeneity, and consequently requires very high order terms (especially for porous media) for convergence. The following example in figure 3.3(a) is considered to illustrate the necessity of adequate stress field representation. A single unit square Voronoi cell element, with a circular void of volume fraction  $V_f = 2.5\%$  is unidirectionally stretched by  $\Delta u_x = 0.008$  units, under plane stress conditions. The material is elastic with Young's modulus  $E = 250$  and Poisson ratio  $\nu = 0.33$ . Two different polynomial stress functions are considered for solving this problem, viz. (a) a 33 term, 7th order stress function ( $\Phi$ ) corresponding to a 5th order stress representation and (b) a 63 term, 10th order  $\Phi$  corresponding to a 8th order stress representation. The deformed configurations are depicted in figure 3.3(b). It clearly shows that lower order stress representations gives rise to unstable deformation modes at the void interface, probably triggered through under-represented element energy. Extremely poor approximation to the stress concentration is observed in figure 3.3(d), which shows its distribution along a line through the element center. Though the interface deformation improves with higher order stress terms (figure 3.3(b)), the stress values are less than acceptable near the interface. The results emphasize the importance of proper matrix stress function selection in VCFEM formulation.

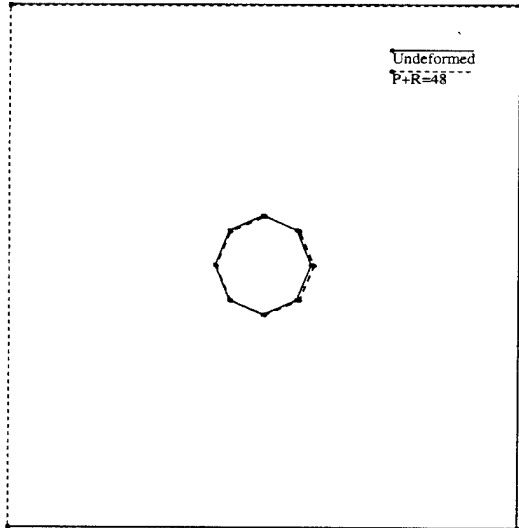
Problems of stress concentrations around voids have been traditionally handled by the use of specialized stress functions, that account for its shape. Analytical solutions by Muskhelishvili [27] and Sarin [28] use the Schwarz-Christoffel conformal mapping to transform an



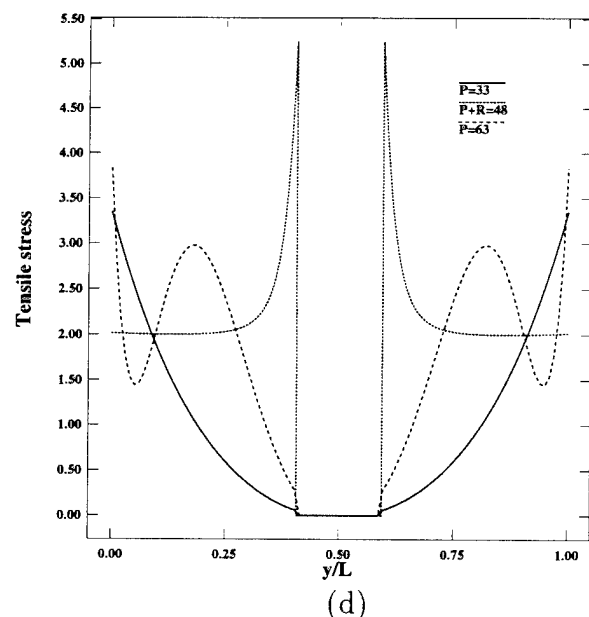
(a)



(b)



(c)



(d)

Figure 3.3: (a) VCFEM mesh for a unit square with a circular hole of volume fraction  $V_f = 2.5\%$  (b) Computed deformed shape with pure polynomial stress functions ( $\mathbf{P}$ ) (c) Computed deformed shape with shape based stress functions ( $\mathbf{P+R}$ ) (b) Tensile stress distribution along the line  $x/L=0.5$  for both cases

arbitrary shaped void into a circle in the complex plane. Analytic functions are then defined in the transformed plane and used to generate accurate stress functions. Complex functions and conformal mapping techniques have been used by Tong et.al [36] and Piltner [37] to construct trial stress functions in the assumed stress hybrid finite element method, for elastic problems with cracks and holes. The stress functions are chosen to satisfy the biharmonic equation because of linear elastic materials.

Stress functions for the VCFEM with material nonlinearity are based on the three conditions mentioned above. Consider a typical embedded heterogeneity as shown in figure 3.1(b). Suppose that equation of the interface  $\partial\Omega_c$  can be expressed in polar coordinates as  $g(r, \theta) = 0$ , where the  $r$  coordinate is measured from the centroid of the heterogeneity. A Fourier series expansion for  $r$  in terms of the polar angle  $\theta$  may be expressed as:

$$r = a_o + \sum_n a_n \cos(n\theta) + \sum_n b_n \sin(n\theta) \quad \text{on } \partial\Omega_c \quad (3.25)$$

where the Fourier coefficients  $a_n$  and  $b_n$  are given as:

$$\begin{aligned} a_o &= \frac{1}{2\pi} \int_{d\Omega_c} r d\Omega \\ a_n &= \frac{1}{\pi} \int_{d\Omega_c} r \cos(n\theta) d\Omega \quad n = 1, 2, \dots \\ b_n &= \frac{1}{\pi} \int_{d\Omega_c} r \sin(n\theta) d\Omega \quad n = 1, 2, \dots \end{aligned}$$

The interface equation may then be expressed from (3.25) as,

$$g(r, \theta) = f - \frac{r}{a_0} - \sum_n \frac{a_n}{a_0} \cos(n\theta) - \sum_n \frac{b_n}{a_0} \sin(n\theta) = 0 \quad (3.26)$$

Here  $f$  corresponds to a function that transforms any arbitrary shaped interface to an approximate unit circle, since  $f(x, y) = 1$  on  $\partial\Omega_c$ . A typical numerical transformation of a voided cell is shown in figure 3.2. The mapped function  $f(r, \theta)$  may be thought of as a special radial coordinate with the property that  $\frac{1}{f} \rightarrow 0$  as  $(x, y) \rightarrow \infty$ . This function is now used to construct shape based reciprocal stress functions associated with polynomial functions. Thus if the polynomial stress function is represented by  $\Phi_{poly}^m = \sum_{p,q} \beta_{pq} \xi^p \eta^q$ , then for each term there exists reciprocal terms expressed by  $\Phi_{rec}^m$ , that give rise to stresses equilibrating the traction field on  $\partial\Omega_c$ . This is written as:

$$\Phi_{rec}^m = \sum_{p,q} \xi^p \eta^q \left( \frac{\Delta \beta_{pq1}}{f^{p+q}} + \frac{\Delta \beta_{pq2}}{f^{p+q+1}} + \dots \right)$$

The Voronoi cell element stress function in the matrix phase is then written as:

$$\Phi^m = \Phi_{poly}^m + \Phi_{rec}^m \quad (3.27)$$

Computation of stress increments from  $\Phi^m$  takes place in the following manner. Increment of traction vector  $\Delta t$  may be related to the stress function  $\Phi^m$  using equation (3.5) as:

$$\Delta t_x = \frac{\partial \Phi^m}{\partial y} , \quad \Delta t_y = -\frac{\partial \Phi^m}{\partial x}$$

Substituting equation (3.27) in the traction increments gives

$$\begin{aligned} \Delta t_x &= \sum_{p,q} q \xi^p \eta^{n-1} (\Delta \beta_{pq} + \sum_{i=p+q}^{\infty} \Delta \beta_{pqi} \frac{1}{f^i}) - \sum_{p,q} \xi^p \eta^q \sum_{i=p+q}^{\infty} \Delta \beta_{pqi} i \frac{1}{f^{i+1}} \frac{\partial f}{\partial y} \\ \Delta t_y &= -\sum_{p,q} p \xi^{m-1} \eta^q (\Delta \beta_{pq} + \sum_{i=p+q}^{\infty} \Delta \beta_{pqi} \frac{1}{f^i}) + \sum_{p,q} \xi^p \eta^q \sum_{i=p+q}^{\infty} \Delta \beta_{pqi} i \frac{1}{f^{i+1}} \frac{\partial f}{\partial x} \end{aligned} \quad (3.28)$$

Coefficients of the reciprocal stress function  $\Delta \beta_{pqi}$ , in first set of terms in equation (3.28), add more flexibility to polynomial coefficients  $\Delta \beta_{pq}$  for matching desired tractions at the interface ( $f = 1$ ). The gradient of  $f$  in second set of terms account for the interface shape. The reciprocal terms in equation (3.28) have negligible effects on the traction far away from the heterogeneity, by  $f$  becoming extremely large. The far-field tractions are therefore produced predominantly by polynomial terms in the stress function and are unaffected by the shape of the heterogeneity. Matrix phase stress increments are obtained from the traction increments by using equation (3.5) as:

$$\begin{aligned} \begin{Bmatrix} \Delta \sigma_{xx}^m \\ \Delta \sigma_{yy}^m \\ \Delta \sigma_{xy}^m \end{Bmatrix} &= \begin{Bmatrix} \sum_{p,q} \frac{\partial^2 (\xi^p \eta^q)}{\partial \eta^2} \Delta \beta_{pq} + \sum_{p,q,i} \frac{\partial^2 (\xi^p \eta^q / f^i)}{\partial \xi^2} \Delta \beta_{pqi} \\ \sum_{p,q} \frac{\partial^2 (\xi^p \eta^q)}{\partial \xi^2} \Delta \beta_{pq} + \sum_{p,q,i} \frac{\partial^2 (\xi^p \eta^q / f^i)}{\partial \xi^2} \Delta \beta_{pqi} \\ -\sum_{p,q} \frac{\partial^2 (\xi^p \eta^q)}{\partial \xi \partial \eta} \Delta \beta_{pq} - \sum_{p,q,i} \frac{\partial^2 (\xi^p \eta^q / f^i)}{\partial \xi \partial \eta} \Delta \beta_{pqi} \end{Bmatrix} \\ &= [\mathbf{P}_{poly}] \begin{Bmatrix} \Delta \beta_{11} \\ \vdots \\ \Delta \beta_{pq} \\ \vdots \end{Bmatrix} + [\mathbf{P}_{rec}] \begin{Bmatrix} \Delta \beta_{111} \\ \vdots \\ \Delta \beta_{pqi} \\ \vdots \end{Bmatrix} \\ &= [\mathbf{P}^m] \{ \Delta \beta^m \} \end{aligned} \quad (3.29)$$

The single Voronoi cell element problem of figure 3.3 is solved again using a fourth order complete polynomial expansion for the stress function and 3 reciprocal terms per polynomial term, i.e.  $p + q = 2 \cdots 4$ ,  $i = 1 \cdots 3$ . This corresponds to 48  $\beta$  parameters in the matrix stress field. Figures 3.3(c) and (d) shows a marked improvement in the deformed void shape as well as in the stress concentration ( $P + R$ ). The stress field enrichment also reduces the number of required  $\beta$  coefficients, thus enhancing the efficiency significantly.

### 3.3.1 Numerical Implementation of Reciprocal Stress Functions

In practice, smooth heterogeneities in each Voronoi cell element are modeled as discrete  $n$  sided polygons. For example, figure 3.2(a) shows a 8-sided polygonal approximation to an

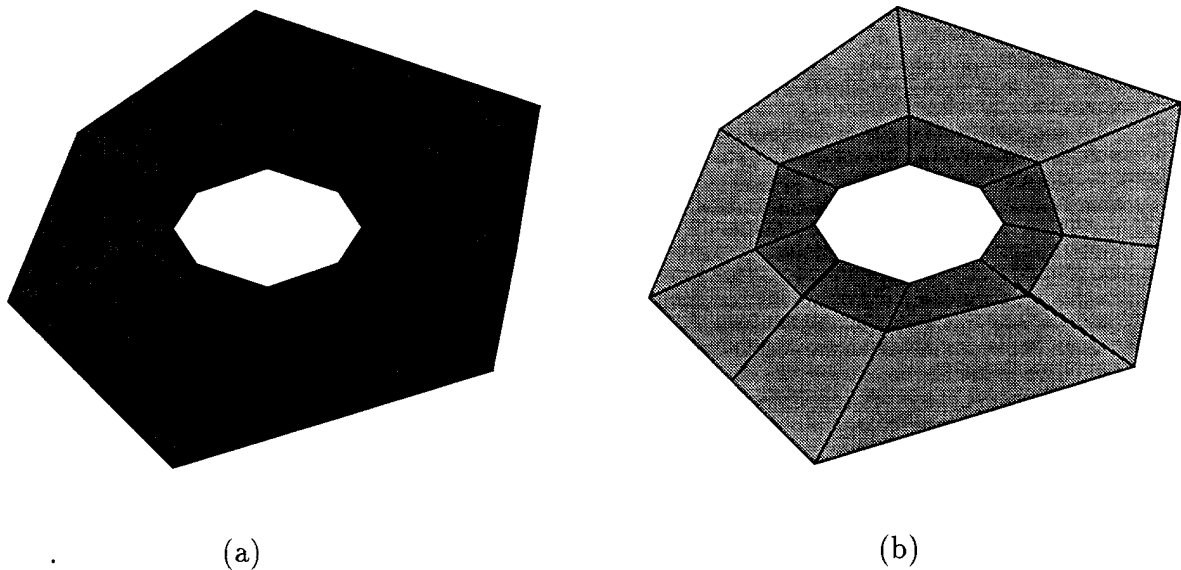


Figure 3.4: Integration subdomains of a Voronoi cell for (a) pure polynomial stress functions (b) shape based stress functions

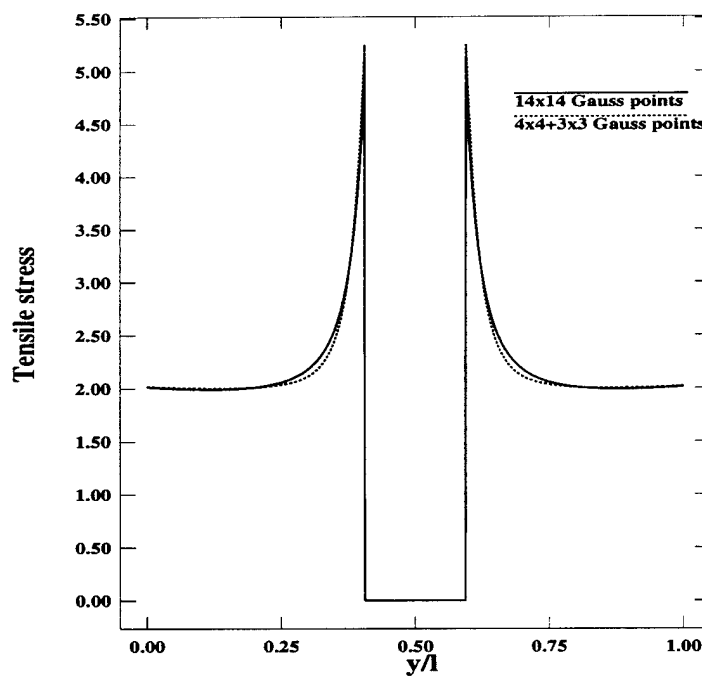


Figure 3.5: Comparison of integration accuracy for tensile stress distribution with old and new integration domains

elliptical heterogeneity. The Fourier coefficients in equation (3.25) are generated using the values of  $(r, \theta)$  at interfacial nodal points. Also a truncated Fourier series is used for the transformation function  $f$  in equation (3.26). Deviations from a circle in figure 3.2(b) correspond to these numerical approximations in the Fourier expansion.

As mentioned in section 2.5, numerical integration of  $[\mathbf{H}_m]$  is performed by Gauss quadrature rules, applied over quadrilaterals subdividing Voronoi cells. For polynomial stress functions, this can be done with accuracy by estimating the desired number of integration points from the order of the polynomial. However, when reciprocal stress functions are used, the number of quadrature points are not easily defined. Steep stress gradients arising from rapidly changing  $(\frac{1}{f})$  terms occur near the interface, but stabilize in the far field. This calls for a large number of integration points for quadrilaterals in figure 3.4(a). Alternatively the matrix in each Voronoi cell is divided into a narrow band around the interface, and the remainder of the cell, as shown in figure 3.4(b). Both these regions are subdivided into quadrilaterals for numerical integration. Quadrilaterals in the band are integrated using higher number of integration points to accommodate the sharp gradients. To examine the effectiveness of this scheme, the voided element example is solved again using original and modified integration domains. A set of 14x14 or 196 Gauss points per quadrilateral is used for the old scheme, whereas the new scheme has 4x4 or 16 Gauss points for the inner band and 3x3 or 9 Gauss points elsewhere. The resulting stress distribution along the mid-section in figure 3.5 indicates that the modified scheme enjoys similar accuracy for a considerably low effort.

### 3.3.2 A Simple Convergence Study

A study is conducted to investigate the sensitivity of the Voronoi cell elements to the order terms in the stress function, for convergence. Simulations are conducted by (a) varying the polynomial order with constant number of reciprocal terms, and (b) varying the order of reciprocal terms, keeping the polynomial terms constant. The VCFEM mesh is a single element with a heterogeneity in the form of a circular voids or inclusion as shown in figure 3.3. It is subjected to uniaxial stretching with  $\Delta u_x/L = 0.008$  under plain strain conditions. Material properties are as follows:

Matrix (Elastic-Plastic)

$$E = 69 \text{ GPa} \text{ (Young's Modulus)}, \quad \nu = 0.33 \text{ (Poisson's Ratio)}$$

$$Y_0 = 43 \text{ MPa} \text{ (Initial Yield Stress)}, \quad \sigma_{eqv} = Y_0 + \epsilon_{eqv}^{0.125} \text{ (Post Yield Hardening Law)}$$

Inclusion (Elastic)

$$E = 410 \text{ GPa} \text{ (Young's Modulus)}, \quad \nu = 0.2 \text{ (Poisson's Ratio)}$$

Results of the VCFEM are compared with those generated by a general purpose finite element code ABAQUS with an extremely refined (approximately 1200 elements) mesh of QUAD4 elements. The first example is for a circular void of volume fractions  $V_f = 5\%$  in a unit square matrix. 3 different ranges for the matrix stress function in equation (3.29) are considered. They include:

- (a) In  $\Phi_{poly}^m$ :  $p + q = 2..4$ , In  $\Phi_{rec}^m$ :  $p + q = 2..4$ ,  $i = 1..2$ ; 36 terms in  $\Phi$

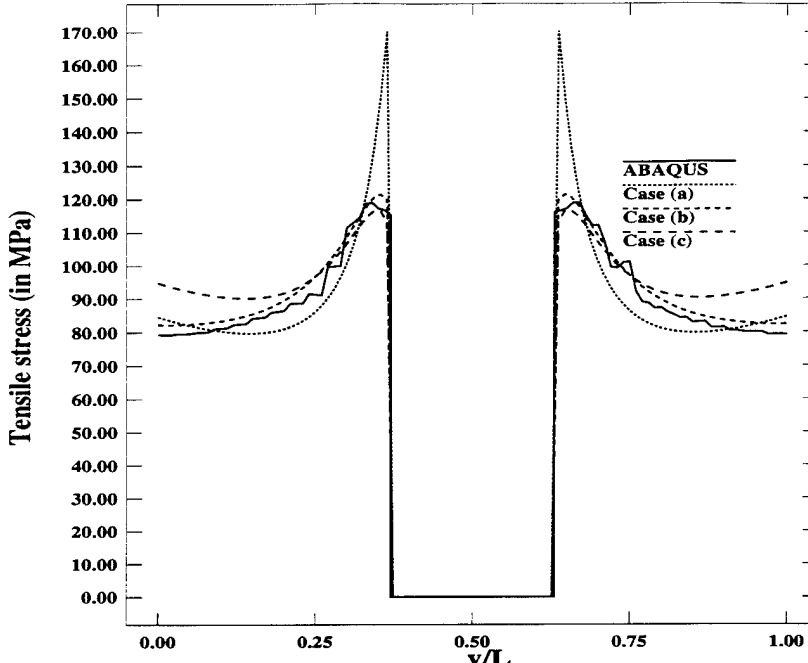


Figure 3.6: Tensile stress distribution along  $x/L = 0.5$  with various stress functions for a square domain with void, at void volume fraction  $V_f = 5\%$

- (b) In  $\Phi_{poly}^m$ :  $p + q = 2.4$ , In  $\Phi_{rec}^m$ :  $p + q = 2.4$ ,  $i = 1..3$ ; 48 terms in  $\Phi$
- (c) In  $\Phi_{poly}^m$ :  $p + q = 2.6$ , In  $\Phi_{rec}^m$ :  $p + q = 2.4$ ,  $i = 1..3$ ; 61 terms in  $\Phi$

Cases (a) and (b) are intended to study the effect of additional reciprocal terms, while cases (b) and (c) study the effect of the polynomial terms. A comparison of resulting stresses along the mid-section in figure 3.6 shows that an increase in the number of reciprocal terms from case (a) to case (b) significantly improves the results. On the other hand, an increase in the number of polynomial terms from case (b) to case (c) does not significantly alter results. Thus, from both efficiency and accuracy point of view,  $\Phi^m$  with 48 terms (case b) appears to be the optimal choice for Voronoi cells with voids.

A volume fraction of  $V_f = 35\%$  is considered for the convergence test of a composite cell with single inclusion. The stress field in the inclusion is generated with a 25 term polynomial stress function (i.e.  $\Phi_{poly}^c$ :  $p + q = 2.6$ ). Different cases studies for the matrix stress function include:

- (a) In  $\Phi_{poly}^m$ :  $p + q = 2.5$ , In  $\Phi_{rec}^m$ :  $p + q = 2$ ,  $i = 1..3$ ; 24 terms in  $\Phi$
- (b) In  $\Phi_{poly}^m$ :  $p + q = 2.6$ , In  $\Phi_{rec}^m$ :  $p + q = 2$ ,  $i = 1..3$ ; 34 terms in  $\Phi$
- (c) In  $\Phi_{poly}^m$ :  $p + q = 2.6$ , In  $\Phi_{rec}^m$ :  $p + q = 2.3$ ,  $i = 1..3$ ; 46 terms in  $\Phi$

Cases (a) and (b) exhibit the effect of adding polynomial terms, while cases (b) and (c) study the effect of reciprocal terms. Figure 3.6 shows that an increase in the number of polynomial terms from (a) to (b) produces a significantly improved stress distribution in the inclusion.

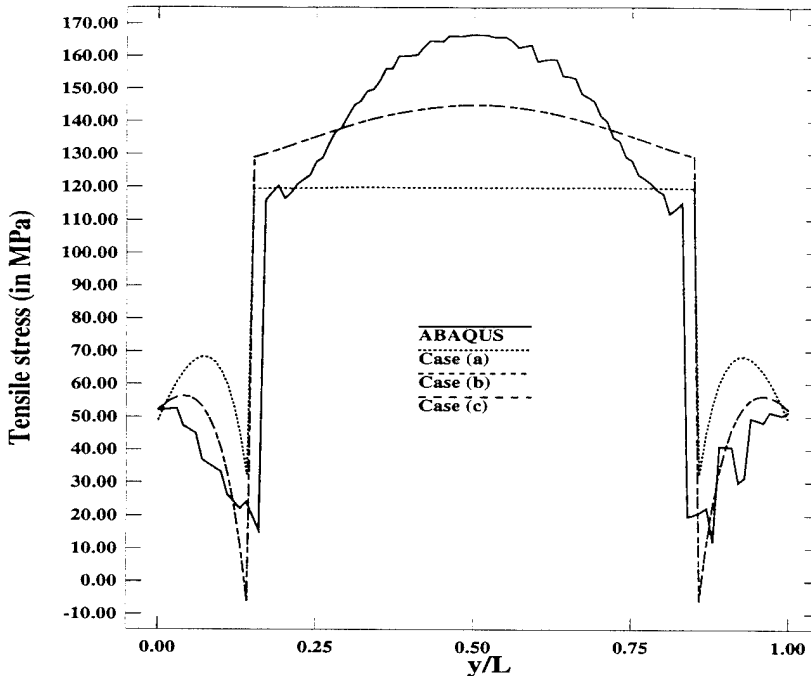


Figure 3.7: Tensile stress distribution along  $x/L = 0.5$  with various stress functions for a square domain with inclusion, at inclusion volume fraction  $V_f = 35\%$

An increase in the number of reciprocal terms from (b) to (c) does not yield any significant advantages. The 34 term expansion (case b) is thus chosen as the optimal stress function for Voronoi cells with inclusions.

## 3.4 VCFEM for Porous Microstructures

### 3.4.1 Numerical Validation

The competence of the Voronoi cell finite element model in analyzing porous microstructures is ascertained by comparison with two conventional FEM packages (ABAQUS and ANSYS). Assuming that the domain of investigation corresponds to a microstructural representative material element or *RME*, both macroscopic (volume averaged) and microscopic (detailed) behavior are investigated. The macroscopic variables are denoted with an overbar, with macroscopic stresses  $\bar{\sigma}$  expressed as:

$$\bar{\sigma} = \frac{\int_{\Omega_{RME}} \sigma d\Omega}{\int_{\Omega_{RME}} d\Omega} \quad (3.30)$$

#### Regular Packing

Square edge packed representative material elements (RME) with circular void of volume fractions  $V_f = 20\%, 35\%, 50\%$  and square shaped void of volume fraction  $V_f = 25\%, 50\%, 75\%$  are considered. The matrix material is Aluminum with the following properties:

$E = 69 \text{ GPa}$  (Young's Modulus),  $\nu = 0.33$  (Poisson's Ratio)

$Y_0 = 43 \text{ MPa}$  (Initial Yield Stress),  $\sigma_{eqv} = Y_0 + \epsilon_{eqv}^{0.125}$  (Post Yield Hardening Law)

The VCFEM meshes consisting of only one element are shown in figures 3.8(a) and (b), while

the ABAQUS meshes are shown in figure 3.8(c) and (d). Plane strain uniaxial tension loading is considered to a maximum of 0.5% macroscopic strain. Periodic construct of the RME is achieved through repeatability conditions on the traction free face ( $y = L$ ). This constraint condition requires the RME to deform into rectangular shapes, and for the uniaxial case is written as:

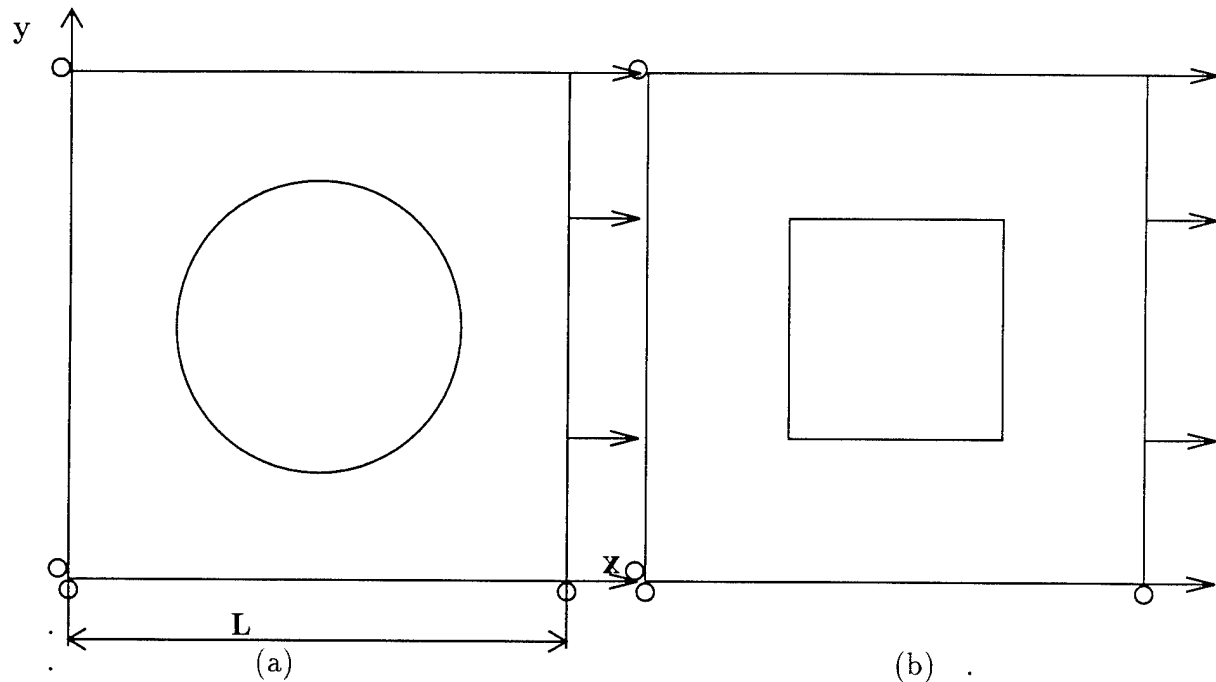
$$\Delta u_y = \Delta \bar{u} \text{ on } y = L \text{ such that } \int_{y=L} t_y dx = 0$$

The VCFEM analysis uses a 48 term stress function ( $p+q = 2..4$  and  $i = 1..3$ ) in the matrix. The VCFS mesh consists of 8 nodes on the element boundary and 8 nodes on the interface. Thus VCFEM uses a total 80 D.O.F (48 D.O.F for the stress parameters and 32 D.O.F for the nodal displacements, in contrast to the ABAQUS meshes that have 1972 and 1246 D.O.F for the circular and square voids respectively. The macroscopic behavior of these two RME's are shown in figures 3.9(a) and (b), and shows excellent convergence to the ABAQUS results. Figures 3.10(a) and (b) shows the stress distributions along the mid-section of the void at a 0.5% macroscopic strain level. These results establish the accuracy of the VCFEM formulations for porous materials with different void shapes.

### *Random Packing*

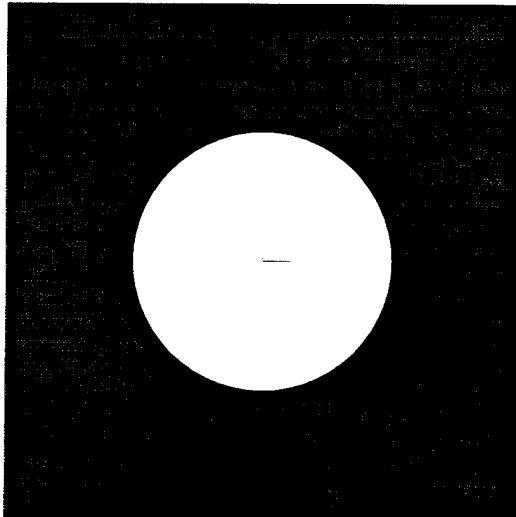
VCFEM analysis of a RME consisting of 29 randomly located circular voids ( $V_f = 20\%$ ) is compared with results generated by ANSYS. Void locations are generated by a random number generator. Figures 3.11(b) and (a) show the VCFEM mesh with 29 elements and the ANSYS mesh with 5282 QUAD4 elements respectively. Material properties and loading conditions are identical to those in the previous example, with the maximum macroscopic strain changed to 0.8%. Comparison of the macroscopic response in figure 3.12(a) clearly establishes VCFEM as an accurate method for modeling overall behavior of random microstructures. The microscopic stress distribution through the section A-A in figure 3.11(b) at 0.8% strain is depicted in figure 3.12(b). Once again the comparison is very satisfactory, with VCFEM producing similar patterns and peak stresses with a maximum difference of 18.7%.

The equivalent microscopic plastic strain distribution at a macroscopic strain  $\bar{\epsilon}_{xx} = 0.5\%$ , is shown in figure 3.13. The RME's include square edge packing with circular voids (figure 3.8(a)) with different volume fractions and random packing (figure 3.11(b)). As noted in [31], figure 3.13(a) shows that at low void volume fractions, plastic strains are localized in narrow diagonal bands in the form of ligaments that originate from the void boundary. As the void boundary approaches the cell boundary with increasing volume fractions (figures 3.13(a) and (b)), the localization effects abate. For the random packed RME in figure 3.13(d), the maximum plastic strain is concentrated around a few void boundaries. It is interesting to note that the maximum plastic strain for the random RME increases approximately tenfold with respect to the square edge packing with same volume fraction.

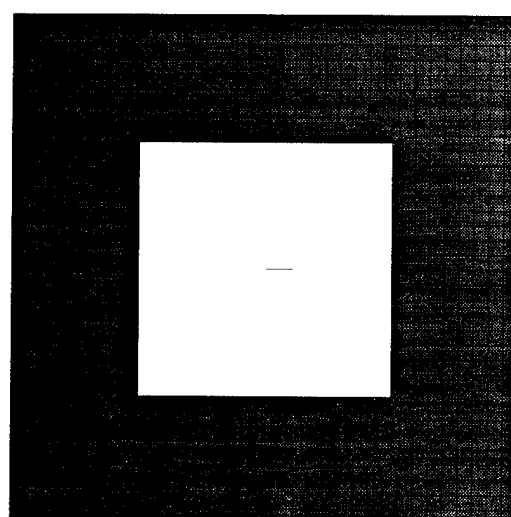


(a)

(b)

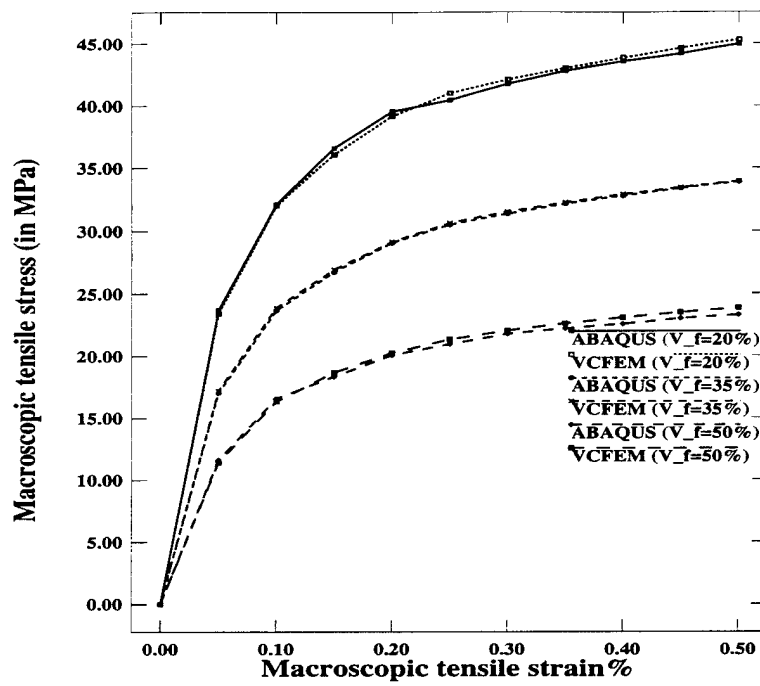


(c)

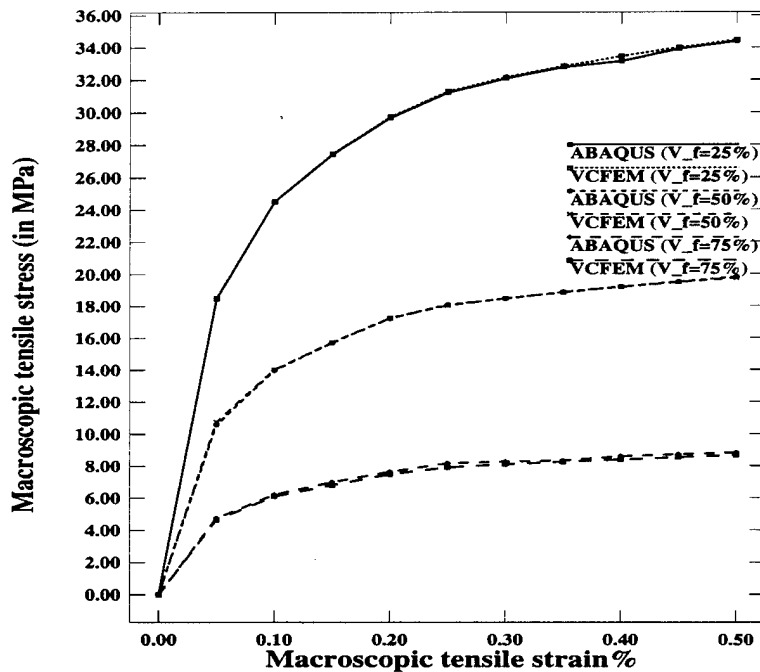


(d)

Figure 3.8: VCFEM mesh for squared edge packing with (a) circular voids ( $V_f = 20\%$ ) (b) square voids ( $V_f = 25\%$ ) and corresponding ABAQUS mesh with (c) circular voids (d) square voids



(a) .



(b)

Figure 3.9: Macroscopic stress-strain response at various volume fractions for square edge packed  
 (a) circular voids (b) square voids

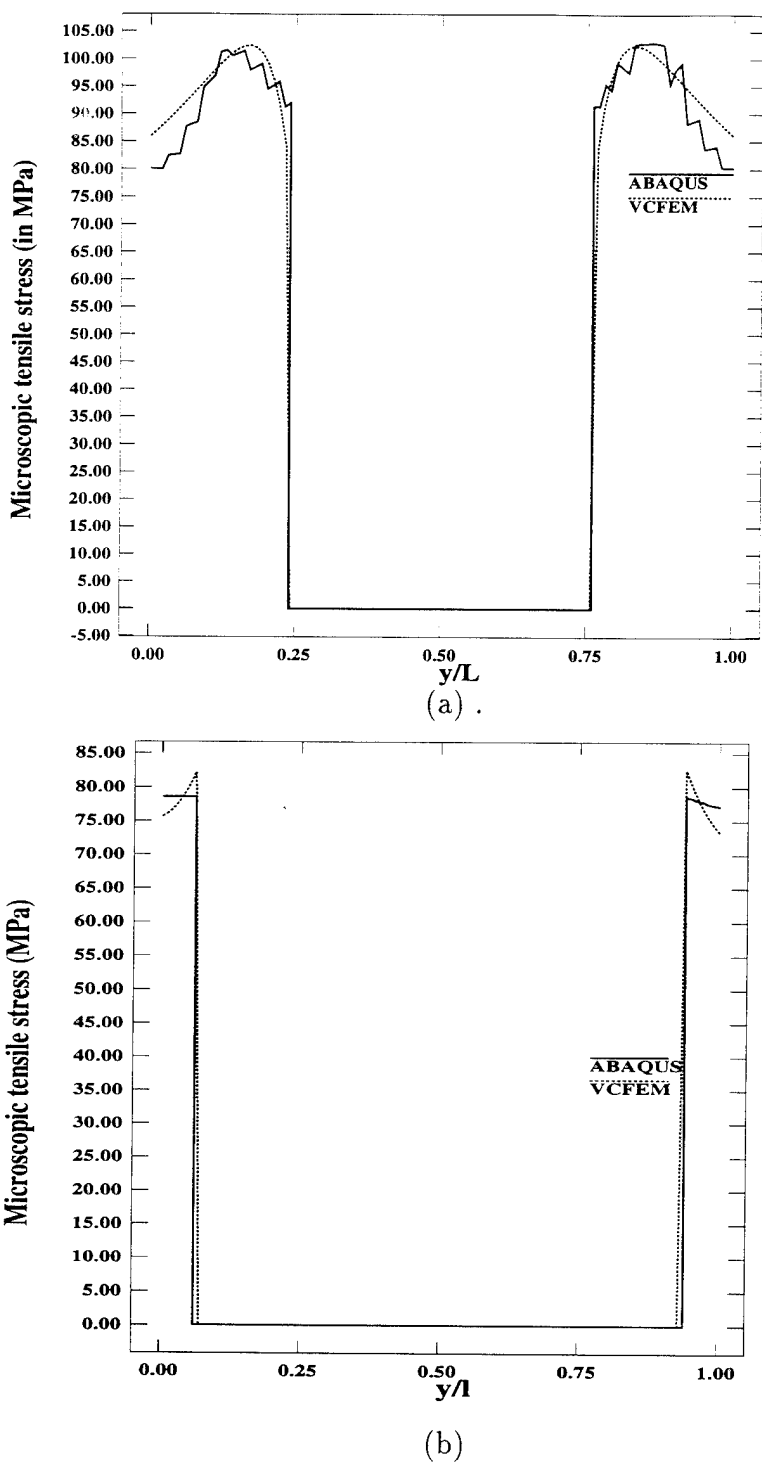
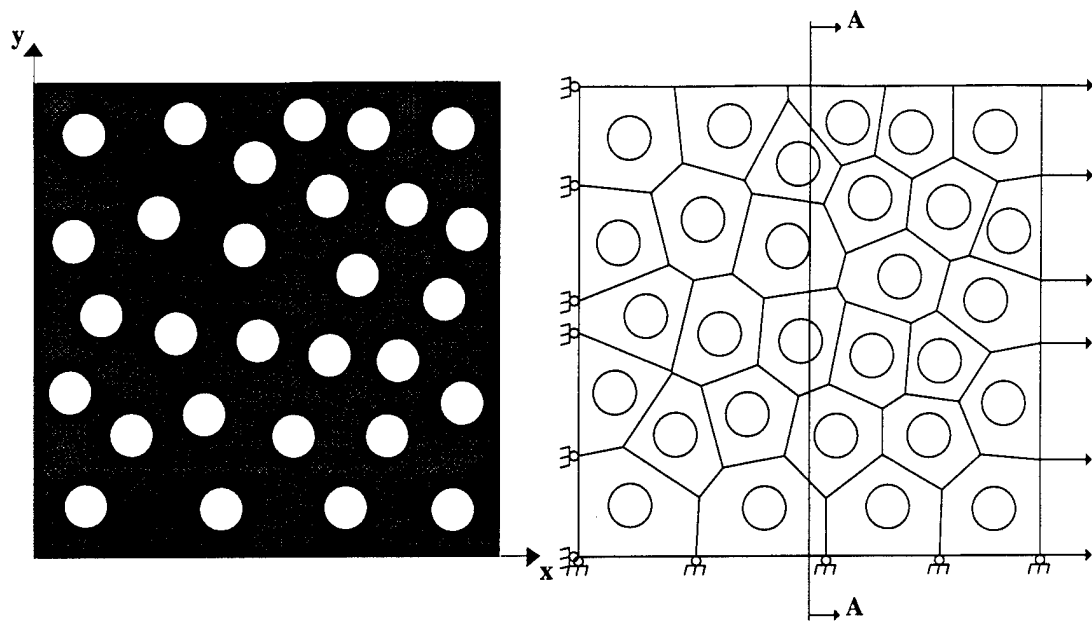


Figure 3.10: Microscopic stress distribution at 0.5% strain along the center-line for square edge packed (a) circular voids ( $V_f = 20\%$ ) (b) square voids ( $V_f = 75\%$ )



(a)

(b)

Figure 3.11: (a) ANSYS and (b) VCFEM meshes for random packed RME with circular voids ( $V_f = 20\%$ )

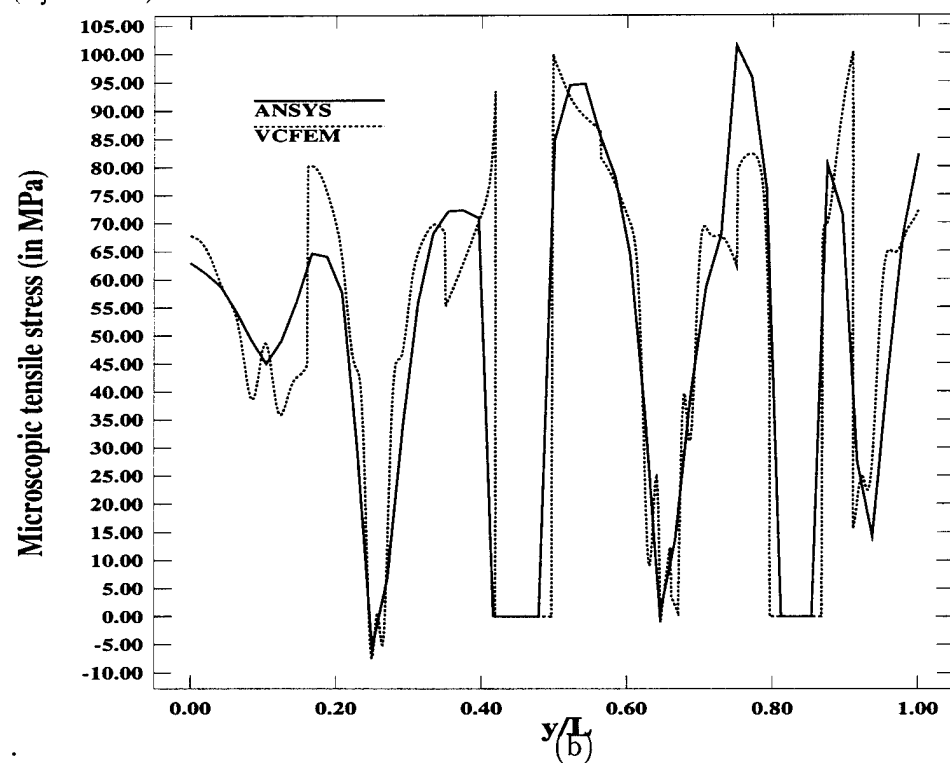
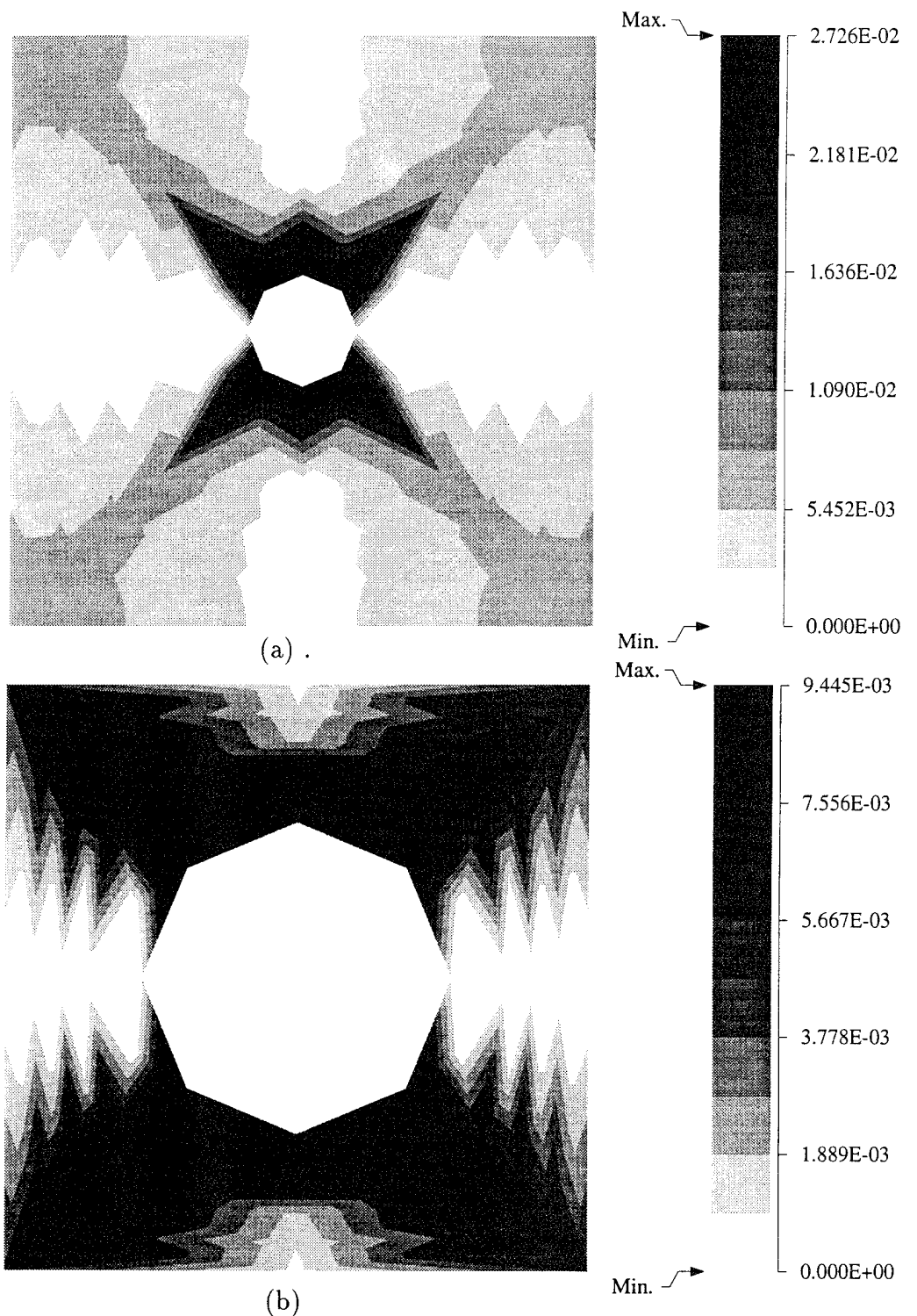
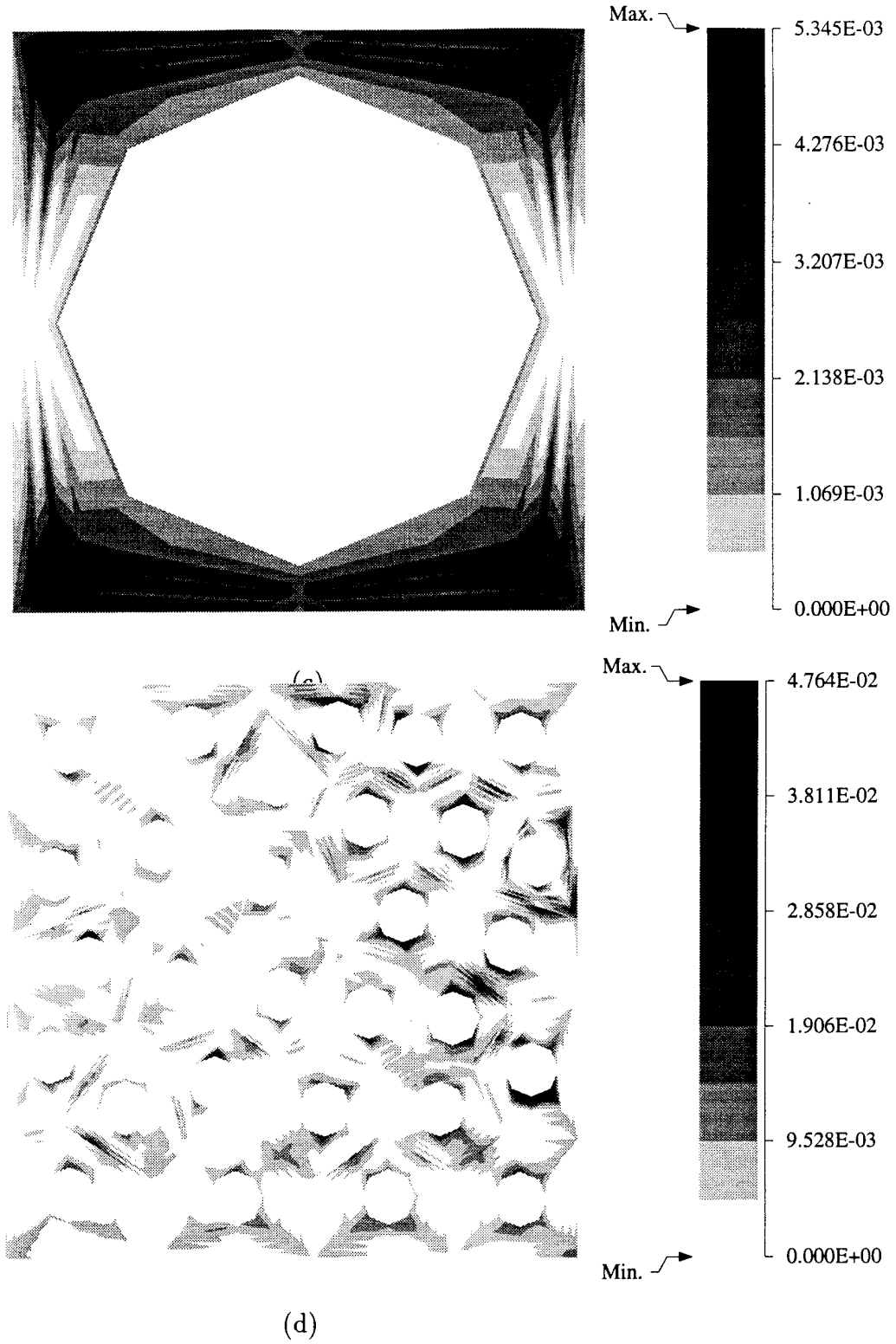


Figure 3.12: (a) Macroscopic stress-strain response and (b) Microscopic stress distribution at 0.8% strain for random packed RME with circular voids, along  $x/L = 0.5$





(d)

Figure 3.13: Effective plastic strain distribution at strain level  $\epsilon_{xx} = 0.5\%$  for (a) square edge packing ( $V_f = 2.5\%$ ), (b) square edge packing ( $V_f = 20\%$ ), (c) square edge packing ( $V_f = 50\%$ ) and (d) random packing ( $V_f = 20\%$ ) RME

### 3.4.2 Effect Of Microstructural Morphology On Yield Surfaces

Effects of size, distribution and shape on macroscopic yield surfaces used to characterize the onset of overall elastic-plastic behavior are considered in this section. The Tvergaard-Gurson (T-G) model [31] for square edge packed cylindrical voids, is used as a benchmark for comparison. The T-G model assumes that the macroscopic yield surface is independently a function of hydrostatic and equivalent components (first and second invariants) of the macroscopic stress and is expressed as:

$$\phi = \left( \frac{\bar{\sigma}_{eqv}}{\sigma_0} \right)^2 + 2q_1 f \cosh\left( \frac{\sqrt{3}}{2} q_2 \frac{\bar{\sigma}_{hyd}}{\sigma_0} \right) - 1 - f^2 = 0$$

where  $\bar{\sigma}_{eqv} = \sqrt{\frac{3}{2} \bar{\sigma}'_{ij} \bar{\sigma}'_{ij}}$  and  $\bar{\sigma}_{hyd} = \bar{\sigma}_{kk}$ ,  $\bar{\sigma}'_{ij}$  is the macroscopic deviatoric stress.  $\sigma_0$  corresponds to the matrix flow stress,  $f$  is the void volume fraction and coefficients  $q_1 = 1$  and  $q_2 = 1.5$ . Yield surfaces are generated from VCFE results by applying various different boundary conditions on the RME with the repeatability assumption. These conditions include simple shear (tension in the x-direction and compression in the y-direction), biaxial tension (equal tension in both directions) and a number of loading types in between. For each of these loadings, an overall equivalent stress-strain curve is drawn. The yield point is then designated as the point where the tangent modulus undergoes a rapid reduction. This assumption is consistent with finite element calculations performed by Hom and McMeeking [37] for spherical voids. For this problem, the matrix material is assumed to have the following properties.

$E = 250$  Units (Young's Modulus),  $\nu = 0.33$  (Poisson's Ratio)

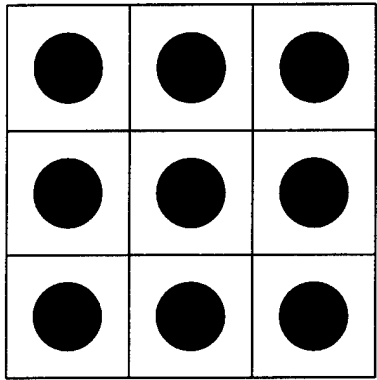
$Y_0 = 1$  Unit (Initial Yield Stress),  $\epsilon_{eqv} = 0.00354 * (\sigma_{eqv})^{10}$  (Post Yield Hardening Law)

#### Effect of Void Location

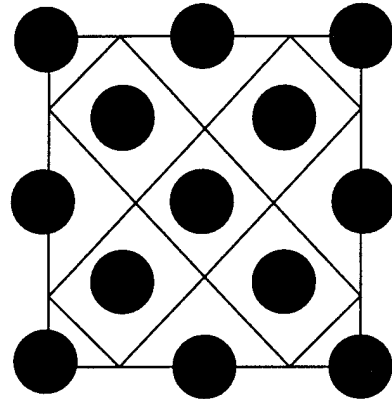
For circular voids, the effects of three position distributions, viz. (a) Square edge packing (S.E) (figure 3.14(a)) (b) Square diagonal packing (S.D) (figure 3.14(b)) and (c) Random packing (figure 3.14(c)), on the yield surface is studied. Four different void volume fractions of 2.5%, 5%, 7.5% and 10% are considered to examine the dependence on volume fraction. Figure 3.15 shows the yield function plotted in terms of equivalent stress as a function of hydrostatic stress for these cases. As is expected, VCFEM simulated yield functions for square edge packing are in very close agreement with the Tvergaard-Gurson predictions at all volume fractions. It is interesting to note that the yield surfaces for random packing also closely follow the Tvergaard-Gurson model at lower volume fractions, though the deviations slightly increase at higher volume fractions. The square diagonal packing, however, is at significant variance with the Tvergaard-Gurson model at all volume fractions. From these simulations, it appears that hydrostatic stress has a less pronounced effect on the yield surface for the square diagonal packing. The effect of void distribution is much more pronounced at higher volume fractions as evidenced from figure 3.17, where yield surfaces are depicted at  $V_f = 35\%$ .

#### Size Effect

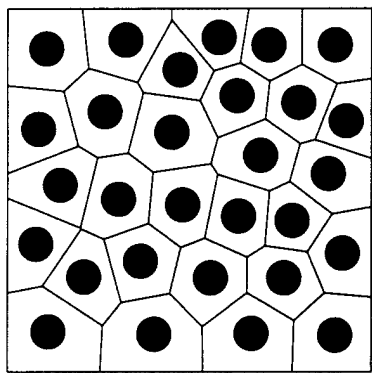
The yield surface of circular voids in a square edge packing arrangements at volume fractions



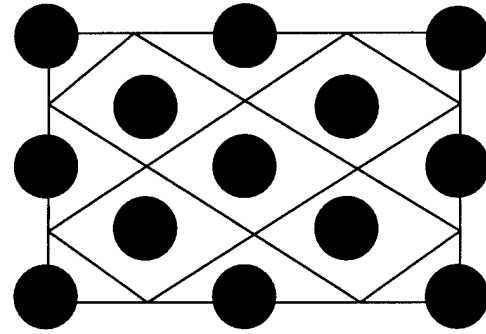
(a)



(b)

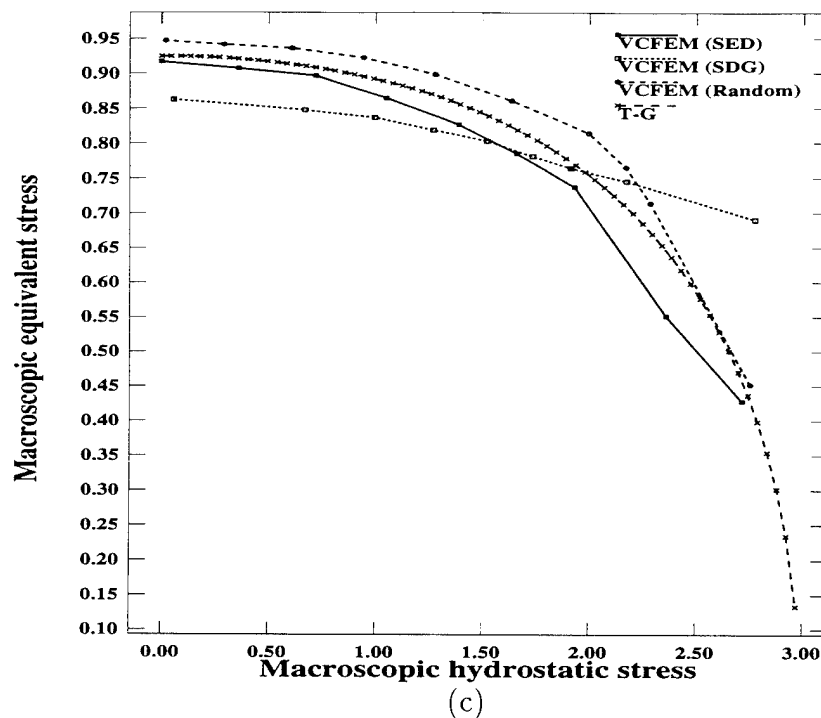


(c)

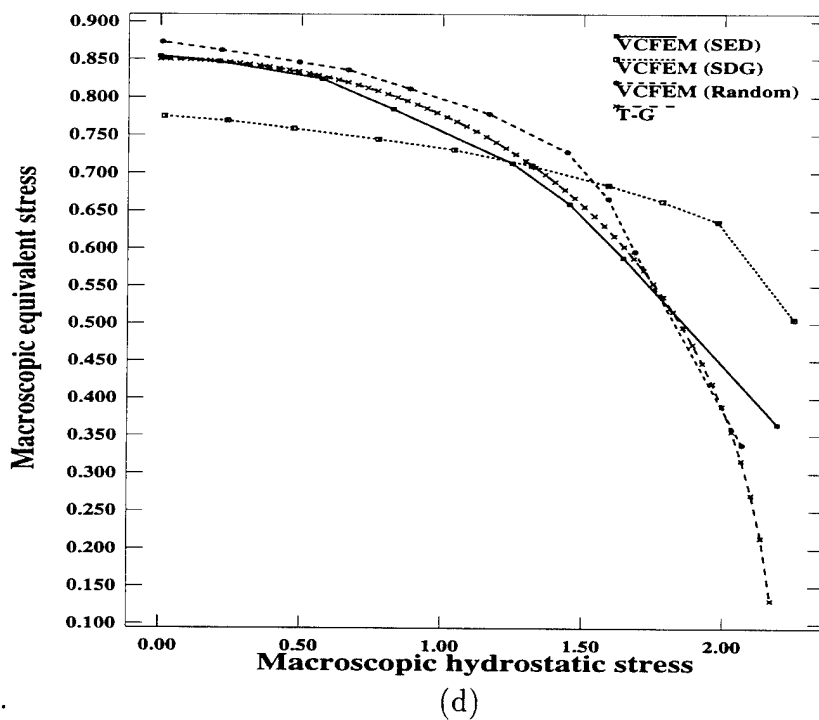


(d)

Figure 3.14: VC-FEM meshes for (a) square edge packing (SE), (b) square diagonal packing (SD), (c) random packing (R) , and (d) hexagonal close packing (HCP) RMEs



(c)



(d)

Figure 3.15: Initial macroscopic yield surfaces for various distributions with circular voids at (a)  $V_f = 2.5\%$ , (b)  $V_f = 5\%$ , (c)  $V_f = 7.5\%$ , (d)  $V_f = 10\%$

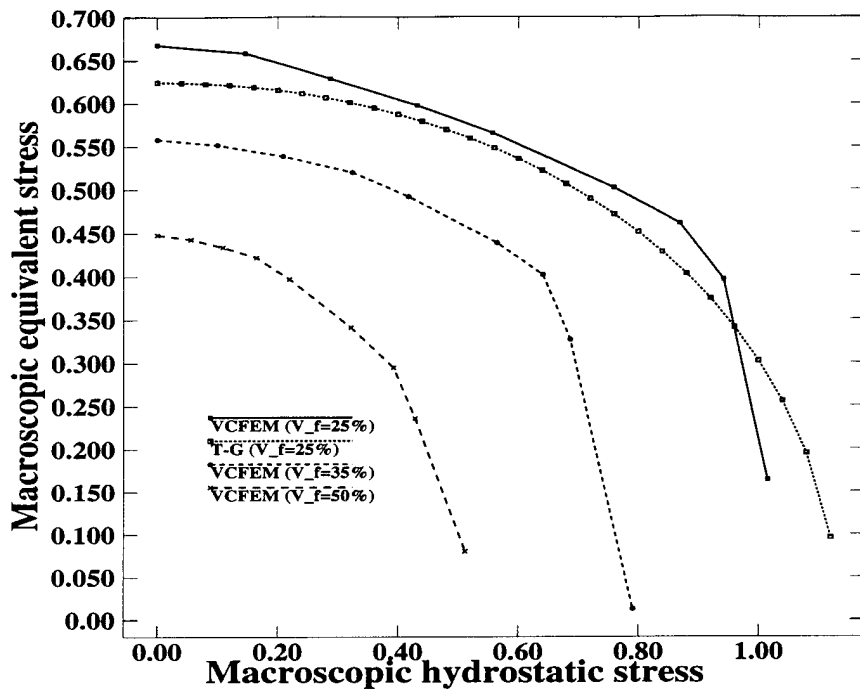


Figure 3.16: Size effect on yield surfaces of square edge packed RMEs' with circular voids

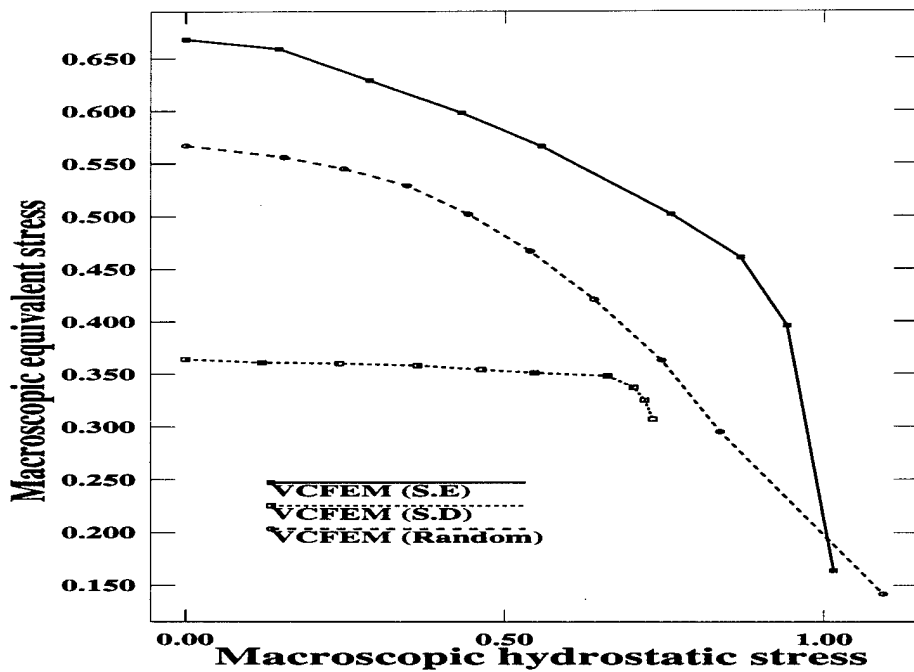


Figure 3.17: Initial macroscopic yield surfaces at a higher void volume fraction ( $V_f = 35\%$ )

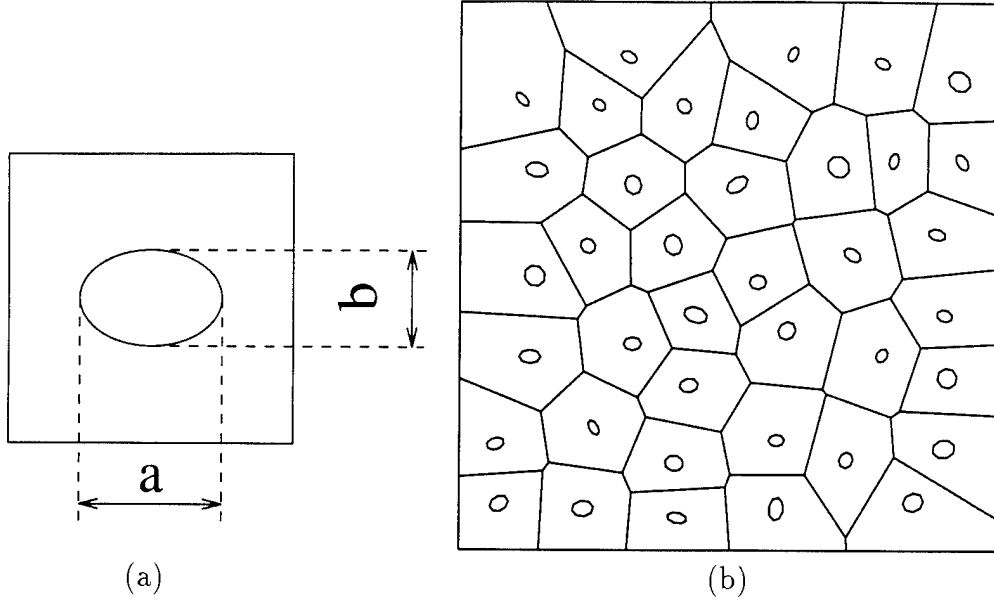


Figure 3.18: VCFEM meshes for elliptic voids in (a) square edge, and (b) random packing arrangements

of  $V_f = 25\%, 35\%, 50\%$  are shown in figure 3.16. The equivalent stress - hydrostatic stress plot shows that the yield surface shrinks rapidly with increase in void size. A comparison with the Tvergaard-Gurson model at  $V_f = 25\%$  shows significant variance with the VCFEM results. This may be attributed to the fact that the continuum derivation of Tvergaard-Gurson model is only valid for smaller volume fractions, at which the voids do not interfere with tractions boundaries of the RME.

### Void Shape and Orientation Effects

Orientation and void shape effects on the yield surface are investigated in this example. Figure 3.18(a) shows an elliptic void in a square edge arrangement. The yield surfaces in figure 3.21 are drawn for this RME with  $a/b = 1.5$  with the major axis oriented at  $0^\circ$ ,  $30^\circ$ , and  $45^\circ$  to the x-axis. The yield surface is symmetric about the  $(\bar{\sigma}_{kk} = 0)$  line for the  $45^\circ$  orientation due to reflective properties. However for the  $0^\circ$  and  $30^\circ$  orientations, the yield surface exhibits nonsymmetry as the stress state progresses from hydrostatic ( $\bar{\sigma}_{eqv} = 0$ ) to pure shear ( $\bar{\sigma}_{kk} = 0$ ). This indicates that if a biaxial tension loading is replaced by a biaxial compression loading of equal magnitude, the yield points will not reciprocate, even though the overall equivalent stress remains unchanged. It implies that for each point  $(\bar{\sigma}_{kk}, \bar{\sigma}_{eqv})$  on the yield surface, the point  $(-\bar{\sigma}_{kk}, \bar{\sigma}_{eqv})$  may not belong on the yield surface. This leads to the conclusion that a representation of yield surface in the  $\bar{\sigma}_{kk}$ - $\bar{\sigma}_{eqv}$  plane is no longer appropriate for elliptical voids with orientation. One remedy is to represent the yield surface in the space of invariants, i.e.  $\bar{\sigma}_{kk}$ - $\bar{\sigma}_{eqv}$ - $|\bar{\sigma}|$  space. Alternatively, the yield surface can be represented in the  $\bar{\sigma}_{xx}$ - $\bar{\sigma}_{yy}$  plane as shown in figure 3.19. The yield surface for the  $0^\circ$  and  $30^\circ$  orientations deviate from that for the  $45^\circ$  orientation. Anisotropy of the  $0^\circ$  and  $30^\circ$

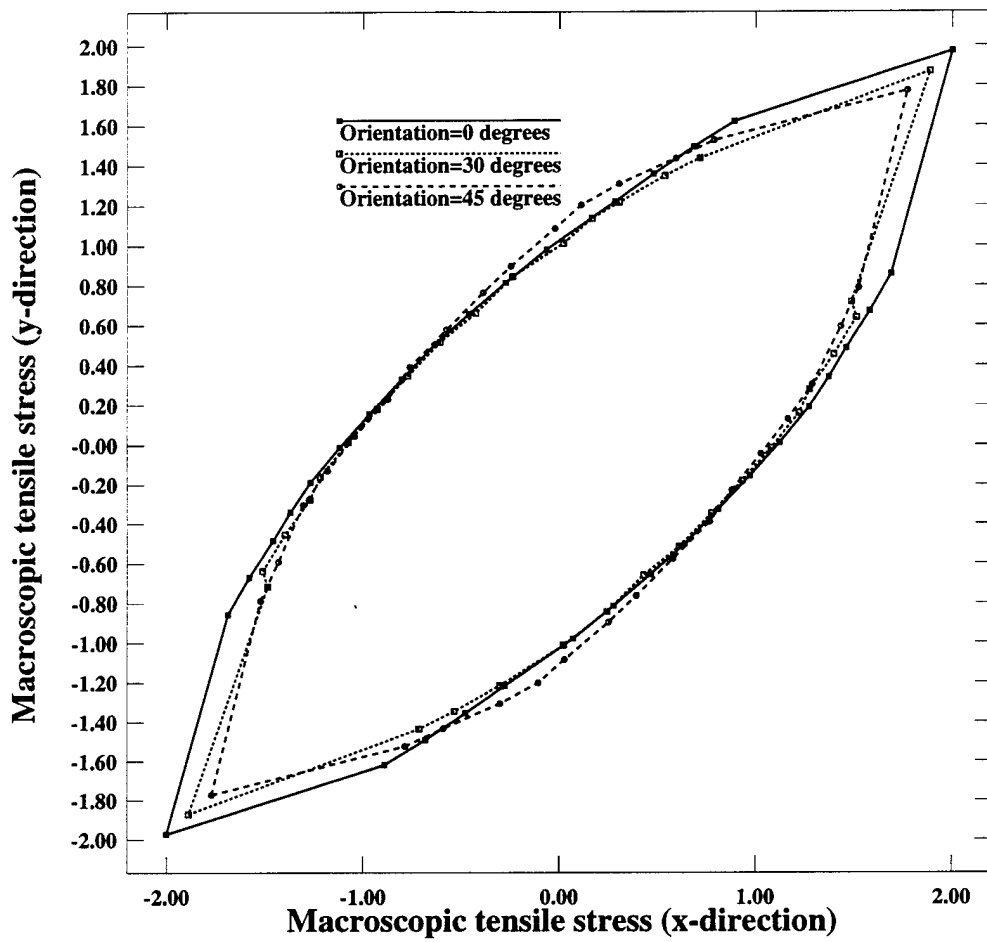
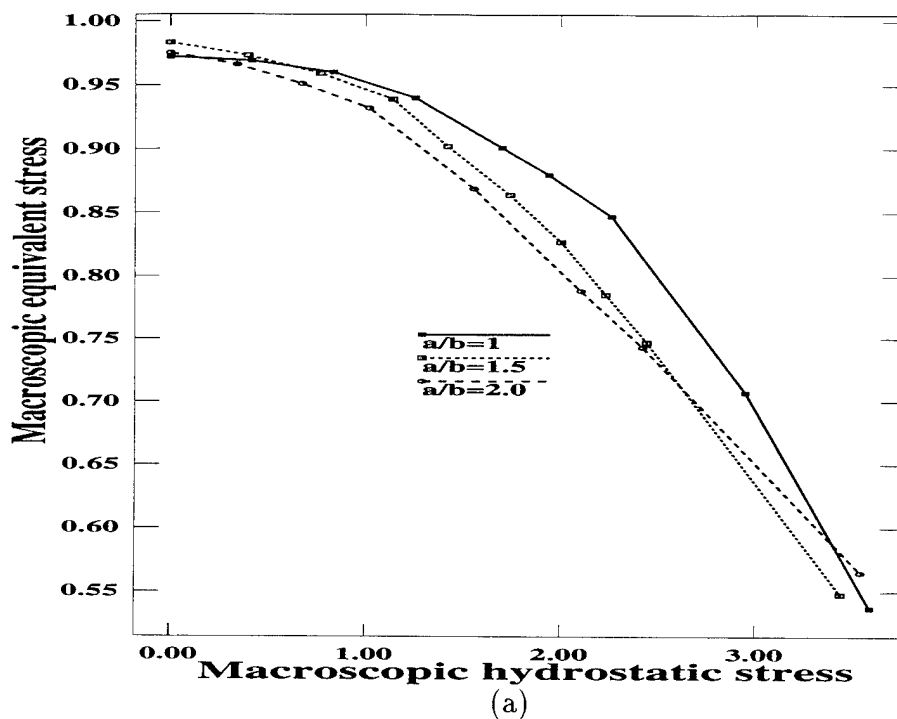
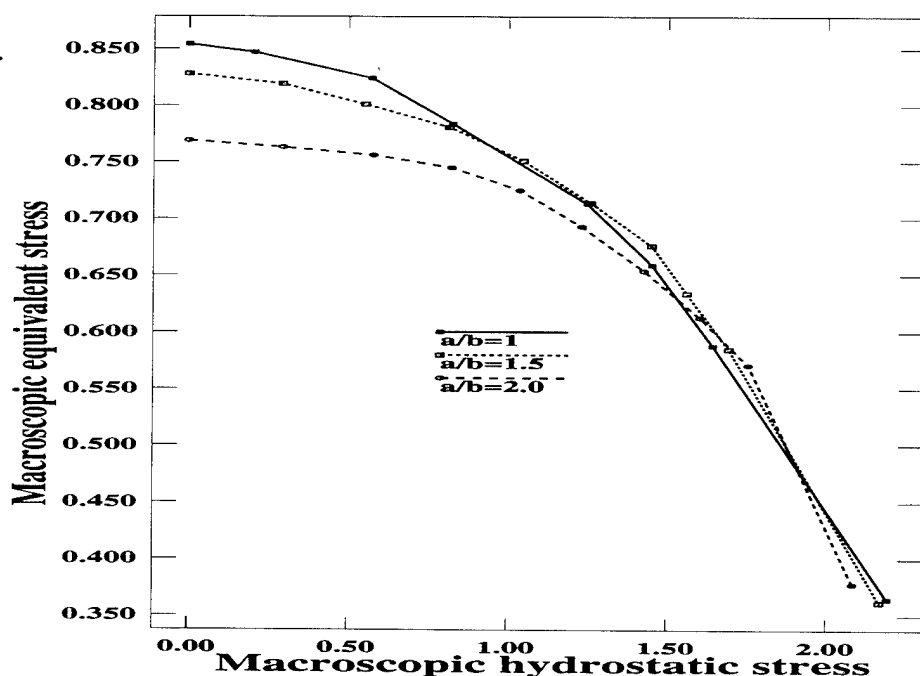


Figure 3.19: Orientation effect on yield surfaces for square edge packed elliptic voids in  $\bar{\sigma}_{xx}$ - $\bar{\sigma}_{yy}$  space



(a)



(b)

Figure 3.20: Void Shape effect on the yield surface for elliptic voids in a square edge packing at (a)  $V_f = 2.5\%$ , and (b)  $V_f = 10\%$

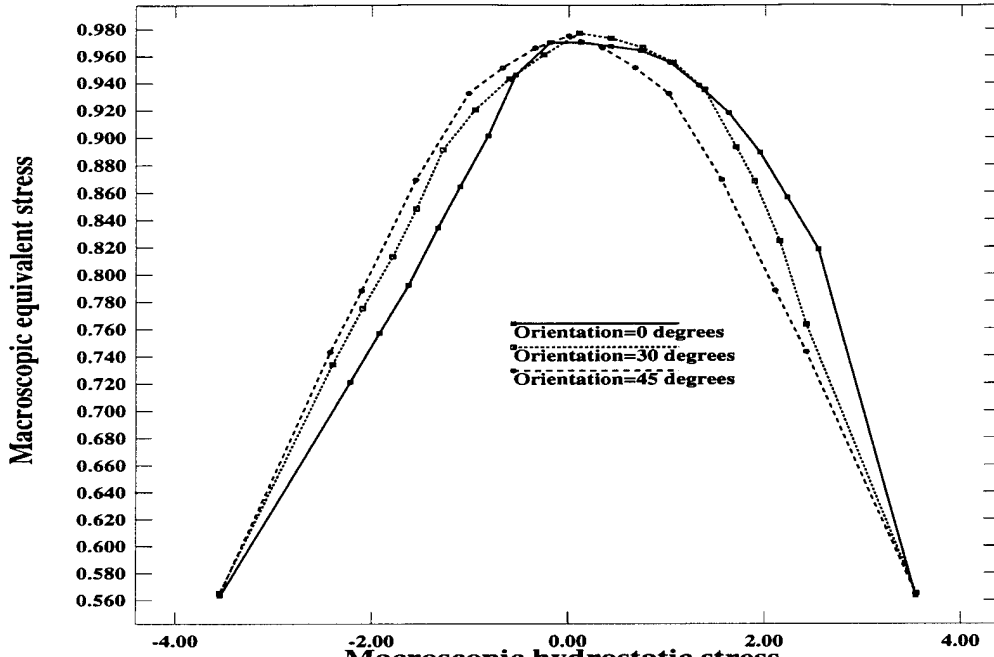


Figure 3.21: Orientation effect on yield surfaces for square edge packed elliptic voids in  $\bar{\sigma}_{kk}$ - $\bar{\sigma}_{eqv}$  space

orientation yield surfaces is observed from their differences with the  $45^\circ$  yield surfaces in each of the 4 quadrants. Figure 3.20(a) and (b) illustrates the effect of void shape, by considering three shapes viz.  $a/b = 1.0$ ,  $a/b = 1.5$  and  $a/b = 2.0$  for volume fractions  $V_f = 2.5\%$  and  $V_f = 10\%$ . The orientation is set at  $45^\circ$  for symmetry. The increase in aspect ratio the results in a lowering of the yield surface, with the shape effect becoming more pronounced at higher volume fractions. As a final example, a comparison between yield surfaces for a perfectly random (distribution, shape and orientation) RME with 39 voids in figure 3.18(b), and a RME with randomly distributed circular voids in figure 3.11(b), is made. Figure 3.22 shows the yield surfaces for  $V_f = 2.5\%$  and  $V_f = 10\%$ . In general, the circular voids result in higher values of yield functions at lower hydrostatic stress values. The difference is considerably magnified at higher volume fractions, with the conclusion that size plays a more important role than shape for this behavior.

### 3.5 VCFEM for Composite Microstructures

A number of examples for various types of composite microstructures using polynomial stress functions have been discussed in Ghosh and Moorthy [27]. In this section a few examples are considered to demonstrate the advantage of using reciprocal stress functions in the Voronoi cell element formulation with embedded inclusions.

#### RME with Randomly Distributed Inclusions

The representative material element illustrated in figure 3.11, is considered for an Aluminum matrix embedded with brittle Boron inclusions. The material properties are as follows:

Aluminum

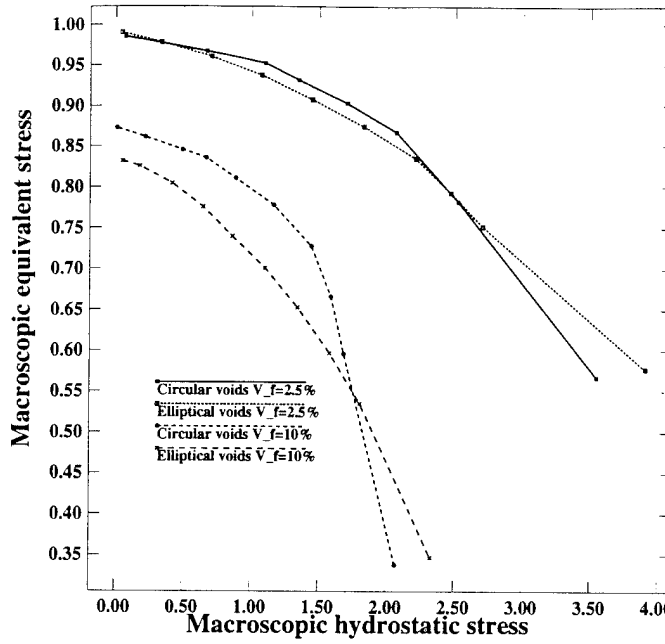


Figure 3.22: Effect of void-shape on the yield surface for random packed RMEs' at  $V_f = 2.5\%$  and  $V_f = 10\%$

$E = 69 \text{ GPa}$  (Young's Modulus),  $\nu = 0.33$  (Poisson's Ratio)

$Y_0 = 43 \text{ MPa}$  (Initial Yield Stress),  $\sigma_{eqv} = Y_0 + \epsilon_{eqv}^{0.125}$  (Post Yield Hardening Law )

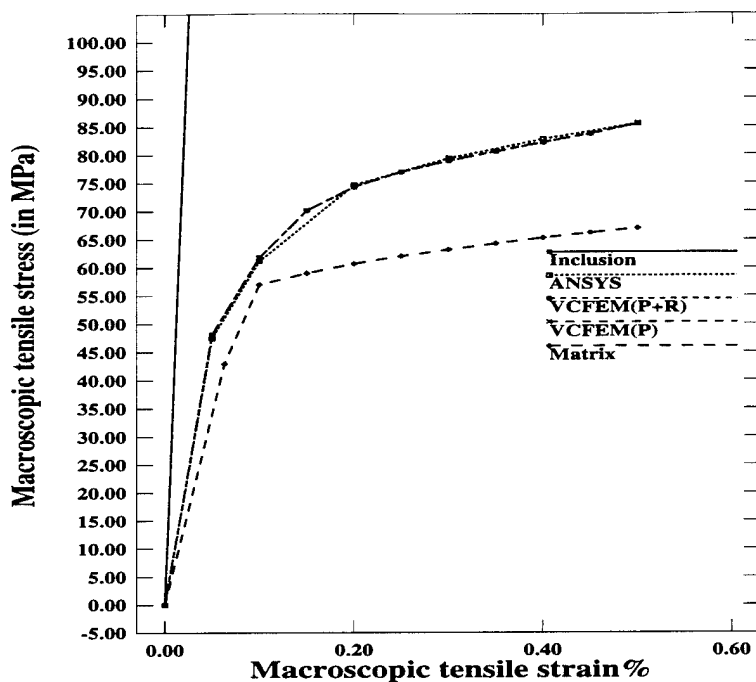
Boron

$E = 420 \text{ GPA}$  (Young's Modulus),  $\nu = 0.2$  (Poisson's Ratio)

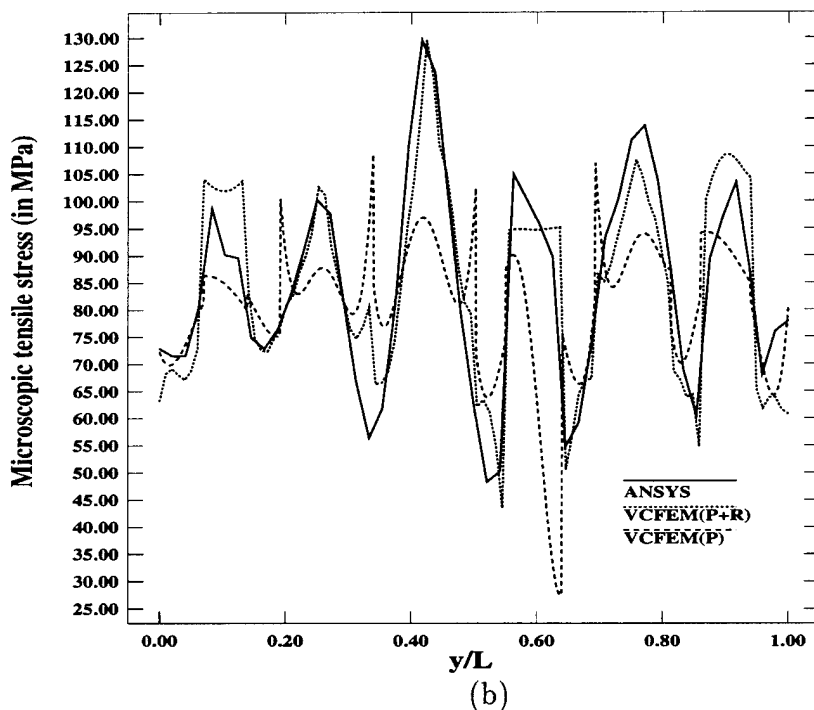
The RME is uniaxially loaded under plane strain conditions to a macroscopic strain of 0.5%. A 34 term matrix stress function is used for the modified formulation, and compared with a 25 term ( $p+q = 2 \dots 6$ ) polynomial stress function in the old formulation. The macroscopic response of the RME is shown in figure 3.23(a), while figure 3.23(b) depicts the microscopic stress distribution along  $x = 0.7 L$  at 0.5% overall strain. VCFEM results are compared with ANSYS using a very refined mesh. VCFEM simulations with both polynomial stress functions (P) and polynomial with reciprocal stress functions (P+R) are in excellent agreement with ANSYS results for the macroscopic response. However the microscopic stress distributions in figure 3.23(b) establishes the superiority of the modified VCFEM formulation beyond doubt for composites. The stress shows very good convergence to ANSYS results, with a maximum difference of 9.8% in the peak stress.

### Size Effects on Composite Yield Stress

Effect of various fiber arrangements on overall strength of metal matrix composites are investigated by VCFEM and compared with results by Zahl et. al. [34]. Zahl et. al. [34] have used ABAQUS to obtain their results for MMC's with ductile matrices and rigid inclusions. The parameter chosen to be examined is the asymptotic yield stress, defined as  $\sigma_N$  in the power law hardening model  $\bar{\sigma} = \sigma_N(\bar{\epsilon}/\epsilon_o)^m$ . Bao et.al.[33] have concluded, that for fully developed plastic zones with rigid inclusions, the overall post-yield behavior of the composite can be obtained by replacing  $\sigma_{mat}$  with a different  $\sigma_N$ , in the matrix hardening



(a)



(b)

Figure 3.23: (a) Macroscopic stress-strain response of random packed composite with circular inclusions ( $V_f = 20\%$ ) and (b) Microscopic stress distribution along  $x/L = 0.7$

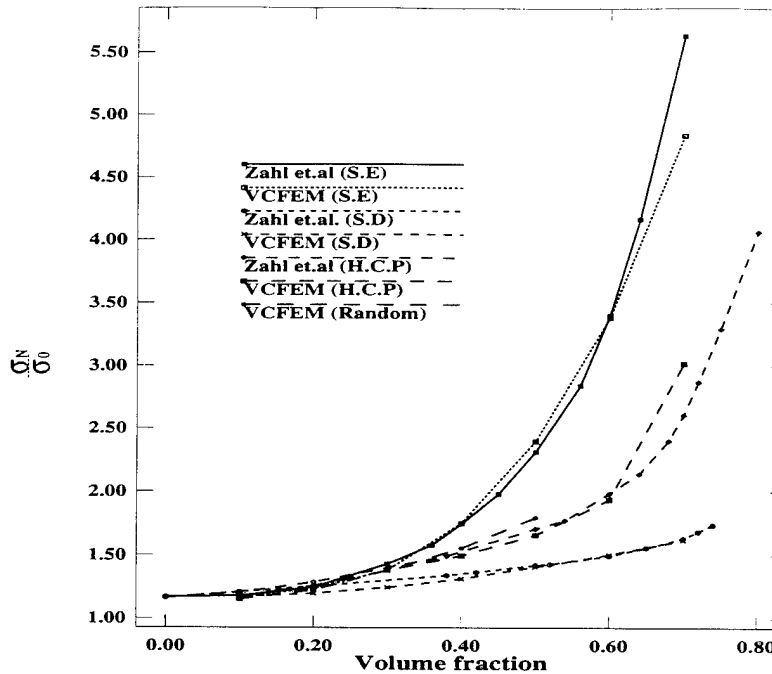


Figure 3.24: Size effect on the asymptotic yield stress for various distributions

law  $\bar{\sigma} = \sigma_{mat}(\bar{\epsilon}/\epsilon_0)^m$ . The matrix material in this example has the following properties.  
 $E = 88.867$  Units (Young's Modulus),  $\nu = 0.33$  (Poisson's Ratio)  
 $\sigma_{mat} = 1$  Unit (Initial Yield Stress),  $\sigma_{eqv} = \sigma_{mat}(\epsilon_{eff}/0.001)^{0.2}$  (Post Yield Hardening Law)

A square edge (S.E), square diagonal (S.D), hexagonal close packing (H.C.P) and a random packed RME, as shown in figure 3.14, are uniaxially loaded with repeatability conditions. Figure 3.24 compares the VCFEM generated asymptotic yield stresses with results in [34], for different volume fractions. Excellent agreement is obtained for all packings.

#### Comparisons with Some Analytical and Experimental Results

Plane strain VCFEM results are compared with analytical 2 and 3-phase model predictions due to Zhao and Weng [35] and experimental results due to Adams [42] for unidirectional composites. The material properties are:

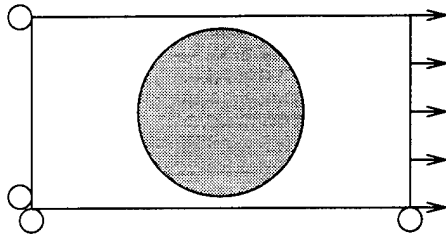
##### Aluminum

$E = 58$  GPa (Young's Modulus),  $\nu = 0.33$  (Poisson's Ratio)  
 $Y_0 = 89$  MPa (Initial Yield Stress),  $\sigma_{eqv} = Y_0 + 175(\epsilon_{eqv}^{pl})^{0.125}$  MPa (Post Yield Hardening Law)

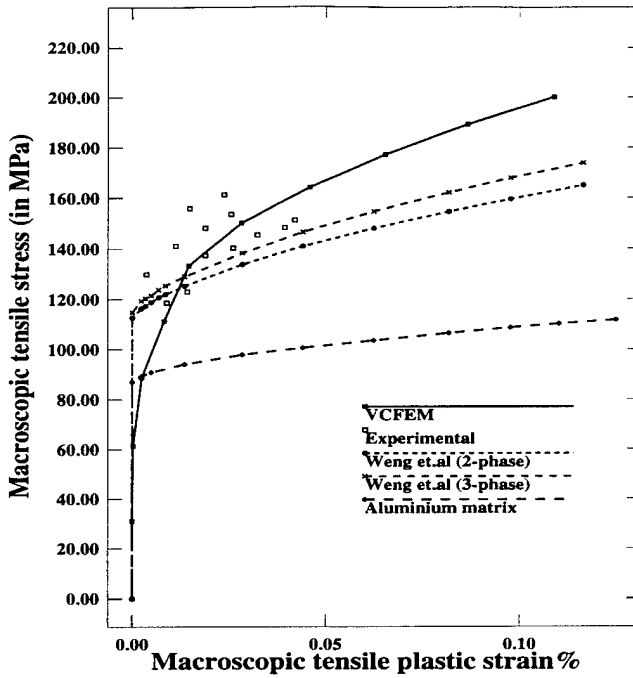
##### Boron

$E = 385$  GPa (Young's Modulus),  $\nu = 0.2$  (Poisson's Ratio)

A  $2 \times 1$  rectangular edge packed RME with a circular inclusion of  $V_f = 34\%$  is loaded in uniaxial tension with repeatability, as shown in figure 4.13(a). Figure 4.13(b) shows that VCFEM results provide a better agreement with experimental results than the analytical model. This is probably because of the square arrays used in [35] to approximate the rectangular RME.



(a)



(b)

Figure 3.25: (a) Rectangular edge packing composite RME ( $V_f = 34\%$ ) (b) Macroscopic stress-strain responses by VCFEM, analytical and experimental methods

### 3.6 Conclusions

In this work, the Voronoi cell finite element model is further developed and enhanced for accurate and efficient 2-D analysis of heterogeneous materials. Specifically, small deformation elasto-plastic deformation of porous and composite media, with an arbitrary dispersion of microscopic phases is considered. Stress functions in the modified scheme are motivated from the essential characteristics of micromechanics by accounting for the heterogeneity shape and influence. This is achieved by transforming arbitrary shaped heterogeneities to a unit circle using a method similar to the Schwarz-Christoffel conformal mapping. Reciprocal stress functions of singular nature are then constructed. This is a significant advancement over polynomial stress functions commonly used in hybrid finite element methods. It enhances the accuracy for various microstructures tremendously at very moderate computational efforts. It would take a prohibitively large number of terms and consequently incur enormous computational costs to generate results of comparable accuracy by pure polynomial stress expansion.

The accuracy and efficiency of VCFEM are established by comparing with conventional FEM commercial packages. For a wide range of problems VCFEM delivers very similar accuracy at a considerably low computational effort. This is evidenced by the drastically reduced degrees of freedom needed for convergence, compared with the conventional codes. The D.O.F. ratio varies from as low as 20 for simple microstructures, to even 100 for more complex cases. This translates into a reduction factor of 15-30 in the CPU time for execution, even with a non-optimized research code. Furthermore, user effort required to generate

the model is much lower for VCFEM than for commercial packages.

Mechanical responses and their qualitative comparison for various microstructures are possible through VCFEM analysis. For porous materials, VCFEM generated yield functions are compared with predictions of the continuum Tvergaard-Gurson (T-G) models. Though VCFEM results agree with the T-G models at lower void volume fractions, it is noted that increasing void size produces considerable deviations. Distribution and void shape also have a significant influence on the overall performance, and these effects are magnified with increasing size. This is also evidenced through the difference in yield surfaces generated by VCFEM and the T-G model. An interesting observation is that void orientation plays a more important role than void shape in yielding of the overall material. VCFEM is also proved to be accurate in modeling composite microstructures. VCFEM comparisons with ANSYS and ABAQUS simulations, as well as with experimental and analytical results establish this claim.

In conclusion, the Voronoi Cell finite element model has emerged as an important tool for analyzing arbitrary microstructures in many materials. Its strength is derived from the combination of basic micromechanics concepts with the essentials of finite element methods. It has the potential for direct correlation between quantitative characterization and material response. Multiple scale coupling between structural and microstructural scales involving commercial packages at the structural scale is easily accomplished with this method, as shown by the authors in [30, 21].

# Bibliography

- [1] T. Christman, A. Needleman and S. Suresh, An experimental and numerical study of deformation in metal-ceramic composites, *Acta Metallurgica*, **37**, 3029-3050, (1989).
- [2] Z. Hashin and S. Strikman, A variational approach to the theory of the elastic behavior of multiphase materials., *J. Mech Phys. Solids.*, **11**, 127-140, (1963).
- [3] H.S. Chen and A. Acrivos, The effective elastic moduli of composite materials containing spherical inclusions at non-dilute concentrations *Int. J. Solids. Structures*, **14**, 349-364, (1978).
- [4] R. Hill, A self consistent mechanics of composite materials., *J. Mech Phys. Solids.*, **13**, 213-222, (1965).
- [5] B. Budiansky, On the elastic modulii of some heterogeneous materials, *J. Mech. Phys. Solids.*, **13**, 223-227, (1965).
- [6] R.M. Christensen and K.H. Lo, Solutions for effective shear properties in three phase sphere and cylinder models, *J. Mech. Phys. Solids.*, **27**, 315-330, (1979).
- [7] G.P. Tandon and G.J. Weng, A theory of particle reinforced plasticity, *J. Appl. Mech.*, **55**, 126-135, (1988).
- [8] G. Dvorak and Y.A. Bahei-el-din, Plasticity analysis of fibrous composites, *Jour. Appl. Mech.*, **49**, 327-335, (1982).
- [9] G. Dvorak and Y.A. Bahei-el-din, A bimodal plasticity theory of fibrous composite materials, *Acta Mechanica*, **69**, 219-241, (1987).
- [10] J. Aboudi, Constitutive relations for cracked metal matrix composites, *Mech. Mater.*, **6**, 305-315, (1987).
- [11] S. Nemat-Nasser, T. Iwakuma and M. Hejazi, On composites with periodic structure, *Mech. Mater.*, **1**, 239-267. (1982).
- [12] G. Bao, J.W. Hutchinson and R.M. McMeeking, Plastic reinforcement of ductile matrices against plastic flow and creep, *Acta Metallur. et Mater.*, **39**, 1871-1882, (1991).
- [13] V. Tvergaard, Analysis of tensile properties for a whisker -reinforced metal matrix composite, *Acta Metall. et Mater.*, **38**, 185-194, (1990).

- [14] S. Moorthy, S. Ghosh and Y. Liu, Voronoi cell finite element method for micropolar thermo-elastic, elasto-plastic heterogeneous materials, *ASME Appl. Mech. Rev.*, **47**, 207-221, (1993).
- [15] S. Ghosh and S. Moorthy, Elastic-plastic analysis of arbitrary heterogeneous materials with the Voronoi cell finite element method, *Comp. Meth. Appl. Mech. Engrg.*, **121**, 373-409, (1995).
- [16] S. Ghosh and S.N. Mukhopadhyay, A material based finite element analysis of heterogeneous media involving Dirichlet tessellation, *Comp. Meth. Appl. Mech. Engrg.*, **104**, 211-247, (1993).
- [17] S. Ghosh and R.L. Mallett, Voronoi cell finite elements, *Comput. Struct.*, **50(1)**, 33-46, (1994).
- [18] S. Ghosh and Y. Liu, Voronoi cell finite element method for micropolar thermo-elastic heterogeneous materials, *Int. J. Numer. Meth. Engrg.*, **38**, No. 8, 1361-1398, (1995).
- [19] S. Ghosh and S.N. Mukhopadhyay, A two dimensional automatic mesh generator for finite element analysis of random composites, *Comput. Struct.*, **41**, 245-256, (1991).
- [20] S. Ghosh, K. Lee and S. Moorthy, Multiple scale analysis of heterogeneous elastic structures using homogenization theory and Voronoi cell finite element method, *Int. J. Solids Struct.*, **32(1)**, 27-62, (1995).
- [21] K. Lee and S. Moorthy and S. Ghosh, Multiple scale elastic-plastic analysis of heterogeneous structures; Asymptotic homogenization and Voronoi cell finite element model, *Submitted for publication*.
- [22] W.A. Spitzig, J.F. Kelly and O. Richmond, Quantitative characterization of second phase populations, *Metallography*, **18**, 235-261, (1985).
- [23] T.H.H. Pian, 'Derivation of element stiffness matrices by assumed stress distribution', *AIAA Journal*, **2**, 1333-1336 (1964).
- [24] S.N. Atluri, On the hybrid finite element model for incremental analysis of large deformation problems, *Int. J. Solids Struct.*, **9**, 1177-1191, (1973).
- [25] S.N. Atluri, On some new general and complimentary energy theorems for the rate problems in finite Strain, classical elastoplasticity, *J. Struct. Mech.*, **8(1)**, 61-92, (1980).
- [26] S.W. Attaway, A stress-based finite element method for computational elasto-plastic analysis, using an endochronic theory of plasticity, *Ph.D. Dissertation, Georgia Institute of Technology*, (1986).
- [27] N.I. Muskhelishvili, *Some Basic Problems in the Mathematical Theory of Elasticity*, P.Nordhoff Ltd., Netherlands, 1965.
- [28] N.I. Muskhelishvili, *Stress Concentrations Around Holes*, Permagon Press, Great Britain, 1951.

- [29] Pin Tong, T.H.H. Pian, and S.J. Lasry, A hybrid-element approach to crack problems in plane elasticity, *Int. J. Numer. Meth. Engrg.*, **7**, 197-308, (1973).
- [30] R. Piltner, Special finite elements with holes and internal cracks, *Int. J. Numer. Meth. Engrg.*, **21**, 197-308, (1973).
- [31] V. Tvergaard, Influence of voids on shear band instabilities under plane strain conditions, *Int. J. Fract.*, **17**, 389-407, (1982).
- [32] C.L. Hom and R.M. McMeeking, Void growth in elastic-plastic materials, *ASME, J. Appl. Mech.*, **56**, 309-317, (1989).
- [33] G. Bao, J.W. Hutchinson and R.M. McMeeking, Particle reinforcement of ductile matrices against plastic flow and creep, *Acta Metall. et Mater.*, **39**, 1871-1892, (1991).
- [34] D.B. Zahl, S. Schmauder and R.M. McMeeking, Transverse strength of metal matrix composites reinforced with strongly bonded continuous fibers in regular arrangements, *Acta Metall. et Mater.*, **42**, 2983-2997, (1994).
- [35] Y.H. Zhao and G.J. Weng, Theory of plasticity for inclusion and fiber-reinforced composite, in: G.J. Weng, M. Taya and H. Abe, eds., *Micromechanics and Inhomogeneity, The Toshio Mura Anniversary Volume*, Springer-Verlag, 599-622, 1989.
- [36] D.F. Adams, Inelastic analysis of a unidirectional composite subjected to transverse normal loading, *J. Composite Materials*, **4**, 310-328, (1970).

## Chapter 4

# Multiple Scale Modeling of Heterogeneous Materials Using Asymptotic Homogenization and the Voronoi Cell FEM

### Summary

In this work, a multiple scale finite element model (VCFEM-HOMO) has been developed for elastic-plastic analysis of heterogeneous (porous and composite) materials by combining asymptotic homogenization theory with the Voronoi Cell finite element model (VCFEM). VCFEM for microstructural modeling originates from Dirichlet tessellation of representative material elements at sampling points in the structure. Structural modeling is done by the general purpose finite element code ABAQUS, and interfacing with the microscale VCFEM analysis is done through the user subroutine in ABAQUS for material constitutive relation, UMAT. Asymptotic homogenization in UMAT generates macroscopic material parameters for ABAQUS. Following the macroscopic analysis, a local VCFEM analysis is invoked to depict the true evolution of microstructural state variables. Various numerical examples are executed for validating the effectiveness of VCFEM-HOMO, and the effect of size, shape and distribution of heterogeneities on local and global response is examined.

### 4.1 Introduction

The last three decades have experienced a surge in the advancement of science and technology for heterogeneous materials that contain dispersions of multiple phases in the microstructure. Examples are metal/alloy systems with second phase in the form of precipitates and pores, and composite materials containing a dispersion of fibers, whiskers or particulates in the matrix. In alloy systems, precipitates and pores are results of conventional processing routes. In reinforced composites, stiff, strong and brittle second phase inclusions e.g. silicon

carbide, boron or aluminum oxide, etc. are added to titanium, nickel or aluminum matrices to enhance flow strength, creep resistance and wear resistance of structures. These functionally superior materials have found increasing utilization in the aerospace, automotive, materials and ordnance industries for replacing some of the traditionally used structural materials. The degree of mechanical and thermal property enhancements depends on the size, shape and properties of the second phase, as well as on their spatial distribution within the matrix. For example, ductility is reduced with increasing volume fraction of reinforcements in metal-matrix composites. Christman et. al. [1] have shown that local plastic flow is highly sensitive to shape of the reinforcements under identical global stresses. It is clear that rigorous fundamental studies are warranted for understanding deformation and failure mechanisms prior to design of advanced materials in high performance applications. Studies reflecting the details of actual heterogeneous microstructures are indispensable in this respect. It is through these models, that the effect of second phase shapes, sizes and distributions on evolving state variables like stresses, plastic strains, void initiation and growth, and evolving material variables like strain hardening and flow stress can be investigated.

A number of analytical micromechanical models for predicting macroscopic response have evolved within the framework of small deformation linear elasticity theory. Notable among them are models based on : (i) variational approach using extremum principles [2, 3], (ii) probabilistic approach [4], (iii) self-consistent schemes [5, 6] and (iv) the generalized self consistent model [7, 3]. These models follow the idea of equivalent inclusion methods based on eigenstrain formulation. Though analytical micro-mechanical models are reasonably effective in predicting equivalent material properties for relatively simple geometries and low volume fractions, they are often incapable in depicting the evolution of stresses and strains in the microstructure. Arbitrary microstructural morphology, that are frequently encountered in actual materials cannot be deterministically treated with these models. Constitutive response of the constituent phases are also somewhat restricted and predictions with large property mismatches are not very reliable. Additionally, due to lack of proper representation of microscopic stresses and strains, they cannot capture the effect of local inhomogeneities on damage and failure. The state of the art in analytical modeling for ductile materials is not as mature. Important contributions have been made by Tandon and Weng [8] for small strain, deformation theory of elasto-plasticity of metals with elastic particles, and by Dvorak and Bahei-El-Din [9, 10] for rate-independent plastic matrix and elastic fibers using a “vanishing fiber diameter” model, and more recently the bimodal plasticity theory. Paley and Aboudi [11] have developed a semi-analytical generalized method of cells for elastic-plastic and viscoplastic materials, while Nemat-Nasser and coworkers [12] have used Fourier series expansions to develop elastic-plastic and creep models. The applications of these nonlinear models to complex microstructures in many real materials are even less effective than the linear models. This is substantiated by the fact that when plastic flow occurs, the deformation is no longer homogeneous. Local properties become stress dependent and the overall constitutive response is influenced by the distributions and shapes of second phase.

Intractability of analytical models in situations of arbitrary phase dispersions have necessitated the introduction of *Unit Cell* formulations [1, 13, 14] using computational methods.

These models generate overall material response through detailed discretization of a representative volume element (RVE) of the composite microstructure. In unit cell models, global properties are ascertained by assuming macroscopic periodicity conditions on the RVE's. Despite their widespread success, the unit cell models are faced with some shortcomings in modeling real materials, stemming from global and local periodicity assumptions. Global periodicity assumes that the same RVE is valid for all points of a structure, which is not realistic for many commercial materials. A majority of these models also make assumptions of "perfect" local periodicity and uniform distribution of the second phase. Effectively, this local periodicity assumption can reduce the representative volume element (RVE) to a basic structural element (BSE), thereby making the unit cells very simple. A basic structural element is defined as the smallest element of the microstructure reflecting basic geometrical features (see figure 1(c)). Micrographs of many real materials often show arbitrariness in distribution (figure 1(b)) thereby making this assumption too restrictive. Another limitation is that unit cell models typically formulate constitutive relations based on a single RVE subjected to a given load history. This makes them amenable to misrepresentation of the actual interaction between macro- and micro-scale deformations. This calls for simultaneous computations at *multiple levels* for concurrent evolution of macroscopic and microscopic variables.

In the 1970's a mathematical theory called **Asymptotic Homogenization Theory** [15, 16], originated for analyzing physical systems containing two or more length scales. It is suitable for multi-phase materials in which the natural scales are the microscopic scale characterized by inter-heterogeneity/local discontinuity spacing and the macroscopic scale characterizing overall dimensions of the structure. This method is based on asymptotic expansions of displacement and stress fields about their respective macroscopic values and uses variational principles for creating a link between scales. Resulting boundary value problems at the macroscopic and microscopic levels are solved by invoking numerical methods at both levels. Figure 1 shows the various levels in a structure and its corresponding computational model. Computer simulations simultaneously provide global response through homogenized material parameters and averaged stress/strain fields, and microstructural behavior through a depiction of local stress/strain fields. This method can overcome shortcomings inflicted by global periodicity restrictions in unit cell models. The analysis however, makes the assumption of local periodicity through the introduction of spatially repeated microscopic cells.

The finite element method has been successfully applied in conjunction with the homogenization theory for analysis of linear elastic, particulate and fiber reinforced composites by Toledano and Murakami [17] and by Guedes and Kikuchi [18, 23]. These models are constructed by considering very simple unit cells that represent uniform distributions in the microstructure. For nonlinear regimes, homogenization theories have been established by Suquet [19]. Important contributions to the application of homogenization method in finite deformation elasto-plasticity has been made by Guedes [20] and Cheng [21]. The method has been extended to model damage evolution by fiber rupture for linear elastic materials in [25]. A comprehensive review of this method for various problems is presented in [22]. In spite of its promise, the homogenization theory has not enjoyed a wide acceptance thus far. A prime reason is the assumptions of over-simplified microscopic RVE's for reducing

enormous computing costs.

The material based *Voronoi Cell Finite Element Model* (VCFEM) [26, 27, 28, 29, 30], developed by Ghosh and coworkers, attempts to overcome difficulties in modeling arbitrary microstructures by conventional finite element methods. The VCFEM mesh evolves naturally from a heterogeneous microstructural material element (RME) by *Dirichlet tessellation* into a network of multi-sided “Voronoi” polygons. The polygons contain one second phase inclusion each, at most as shown in figure 1(b). A robust mesh generator to create these polygons based on shape, size and location of the heterogeneities is developed in [30]. The multi-phase Voronoi polygons, identified with the basic structural elements as depicted in figure (1c), constitute elements in VCFEM. Element formulations have been developed for micropolar thermo-elasticity problems in [29], and for elastic-plastic problems in [26, 27]. VCFEM with asymptotic homogenization for elastic problems have been presented in [28].

This work presents a coupled multiple scale computational model for heterogeneous elastic-plastic structures. Only two dimensional problems are considered. Microstructural analysis for various different representative material element arrangements, is done with the Voronoi Cell finite element model. The commercial general purpose code ABAQUS [31] is used for global analysis at the level of overall structural geometry and applied loads. The interfacing between macro- and micro- calculations are done through the user subroutine window UMAT in ABAQUS. Numerical examples are conducted to investigate the advantages of coupled multiple scale analysis over other unit cell and continuum based theories. Effect of shapes, sizes and locations of microscopic inclusions on the structural performance and the evolution of microstructural stresses and strains are also studied.

## 4.2 Asymptotic Homogenization for Multiple Scale Analysis

Consider a heterogeneous body occupying a region  $\Omega_{structure}$  in figure 4.1(a), for which the microstructure constitutes of spatially periodic representative material elements (RME’s) as shown in figure 4.1(b). Only small deformation elastic-plastic deformation of the body is considered in the absence of inertia. The body is subjected to a system of time/load dependent body forces  $\mathbf{f}(t)$ , surface tractions  $\mathbf{t}(t)$  on the boundary  $\Gamma_t$  and prescribed displacement fields on the boundary  $\Gamma_u$ . In real heterogeneous materials, dimensions of the RME of characteristic length  $l$  are typically very small in comparison with the dimensions of the body of characteristic length  $L$ . The ratio of these microscopic and macroscopic scales  $l/L$  is represented by a very small positive number  $\epsilon$ . When subjected to structural level loads and displacements, the resulting evolutionary variables e.g. deformation and stresses, vary from point to point at the macroscopic scale  $\mathbf{x}$ . Furthermore, a high level of heterogeneity in the microstructure causes a rapid variation of these variables in a small neighborhood  $\epsilon$  of the macroscopic point  $\mathbf{x}$ . This corresponds to a microscopic scale  $\frac{\mathbf{x}}{\epsilon}$  and consequently, all variables are assumed to exhibit dependence on both length scales i.e.  $\Phi^\epsilon = \Phi(\mathbf{x}, \frac{\mathbf{x}}{\epsilon})$ . The superscript  $\epsilon$  denotes association of the function with the two length scales. In this notation,  $\Omega^\epsilon$  corresponds to a connected domain that extends the structural domain to its

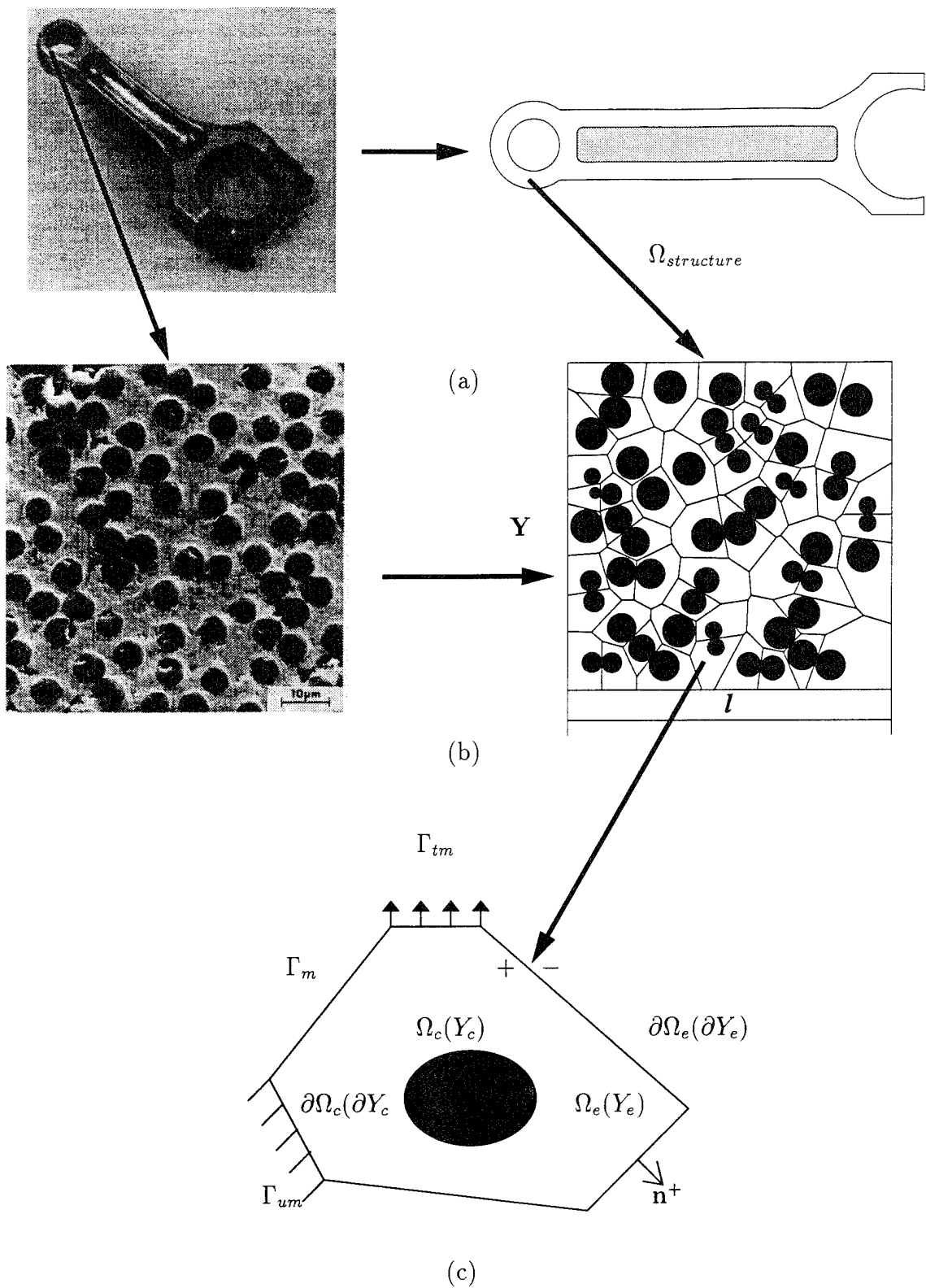


Figure 4.1: A heterogeneous structure with various levels (a) The global structure and computational geometry (b) Representative material elements (RME) at a point and the corresponding VCCE model and, (c) A basic structural element (BSE) represented by a Voronoi Cell.

microstructure. Mathematically speaking,

$$\Omega^\epsilon = \{\mathbf{x} \in \Omega : \Theta\left(\frac{\mathbf{x}}{\epsilon}\right) = 1\} \quad (4.1)$$

in which  $\Theta(\mathbf{y}) = 1$  when  $\mathbf{y}$  lies in the microscopic RME. In most of the work on homogenization theory [22, 18, 20, 25], a periodic repetition of the microstructure about a macroscopic point  $\mathbf{x}$  has been assumed, thereby making the dependence of the function on  $\mathbf{y} = (\frac{\mathbf{x}}{\epsilon})$ , periodic. This characteristic is often termed as  $\mathbf{Y}$ -periodicity, where  $\mathbf{Y}$  corresponds to a RME. The instantaneous tangent modulus tensor  $E_{ijkl}^\epsilon$ , relating the stress rate (increment) to the strain rate (increment), and the corresponding instantaneous compliance tensor  $S_{ijkl}^\epsilon$  in the connected domain are expressed as:

$$E_{ijkl}^\epsilon(\mathbf{x}) = E_{ijkl}(\mathbf{x}, \mathbf{y}) \quad \text{in } \Omega^\epsilon \quad (4.2)$$

$$S_{ijkl}^\epsilon(\mathbf{x}) = E_{ijkl}^{-1}(\mathbf{x}, \mathbf{y}) \quad \text{in } \Omega^\epsilon \quad (4.3)$$

It is assumed that the stress, strain and displacement fields satisfy the rate or incremental forms of the equilibrium equation, kinematic relation, and constitutive relations given as:

$$\dot{\sigma}_{ij,j}^\epsilon = -\dot{f}_i \quad \text{in } \Omega^\epsilon \quad (4.4)$$

$$\dot{e}_{kl}^\epsilon = \frac{1}{2} \left( \frac{\partial \dot{u}_k^\epsilon}{\partial x_l^\epsilon} + \frac{\partial \dot{u}_l^\epsilon}{\partial x_k^\epsilon} \right) \quad \text{in } \Omega^\epsilon \quad (4.5)$$

$$\dot{\sigma}_{ij}^\epsilon = E_{ijkl}^\epsilon \dot{e}_{kl}^\epsilon \quad \text{in } \Omega^\epsilon \quad (4.6)$$

where  $\dot{u}_i^\epsilon = \dot{u}_i^\epsilon(\mathbf{x}, \mathbf{y})$  is a  $\mathbf{Y}$ -periodic rate of displacement field in  $\mathbf{y}$ . Furthermore the boundary conditions are assumed to satisfy the following equations on the prescribed traction and displacement boundaries respectively.

$$\dot{\sigma}_{ij}^\epsilon n_j = \dot{t}_i \quad \text{on } \Gamma_t \quad (4.7)$$

$$\dot{u}_i^\epsilon = \dot{\bar{u}}_i \quad \text{on } \Gamma_u \quad (4.8)$$

where  $\mathbf{n}$  is the unit normal to the boundary. Since small deformation is assumed in this analysis, the normal vector does not change significantly with load. In homogenization theory, the  $\mathbf{Y}$ -periodic displacement rate or increment field is approximated by an asymptotic expansion with respect to parameter  $\epsilon$ :

$$\dot{\mathbf{u}}^\epsilon(\mathbf{x}) = \dot{\mathbf{u}}^0(\mathbf{x}, \mathbf{y}) + \epsilon \dot{\mathbf{u}}^1(\mathbf{x}, \mathbf{y}) + \epsilon^2 \dot{\mathbf{u}}^2(\mathbf{x}, \mathbf{y}) + \dots, \quad \mathbf{y} = \frac{\mathbf{x}}{\epsilon} \quad (4.9)$$

Noting that the spatial  $\mathbf{x}^\epsilon$  derivative of any function depends on the two length scales and is given as:

$$\frac{\partial}{\partial x_i^\epsilon} \left( \Phi(\mathbf{x}, \mathbf{y} = \frac{\mathbf{x}}{\epsilon}) \right) = \frac{\partial \Phi}{\partial x_i} + \frac{1}{\epsilon} \frac{\partial \Phi}{\partial y_i} \quad (4.10)$$

the strain rate tensor may be expressed as:

$$\dot{e}_{kl}^\epsilon = \frac{\partial \dot{u}_k^\epsilon}{\partial x_l^\epsilon} = \frac{1}{\epsilon} \frac{\partial \dot{u}_k^0}{\partial y_l} + \left( \frac{\partial \dot{u}_k^0}{\partial x_l} + \frac{\partial \dot{u}_k^1}{\partial y_l} \right) + \epsilon \left( \frac{\partial \dot{u}_k^1}{\partial x_l} + \frac{\partial \dot{u}_k^2}{\partial y_l} \right) + \dots \quad (4.11)$$

Substituting this in the constitutive relation (4.6), the stress rate  $\dot{\sigma}_{ij}^\epsilon$  can be expanded as

$$\dot{\sigma}_{ij}^\epsilon = \frac{1}{\epsilon} \dot{\sigma}_{ij}^0 + \dot{\sigma}_{ij}^1 + \epsilon \dot{\sigma}_{ij}^2 + \epsilon^2 \dot{\sigma}_{ij}^3 \dots \quad (4.12)$$

where

$$\begin{aligned} \dot{\sigma}_{ij}^0 &= E_{ijkl}^\epsilon \frac{\partial \dot{u}_k^0}{\partial y_l} \\ \dot{\sigma}_{ij}^1 &= E_{ijkl}^\epsilon \left( \frac{\partial \dot{u}_k^0}{\partial x_l} + \frac{\partial \dot{u}_k^1}{\partial y_l} \right) \\ \dot{\sigma}_{ij}^2 &= E_{ijkl}^\epsilon \left( \frac{\partial \dot{u}_k^1}{\partial x_l} + \frac{\partial \dot{u}_k^2}{\partial y_l} \right) \end{aligned} \quad (4.13)$$

Putting the expansion of  $\dot{\sigma}_{ij}^\epsilon$  (4.12) in the rate form of equilibrium equation (4.4), and setting each coefficient of  $\epsilon^i$ , ( $i = -1, 0, 1, 2, \dots$ ) to zero, results in the following set of equations.

$$\begin{aligned} \frac{\partial \dot{\sigma}_{ij}^0}{\partial y_j} &= 0 \\ \frac{\partial \dot{\sigma}_{ij}^1}{\partial y_j} + \frac{\partial \dot{\sigma}_{ij}^0}{\partial x_j} &= 0 \\ \frac{\partial \dot{\sigma}_{ij}^2}{\partial y_j} + \frac{\partial \dot{\sigma}_{ij}^1}{\partial x_j} + f_i &= 0 \end{aligned} \quad (4.14)$$

If  $\mathbf{x}$  and  $\mathbf{y}$  are considered as independent variables, equations (4.14) form a recursive system of differential equations for the functions  $\dot{u}_i^0, \dot{u}_i^1, \dot{u}_i^2 \dots$  parameterized by  $\mathbf{x}$ . An important result that is used to solve the system of equations (4.14) is given as follows [24]. The equation

$$-\frac{\partial}{\partial y_i} (a_{ij}(y) \frac{\partial \Phi}{\partial y_j}) = F \quad \text{in } \mathbf{Y} \quad (4.15)$$

for a  $\mathbf{Y}$ -periodic function  $\Phi = \Phi(\mathbf{x}, \mathbf{y})$  has a unique solution if the mean value of  $F$ , defined by

$$\langle F \rangle = \frac{1}{|\mathbf{Y}|} \int_{\mathbf{Y}} F dy = 0 \quad (4.16)$$

where  $|\mathbf{Y}|$  denotes the volume of the RME. Equations (4.14) and (4.13) together with results (4.16) leads to the trivial value for  $\dot{\sigma}_{ij}^0$ , and therefore establishes that  $\dot{\mathbf{u}}^0$  is only a function of  $\mathbf{x}$  as shown in [25], i.e.

$$\dot{\sigma}_{ij}^0 = 0, \quad \text{and} \quad \dot{u}_i^0 = \dot{u}_i^0(\mathbf{x}) \quad (4.17)$$

#### 4.2.1 Microscopic Equilibrium Equation and Homogenized Constitutive Relation

Substituting (4.17) into the second of equation (4.14) leads to the  $\mathbf{Y}$ - domain equilibrium equation

$$\frac{\partial \dot{\sigma}_{ij}^1}{\partial y_j} = 0 \quad (4.18)$$

From equations (4.6), (4.11) and (4.12), by neglecting the terms associated with  $\epsilon$  or higher, the constitutive relation in  $\mathbf{Y}$  is expressed as

$$\dot{\sigma}_{ij}^\epsilon = \dot{\sigma}_{ij}^1 = E_{ijkl}^\epsilon \dot{e}_{kl}^\epsilon \quad (4.19)$$

where

$$\dot{e}_{kl}^\epsilon = \dot{\bar{e}}_{kl} + \dot{e}_{kl}^* = \frac{\partial \dot{u}_k^0}{\partial x_l} + \frac{\partial \dot{u}_k^1}{\partial y_l} \quad (4.20)$$

Here  $\dot{e}_{kl}^\epsilon$  is the local or microstructural strain rate tensor, for which  $\dot{\bar{e}}_{kl} = \frac{\partial \dot{u}_k^0}{\partial x_l}$  is an averaged macroscopic part, and  $\dot{e}_{kl}^* = \frac{\partial \dot{u}_k^1}{\partial y_l}$  is denoted as a fluctuating strain rate tensor (Suquet [32]). With the equilibrated microscopic stress rate  $\dot{\sigma}_{ij}^1$  and displacement rate  $\dot{u}_k^1$  fields completely determined by equations (4.18), (4.19) and (4.20), a local structure tensor denoted by  $M_{pm}^{kl}$  is calculated by applying a unit components of a macroscopic strain rate tensor. The local structure tensor  $M_{pm}^{kl}$  is used to establish a relation between the local microscopic strain rate  $\dot{e}_{kl}^\epsilon$ , and the macroscopic strain rate  $\dot{\bar{e}}_{kl}$  as:

$$\dot{e}_{kl}^\epsilon = M_{pm}^{kl} \dot{\bar{e}}_{pm} \quad (4.21)$$

Due to linearity of the rate(incremental) problem,  $\dot{\sigma}_{ij}^1$  and  $\dot{u}_i^1$  can be expressed in the forms

$$\dot{\sigma}_{ij}^1 = \hat{\sigma}_{ij}^{kl}(\mathbf{y}) \frac{\partial \dot{u}_k^0}{\partial x_l}, \quad \dot{u}_i^1 = \chi(\mathbf{y})_i^{kl} \frac{\partial \dot{u}_k^0}{\partial x_l} \quad (4.22)$$

where

$$\frac{\partial \hat{\sigma}_{ij}^{kl}(\mathbf{y})}{\partial y_j} = 0 \quad (\text{microscopic equilibrium}) \quad (4.23)$$

In equation (4.22),  $\hat{\sigma}_{ij}^{kl}$  is a  $\mathbf{Y}$ -antiperiodic function and  $\chi_i^{kl}$  is a  $\mathbf{Y}$ -periodic function representing characteristic modes of the RME. Substituting equations (4.22) and (4.21) in equation (4.13) yields the microscopic constitutive relations as:

$$\hat{\sigma}_{ij}^{kl}(\mathbf{y}) = E_{ijpm}^\epsilon M_{pm}^{kl} \quad (4.24)$$

The local structure tensor is related to the  $\mathbf{Y}$ -periodic function  $\chi_i^{kl}$  as:

$$M_{pm}^{kl} = [T_{pm}^{kl} + \frac{\partial \chi_p^{kl}}{\partial y_m}] \quad (4.25)$$

where  $T_{ij}^{kl}$  is a fourth order identity tensor expressed as:

$$T_{ij}^{kl} = \frac{1}{2}(\delta_{ik}\delta_{jl} + \delta_{il}\delta_{jk}) \quad (4.26)$$

The set of equations (4.22) and (4.25) determine the vector  $\chi(\mathbf{y})_k^{ij}$  to within an additive constant. The mean of equation (4.25) yields the homogenized elastic-plastic tangent modulus, for use in the macroscopic analysis, in the form

$$E_{ijkl}^H = \langle \hat{\sigma}_{ij}^{kl} \rangle = \frac{1}{|\mathbf{Y}|} \int_Y \hat{\sigma}_{ij}^{kl} dY = \frac{1}{|\mathbf{Y}|} \int_Y E_{ijpm}^\epsilon (T_{pm}^{kl} + \frac{\partial \chi_p^{kl}}{\partial y_m}) dY \quad (4.27)$$

#### 4.2.2 Macroscopic Equations

Taking the mean of the third equation in (4.14) on  $\mathbf{Y}$  and applying the condition (4.16) to the first term  $\frac{\partial \dot{\sigma}_{ij}^2}{\partial y_j}$  leads to an averaged form of the global equilibrium equation as:

$$\frac{\partial \langle \dot{\sigma}_{ij}^1 \rangle}{\partial x_j} + \dot{f}_i = 0 \quad \text{in } \Omega_{structure} \quad (4.28)$$

Note that the above equation (4.28) is now valid for the macroscopic domain  $\Omega_{structure}$ . Thus in the macroscopic domain, the averaged stress rate  $\dot{\Sigma} = \langle \dot{\sigma}^1 \rangle$  and displacement rate  $\dot{\mathbf{u}}^0$  fields are the solutions to the elastic-plastic problem delineated by the equations:

$$\begin{aligned} \frac{\partial \dot{\Sigma}_{ij}}{\partial x_j} &= -\dot{f}_i && \text{in } \Omega_{structure} \\ \dot{\Sigma}_{ij} &= E_{ijkl}^H \dot{\epsilon}_{kl} \\ \dot{\Sigma}_{ij} n_j &= \dot{t}_i && \text{on } \Gamma_t \\ \dot{u}_i^0 &= \dot{u}_i && \text{on } \Gamma_u \end{aligned} \quad (4.29)$$

An incremental small deformation analysis is pursued with the equations (4.29) at the macroscopic level, and by using the Voronoi cell finite element model (VCFEM) for solving the microscopic problem. Developments of the incremental VCFEM model for heterogeneous microstructures are presented in the next section.

### 4.3 Microstructural Analysis with VCFEM

Voronoi cells, resulting from Dirichlet tessellation of a heterogeneous microstructure, make rather unconventional elements, due to the arbitrariness in the number of edges. The Voronoi Cell finite element model developed by Ghosh and coworkers [26, 27, 28, 29] avoids difficulties of conventional displacement based FEM formulations by invoking the assumed stress hybrid method, introduced by Pian [33]. In this formulation, independent assumptions are made on an equilibrated stress field in the interior of each element and a compatible displacement field on the element boundary. Small deformation elastic-plastic analysis of materials with

embedded second phase has shown significant promise with respect to efficiency and accuracy [26, 27]. Details of this development based on the hybrid formulation, originally proposed by Atluri and coworkers [34, 35]), are presented in [26, 27]. In this section, a brief account of this formulation is presented for completeness.

#### 4.3.1 Variational Principles in VCFEM

Consider a typical representative material element (RME)  $Y$  tessellated into  $N$  Voronoi cells, as shown in figure 4.1(b). This is based on the location, shape and size of  $N$  heterogeneities as explained in [30]. The matrix phase in each Voronoi cell  $Y_e$  is denoted by  $Y_m$  and the heterogeneity (void or inclusion) is denoted by  $Y_c$ . The matrix-heterogeneity interface  $\partial Y_c$  has an outward normal  $\mathbf{n}^c$ , while  $\mathbf{n}^e$  is the outward normal to the element boundary  $\partial Y_e$ . In this presentation, an incremental finite element formulation is invoked to account for rate independent plasticity. At the beginning of the  $p$ -th increment, let  $\boldsymbol{\sigma}$  be an equilibrated stress field with a strain field  $\mathbf{e}(\boldsymbol{\sigma}, \text{load history})$ , and  $\mathbf{u}$  be a compatible displacement field on the element boundary. Also let  $\Delta\boldsymbol{\sigma}$  correspond to an equilibrated stress increment in  $Y_e$ ,  $\Delta\mathbf{u}$  to a compatible displacement increment on  $\partial Y_e$ , and  $\Delta\bar{\mathbf{t}}$  to a traction increment on the traction boundary  $\Gamma_{tm}$ . The incremental problem is solved by using a two field assumed stress hybrid variational principle, derived from an element energy functional as:

$$\begin{aligned} \Pi_e(\Delta\boldsymbol{\sigma}, \Delta\mathbf{u}) = & - \int_{Y_e} \Delta B(\boldsymbol{\sigma}, \Delta\boldsymbol{\sigma}) \, dY - \int_{Y_e} \mathbf{e} : \Delta\boldsymbol{\sigma} \, dY \\ & + \int_{\partial Y_e} (\boldsymbol{\sigma} + \Delta\boldsymbol{\sigma}) \cdot \mathbf{n}^e \cdot (\mathbf{u} + \Delta\mathbf{u}) \, \partial Y - \int_{\Gamma_{tm}} (\bar{\mathbf{t}} + \Delta\bar{\mathbf{t}}) \cdot (\mathbf{u} + \Delta\mathbf{u}) \, d\Gamma \\ & - \int_{\partial Y_c} (\boldsymbol{\sigma}^m + \Delta\boldsymbol{\sigma}^m - \boldsymbol{\sigma}^c - \Delta\boldsymbol{\sigma}^c) \cdot \mathbf{n}^c \cdot (\mathbf{u}' + \Delta\mathbf{u}') \, \partial Y \end{aligned} \quad (4.30)$$

where  $\Delta\mathbf{u}'$  is the displacement of the interface and  $\Delta\mathbf{B}$  is the increment in element complementary energy. Superscripts  $m$  and  $c$  represent respectively the matrix and second phase parts of the Voronoi cell element. The energy functional for the entire domain is obtained by adding each element functional as

$$\Pi = \sum_{e=1}^N \Pi_e \quad (4.31)$$

The first variation of  $\Pi_e$  with respect to the stress increments  $\Delta\boldsymbol{\sigma}$ , results in the kinematic relations as the Euler equation,

$$\nabla \Delta\mathbf{u} = \Delta\mathbf{e} \text{ in } Y_e \quad (4.32)$$

while the first variation of  $\Pi$  with respect to boundary displacement increments  $\Delta\mathbf{u}$  yields traction conditions as Euler equations,

$$\begin{aligned} (\boldsymbol{\sigma} + \Delta\boldsymbol{\sigma}) \cdot \mathbf{n}^{e+} &= -(\boldsymbol{\sigma} + \Delta\boldsymbol{\sigma}) \cdot \mathbf{n}^{e-} \text{ on cell boundary } \Gamma_m \quad (\text{Interelement traction reciprocity}) \\ (\boldsymbol{\sigma} + \Delta\boldsymbol{\sigma}) \cdot \mathbf{n}^e &= \bar{\mathbf{t}} + \Delta\bar{\mathbf{t}} \text{ on traction boundary } \Gamma_{tm} \\ (\boldsymbol{\sigma}^c + \Delta\boldsymbol{\sigma}^c) \cdot \mathbf{n}^c &= (\boldsymbol{\sigma}^m + \Delta\boldsymbol{\sigma}^m) \cdot \mathbf{n}^c \text{ on interface } \partial Y_c \quad (\text{Interface traction reciprocity}) \end{aligned} \quad (4.33)$$

Equilibrated stress increments  $\Delta\sigma$ , constitutive relations, along with the incremented form of the energy functional completely define the microstructural problem in the  $p$ -th increment.

### Element formulations and assumptions

In the Voronoi cell finite element model (VCFEM) formulation, independent assumptions on stress increments  $\Delta\sigma$  are made in the matrix and heterogeneity phases to accommodate stress jumps across the interface. Use of stress functions  $\Phi(x, y)$  is a convenient way of deriving stress increments in two-dimensional analysis. Different expressions may be assumed for  $\Phi$  in the matrix and inclusion phases. In general, these can be arbitrary functions of location, yielding stress increments in the form

$$\begin{aligned}\{\Delta\sigma^m\} &= [\mathbf{P}^m(x, y)]\{\Delta\beta^m\} \\ \{\Delta\sigma^c\} &= [\mathbf{P}^c(x, y)]\{\Delta\beta^c\}\end{aligned}\quad (4.34)$$

where  $\{\Delta\beta\}$ 's correspond to a set of yet undetermined stress coefficients and  $[\mathbf{P}]$  is a matrix of interpolation functions. Compatible displacement increments on the element boundary  $\partial Y_e$  as well as on the interface  $\partial Y_c$ , are generated by interpolation in terms of generalized nodal values. The displacement increments on the element boundary and interface may then be written as,

$$\begin{aligned}\{\Delta\mathbf{u}\} &= [\mathbf{L}^e]\{\Delta\mathbf{q}\} \\ \{\Delta\mathbf{u}'\} &= [\mathbf{L}^c]\{\Delta\mathbf{q}'\}\end{aligned}\quad (4.35)$$

where  $\{\Delta\mathbf{q}\}$  and  $\{\Delta\mathbf{q}'\}$  are generalized displacement increment vectors and  $[\mathbf{L}]$  is an interpolation matrix. Substituting element approximations for stresses (4.34) and displacements (4.35), in the energy functional (4.30), and setting the first variations with respect to the stress coefficients  $\Delta\beta^m$  and  $\Delta\beta^c$  respectively to zero, results in the following two weak forms of the kinematic relations (4.32),

$$\begin{aligned}\int_{Y_m} [\mathbf{P}^m]^T \{\mathbf{e} + \Delta\mathbf{e}\} dY &= \int_{\partial Y_e} [\mathbf{P}^m]^T [\mathbf{n}^e] [\mathbf{L}^e] dY \{\Delta\mathbf{q}\} - \int_{\partial Y_c} [\mathbf{P}^m]^T [\mathbf{n}^c] [\mathbf{L}^c] dY \{\Delta\mathbf{q}'\} \\ \int_{Y_c} [\mathbf{P}^c]^T \{\mathbf{e} + \Delta\mathbf{e}\} dY &= \int_{\partial Y_c} [\mathbf{P}^c]^T [\mathbf{n}^c] [\mathbf{L}^e] dY \{\Delta\mathbf{q}'\}\end{aligned}\quad (4.36)$$

Setting the first variation of the total energy functional (4.31) with respect to  $\Delta\mathbf{q}$  and  $\Delta\mathbf{q}'$  to zero, results in the weak form of the traction reciprocity conditions as

$$\begin{aligned}\sum_{e=1}^N \begin{bmatrix} \int_{\partial Y_e} [\mathbf{L}^e]^T [\mathbf{n}^e]^T [\mathbf{P}^m] dY & \mathbf{0} \\ - \int_{\partial Y_c} [\mathbf{L}^c]^T [\mathbf{n}^c]^T [\mathbf{P}^m] dY & \int_{\partial Y_c} [\mathbf{L}^c]^T [\mathbf{n}^c]^T [\mathbf{P}^c] dY \end{bmatrix} \begin{Bmatrix} \beta^m + \Delta\beta^m \\ \beta^c + \Delta\beta^c \end{Bmatrix} &= \\ \sum_{e=1}^N \left\{ \begin{array}{c} \int_{\Gamma_{tm}} [\mathbf{L}^e]^T \{\bar{\mathbf{t}} + \bar{\Delta\mathbf{t}}\} dY \\ \{\mathbf{0}\} \end{array} \right\} & \quad (4.37)\end{aligned}$$

For an elastic-plastic material, the strain increments  $\Delta\boldsymbol{e}$  in equation (4.36) are non-linear functions of the current state of stress  $\boldsymbol{\sigma}$  as well as of their increments  $\Delta\boldsymbol{\sigma}$ . The non-linear finite element equations (4.36) and (4.37) are solved for the stress parameters ( $\Delta\boldsymbol{\beta}^m$ ,  $\Delta\boldsymbol{\beta}^c$ ) and the nodal displacement increments ( $\Delta\mathbf{q}$ ,  $\Delta\mathbf{q}'$ ) at the  $p$ -th increment.

#### 4.4 Elastic-plastic Homogenization with VCFEM

In this section, the Voronoi Cell finite element model is formulated to be applied in conjunction with the homogenization method for coupling global and local analyses. VCFEM is used to model an arbitrary microstructural RME, and consequently,  $\mathbf{Y}$  represents a RME with a boundary  $\partial\mathbf{Y}$ . In an incremental formulation, the equilibrated microscopic stress increment corresponds to  $\Delta\boldsymbol{\sigma}^1 (= \Delta\boldsymbol{\sigma}^\epsilon)$  in equation (4.22) and the microstructural strain increments are designated as  $\Delta\boldsymbol{e}^\epsilon$  in equation (4.20). Similarly, the increments in microscopic displacements on the cell boundaries  $\partial Y_e$  are identified with  $\Delta\mathbf{u}^1$  in equation (4.22) and those on the interface are denoted by  $\Delta\mathbf{u}^{1'}$ . In the absence of traction boundaries due to periodicity conditions, the incremental energy functional for each Voronoi cell element in equation (4.30) is modified for the homogenization process as:

$$\begin{aligned} \Pi_e = & - \int_{Y_e} \frac{1}{2} S_{ijkl}^\epsilon \Delta\sigma_{ij}^\epsilon \Delta\sigma_{kl}^\epsilon dY - \int_{Y_e} e_{ij}^\epsilon \Delta\sigma_{ij}^\epsilon dY + \int_{\partial Y_e} (\sigma_{ij}^\epsilon + \Delta\sigma_{ij}^\epsilon) (u_i^1 + \Delta u_i^1) n_j^e d\partial Y \\ & - \int_{\partial Y_e} (\sigma_{ij}^{\epsilon m} + \Delta\sigma_{ij}^{\epsilon m} - \sigma_{ij}^{\epsilon c} - \Delta\sigma_{ij}^{\epsilon c}) (u_i^{1'} + \Delta u_i^{1'}) n_j^c d\partial Y + \int_{Y_e} (\bar{e}_{ij} + \Delta\bar{e}_{ij}) \Delta\sigma_{ij}^\epsilon dY \end{aligned} \quad (4.38)$$

where  $S_{ijkl}^\epsilon$  is an instantaneous elastic-plastic compliance tensor. The last term in equation (4.38) incorporates the effect of macroscopic strains in the microstructure. The stationary condition of  $\Pi_e$  with respect to stress increment  $\Delta\sigma_{ij}^\epsilon$  yields, as Euler's equations, the incremental form of kinematic relations (4.20)

$$e_{ij}^\epsilon + \Delta e_{ij}^\epsilon = \bar{e}_{ij} + \Delta\bar{e}_{ij} + \frac{\partial(u_i^1 + \Delta u_i^1)}{\partial y_j} \quad (4.39)$$

Furthermore, stationarity of the total energy functional  $\Pi = \sum_{e=1}^N \Pi_e$  with respect to displacement increments  $\Delta u_i^1$  and  $u_i^{1'}$  respectively, result in the inter-element and interface traction reciprocity conditions:

$$(\sigma_{ij}^\epsilon + \Delta\sigma_{ij}^\epsilon) \cdot n_j^{e+} = -(\sigma_{ij}^\epsilon + \Delta\sigma_{ij}^\epsilon) \cdot n_j^{e-} \quad \text{on } \partial Y_e \quad (4.40)$$

$$(\sigma_{ij}^{\epsilon c} + \Delta\sigma_{ij}^{\epsilon c}) \cdot n_j^c = (\sigma_{ij}^{\epsilon m} + \Delta\sigma_{ij}^{\epsilon m}) \cdot n_j^c \quad \text{on } \partial Y_c \quad (4.41)$$

where superscript + and - denote values on opposite sides of the inter element boundary  $\partial Y_e$ . The three Euler's equations together with (a) the assumed equilibrated stress fields satisfying  $\Delta\sigma_{ij,j}^\epsilon = 0$  in  $Y_e$ , (b) assumed compatible displacement increment fields in  $\partial Y_e$  and  $\partial Y_c$ , and the instantaneous constitutive relation  $\Delta e_{ij}^\epsilon = S_{ijkl}^\epsilon \Delta\sigma_{kl}^\epsilon$  describe the incremental boundary value problem for the microstructure.

The microscopic VCFEM module is executed for two purposes in each increment of the macroscopic module. The first is to evaluate the microscopic stress increments  $\Delta\sigma^\epsilon$  from given values of the macroscopic strain  $\bar{\mathbf{e}}$  at the beginning of the step, and its increment  $\Delta\bar{\mathbf{e}}$ . The second is to calculate the instantaneous homogenized tangent modulus  $E_{ijkl}^H$  at the end of the increment in the macroscopic module.

#### 4.4.1 Calculation of Microscopic Stresses

This step involves the iterative solution of modified forms of the kinematic relations (4.36) and the traction reciprocity conditions (4.37) to yield the incremental stress parameters  $\Delta\beta$  and the nodal displacement increments  $\Delta\mathbf{q}$  and  $\Delta\mathbf{q}'$ . The weak form of the element kinematic relation (4.39) is obtained by modifying (4.36) for homogenization in the multiple scale model as:

$$\int_{Y_e - Y_c} [\mathbf{P}^m]^T \{ \mathbf{e}^\epsilon + \Delta\mathbf{e}^\epsilon - \bar{\mathbf{e}} - \Delta\bar{\mathbf{e}} \} dY = \int_{\partial Y_e} [\mathbf{P}^m]^T [\mathbf{n}^e] [\mathbf{L}^e] dY \{ \mathbf{q} + \Delta\mathbf{q} \}_e - \int_{\partial Y_c} [\mathbf{P}^m]^T [\mathbf{n}^c] [\mathbf{L}^c] dY \{ \mathbf{q}' + \Delta\mathbf{q}' \}_e \quad (4.42)$$

$$\int_{Y_c} [\mathbf{P}^c]^T \{ \mathbf{e}^\epsilon + \Delta\mathbf{e}^\epsilon - \bar{\mathbf{e}} - \Delta\bar{\mathbf{e}} \} dY = \int_{\partial Y_c} [\mathbf{P}^c]^T [\mathbf{n}^c] [\mathbf{L}^c] dY \{ \mathbf{q}' + \Delta\mathbf{q}' \}_e \quad (4.43)$$

As mentioned in section 3.2, an iterative solution process is implemented for evaluating stresses from given values of the nodal displacements. In the  $i$ -th iteration, the total strain increment  $\{\Delta\mathbf{e}^\epsilon\}$  is linearized with respect to stress increment  $\{\Delta\sigma^\epsilon\}$  in the form:

$$\{\Delta\mathbf{e}^\epsilon\} = \{\Delta\mathbf{e}^\epsilon(\sigma^\epsilon, \Delta\sigma^\epsilon)\}^i + [\mathbf{S}^\epsilon] : \{d\sigma^\epsilon\} \quad (4.44)$$

where the correction  $\{d\sigma^\epsilon\}^i$  to stress increment is expressed as,

$$\{d\sigma^\epsilon\}^i = [\mathbf{P}] \{d\beta\}^i \quad \text{in } Y_e \quad (4.45)$$

Substitution in (4.42) and (4.43) leads to the linearized kinematic equations (3.22) in conjunction with the homogenization procedure as:

$$\begin{bmatrix} \mathbf{H}_m & 0 \\ 0 & \mathbf{H}_c \end{bmatrix} \begin{Bmatrix} d\beta^m \\ d\beta^c \end{Bmatrix}^i = \begin{bmatrix} \mathbf{G}_e & -\mathbf{G}_{cm} \\ 0 & \mathbf{G}_{cc} \end{bmatrix} \begin{Bmatrix} \mathbf{q} + \Delta\mathbf{q} \\ \mathbf{q}' + \Delta\mathbf{q}' \end{Bmatrix} - \begin{Bmatrix} \int_{Y_e - Y_c} [\mathbf{P}^m]^T \{ \mathbf{e}^\epsilon + \Delta\mathbf{e}^{\epsilon i} - \bar{\mathbf{e}} - \Delta\bar{\mathbf{e}} \} dY \\ \int_{Y_c} [\mathbf{P}^c]^T \{ \mathbf{e}^\epsilon + \Delta\mathbf{e}^{\epsilon i} - \bar{\mathbf{e}} - \Delta\bar{\mathbf{e}} \} dY \end{Bmatrix} \quad (4.46)$$

where components of the matrices are explained in equation (3.22). The traction reciprocity equations (3.23) are iteratively solved for nodal displacements in the same way as mentioned in section 3.3. In the  $j$ -th iteration, this corresponds to the solution of the linearized global traction reciprocity equation:

$$\begin{aligned} \sum_{e=1}^N [\mathbf{G}]^T [\mathbf{H}]^{-1} [\mathbf{G}] \begin{Bmatrix} d\mathbf{q} \\ d\mathbf{q}' \end{Bmatrix}^j = \\ - \sum_{e=1}^N \begin{bmatrix} \int_{\partial Y_e} [\mathbf{L}^e]^T [\mathbf{n}^e]^T [\mathbf{P}^m]^T dY & 0 \\ - \int_{\partial Y_e} [\mathbf{L}^c]^T [\mathbf{n}^c]^T [\mathbf{P}^m]^T dY & \int_{\partial Y_c} [\mathbf{L}^c]^T [\mathbf{n}^c] [\mathbf{P}^c]^T dY \end{bmatrix} \begin{Bmatrix} \beta^m + \Delta\beta^m \\ \beta^c + \Delta\beta^c \end{Bmatrix}^j \end{aligned} \quad (4.47)$$

#### 4.4.2 Calculation of Homogenized Tangent Modulus

Evaluation of the homogenized tangent modulus tensor  $E_{ijkl}^H$  is performed at the end of an increment in the global analysis (ABAQUS) after converged values of microscopic variables have been obtained. From the basic definition in equation (4.27), components of  $E_{ijkl}^H$  are obtained by averaging the true stress increments in response to unit increments in components of the strain tensor  $\bar{\mathbf{e}}$ . In two dimensional analysis the individual components correspond to  $\bar{\mathbf{e}}_{11}$ ,  $\bar{\mathbf{e}}_{22}$  and  $\bar{\mathbf{e}}_{12}$ , or in contracted notations  $\bar{\mathbf{e}}_1$ ,  $\bar{\mathbf{e}}_2$  and  $\bar{\mathbf{e}}_3$  i.e.  $\bar{\mathbf{e}}_i$ ,  $i = 1, 2, 3$ . This is obtained first by consistent linearization of the element kinematic relation in equation (3.22) with respect to each component of the macroscopic strain increment  $\bar{\mathbf{e}}_i$  to yield:

$$\begin{bmatrix} \mathbf{H}_m & \mathbf{0} \\ \mathbf{0} & \mathbf{H}_c \end{bmatrix} \begin{Bmatrix} \delta\beta^m \\ \delta\beta^c \end{Bmatrix}_i = \begin{bmatrix} \mathbf{G}_e & -\mathbf{G}_{cm} \\ \mathbf{0} & \mathbf{G}_{cc} \end{bmatrix} \begin{Bmatrix} \delta\mathbf{q} \\ \delta\mathbf{q}' \end{Bmatrix}_i - \begin{Bmatrix} \int_{Y_e - Y_c} [\mathbf{P}^m]^T \{\delta\bar{\mathbf{e}}_i\} dY \\ \int_{Y_c} [\mathbf{P}^c]^T \{\delta\bar{\mathbf{e}}_i\} dY \end{Bmatrix} \quad (4.48)$$

In equation (4.48), it is assumed that the stress coefficients  $\beta$  and generalized nodal displacements  $\mathbf{q}$  are perturbed about their respective equilibrated and compatible values, corresponding to a prescribed perturbation in  $\bar{\mathbf{e}}_i$ . The nodal displacements  $\delta\mathbf{q}$  in equation (4.48) are solved by linearization of the global traction reciprocity condition (4.37) with respect to  $\bar{\mathbf{e}}_i$ , given as:

$$\sum_{e=1}^N [\mathbf{G}]^T \left( [\mathbf{H}]^{-1} [\mathbf{G}] \begin{Bmatrix} \delta\mathbf{q} \\ \delta\mathbf{q}' \end{Bmatrix}_i - [\mathbf{H}]^{-1} \begin{Bmatrix} \int_{Y_e - Y_c} [\mathbf{P}^m]^T \{\delta\bar{\mathbf{e}}_i\} dY \\ \int_{Y_c} [\mathbf{P}^c]^T \{\delta\bar{\mathbf{e}}_i\} dY \end{Bmatrix} \right) = 0 \quad (4.49)$$

The solved values of  $\{\delta\mathbf{q}\}_i$  yield the characteristic modes of deformation as plotted in figures (4.14), (4.15) and (4.16). These are subsequently substituted in the local compatibility equation (4.48) to solve for element stress coefficients  $\{\delta\beta\}_i$ . It should be noted the tangent modulus is evaluated from unit values of  $\{\delta\bar{\mathbf{e}}_i\}$ , i.e.  $\{\delta\bar{\mathbf{e}}_1\} = \begin{Bmatrix} 1 \\ 0 \\ 0 \end{Bmatrix}$ ,  $\{\delta\bar{\mathbf{e}}_2\} = \begin{Bmatrix} 0 \\ 1 \\ 0 \end{Bmatrix}$ ,  $\{\delta\bar{\mathbf{e}}_3\} = \begin{Bmatrix} 0 \\ 0 \\ 1 \end{Bmatrix}$ . Components of the elastic-plastic homogenized tangent modulus tensor  $E_{ijkl}^H$  are then obtained from equation (4.27), by averaging  $[\mathbf{P}]\{d\beta\}_i$  for each component of the macroscopic strain, as

$$[\mathbf{E}^H] = \frac{1}{|\mathbf{Y}|} \left[ \sum_{e=1}^N \int_{Y_e} [\mathbf{P}]\{d\beta\}_1 \quad \sum_{e=1}^N \int_{Y_e} [\mathbf{P}]\{d\beta\}_2 \quad \sum_{e=1}^N \int_{Y_e} [\mathbf{P}]\{d\beta\}_3 \right] \quad (4.50)$$

## 4.5 Numerical Implementation

A number of numerical details have to be considered in the construction of a multiple scale computational model using the microstructural VCFEM model. In this section, a few salient features are discussed.

#### 4.5.1 Incorporation in the Macroscopic Analysis Module

The Voronoi cell finite element module is incorporated in a macroscopic analysis module with the interface being created by the homogenization procedure. In this work, the general purpose commercial code ABAQUS has been chosen to serve as the macroscopic analysis program. Macroscopic ABAQUS models are developed with two dimensional elements. The material constitutive relation at each integration point of ABAQUS elements is input through the homogenization process by using results from the microscopic VCFEM analysis. This interface between ABAQUS and VCFEM is created through UMAT, intended to incorporate user specified constitutive models in ABAQUS. The analysis code resulting from this macro-micro coupling is termed as VCFEM-HOMO. QUAD4 elements with one-point reduced integration and hourglass control are selected in ABAQUS analysis. ABAQUS and VCFEM codes used in this analysis implement implicit time integration schemes, and hence require iterations at both levels for convergence.

Within each iteration loop of macroscopic analysis in the  $p$ -th increment, microscopic state variables are computed in VCFEM using given values of the macroscopic strains at the beginning of the increment and its increment, as shown in the flow chart of figure (4.2). The microscopic stresses are averaged to yield macroscopic stresses. Upon convergence in global and local iterations, the microscopic VCFEM is invoked again to evaluate the homogenized elastic-plastic tangent modulus  $\mathbf{E}^H$  by applying unit components of macroscopic strain. All the history dependent microstructural variables, e.g stresses, strains and plastic strains are retained and updated during the incremental process.

#### 4.5.2 Implementing Periodicity Boundary Condition

An essential step in computing the homogenized material properties is to ensure repeatability boundary conditions on the RME. For a square or rectangular RME, identical displacement functions must be specified for corresponding nodes (equidistant from a coordinate axis) on opposite edges. Implementing the repeatability boundary condition for a regular finite element mesh is straightforward, since a uniform mesh can be generated to have the correspondence between boundary nodes on opposite faces. However boundary nodes of the Voronoi mesh generated by Dirichlet tessellation, are in general quite arbitrary and such a correspondence cannot be easily established. A method which involves representation of nodal boundary displacements by a suitable polynomial function is implemented for enacting the repeatability conditions. In this method, a  $(q - 1)$ th order polynomial is chosen for the displacements, where  $q$  corresponds to the highest number of boundary nodes between the two opposite faces. That is, if one face has 5 nodes while the opposite side consists of 6 nodes, a 5-th order polynomial function is chosen. The edge nodal displacements are then written as:

$$\begin{aligned} u_1 &= a_0 + a_1x_1 + a_2x_1^2 + a_3x_1^3 + a_4x_1^4 + a_5x_1^5 \\ v_1 &= b_0 + b_1y_1 + b_2y_1^2 + b_3y_1^3 + b_4y_1^4 + b_5y_1^5 \\ u_2 &= a_0 + a_1x_2 + a_2x_2^2 + a_3x_2^3 + a_4x_2^4 + a_5x_2^5 \end{aligned}$$

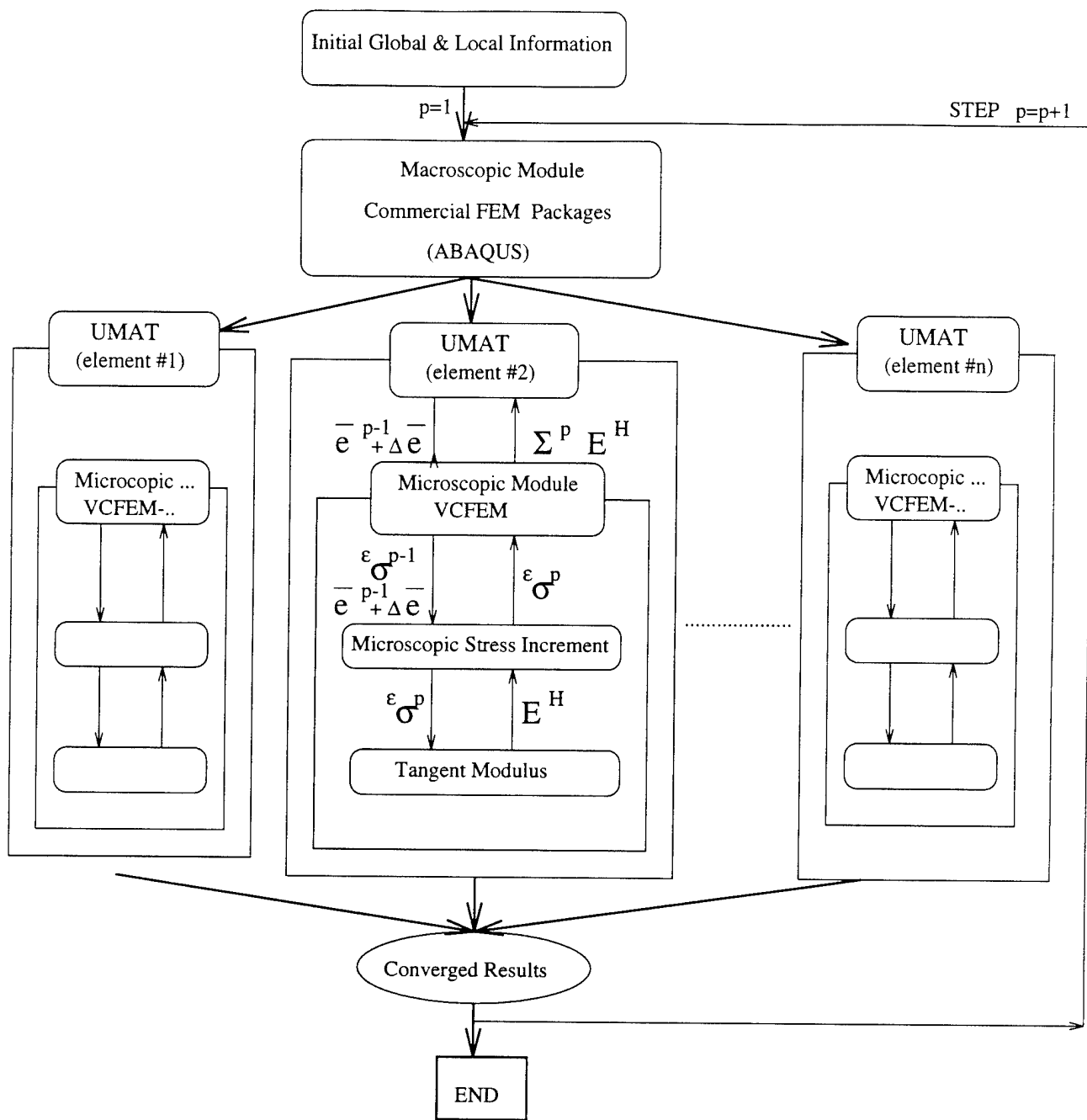


Figure 4.2: Flow chart of microscopic analysis

$$\begin{aligned}
 v_2 &= b_0 + b_1 y_2 + b_2 y_2^2 + b_3 y_2^3 + b_4 y_2^4 + b_5 y_2^5 \\
 &\vdots
 \end{aligned} \tag{4.51}$$

where  $u_1, v_1, u_2, v_2 \dots$  are nodal displacements and  $x_1, y_1, x_2, y_2 \dots$  are boundary coordinates. These lead to displacement constraints in the matrix equations prior to solving.

## 4.6 Numerical Examples

Numerical examples conducted with the multiple scale homogenization module VCFEM-HOMO, are divided into two categories. The first set of examples are intended to validate the effectiveness of the asymptotic homogenization in conjunction with Voronoi cell FEM formulation for heterogeneous materials with both inclusions and voids. This is accomplished through comparison of VCFEM-HOMO results in simple tests, with (a) those generated by Unit cell models using conventional finite element codes such as ABAQUS, (b) experimental/analytical results, and (c) effective continuum models. The comparisons also help in identifying some of the shortcomings of alternative approaches, and where coupled multiple scale analyses is desirable. In the second set of examples, the VCFEM-HOMO code is used to solve more complex multiple scale problems with various microstructural morphologies. Effects of the microstructure in the evolution of macroscopic and microscopic variables are investigated. The material in all the ensuing examples is assumed to be a boron-aluminum composite or aluminum with voids, unless otherwise mentioned. The boron inclusion is assumed to be elastic while the aluminum matrix is an elastic-plastic material with the following properties.

### Material Properties:

#### Boron fiber

Young's Modulus ( $E_c$ ): 344.5 GPa

Poisson Ratio ( $\nu_c$ ): 0.26

#### Aluminum matrix

Young's Modulus ( $E_m$ ): 68.9 GPa

Poisson Ratio ( $\nu_m$ ): 0.32

Initial Yield Stress ( $Y_0$ ): 94 MPa

Post Yield flow rule:  $\epsilon_{eqv} = \frac{Y_0}{E_m} \left\{ \frac{\sigma_{eqv}}{Y_0} \right\}^5$

The microstructural VCFEM analysis uses a 48 term stress function in equation(3.29) ( $p + q = 2.4$  and  $i = 1..3$ ) for the matrix of porous materials, and a 34 term stress function ( $p + q = 2$  and  $i = 1..3$ ) in the matrix of composite materials. The stress field in the inclusion for composite materials is generated with a 25 term polynomial stress function (i.e.  $\Phi_{poly}^c$ :  $p + q = 2..6$ ). It should be noted that elastic problems with homogenization and VCFEM have been successfully solved in [28].

### 4.6.1 Validation of the Homogenization Model

#### Numerical Unit cell models

In this example, results of VCFEM-HOMO are compared with predictions of numerical unit cell models for plane strain elastic-plastic analysis. Two microstructural arrangements viz. square edge distribution (SED) and hexagonal distribution (HD) as shown in figure 4.3, are

considered. For VCFEM-HOMO analysis, the macroscopic ABAQUS mesh consists of a single QUAD4 element, and a single Voronoi cell element is required for microstructural analysis as shown in figure 4.3(a) and (c). Unit cell analyses are conducted at the microstructural level only, with the representative material element (RME) modeled by QUAD4 elements in ABAQUS, illustrated in figure 4.3(b) and (d). The inclusion volume fraction is 55%. The periodic construct of unit cell is achieved through restrictive repeatability conditions enforced on edges  $x = L$  and  $y = L$ . This constraint condition requires rectangular cells to deform into rectangular shapes, i.e. straight line edges ( $x = L, y = L$ ) move uniformly as straight lines. For the SED and HD arrangements, the ABAQUS mesh consists of 1440 QUAD4 and 1482 elements respectively.

Comparisons are made for macroscopic as well as microscopic response by the two approaches. For the unit cell model, macroscopic variables denoted with an overbar, are obtained by volume averaging the microscopic response. For example, macroscopic stresses  $\bar{\sigma}$  are evaluated as:

$$\bar{\sigma} = \bar{\Sigma} = \frac{\int_{\Omega_{RME}} \sigma d\Omega}{\int_{\Omega_{RME}} d\Omega}$$

Figures 4.4 and 4.5 show the macroscopic stress-strain relations and the microscopic stress distribution for the square edge and hexagonal packings respectively when subjected to uniform stretching. Figures 4.4(a) and 4.5(a) show excellent agreement between VCFEM-HOMO and Unit Cell model in the macroscopic responses at all load stages. Figures 4.4(b) and 4.5(b) show the microscopic stress distribution in the direction of applied strain along sections at  $y = \frac{L}{2}$  and  $y = 0$  in figures 4.3(b) and (d) respectively. Though the VCFEM-HOMO results for both packings compare well with unit cell predictions, better agreement is seen with HD packing due to the refined unit cell mesh along the section considered.

VCFEM-HOMO code is next utilized to investigate the effect of microstructural morphology on the material response. Four different arrangements are considered with circular inclusions of 55% volume fraction, viz. (a) square edge distribution (figure 4.3(a)), (b) hexagonal distribution (figure 4.3(c)), (c) square diagonal distribution ( $45^\circ$  rotation of figure 4.3(a)) and (d) random distribution with 29 inclusions (figure 4.6) The ABAQUS macroscopic mesh consists of one plane strain element, subjected to simple tension and simple shear boundary conditions to maximum effective strains of 0.008. The effective macroscopic stress-strain behavior is depicted in figure 4.7. On account of the rotational equivalence of RMEs, the behavior of the square edge and square diagonal distributions are exactly reversed for the two loading conditions. The results indicate the strong anisotropy in overall behavior of these two RME's. The random and hexagonal packings on the other hand exhibit similar response in tension and shear. This establishes the low directional dependency of these RME's, implying near isotropic behavior. The stress-strain curves for the latter two distributions lie within the envelopes of the SE and SD distributions, and hence exhibit more overall ductility.

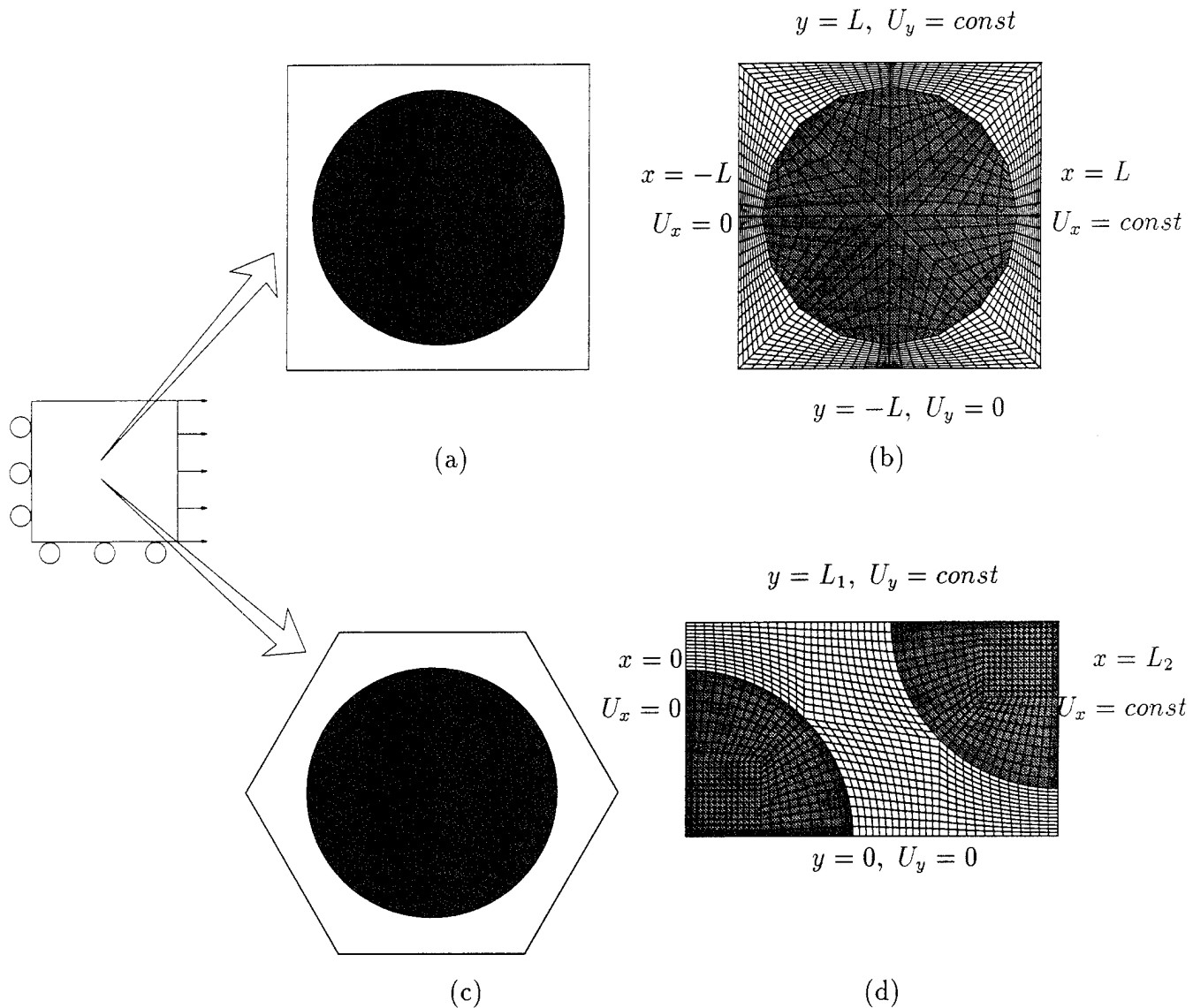
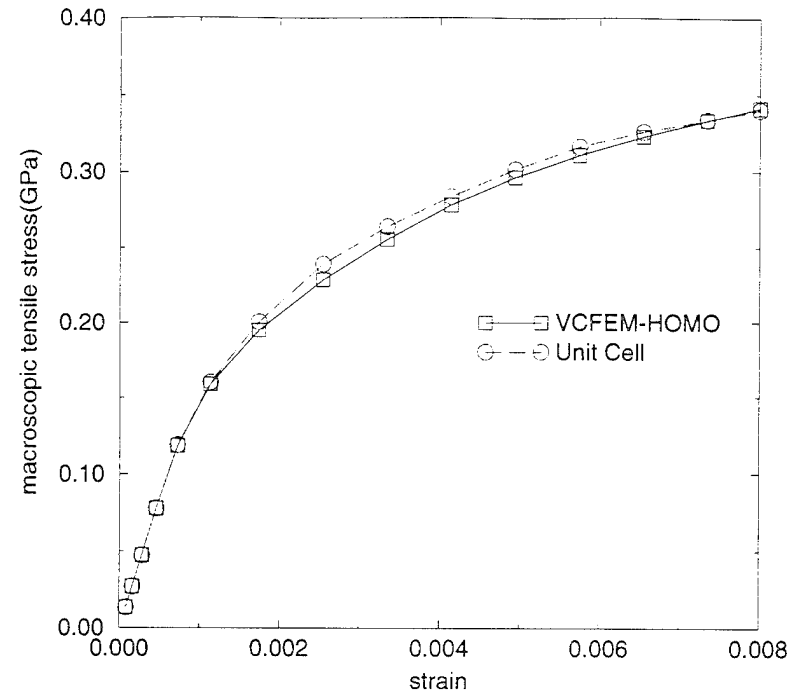
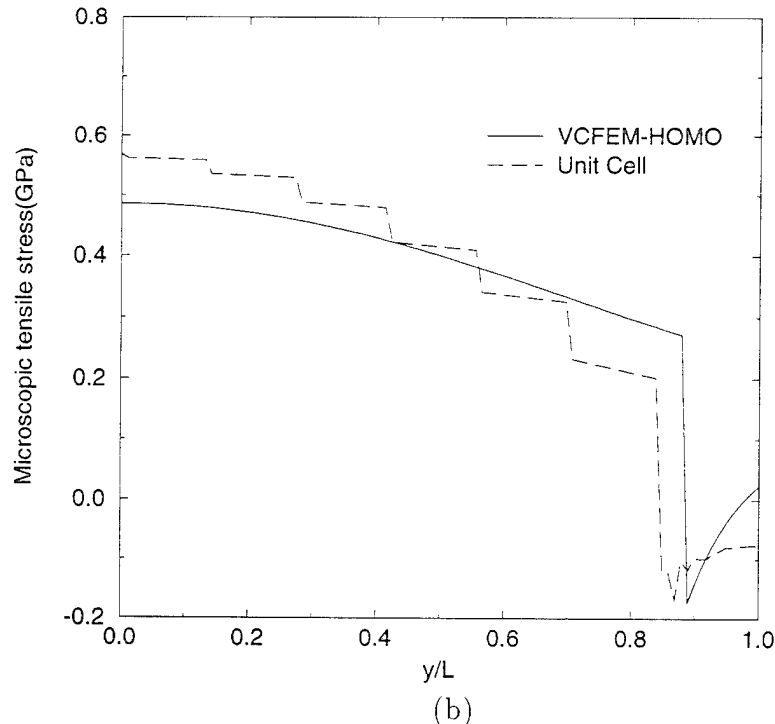


Figure 4.3: Computational model of a composite material with a circular inclusion of volume fraction 55% (a) Macroscopic and microscopic models for Square edge distribution by VCFEM-HOMO, (b) Microstructural ABAQUS Unit Cell model for Square edge distribution (c) Macroscopic and microscopic models for Hexagonal distribution by VCFEM-HOMO, and (d) Microstructural ABAQUS Unit Cell model for Hexagonal distribution.

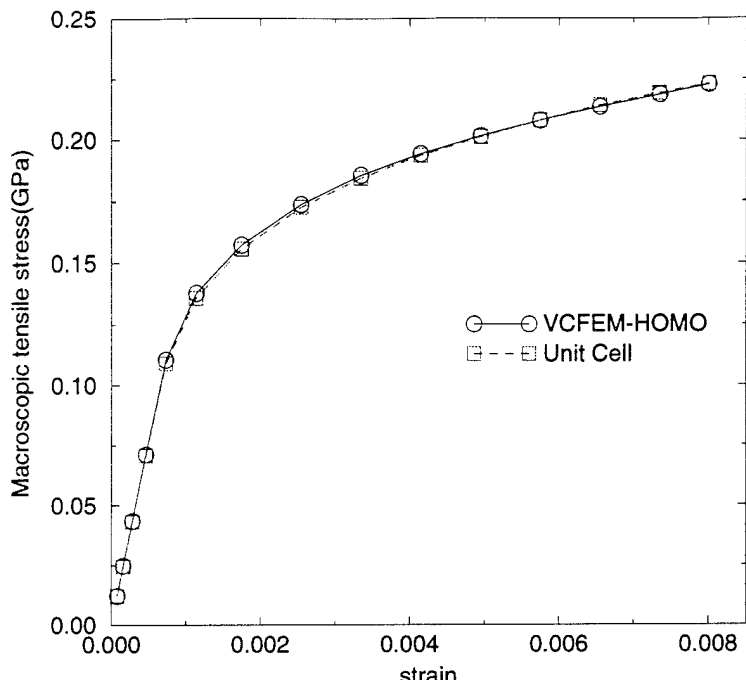


(a)

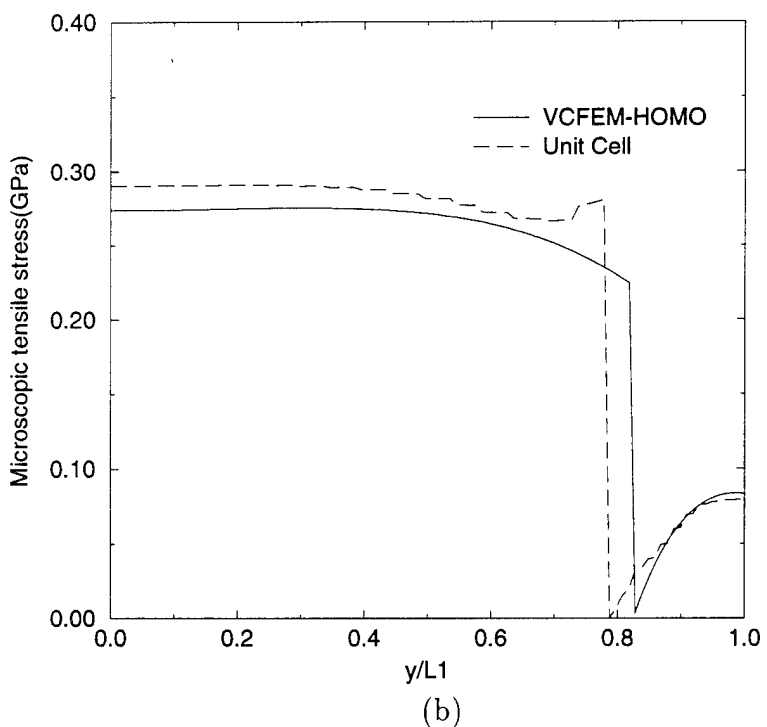


(b)

Figure 4.4: Comparison of macroscopic and microscopic response for Square edge packing composite between VCFEM-HOMO and Unit Cell models (a) macroscopic stress-strain response along the load direction and (b) microstructural stress distribution along a section through the inclusion at  $x = 0.0$



(a)



(b)

Figure 4.5: Comparison of macroscopic and microscopic response for Hexagon packing composite between VCFEM-HOMO and Unit Cell models (a) macroscopic stress-strain response along the load direction and (b) microstructural stress distribution along a section through the inclusion  $x = 0$

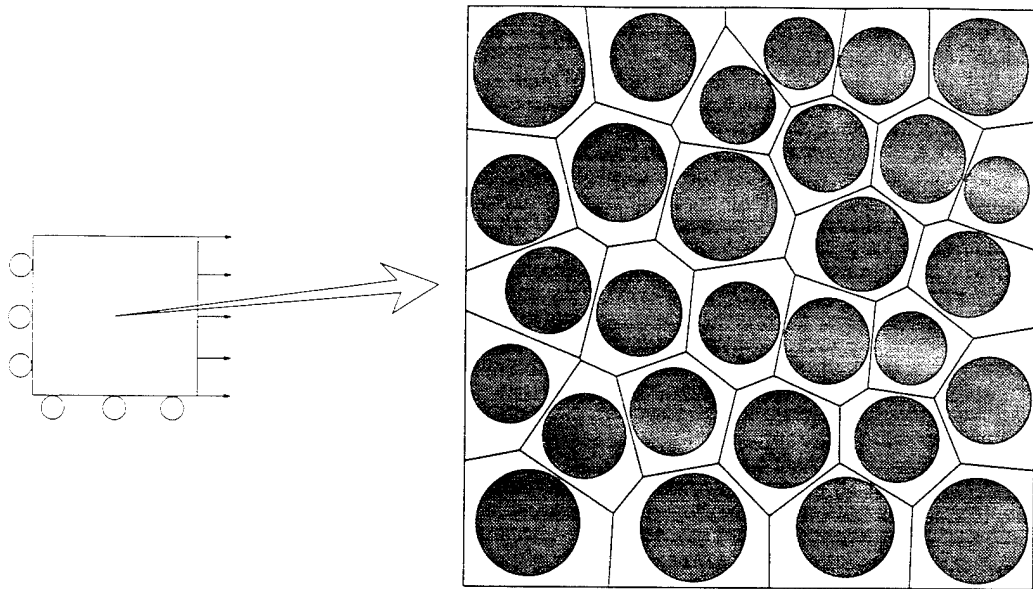


Figure 4.6: RME for a randomly distributed composite with 29 circular inclusions at 55% volume fraction

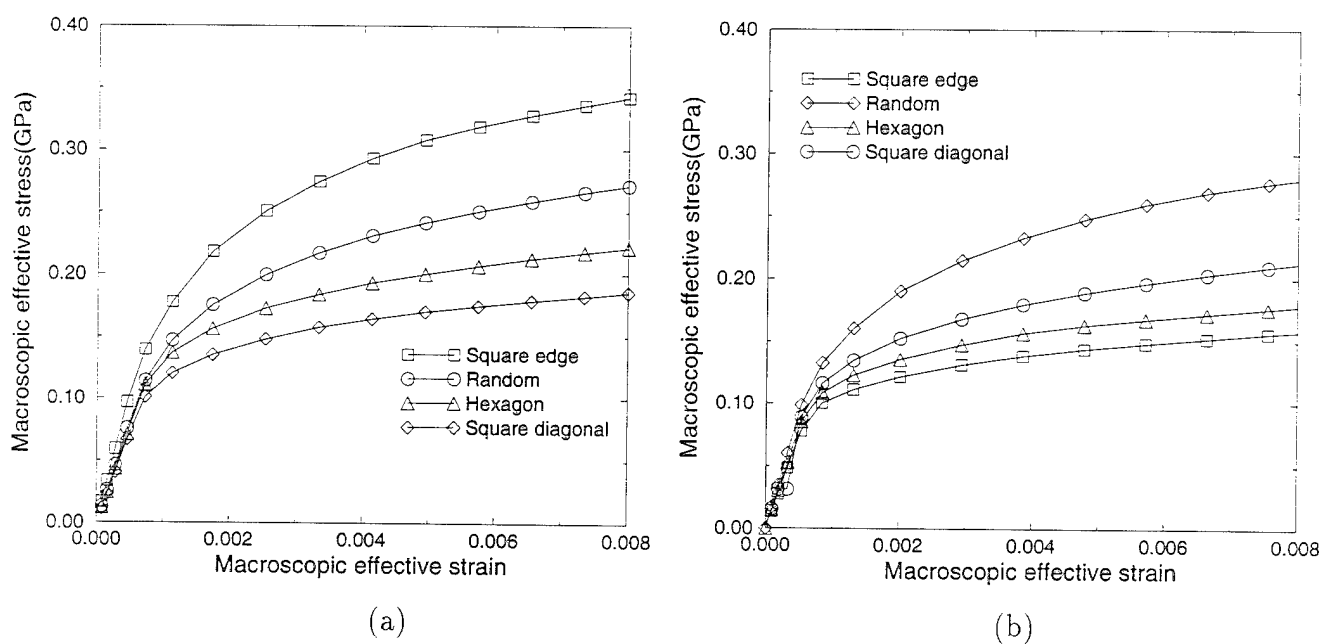


Figure 4.7: Effective macroscopic stress-strain responses of various distributions under (a) simple tension (b) simple shear

## Effective continuum models

This set of examples examines some of the differences between effective continuum models and coupled macro-micro analysis for simple loadings. Furthermore, the VCFEM-HOMO code is also tested against experimental and analytical results.

In the first example, overall stress-strain plots are first generated by uniaxial stretching of VCFEM models in figures 4.3(a) and 4.6 under plane stress conditions. This is then input as the homogenized material law in ABAQUS with isotropic hardening and associated flow rule. The ABAQUS mesh with this effective continuum model consists of one QUAD4 element. Likewise, the macroscopic ABAQUS mesh for VCFEM-HOMO consists of one QUAD4 element and the microscopic models are illustrated in figures 4.3(a) and 4.6. Macroscopic longitudinal stress-strain relations, and transverse-longitudinal strain relations by the two approaches are plotted in figures 4.8 and 4.9. Comparisons are made for three different microstructures, viz. (a) square edge packing with 10% inclusion volume fraction, (b) square edge packing with 55% inclusion volume fraction, and (c) random packing with 55% inclusion volume fraction. The stress and strain plot in the loading direction (figure 4.8) shows excellent agreement between the continuum model and VCFEM-HOMO results. An increase in the inclusion volume fraction leads to a considerable reduction in the ductility due to the higher stiffness of the elastic inclusion. Though the random distribution shows a less stiff response than the square edge distribution for the same volume fraction (55%), this plot confirms that the effect of volume fraction is much more pronounced than that of distribution. The two approaches are at considerable variance in the transverse-longitudinal strain plot (figure 4.9). The continuum model shows nearly identical strain responses for all inclusion volume fractions and distributions. This can be explained by the fact that the continuum models assume total yielding of the microstructure after initial yield, and consequently enforces the constraint that macroscopic plastic strains are volume preserving. This leads to direct dependence of transverse plastic strains on the longitudinal strains, and the microstructure contributes only to the elastic part of the transverse strain. The behavior is however quite different when solved with VCFEM-HOMO. In reality, only a part of the microstructure yields at the strains considered, and this is reflected in the VCFEM-HOMO results. For smaller inclusion volume fractions, a large portion of the unit cell is the matrix that goes plastic at initial yield. This gives the close proximity in prediction by both models. This behavior changes significantly at higher volume fraction, where larger portions of the matrix remain elastic. The absolute value of the transverse strain by VCFEM-HOMO is much smaller than that of effective continuum model. Another observation is that the difference between VCFEM-HOMO and continuum model results for the random microstructure is less than that for the square edge microstructure. This may be attributed to the anisotropic behavior of the latter that is not accounted for in the continuum models. This example clearly points out the need for using the coupled analysis especially at higher volume fractions of heterogeneous microstructures.

The second example deals with porous materials, for which VCFEM-HOMO results are compared with the Tvergaard-Gurson (T-G) continuum model [38, 33]. Plane strain simple

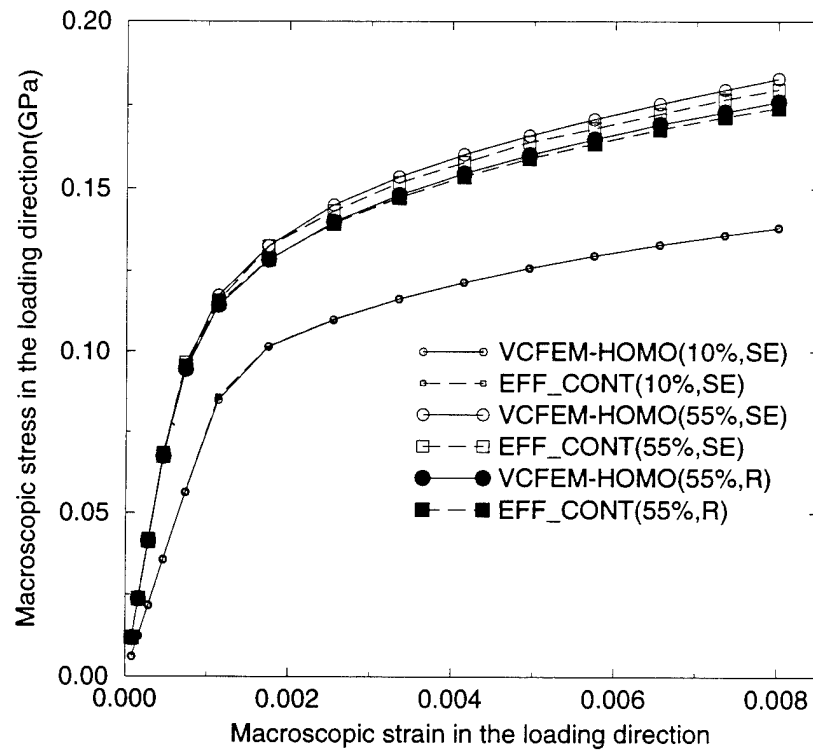


Figure 4.8: Macroscopic stress-strain relations for various microstructures by VCFEM-HOMO and effective continuum model

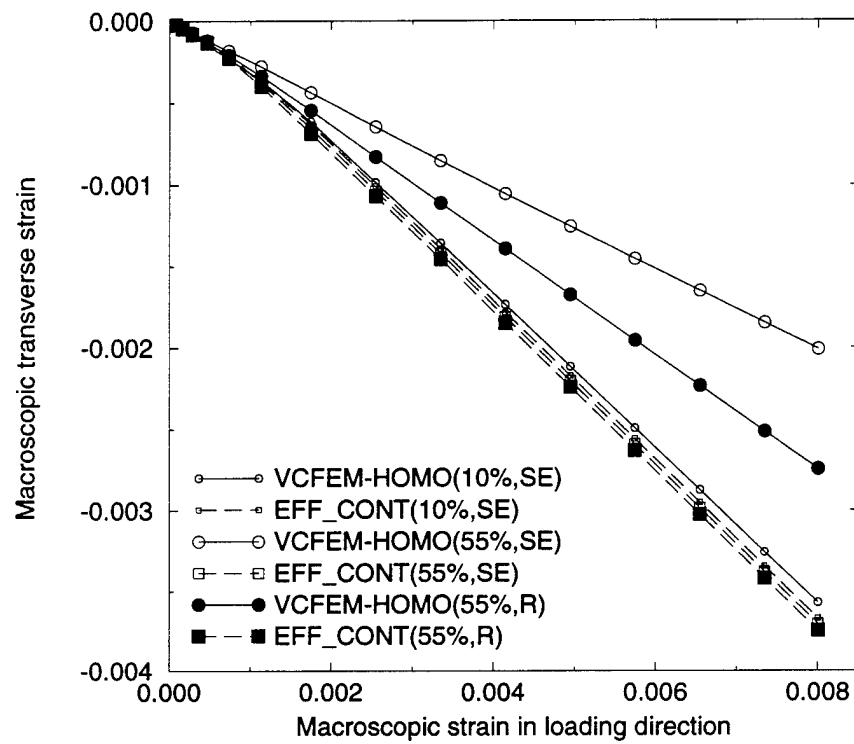


Figure 4.9: Transverse strain-axial strain relations for various microstructures by VCFEM-HOMO and effective continuum model

tension, simple shear, and biaxial tension tests are carried out for square edge packed materials with a low void volume fraction of 5%. For comparison plane strain simulations, the T-G model for long cylindrical voids [38] is implemented in ABAQUS through the UMAT window. In this module, numerical integration of the rates of state variables is carried out in a way similar to Aravas [40], for spherical voids. The macroscopic ABAQUS model for both analyses consists of one QUAD4 element and the microscopic model for VCFEM-HOMO is illustrated in figure 4.3. The yield condition in the plane strain T-G model [38] is stated as :

$$\Phi = \frac{\sigma_e^2}{\sigma_o^2} + 3 f \cosh\left(-\frac{\sqrt{3} (\sigma_{11} + \sigma_{22})}{2 \sigma_o}\right) - (1 + 2.25 f^2) \quad (4.52)$$

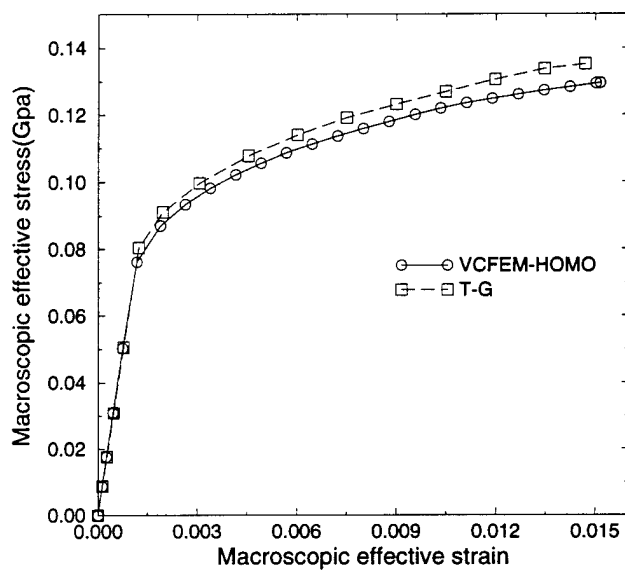
where  $\sigma_e$  is the effective stress,  $\sigma_o$  is the matrix flow stress,  $f$  is the void volume fraction and  $\sigma_{ij}$  are the principal components of the Cauchy stress tensor. An important assumption in this model is:

$$(1 - f)\sigma_o \dot{\epsilon}_o^p = \sigma_{ij} \dot{\epsilon}_{ij}^p \quad (4.53)$$

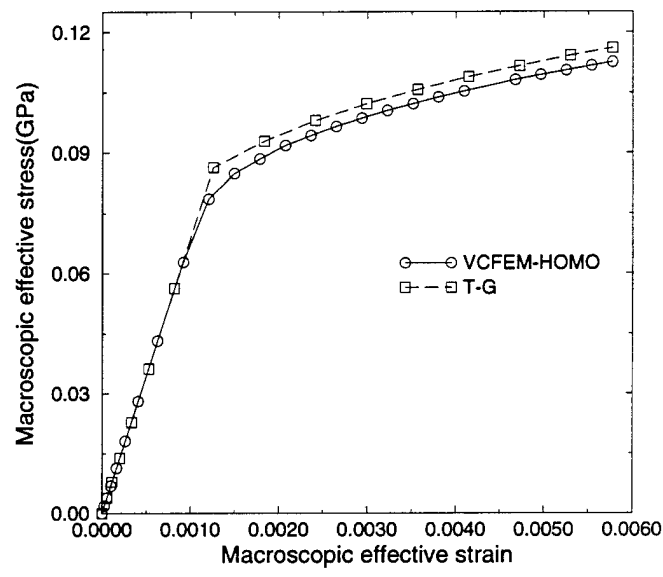
which means that the equivalent plastic work is derived solely from the entire matrix part of the microstructure.

Effective stress-strain plots in simple tension and simple shear (figures 4.10(a) and (b)) show good agreement between two methods, with T-G model producing a slightly higher value of initial yield. This is because, yield in the T-G model is manifested only after a significant portion of the microstructure has become plastic. VCFEM-HOMO on the other hand shows signs of inelasticity at the very onset of plastic deformation in the microstructure. The two approaches are however at significant variance for the biaxial loading case as seen in figure 4.11(a). Though the initial yield points are fairly close, the post yield behavior shows considerable difference between two models. As in the previous example, the main reason for this difference may be attributed to the assumption in T-G model that the entire microstructural matrix becomes plastic upon initial yield. In biaxial loading, as  $(\sigma_{11} + \sigma_{22})$  increases in equation (4.52), the effective macroscopic stress  $\sigma_e$  must diminish to near zero values for satisfying the yield condition. Physically, this also indicates that the large regions of plastic localization causes the effective stress to drop drastically. From the VCFEM-HOMO simulation it is however seen in figure 4.11(b), that a significant portion of the microstructure does not yield. Consequently, the effective stress in figure 4.11(a) is higher by VCFEM-HOMO than by the T-G predictions at the end of loading.

As a final example a multiple scale analysis for a porous plate with a hole is conducted by VCFEM-HOMO and compared with the T-G model incorporated in ABAQUS. Uniaxial tension of the plate is considered under plane strain conditions. The representative material element (RME) in the VCFEM-HOMO analysis is a square edge packing with 5% circular void volume fraction. Figures 4.12(a) and (b) shows excellent agreement in contour plots of effective macroscopic stress distribution by VCFEM-HOMO and ABAQUS with T-G model. The stress-strain evolution at three specific points (A), (B) and (C) are compared in figure 4.12(c). This near perfect match is expected, since most points in the plate are essentially in an uniaxial state of stress.

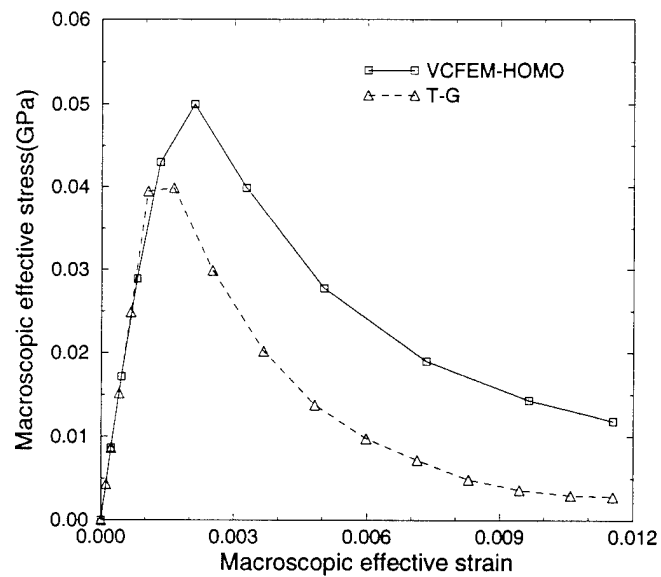


(a)

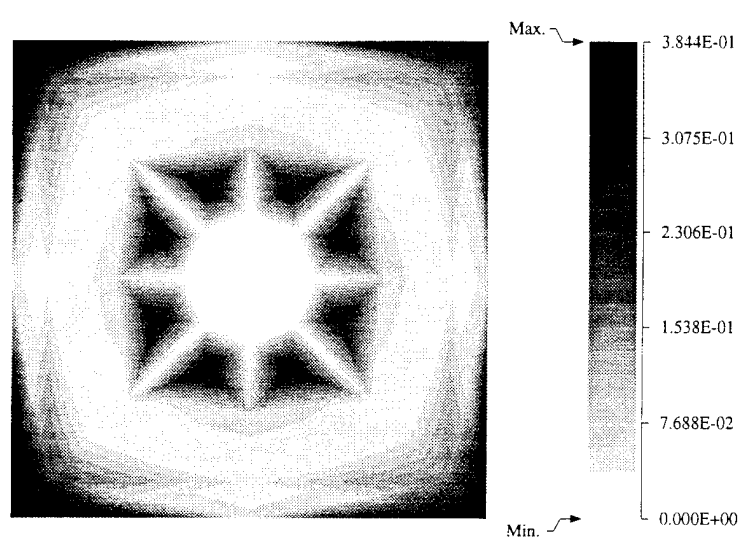


(b)

Figure 4.10: Effective macroscopic stress-strain plots by VCFEM-HOMO and Tvergaard-Gurson model for 5% void volume fraction in plane strain (a) simple tension and (b) simple shear



(a)



(b)

Figure 4.11: (a) Effective macroscopic stress-strain plots by VCFEM-HOMO and Tvergaard-Gurson model for 5% void volume fraction in biaxial tension and (b) Contour plot of microstructural effective plastic strain at the end of loading

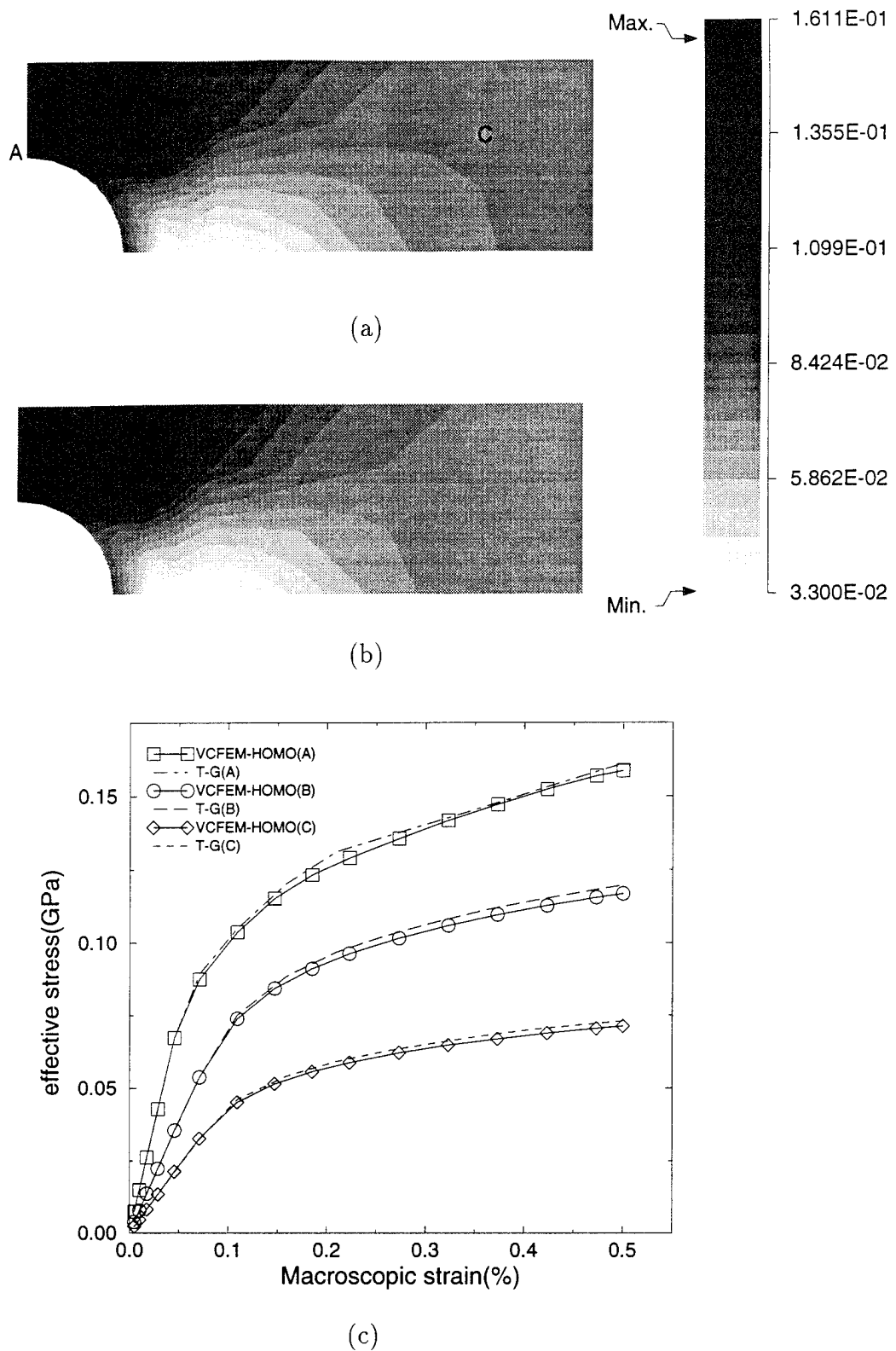


Figure 4.12: Macroscopic effective stress distribution in a plate with a hole in uniaxial tension at 5% strain (a) by VCFEM-HOMO and (b) ABAQUS with T-G model, (c) effective stress-strain evolution plots at three points in the structure

## Comparisons with some analytical and experimental results

Plane strain VCFEM-HOMO results are compared with analytical 2 and 3-phase model predictions due to Zhao and Weng [41] and experimental results due to Adams [42] for unidirectional composites. The material properties are:

### Aluminum

$E = 58 \text{ GPa}$  (Young's Modulus),  $\nu = 0.33$  (Poisson's Ratio)

$Y_0 = 89 \text{ MPa}$  (Initial Yield Stress),  $\sigma_{eqv} = Y_0 + 175(\epsilon_{eqv}^{pl})^{0.125} \text{ MPa}$  (Post Yield Hardening Law)

### Boron

$E = 385 \text{ GPa}$  (Young's Modulus),  $\nu = 0.2$  (Poisson's Ratio)

A square macroscopic element, that has a microstructural RME of a 2 x 1 rectangular edge packing with a circular inclusion of  $V_f = 34\%$ , is loaded in uniaxial tension. Figure 4.13 shows that VCFEM-HOMO results provide a better agreement with experimental results than the analytical model, which assume a square edge packed RME.

## Characteristic modes in elastic-plastic deformation

Characteristic modes in elastic-plastic homogenization represent instantaneous microstructural deformation response to applied unit components of macroscopic strain tensor. These modes  $\chi_p^{kl}$  are obtained from equation (4.49). Characteristic modes are essential in obtaining the elastic-plastic tangent modulus  $E_{ijkl}^H$  for macroscopic analysis.

The macroscopic element is subjected to uniaxial stretching, and the microstructural RMEs considered are square edge/random packing for circular voids (20% volume fraction), and square edge packing for circular inclusion (40% volume fraction). Figure 4.14(a) and (b) show the characteristic modes for the porous material and corresponding tangent modulus at the beginning of the loading and after 1% macroscopic stretching respectively. The initial modes depict the deformed void aligned in the direction of straining, but this changes with plastic straining, implying the influence of internal variable evolution. Figure 4.15 shows corresponding modes for the random microstructure. Figure 4.16 shows characteristic modes for composite microstructure with regular distribution. The difference between the modes for porous and composite materials emanates from the high inclusion stiffness that results in larger matrix deformation.

### 4.6.2 Multiple Scale Analysis

Two problems are considered for multiple scale analysis with VCFEM-HOMO. The effects of various distributions, sizes, and shapes, on the overall behavior of the heterogeneous material is investigated. In particular, the RME's considered are (a) square edge packing with a circular heterogeneity, (b) square diagonal packing with a circular heterogeneity, (c) random packing with 15 circular heterogeneities and (d) random packing with 15 elliptical heterogeneities. The material microstructure is assumed to consist of voids, inclusions, or a combination of both.

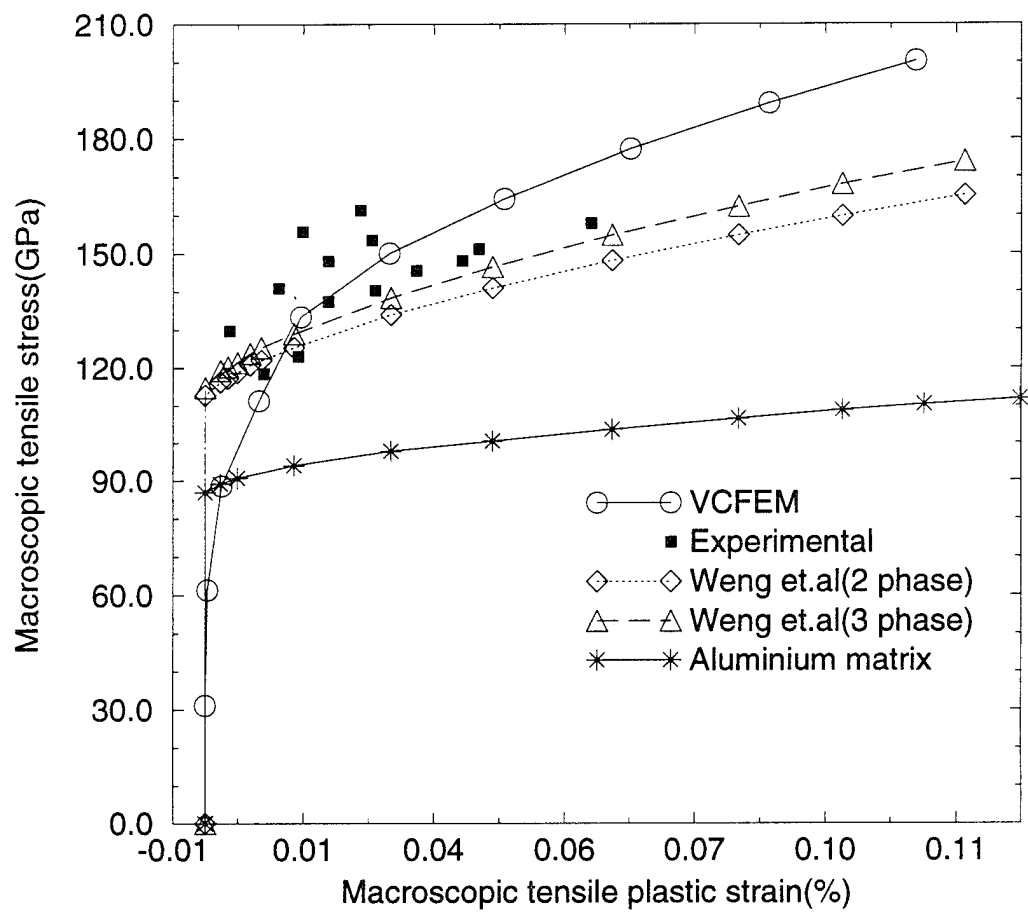
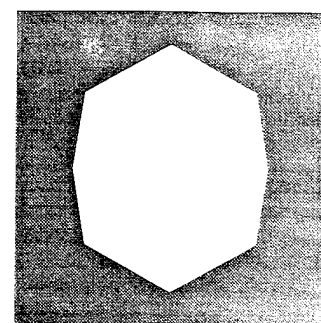
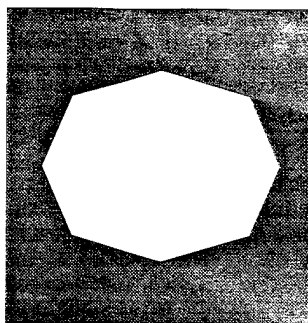
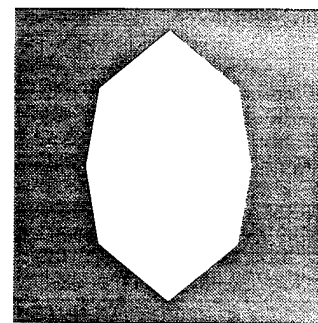
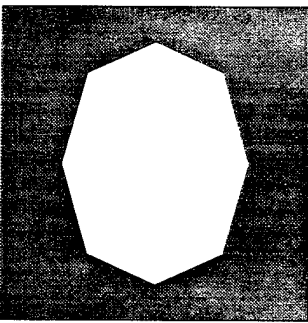


Figure 4.13: Macroscopic stress-strain responses for a Boron-Aluminum composite by VCFEM-HOMO, analytical and experimental techniques

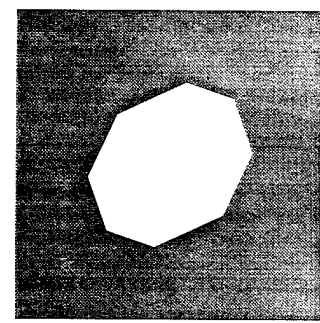
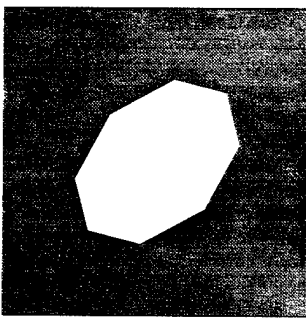
$$\begin{bmatrix} e_{11} & e_{12} \\ e_{21} & e_{22} \end{bmatrix} \quad \downarrow \quad \begin{bmatrix} 1 & 0 \\ 0 & 0 \end{bmatrix}$$



$$\begin{bmatrix} 0 & 0 \\ 0 & 1 \end{bmatrix}$$



$$\begin{bmatrix} 0 & 1 \\ 1 & 0 \end{bmatrix}$$



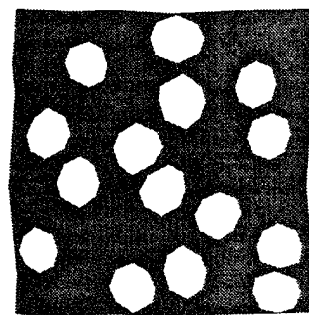
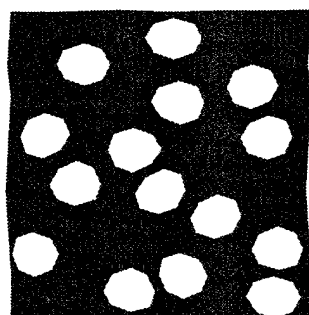
$$\begin{bmatrix} E_{1111} & E_{1122} & E_{1112} \\ E_{2211} & E_{2222} & E_{2212} \\ E_{1211} & E_{1222} & E_{1212} \end{bmatrix} \rightarrow \begin{bmatrix} 56.99 & 22.24 & 0.00 \\ 22.24 & 56.99 & 0.00 \\ 0.00 & 0.00 & 16.79 \end{bmatrix} \quad \begin{bmatrix} 13.67 & 18.95 & 0.00 \\ 18.95 & 31.21 & 0.00 \\ 0.00 & 0.00 & 7.90 \end{bmatrix}$$

Figure 4.14: Characteristic modes for voided RME with square edge distribution, (a) at the start of loading (b) after 1% stretching

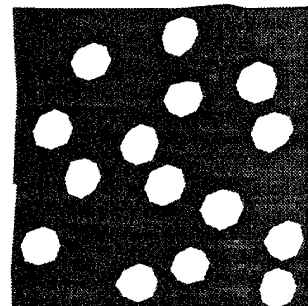
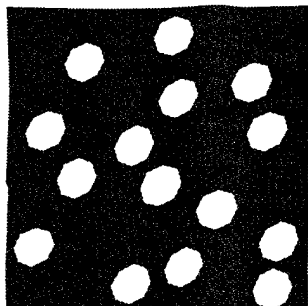
$$\begin{bmatrix} e_{11} & e_{12} \\ e_{21} & e_{22} \end{bmatrix}$$



$$\begin{bmatrix} 1 & 0 \\ 0 & 0 \end{bmatrix}$$

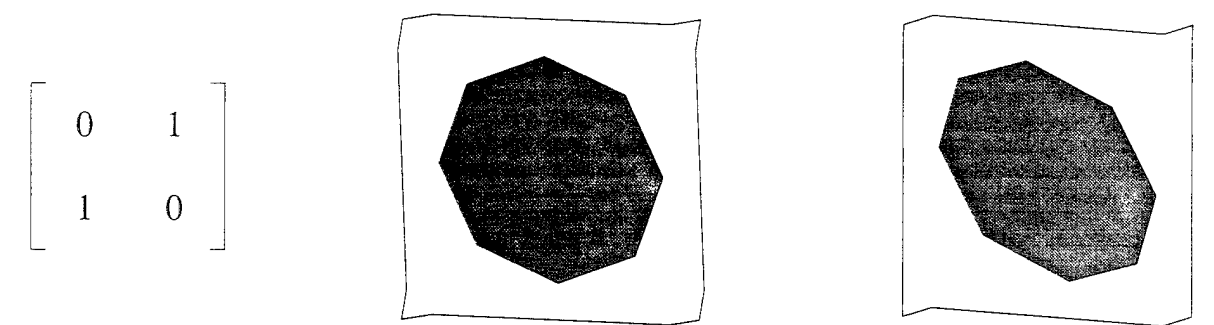
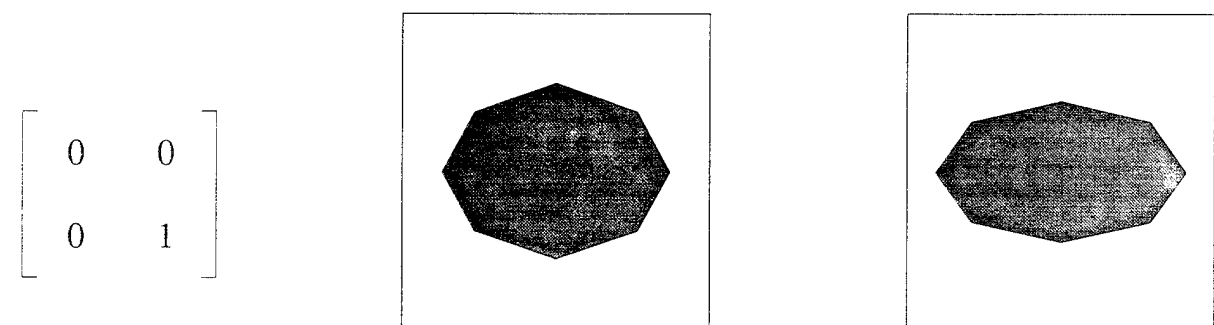
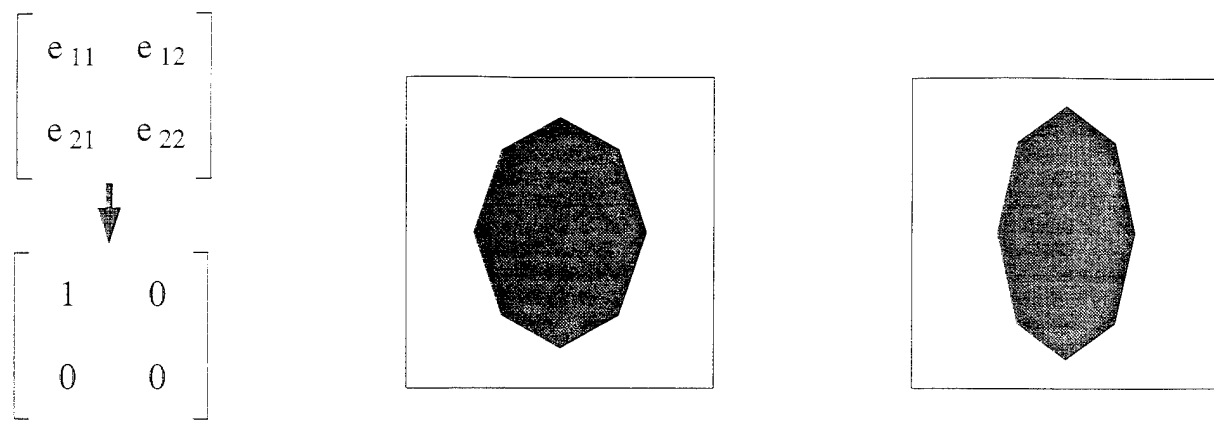


$$\begin{bmatrix} 0 & 1 \\ 1 & 0 \end{bmatrix}$$



$$\begin{bmatrix} E_{1111} & E_{1122} & E_{1112} \\ E_{2211} & E_{2222} & E_{2212} \\ E_{1211} & E_{1222} & E_{1212} \end{bmatrix} \rightarrow \begin{bmatrix} 56.89 & 22.69 & -0.25 \\ 22.69 & 58.19 & -0.07 \\ -0.25 & -0.07 & 17.24 \end{bmatrix} \begin{bmatrix} 11.38 & 15.73 & -0.43 \\ 15.73 & 27.10 & -0.51 \\ -0.43 & -0.51 & 6.53 \end{bmatrix}$$

Figure 4.15: Characteristic modes for voided RME with random distribution, (a) at the start of loading (b) after 1% stretching



$$\begin{bmatrix} E_{1111} & E_{1122} & E_{1112} \\ E_{2211} & E_{2222} & E_{2212} \\ E_{1211} & E_{1222} & E_{1212} \end{bmatrix} \xrightarrow{\quad} \begin{bmatrix} 157.2 & 62.47 & 0.00 \\ 62.47 & 157.2 & 0.00 \\ 0.00 & 0.00 & 40.98 \end{bmatrix} \quad \begin{bmatrix} 104.6 & 102.3 & 0.00 \\ 102.3 & 105.4 & 0.00 \\ 0.00 & 0.00 & 27.70 \end{bmatrix}$$

Figure 4.16: Characteristic modes for composite RME with square edge distribution, (a) at the start of loading (b) after 1% stretching

### Plane strain analysis of plate with holes

This set of examples deals with a thick plate with an uniform array of large circular holes in plane strain uniaxial tension. Only a portion of the plate, shown in figure 4.17(a), is considered from symmetry considerations. Dimensional details are given in the figure 4.17(a). The macroscopic ABAQUS model consists of 128 QUAD4 elements. The left and right edges are constrained to move in vertical straight lines, and the top and bottom edges are pulled to an overall strain of 0.5%.

In the first example, a porous microstructure with a 40% void volume fraction is considered. Various morphologies are considered are shown in figures 4.17 (b), (c), (d) and (e). Figures 4.18, 4.20, 4.22 and 4.24 show the effective stress contours plots, and figures 4.19, 4.21, 4.23 and 4.25 show the contours plots of the effective plastic strains at the structural level and also in a microstructural RME at the corner point **A**. It is observed that the maximum effective stress generally occurs at this point. The macroscopic effective stress distributions exhibit very similar patterns for all microstructures considered. There is a narrow ligament between two large holes along which strains localize as the deformation intensifies. Similarity in the patterns of macroscopic stress distribution is explained from an observation that the macroscopic state of stress at each point is essentially uniaxial. Thus anisotropy emanating from the microstructural morphology does not play an important role in this example. Magnitude of stresses and plastic strains are however considerably different depending on the microstructural arrangement. This is further evidenced in a macroscopic stress-strain plot (figure 4.26 (a)) at the point **A**. The square edge and square diagonal distributions yield nearly identical response. The random void distributions exhibit significantly more ductile behavior compared to the regular distributions. The ductility in the random distribution stems from the plastic strain concentration in regions of clustered voids.

A comparison of the macroscopic and microscopic contour plots reveals that the true stress in the microstructure is significantly higher than the macroscopic stresses. For example, at point **A** the maximum microscopic effective stress is 160% higher for square edge, 175% higher for square diagonal, 265% higher for random circular and 340% higher for random elliptical packing. An interesting observation is that, though the random distribution models shows more ductile behavior, it gives rise to local regions of significantly higher microscopic stresses. In the analysis of porous materials with large void volume fractions, the interaction between microstructural voids, and consequently the inter-void distances appears to play a more dominant role than the arrangement itself, both for macroscopic and microscopic response.

The same problem is considered again with the microstructure changed to a boron-aluminum composite. The same microstructural morphologies are used with 40% fiber volume fraction. Figures 4.27, 4.28, 4.29 and 4.30 show the effective stress contour plots at the end of loading. The macroscopic plots show that the localization ligament between two macroscopic holes is much less severe and more diffused compared to the porous material. For the same level of macroscopic strain, the square edge packing yields the highest

values of effective stress while the square diagonal packing yields the lowest, with the random packings in between. This is also evidenced in the macroscopic stress-strain plot at point **A** in figure 4.26(b). As opposed to the porous microstructure, the arrangement of the composite microstructure has a major effect on the macroscopic response. The distribution pattern is again similar for all RME's due to the predominantly uniaxial state of local stress. The microscopic contour plots reveal that the true stress in the microstructure is significantly higher than the macroscopic counterparts. For example, at point **A** the maximum microscopic effective stress is 91% higher for square edge, 50% higher for square diagonal, 180% higher for random circular and 177% higher for random elliptical packing. This shows that high stress concentration occurs in certain fibers for random microstructures, and are consequently more susceptible to microstructural damage by fiber cracking or debonding for identical levels of macroscopic stresses.

#### Thick cylinder with internal pressure

In this example a thick composite cylinder is subjected to internal pressure that is increased from 0 to a maximum of 0.1 GPa. Only a quarter of the cylinder is modeled from symmetry considerations with 60 QUAD4 elements in ABAQUS. The dimensions of the cylinder and boundary conditions are shown in figure 4.31(a). The cylinder is analyzed for three different microstructures with 40% fiber volume fraction under plane strain conditions. The microstructural VCFEM models for square edge, square diagonal and random packings are displayed in figures 4.31(b), (c) and (d).

Figures 4.32, 4.34, 4.36 show contour plots of the Von Mises stress and 4.33, 4.35, 4.37 show the corresponding effective plastic strains at macroscopic and microscopic levels at the end of loading. The macroscopic plots show that for the random packing the stresses and strains depend only on the radial location ( $r$ ) and not the angular location ( $\theta$ ) of the point. However, for the square edge and square diagonal packings, these state variables depend on both the ( $r$ ) and ( $\theta$ ) coordinates, leading to "earing" effects. The results of the square edge and square diagonal packings are mutually rotated by 45° as expected from the microstructural orientations. Such earing effects are known to be consequences of anisotropy in the microstructures. In this problem, most macroscopic points are in a triaxial state of state, as opposed to the previous example where most points were in a uniaxial stress state. This amplifies the effect of anisotropy in the macroscopic stress and strain distributions. Effective behavior of the random packing is near isotropic and hence the stress strain distributions are independent of  $\theta$  coordinates.

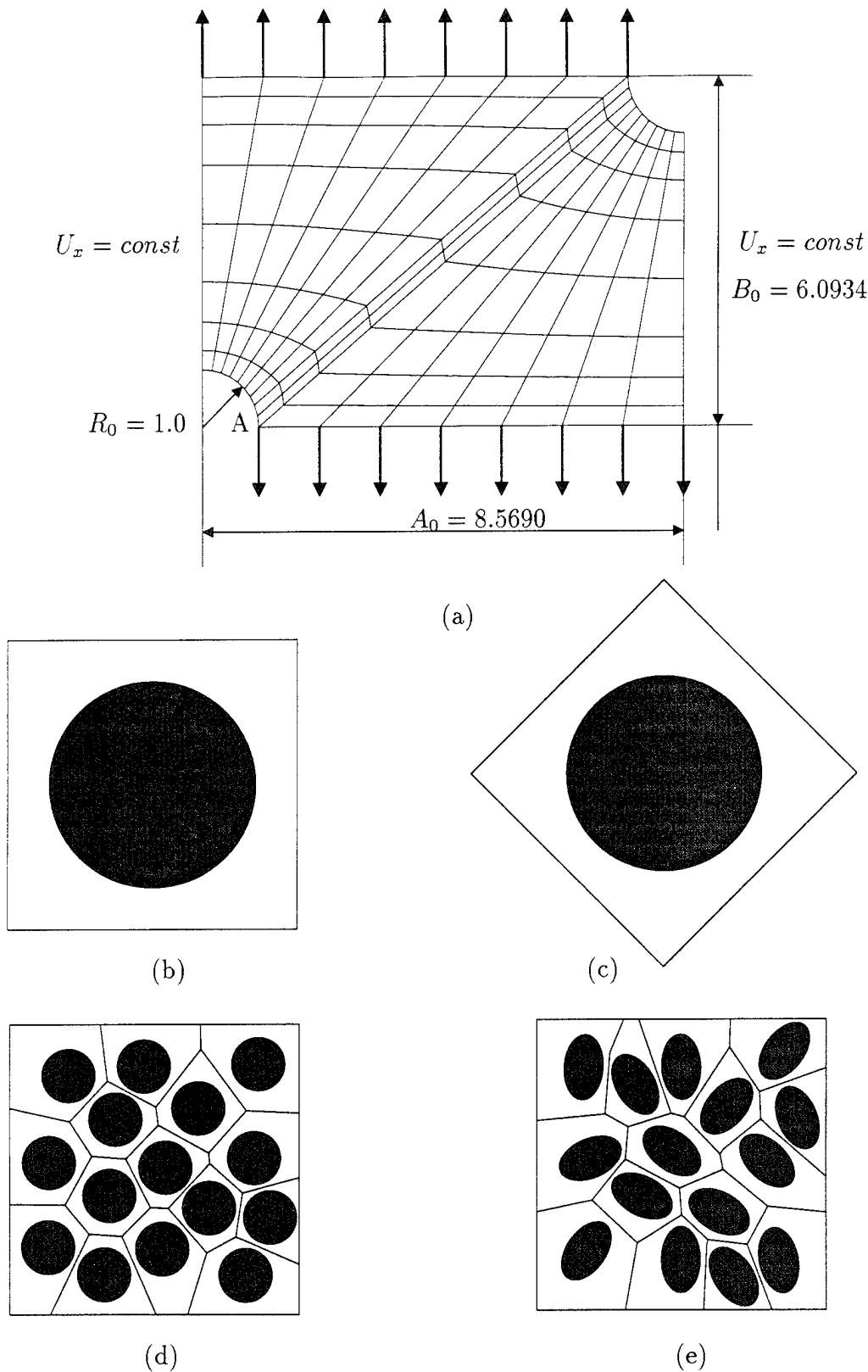
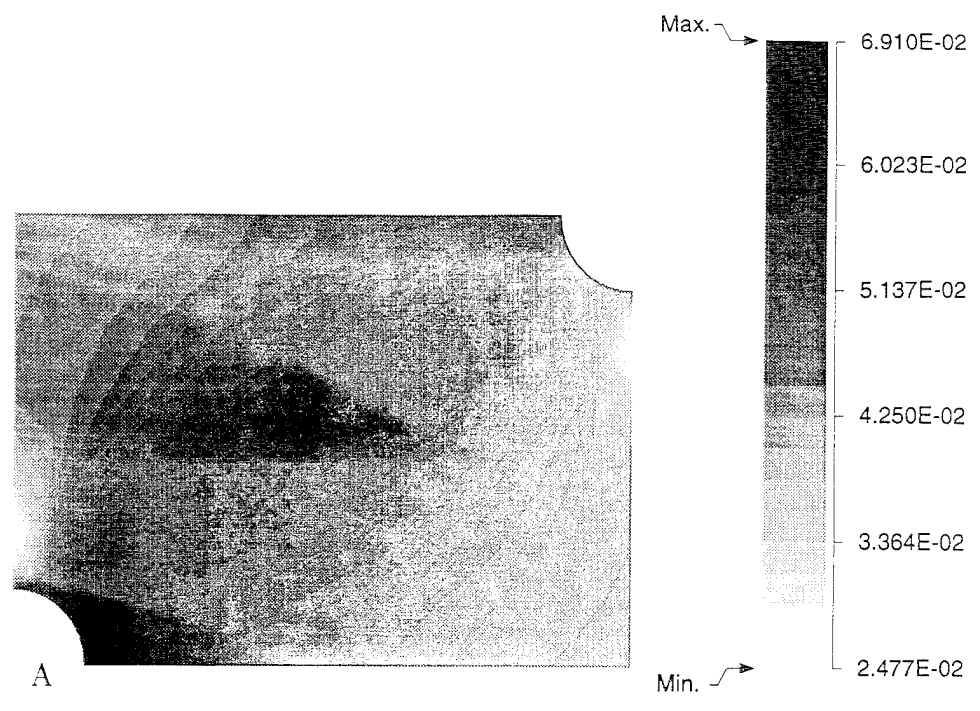
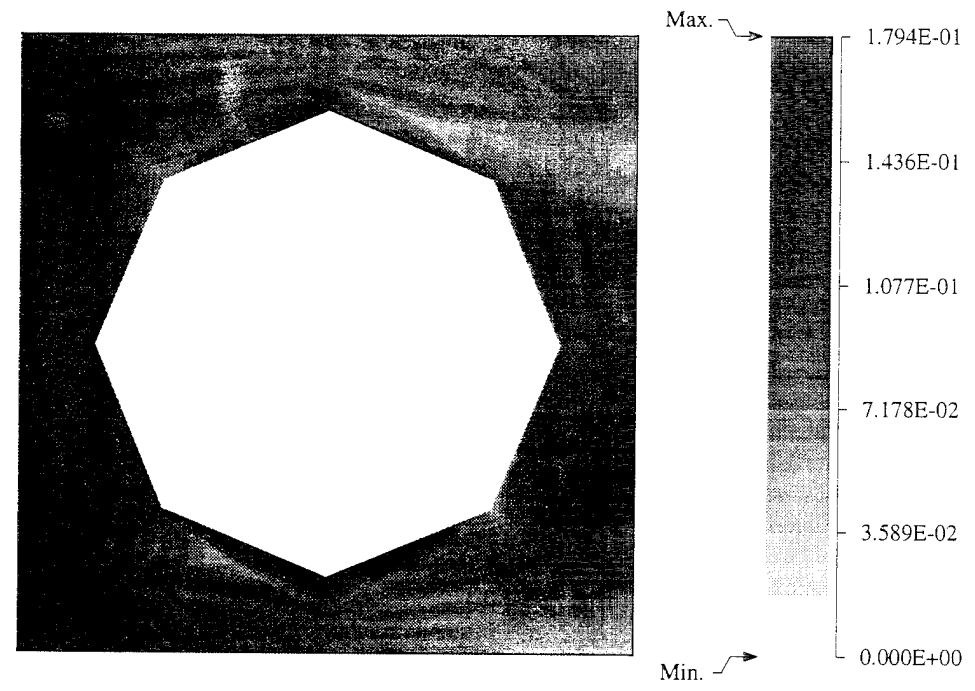


Figure 4.17: (a) ABAQUS model for thick plate with circular holes, Various RME's at 40% volume fraction (b) square edge packing, (c) square diagonal packing, (d) random packing with 15 circular heterogeneities and (e) random packing with 15 elliptical heterogeneities

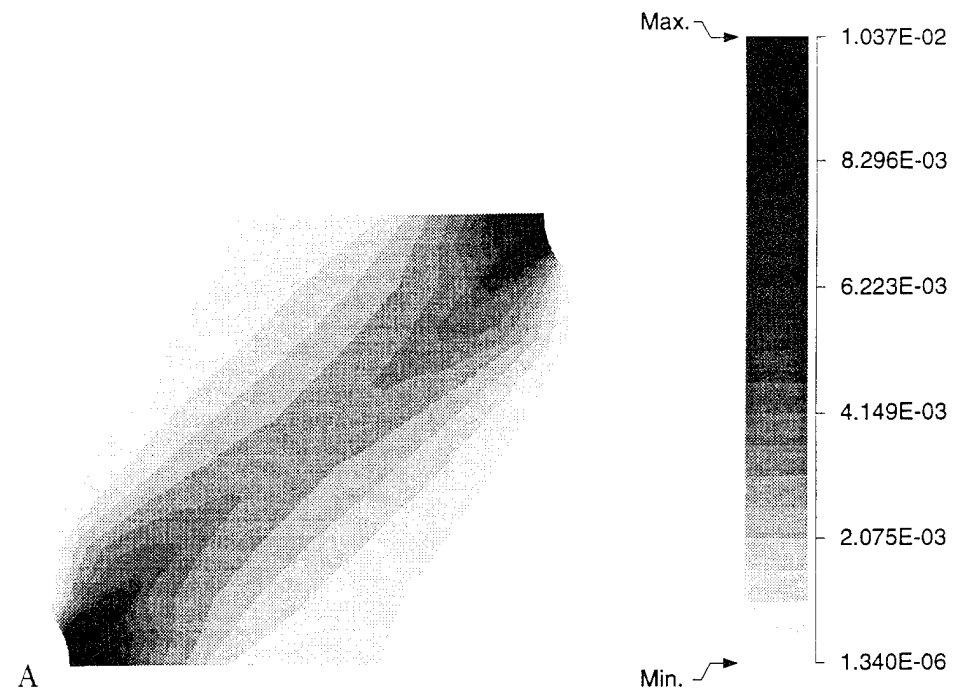


(a)

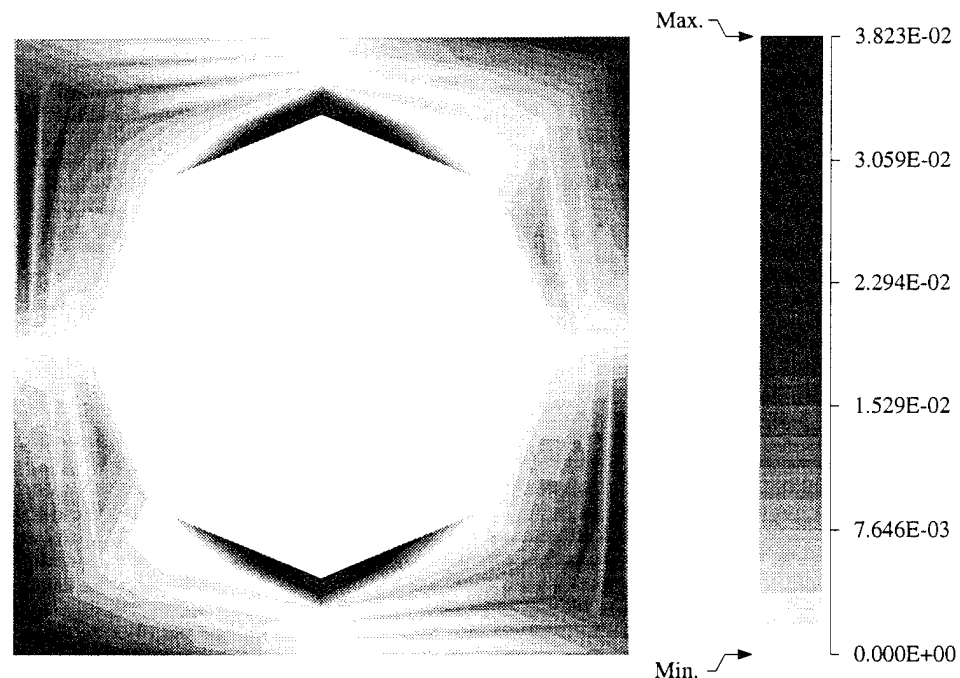


(b)

Figure 4.18: Von Mises stress distribution for porous material with square edge packing (a) macroscopic stress, (b) microscopic stress at point A

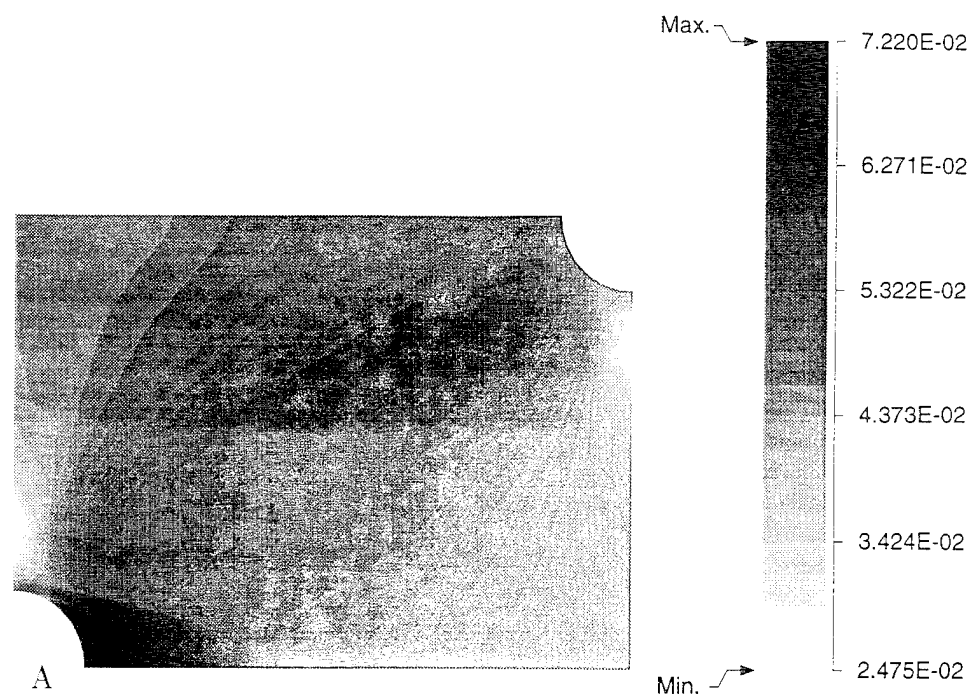


(a)

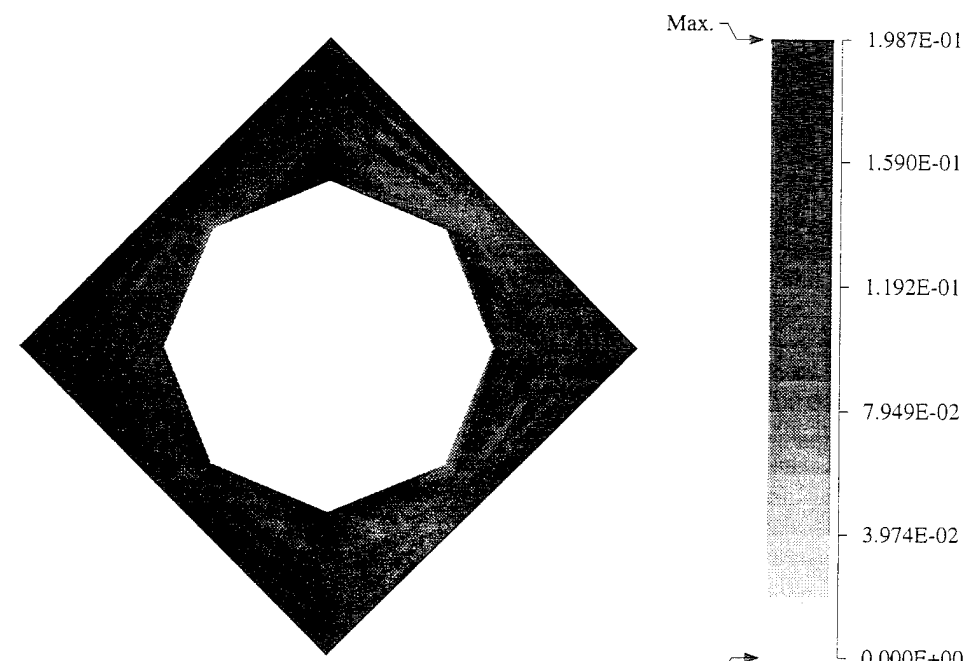


(b)

Figure 4.19: Effective plastic strain distribution for porous material with square edge packing (a) macroscopic strain, (b) microscopic strain at point A

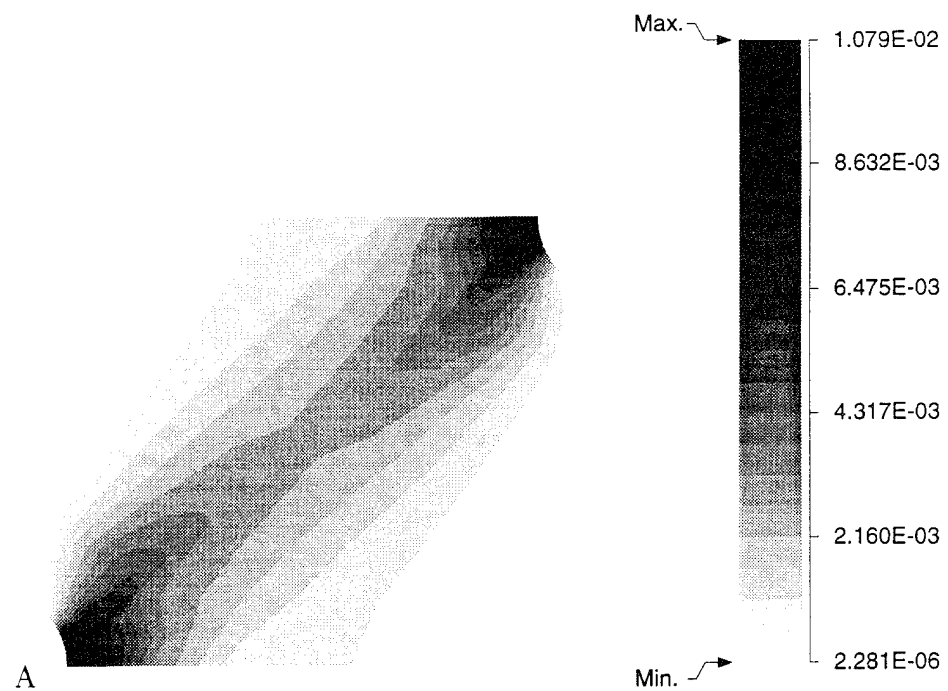


(a)

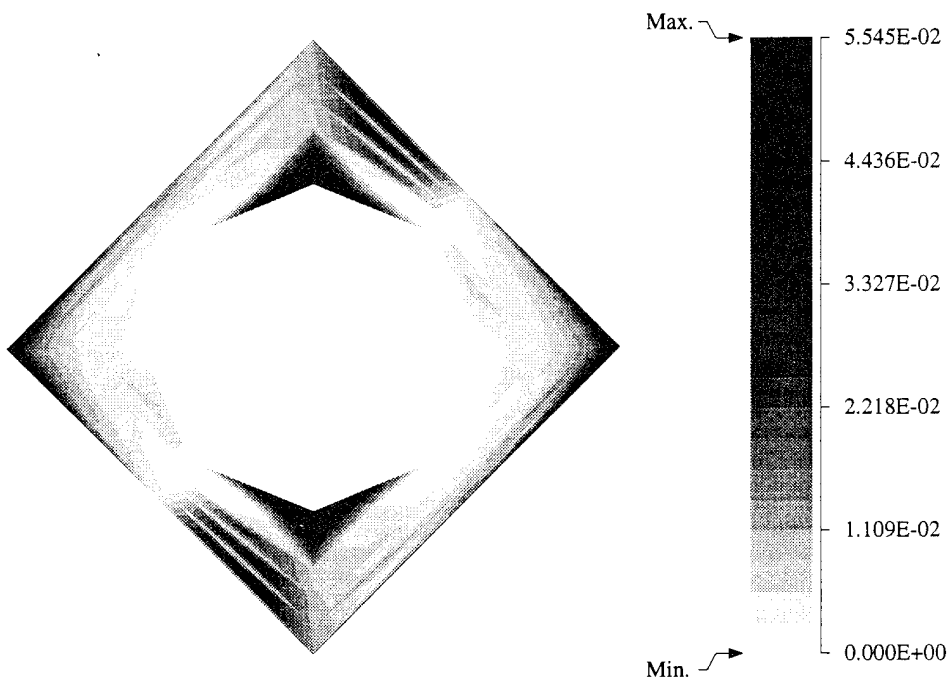


(b)

Figure 4.20: Von Mises stress distribution for porous material with square diagonal packing (a) macroscopic stress, (b) microscopic stress at point A

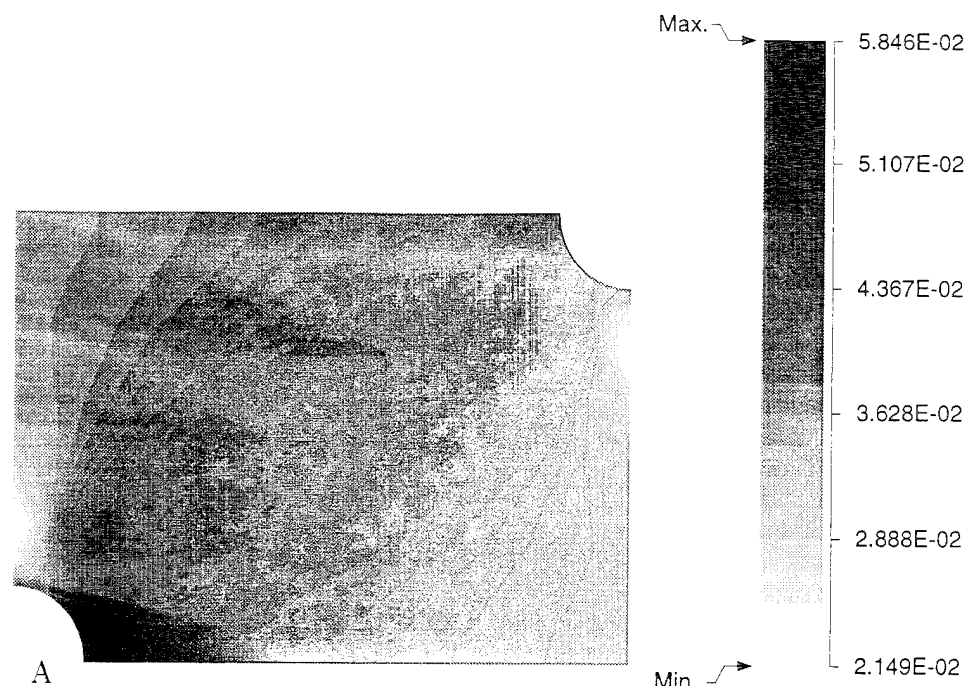


(a)



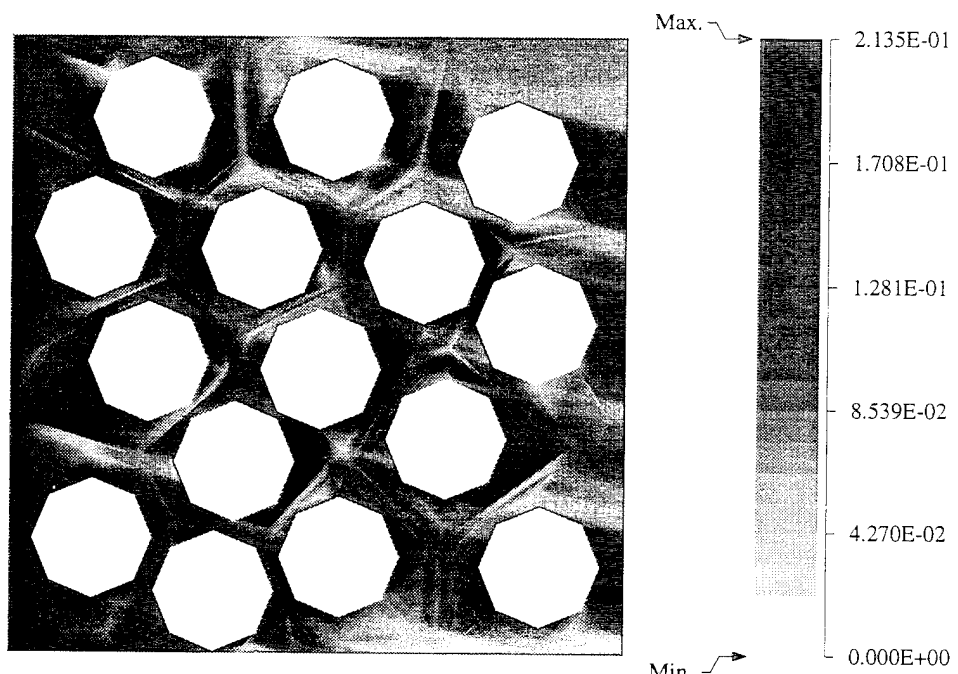
(b)

Figure 4.21: Effective plastic strain distribution for porous material with square diagonal packing  
 (a) macroscopic strain, (b) microscopic strain at point A



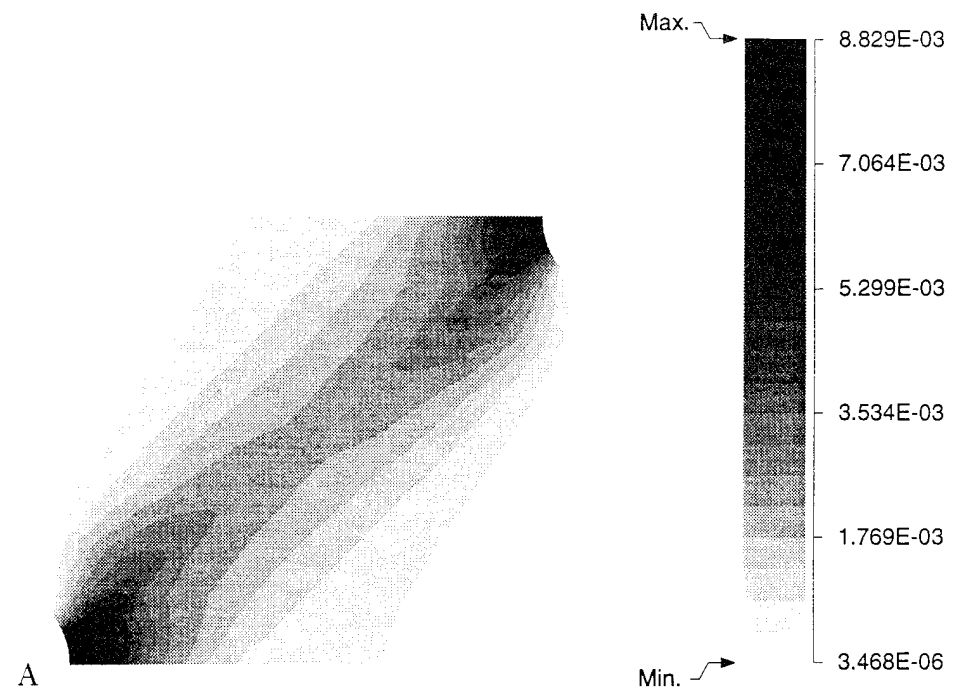
A

(a)

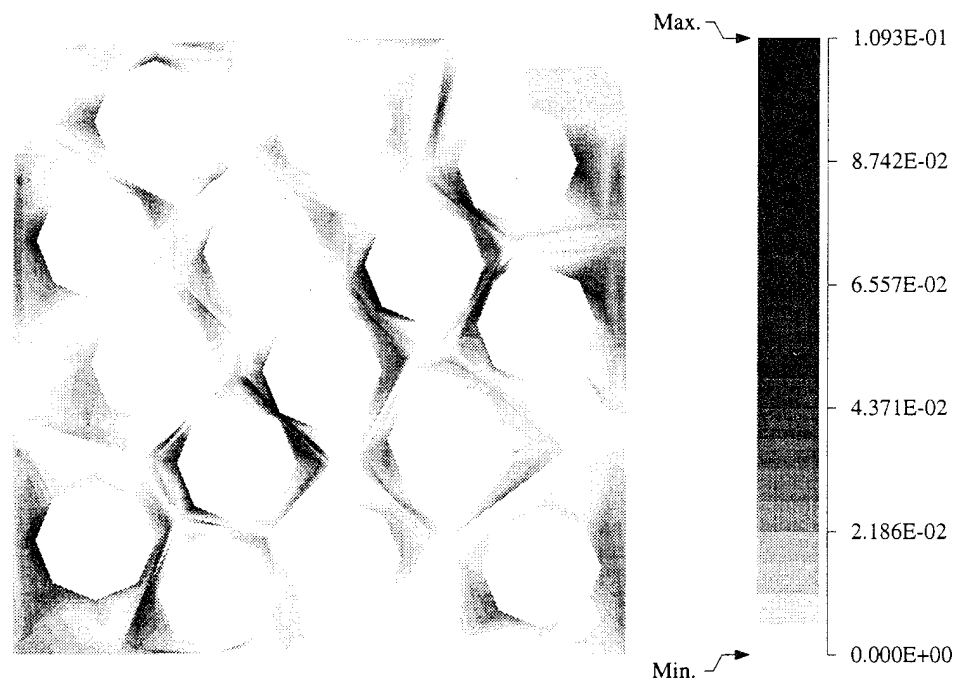


(b)

Figure 4.22: Von Mises stress distribution for porous material with random circular packing (a) macroscopic stress, (b) microscopic stress at point A

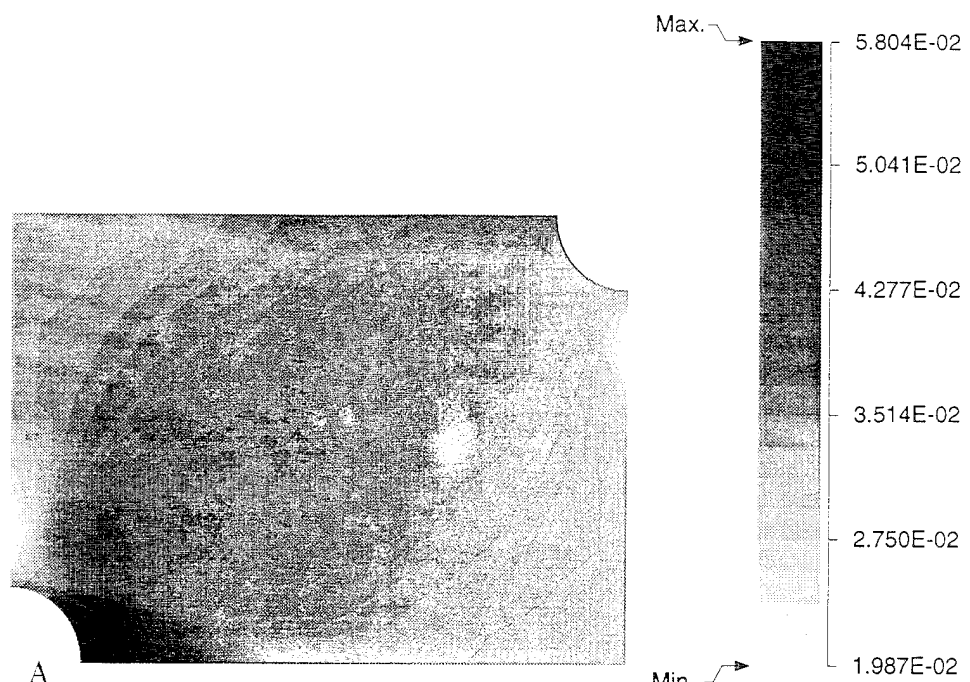


(a)



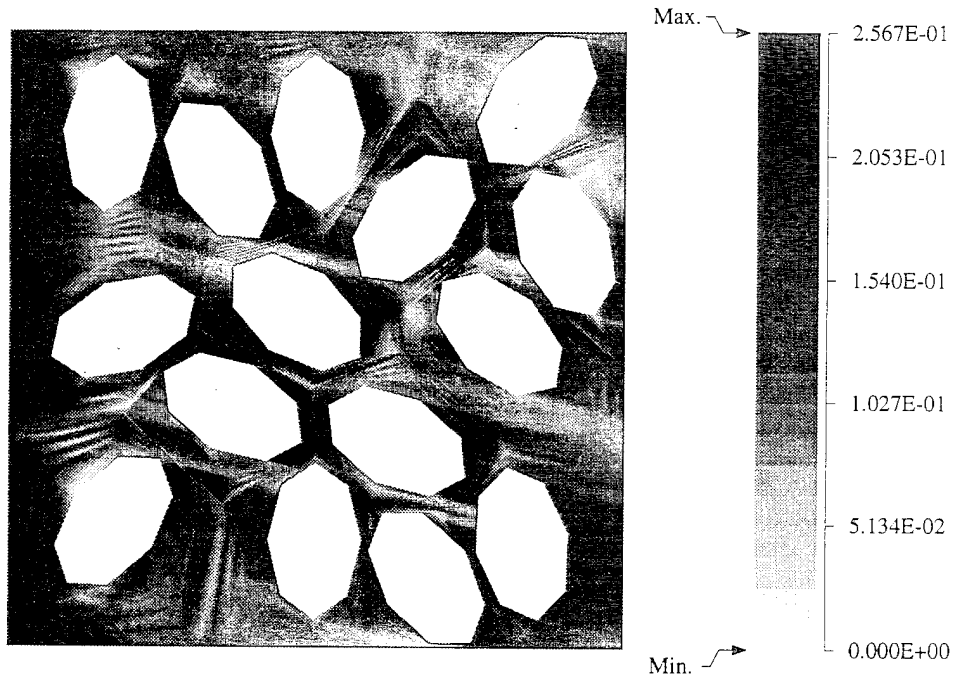
(b)

Figure 4.23: Effective plastic strain distribution for porous material with random circular packing  
(a) macroscopic strain, (b) microscopic strain at point A



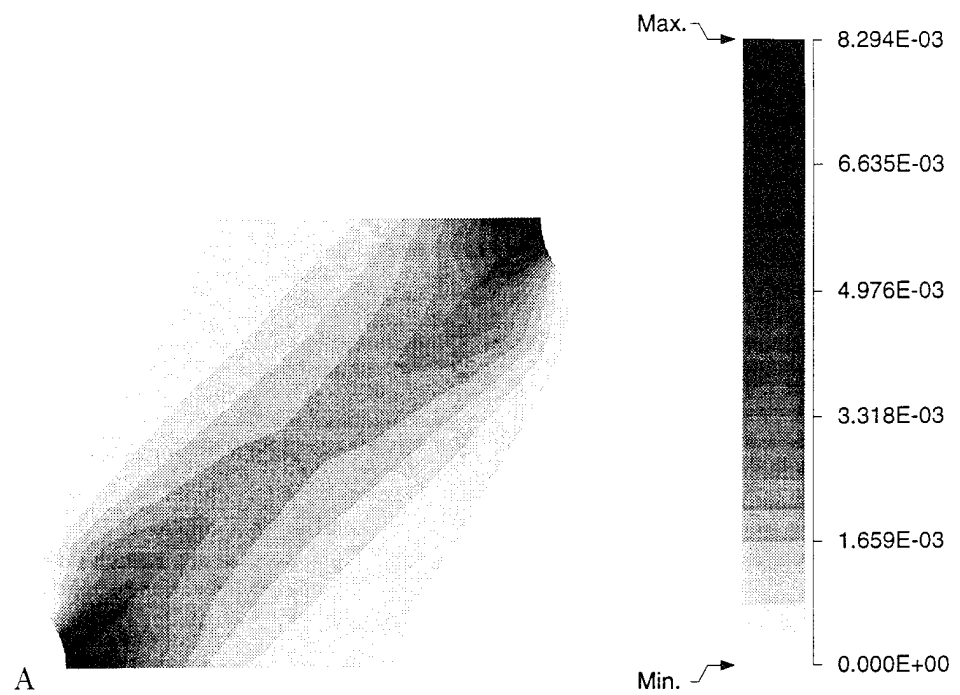
A

(a)

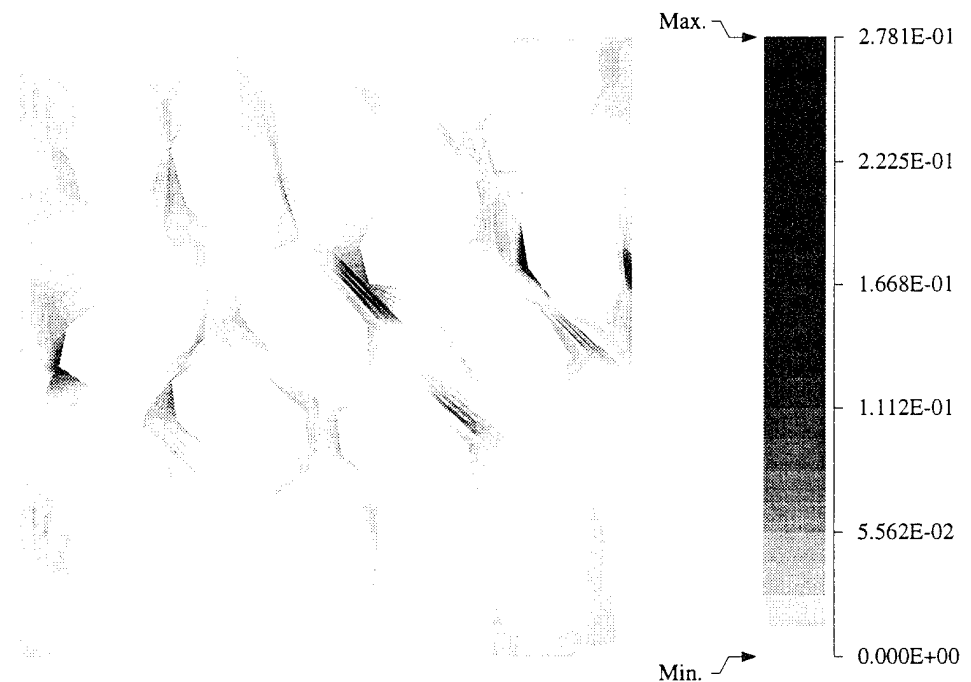


(b)

Figure 4.24: Von Mises stress distribution for porous material with random elliptical packing (a) macroscopic stress, (b) microscopic stress at point A

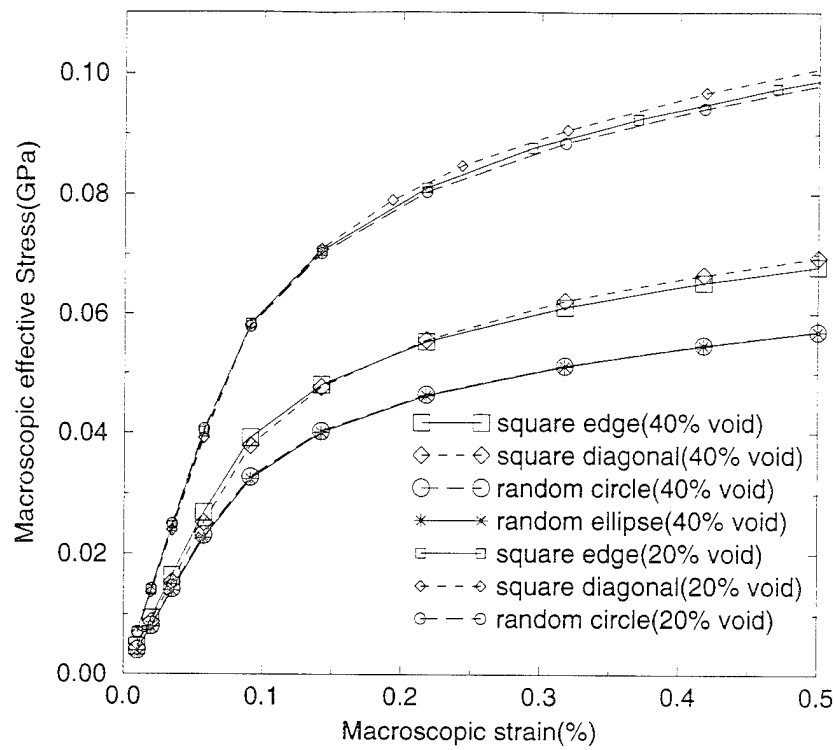


(a)

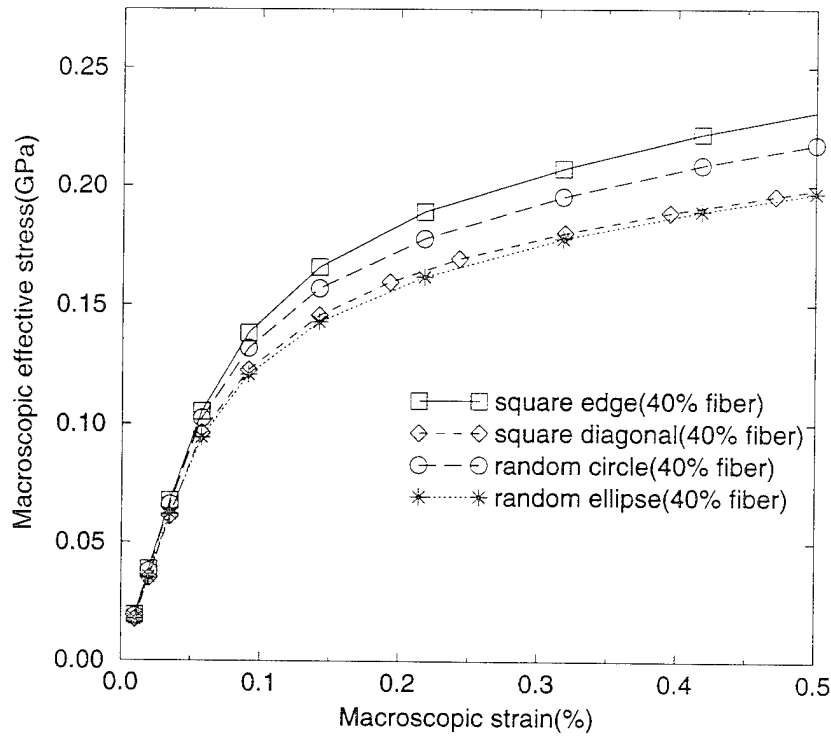


(b)

Figure 4.25: Effective plastic strain distribution for porous material with random elliptical packing  
 (a) macroscopic strain, (b) microscopic strain at point A

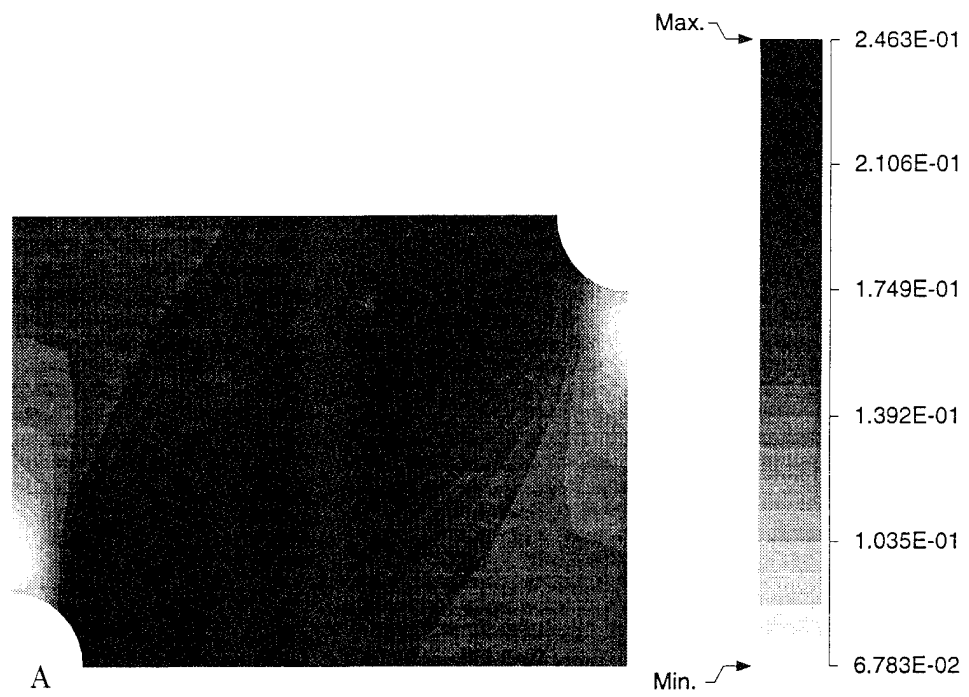


(a)

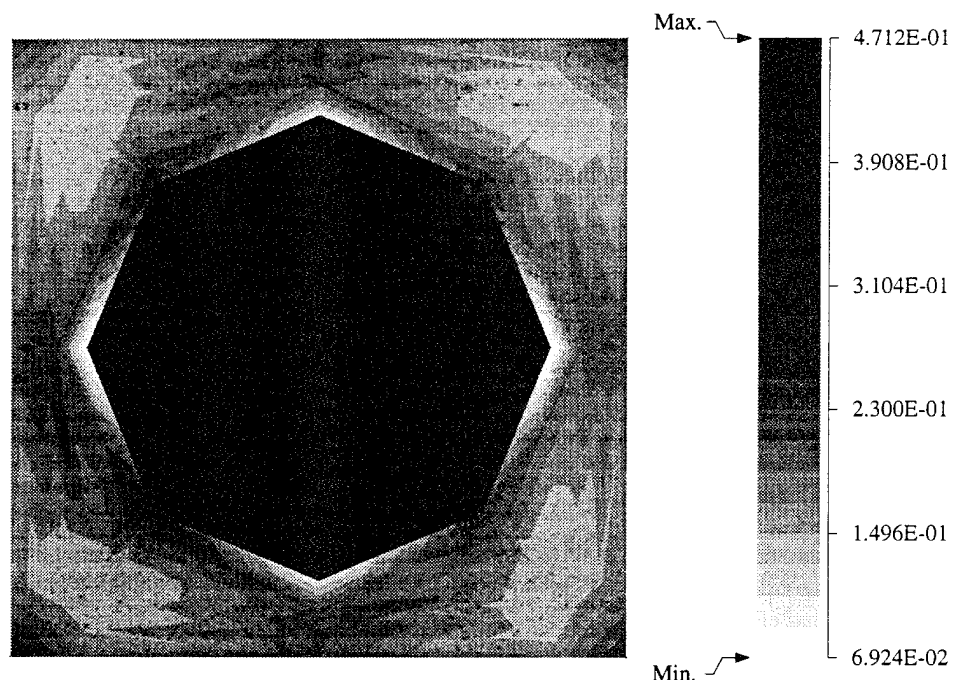


(b)

Figure 4.26: Evolution of effective stress with evolving strain at point A in the heterogeneous plate with 40% second phase volume fraction for (a) porous material (b) composite material

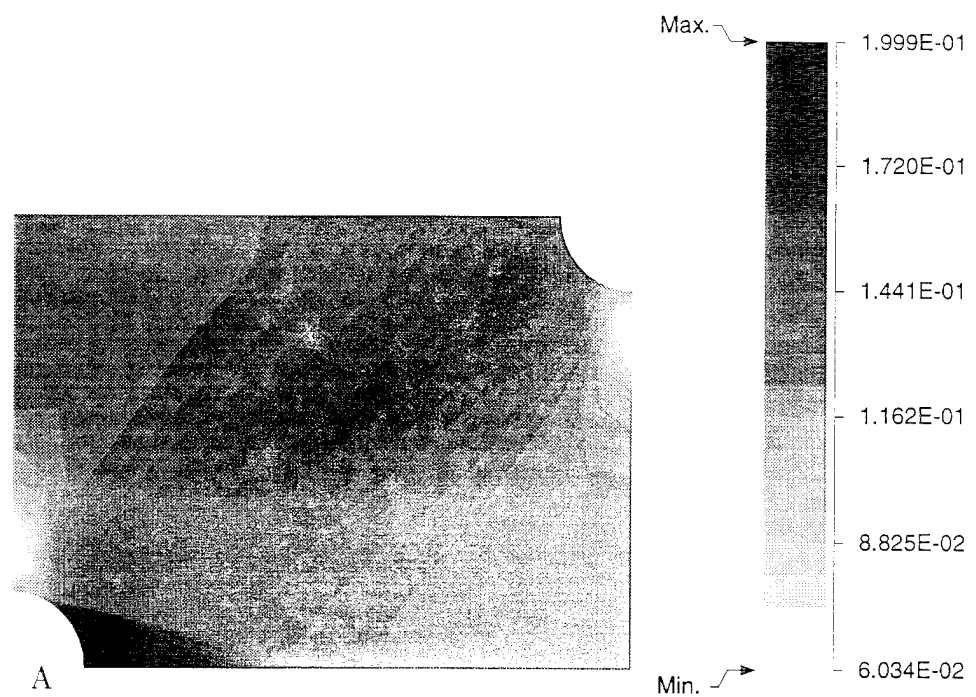


(a)

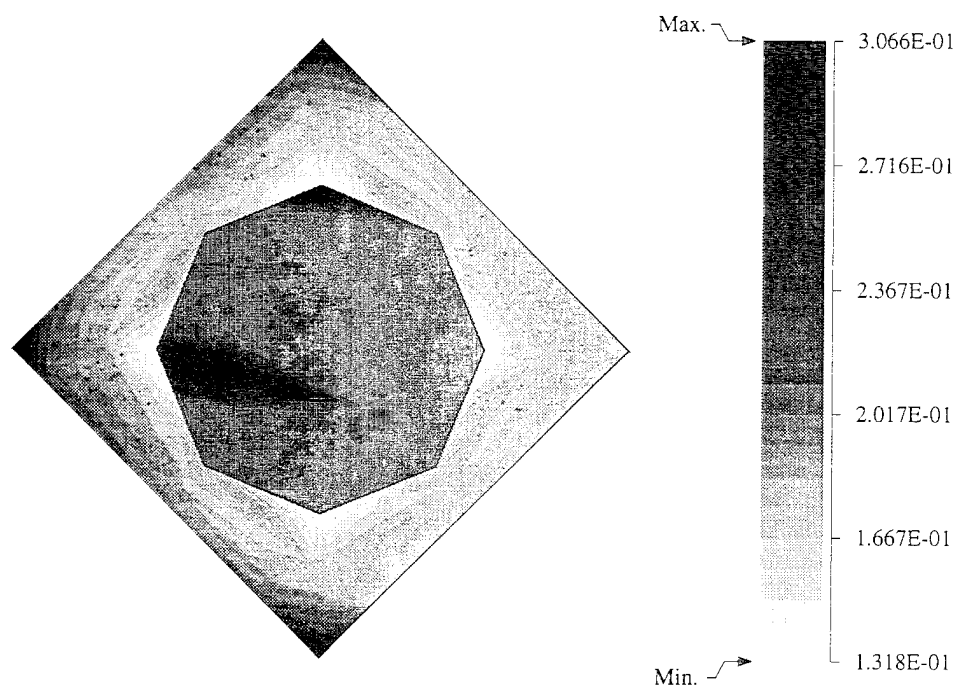


(b)

Figure 4.27: Von Mises stress distribution for composite material with square edge packing (a) macroscopic stress, (b) microscopic stress at point A

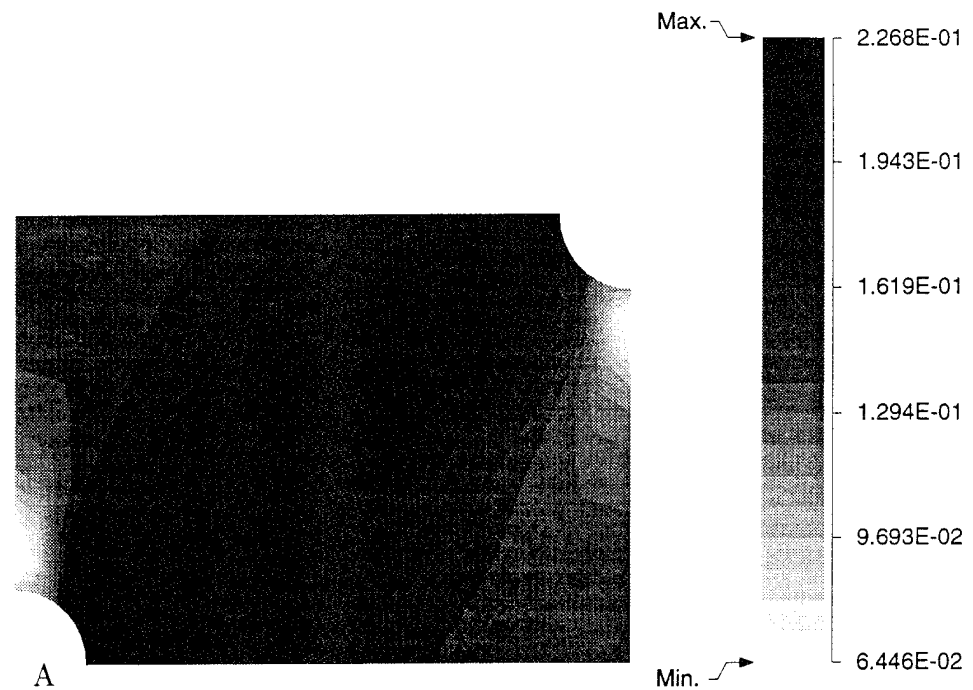


(a)

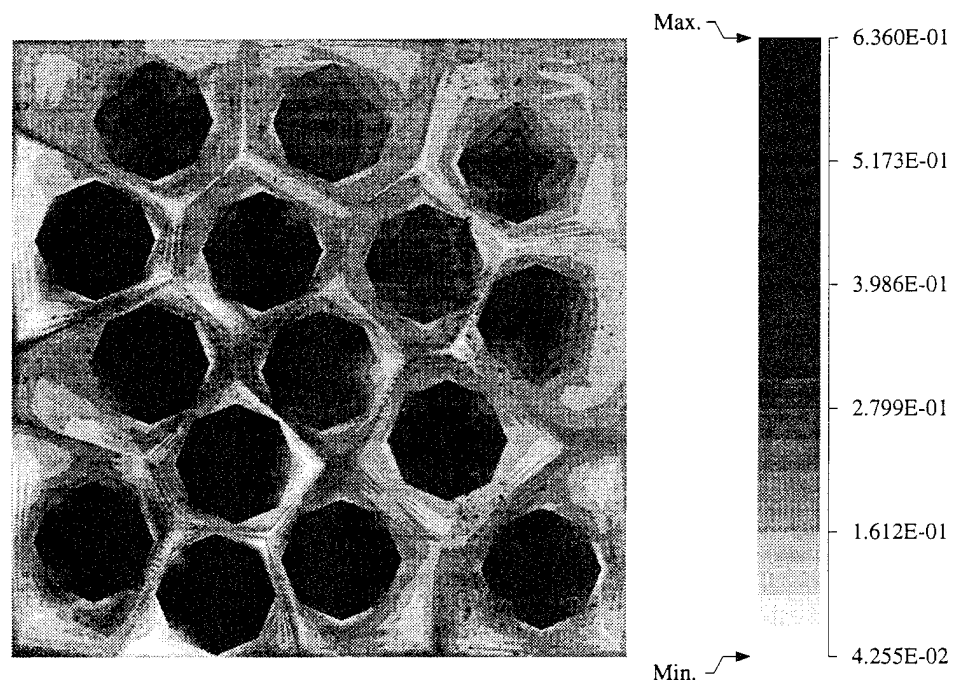


(b)

Figure 4.28: Von Mises stress distribution for composite material with square diagonal packing (a) macroscopic stress, (b) microscopic stress at point A

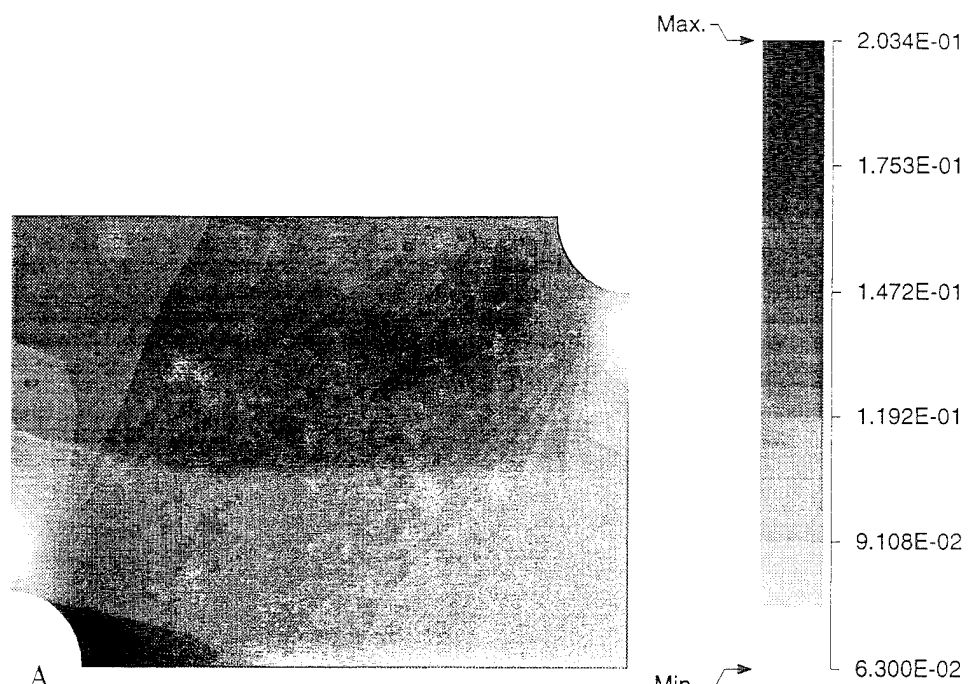


(a)

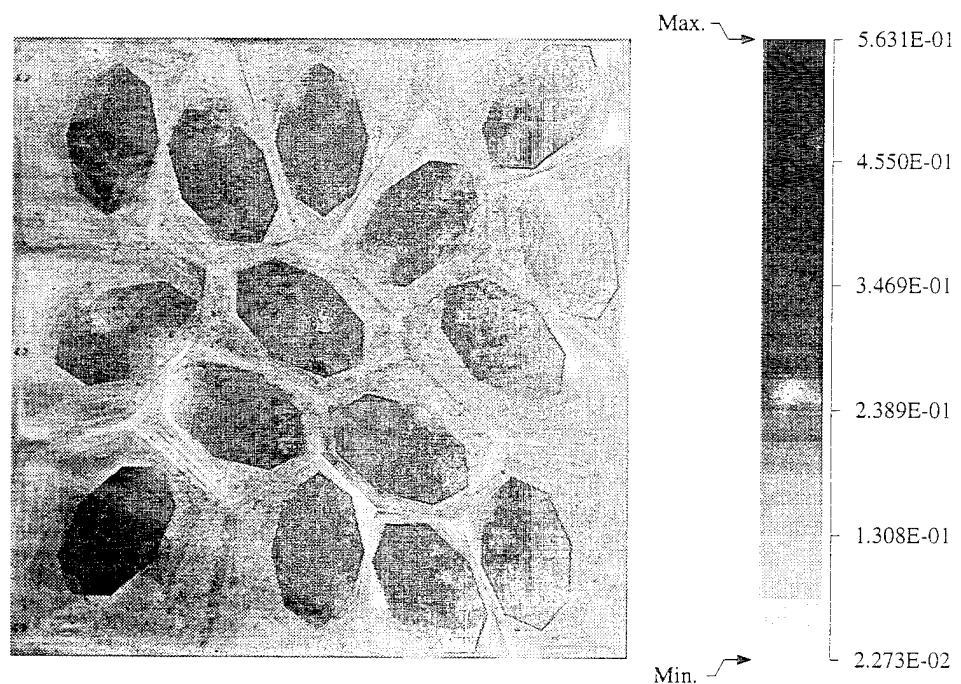


(b)

Figure 4.29: Von Mises stress distribution for composite material with random circular packing (a) macroscopic stress, (b) microscopic stress at point A



(a)



(b)

Figure 4.30: Von Mises stress distribution for composite material with random elliptical packing  
(a) macroscopic stress, (b) microscopic stress at point A

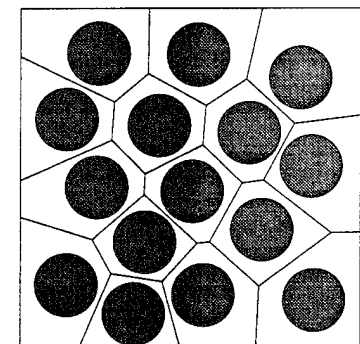
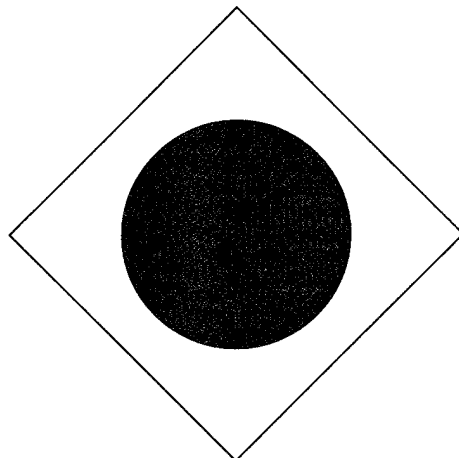
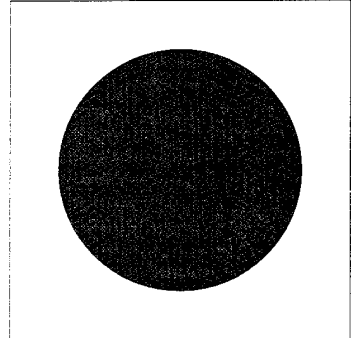
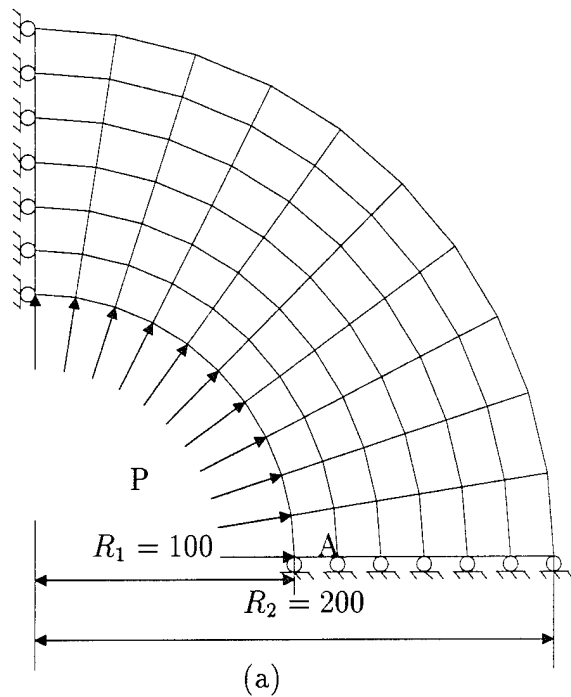
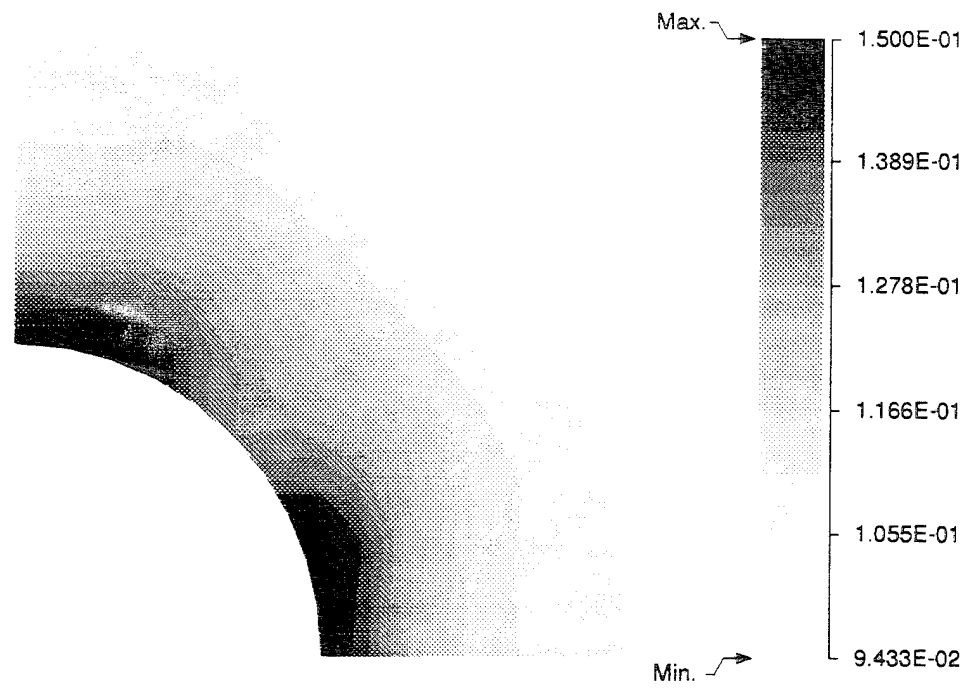
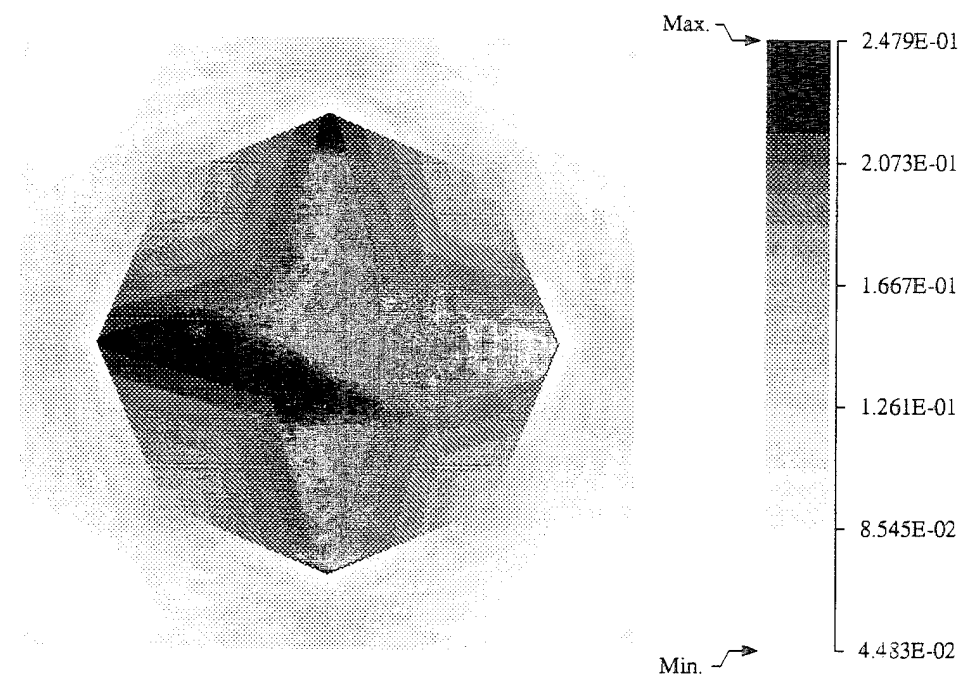


Figure 4.31: (a) Macroscopic ABAQUS model of thick cylinder with internal pressure, microscopic VCFE models for (b) square edge, (c) square diagonal, (d) random packings

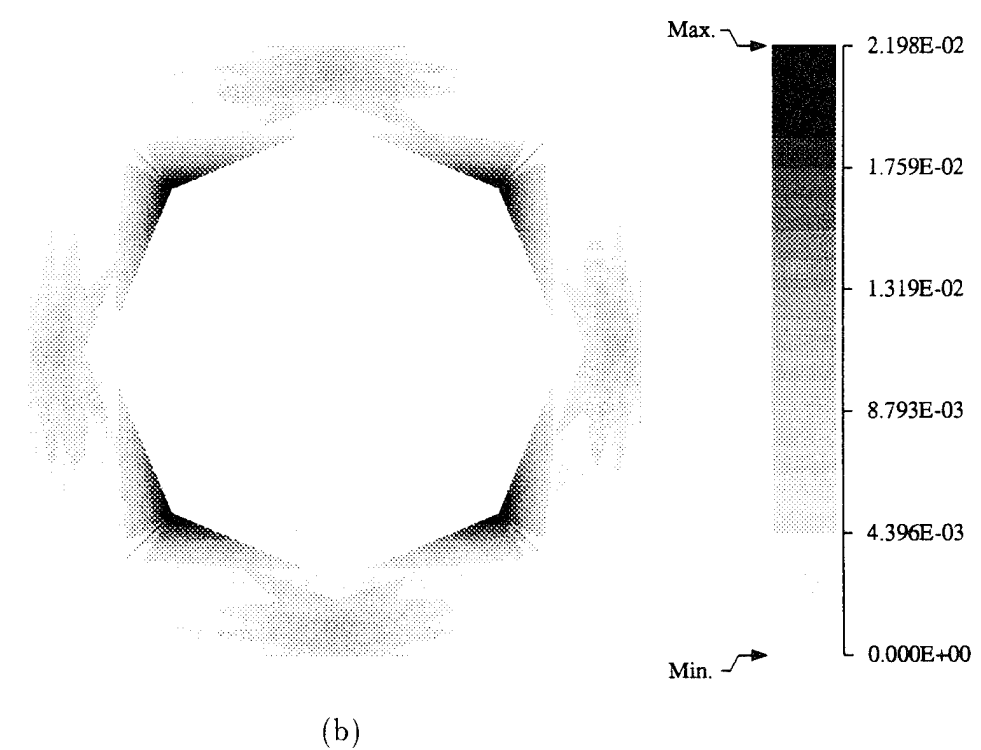
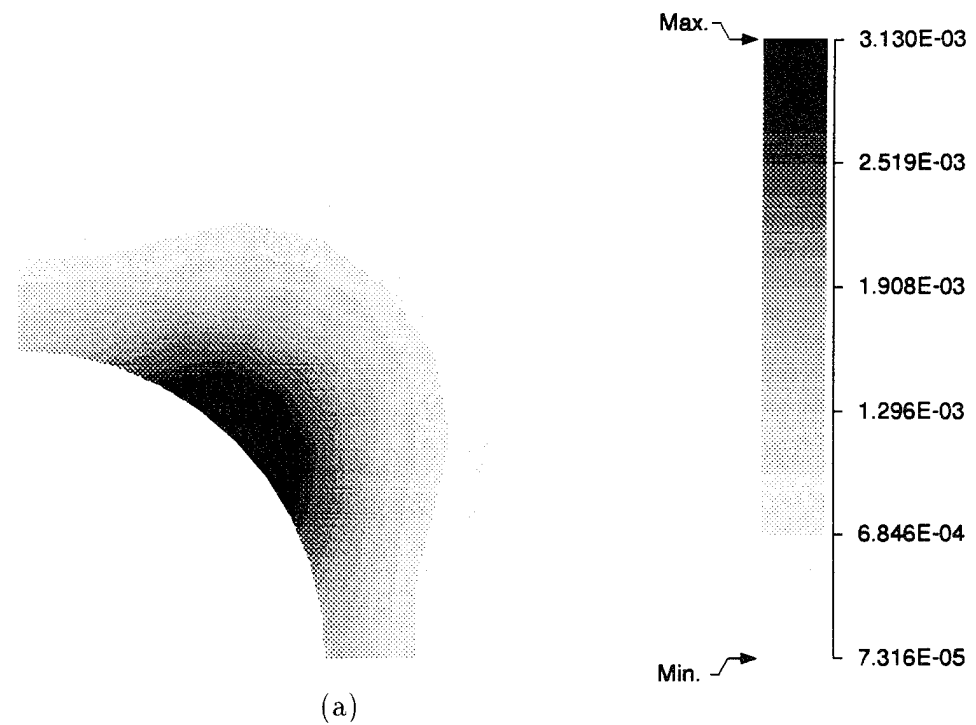


(a)

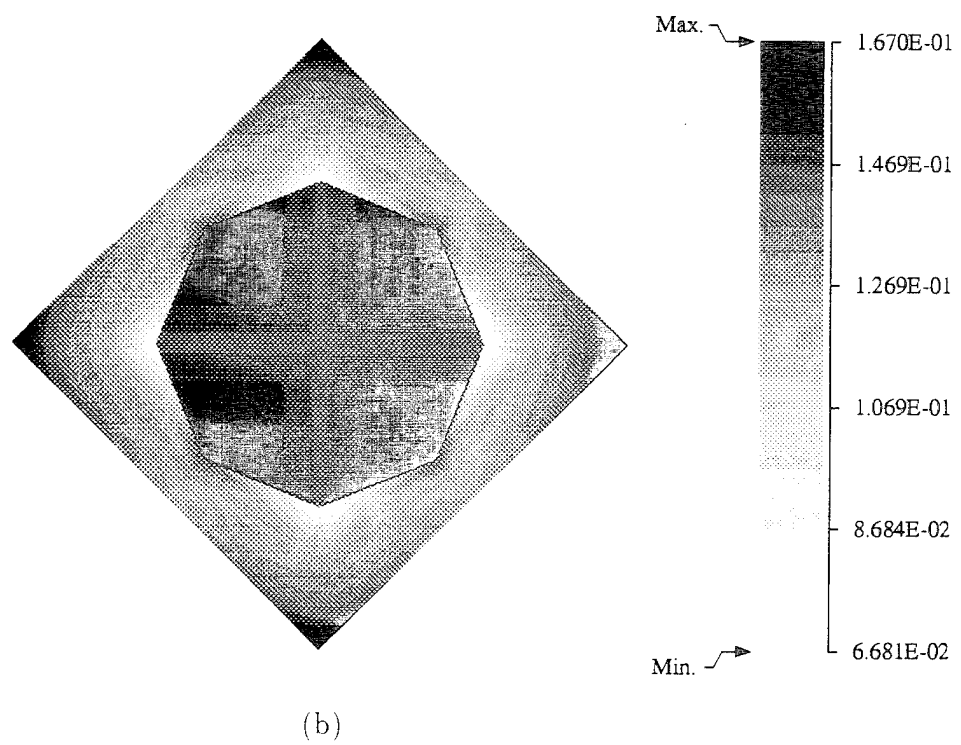
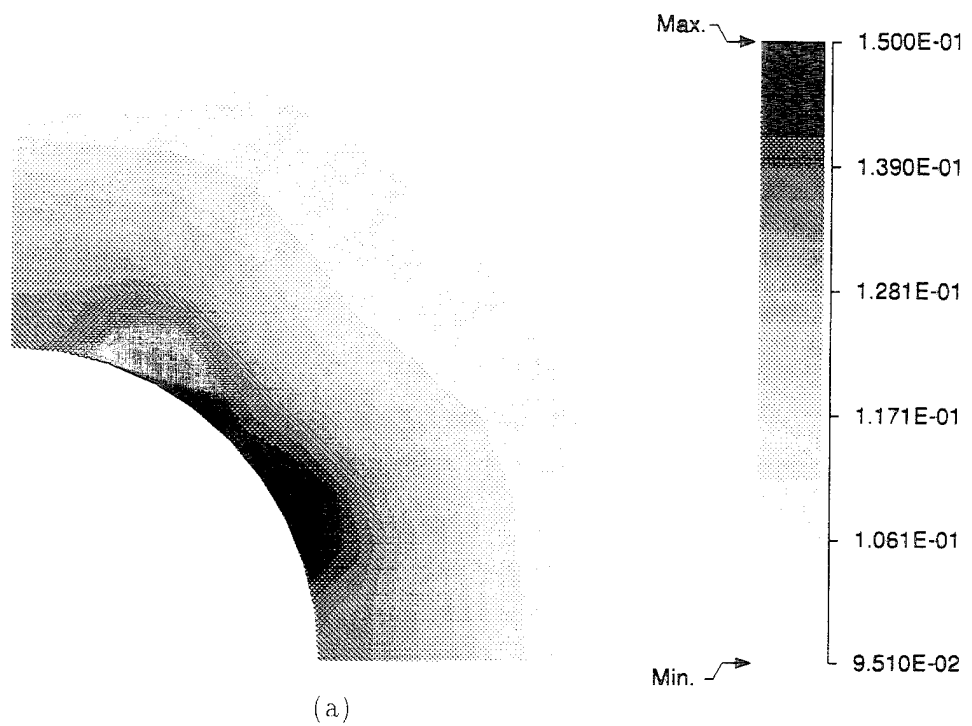


(b)

Figure 4.32: Von Mises stress distribution for square edge packing (a) macroscopic stress, (b) microscopic stress at point A



98  
 Figure 4.33: Effective plastic strain distribution for square edge packing (a) macroscopic stress, (b) microscopic stress at point A



## 4.7 Conclusions

In this work, a multiple-scale computational tool (VCFEM-HOMO) is devised for performing elastic-plastic analysis of heterogeneous materials with inclusions and voids in the microstructure. The microscopic analysis is conducted with the Voronoi Cell finite element model while a conventional displacement based FEM code (ABAQUS in this work) executes the macroscopic analysis. Coupling between the scales is accomplished through the user based UMAT window in ABAQUS, for incorporating the effective constitutive model from VCFEM by asymptotic homogenization.

The VCFEM developed for porous and composite materials in [26, 27] is used in conjunction with homogenization for a wide variety of arbitrary microscopic phase distributions. In this model for small deformation elasto-plasticity, stress functions are motivated from essential characteristics of micromechanics by accounting for the heterogeneity shape and influence. This is achieved by transforming any arbitrary shaped heterogeneity to a unit circle using a mapping similar to the Schwarz-Christoffel conformal mapping. Stress functions are then constructed in terms of mapped coordinates. The introduction of micromechanics consideration tremendously enhances VCFEM accuracy for various microstructures at very moderate computational efforts. The accuracy and efficiency of VCFEM are established by comparing with conventional FEM commercial packages. For a wide range of problems VCFEM delivers very similar accuracy at a considerably low computational effort. This is evidenced by the drastically reduced degrees of freedom needed for convergence, compared with the conventional codes. The D.O.F. ratio varies from as low as 20 for simple microstructures, to even 100 for more complex cases. This translates into a reduction factor of 15-30 in the CPU time for execution, even with a non-optimized research code. Furthermore, user effort required to generate the model is much lower for VCFEM than for many commercial packages.

Numerical examples conducted with VCFEM-HOMO establish the effectiveness of homogenization, when compared with the FEM calculations with constitutive relations from unit cell and effective continuum models. They also point out the limitations of assumptions made in the latter methods, and emphasize situations when coupled multiple scale analysis becomes necessary. The effect of various microscopic arrangements on the mechanical response at the two scales are investigated through these examples. Significant influence is observed in both the microscopic and macroscopic responses. For example, the square edge and square diagonal distributions give severe anisotropic effects, while random distributions are more isotropic at a point in the structure. Multiple scale computations with microscopic FEM models at each element integration point in the structure are in general quite exhaustive. For complex microstructures, the efficiency of microstructural VCFEM makes it possible to realize computations of this magnitude in comparison with conventional FEM. The more complex multiple scale models in this work took approximately 2-3 CPU hours to run on a CRAY-YMP at the Ohio Supercomputer Center. Though reasonable, major improvements in efficiency of the scale coupling is presently being pursued.

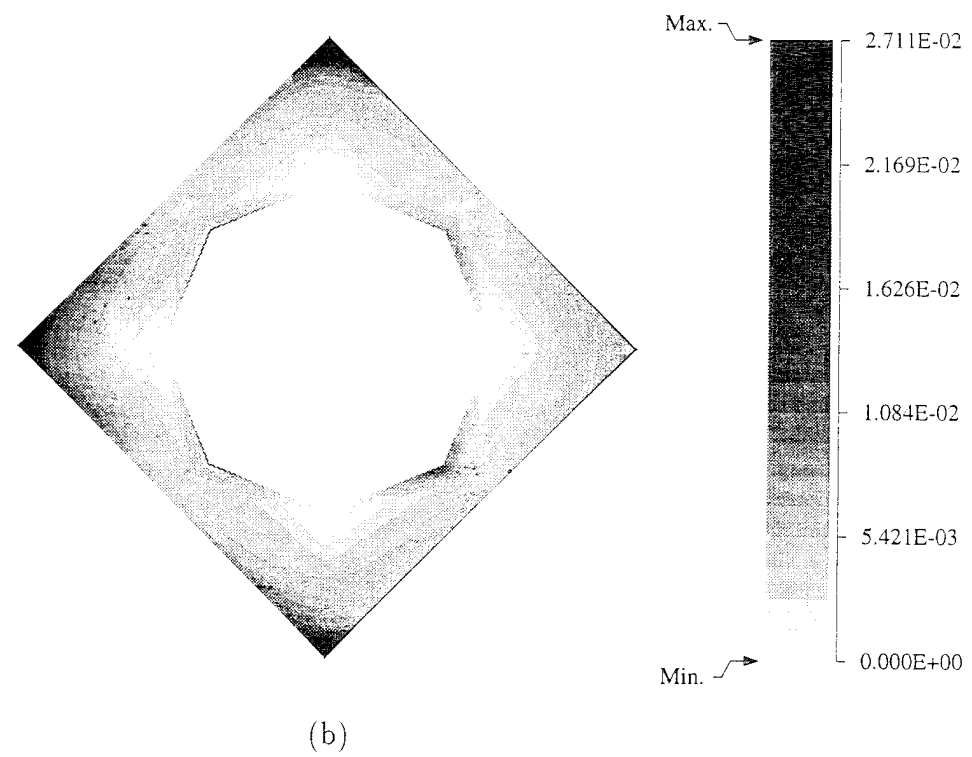
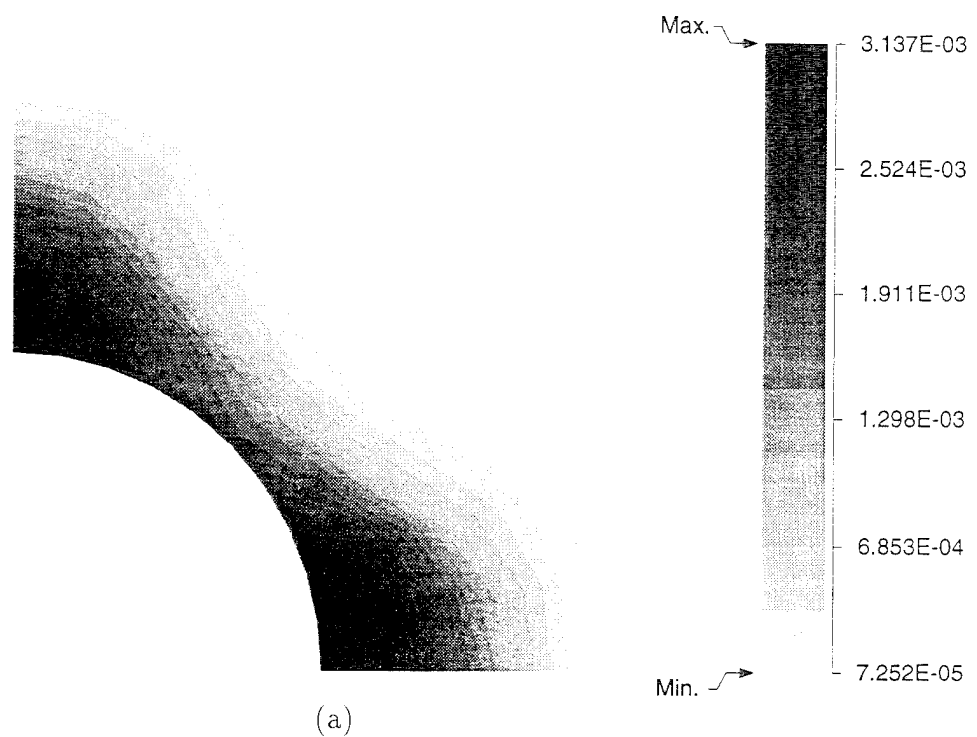
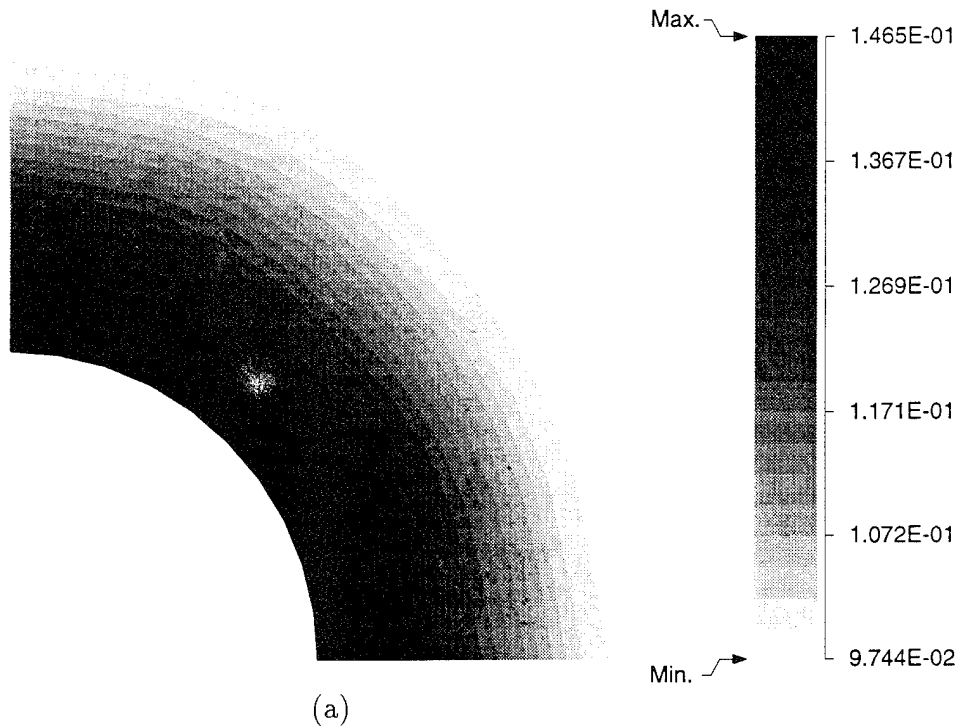
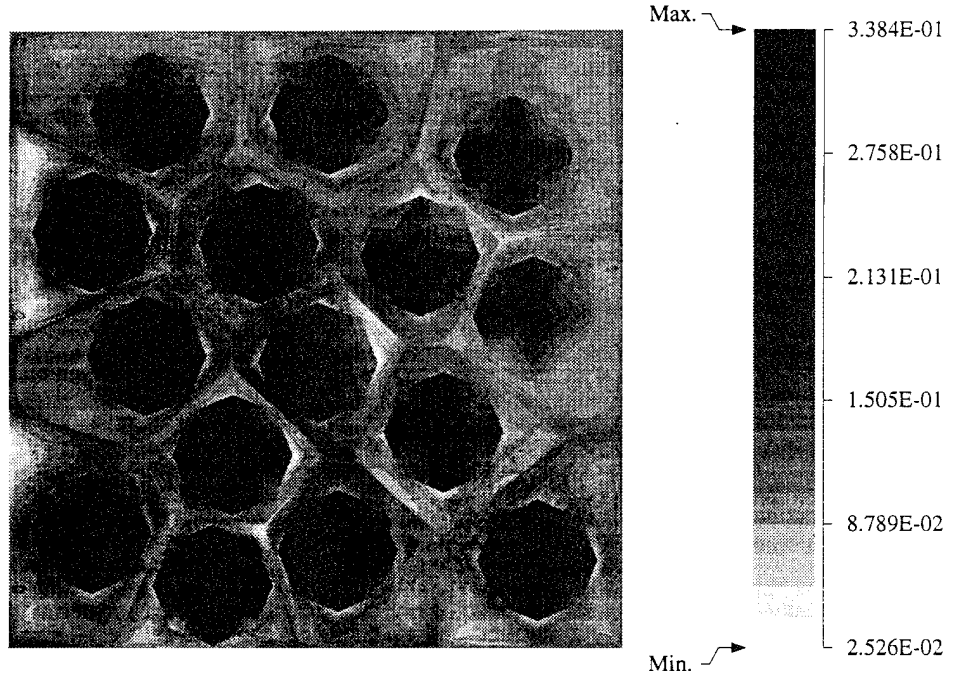


Figure 4.35: Effective plastic strain distribution for square diagonal packing (a) macroscopic stress, (b) microscopic stress at point A <sup>101</sup>



(a)



(b)

Figure 4.36: Von Mises stress distribution for random packing (a) macroscopic stress, (b) microscopic stress at point A

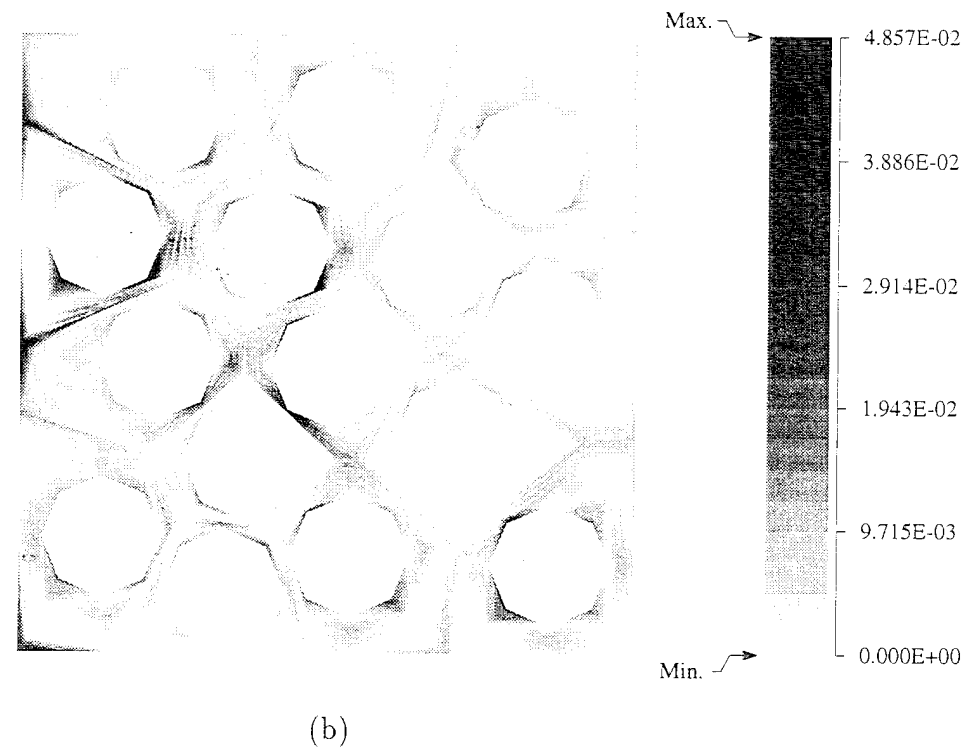
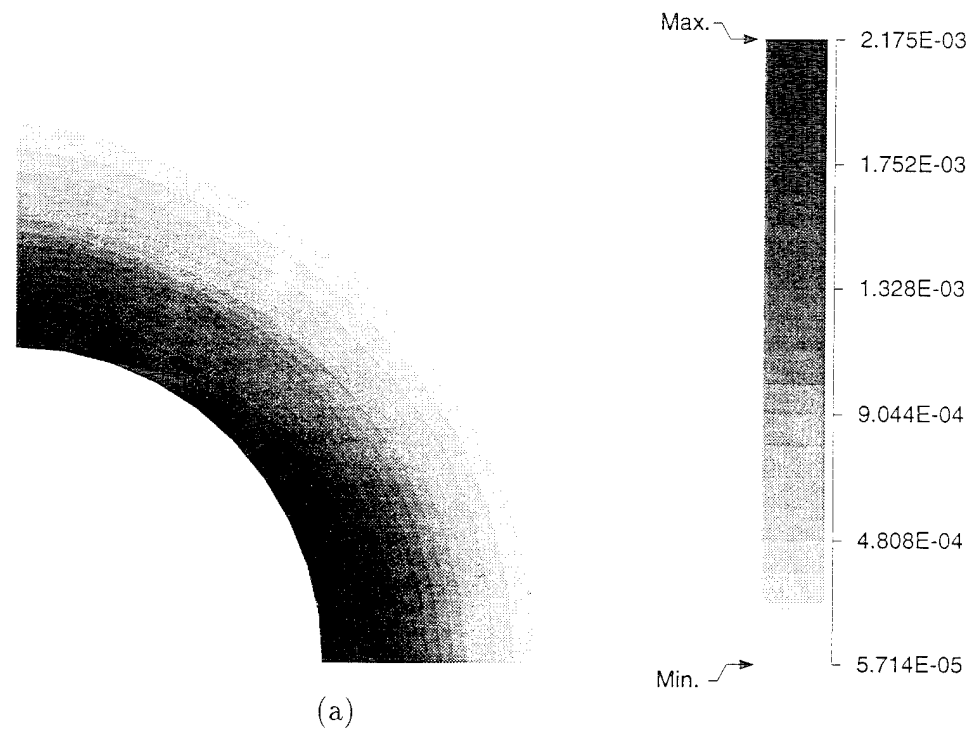


Figure 4.37: Effective plastic strain distribution for random packing (a) macroscopic stress, (b) microscopic stress at point A <sup>103</sup>

In conclusion, the Voronoi Cell finite element model with asymptotic homogenization (VCFEM-HOMO) emerges as an important tool for analyzing arbitrary microstructures in many materials. It is easily adapted with commercial packages at the structural scale, and this makes it very attractive. A shortcoming of the homogenization method in its present form, is however the incorporation of boundary condition at regions of material discontinuity. Boundary conditions should be applied in the microstructure and not at the macroscopic level as is presently done. The boundary effect can become pronounced in some cases, and then homogenization results become less accurate near the boundary (see [22, 23]).

# Bibliography

- [1] T. Christman, A. Needleman and S. Suresh, An experimental and numerical study of deformation in metal-ceramic composites, *Acta Metall. et Mater.* 37, (1989b), 3029–3050.
- [2] Z. Hashin and S. Strikman, A variational approach to the theory of the elastic behavior of multiphase materials, *Jour. Mech. Phys. Solids* 11, (1963), 127–140.
- [3] S. Nemat-Nasser and M. Hori, *Micromechanics: overall properties of heterogeneous materials* (North-Holland, 1993).
- [4] H.S. Chen and A. Acrivos, The effective elastic moduli of composite materials containing spherical inclusions at non-dilute concentrations *Int. Jour. Solids. Struct.* 14, (1978), 349–364.
- [5] R. Hill, A self consistent mechanics of composite materials, *Jour. Mech. Phys. Solids* 13, (1965), 213–222.
- [6] B. Budiansky, On the elastic modulii of some heterogeneous materials, *Jour. Mech. Phys. Solids* 13, (1965), 223-227.
- [7] R.M. Christensen and K.H. Lo, Solutions for effective shear properties in three phase sphere and cylinder models, *Jour. Mech. Phys. Solids* 27, (1979), 315–330.
- [8] G.P. Tandon and G.J. Weng, A theory of particle reinforced plasticity, *Jour. Appl. Mech.* 55, (1988), 126-135.
- [9] G. Dvorak and Y.A. Bahei-el-din, Plasticity analysis of fibrous composites, *Jour. Appl. Mech.* 49, (1982), 327-335.
- [10] G. Dvorak and Y.A. Bahei-el-din, A bimodal plasticity theory of fibrous composite materials, *Acta Mechanica* 69, (1987), 219-241.
- [11] M. Paley and J. Aboudi, Micromechanical analysis of composites by the generalized cell model, *Mech. of Mater.* 14, (1992), 127-139.
- [12] S. Nemat-Nasser, T. Iwakuma and M. Hejazi, On composites with periodic structure, *Mech. Mater.* 1, (1982), 239-267.

- [13] G. Bao, J.W. Hutchinson and R.M. McMeeking, Plastic reinforcement of ductile matrices against plastic flow and creep, *Acta Metallur. et Mater.* 39, (1991) 1871-1882.
- [14] V. Tvergaard, Analysis of tensile properties for a whisker-reinforced metal matrix composite, *Acta Metall. et Mater.* 38, (1990), 185-194.
- [15] A. Benssousan, J.L. Lions and G. Papanicoulau, Asymptotic analysis for periodic structures, (North Holland, Amsterdam, 1978).
- [16] E. Sanchez-Palencia, Non-homogeneous media and vibration theory, (Lecture notes in Physics, 127, Springer-Verlag, Berlin Heidelberg, 1980).
- [17] A. Toledano and H. Murakami, A high order mixture model for periodic particulate composites, *Int. J. Solids. Struct.* 23(7), (1987), 989-1002.
- [18] J.M. Guedes and N. Kikuchi, Preprocessing and Postprocessing for materials based on the homogenization method with adaptive finite element methods, *Comp. Meth. in Appl. Mech. Engng.* 83, (1991), 143-198.
- [19] P. Suquet, Local and global aspects in the mathematical theory of plasticity, *Plasticity Today- Modeling methods and Applications*, A. Sawczuk and G. Bianchi (eds.), (Elsevier, London, 1985).
- [20] J.M. Guedes, Nonlinear computational model for composite material using homogenization, (Ph. D. Dissertation, University of Michigan MI, 1990).
- [21] C. -H. Cheng, Modeling of the elasto-plastic behavior for composite materials using homogenization method, (Ph. D. Dissertation, University of Michigan MI, 1992).
- [22] V.Z. Parton and B.A. Kudryavtsev, *Engineering mechanics of composite structure* (CRC Press, 1993).
- [23] S.J. Hollister and N. Kikuchi, A comparison of homogenization and standard mechanics analyses for periodic porous composites, *Computational Mechanics* 10, (1992), 73-95.
- [24] N. S. Bakhvalov and G. P. Panasenko, *Homogenization in Periodic Media. Mathematical Problems of the Mechanics of Composite Materials*, Nauka, Moscow, (1984).
- [25] F. Devries, H. Dumontet, G. Duvant and F. Lene Homogenization of damage for composite structures. *Int. Jour. Numer. Meth. Engrg.* 27, (1989), 285-298.
- [26] S. Ghosh and S. Moorthy, Elastic-plastic analysis of arbitrary heterogeneous materials with the Voronoi cell finite element method, *Comp. Meth. Appl. Mech. Engrg* 121, (1995), 373-409.
- [27] S. Moorthy and S. Ghosh, A Model for Analysis of Arbitrary Composite and Porous Microstructures with Voronoi Cell Finite Elements, (submitted for publication).

- [28] S. Ghosh, K. Lee and S. Moorthy, Multiple scale analysis of heterogeneous elastic structures using homogenization theory and Voronoi cell finite element method, *Int. J. Solids Struct.* 32(1), (1995), 27-62.
- [29] S. Ghosh and Y. Liu, Voronoi cell finite element method for micropolar thermo-elastic heterogeneous materials, *Int. Jour. Numer. Meth. Engrg.* 38(8), (1995), 1361-1398.
- [30] S. Ghosh and S.N. Mukhopadhyay, A two dimensional automatic mesh generator for finite element analysis of random composites, *Comput. and Struct.* 41, (1991), 245-256.
- [31] ABAQUS/Standard User's Manual, Version 5.4 (Hibbit Karlsson and Sorensen Inc., (1994)).
- [32] P. Suquet, Elements of homogenization theory for inelastic solid mechanics. in: E. Sanchez-Palencia, A. Zaoui eds., *Homogenization techniques for composite media* (Springer-Verlag, 1987), 194-278.
- [33] T.H.H. Pian, Derivation of element stiffness matrices by assumed stress distribution, *AIAA Journal* 2, (1964), 1333-1336.
- [34] S.N. Atluri, On the hybrid finite element model for incremental analysis of large deformation problems, *Int. Jour. Solids and Struct.* 9, (1973), 1177-1191.
- [35] S.N. Atluri, On some new general and complimentary energy theorems for the rate problems in finite Strain, classical elastoplasticity, *Jour. of Struct. Mech.* 8(1), (1980), 61-92.
- [36] P. Tong, T.H.H. Pian, and S.J. Lasry, A hybrid-element approach to crack problems in plane elasticity, *Int. Jour. Numer. Meth. Engrg.* 7, (1973), 197-308.
- [37] R. Piltner, Special finite elements with holes and internal cracks, *Int. J. Numer. Meth. Engrg.* 21, (1973), 197-308.
- [38] V. Tvergaard, Influence of voids on shear band instability under plane strain conditions, *Int. Jour. of Fracture* 17, (1981), 389-407.
- [39] V. Tvergaard, Material failure by void coalescence in localized shear bands, *Int. Jour. Solids Struct.* 18, (1982), 659-672.
- [40] N. Aravas, On the numerical integration of a class of pressure-dependent plasticity models *Int. Jour. Numer. Meth. Engrg.* 24, (1987), 1395-1416.
- [41] Y.H. Zhao and G.J. Weng, Theory of plasticity for inclusion and fiber-reinforced composite, in: G.J. Weng, M. Taya and H. Abe, eds., *Micromechanics and inhomogeneity, The Toshio Mura anniversary volume* (Springer-Verlag, 1989) 599-622.
- [42] D.F. Adams, Inelastic analysis of a unidirectional composite subjected to transverse normal loading, *J. Comp. Mater.* 4, (1970), 310-328.

## Chapter 5

# R-S Adapted Arbitrary Lagrangian-Eulerian Finite Element Method for Metal Forming Problems with Strain Localization

### Summary

In this chapter, an adaptive arbitrary Lagrangian-Eulerian (ALE) finite element method is developed for solving large deformation problems, with applications in metal forming simulation. The ALE mesh movement is coupled with *r-adaptation* of automatic node relocation, to minimize element distortion during the process of deformation. Strain localization is considered in this study through the constitutive relations for ductile porous materials, proposed by Gurson and Tvergaard. Prediction of localized deformation is achieved through a multi-level mesh superimposition method, termed as *s-adaptation*. The model is validated by comparison with established results and codes, and a few metal forming problems are simulated to test its effectiveness.

### 5.1 Introduction

Metal forming processes involve large plastic deformation of a workpiece to conform to the desired shape of the final product. For certain materials and processes severe localized deformation can lead to the formation of localization bands that may render a product defective. It is very important to accurately simulate such large strain problems and redesign the process to avoid the existence of these defects in the product. This paper is aimed at devising an accurate and efficient adaptive finite element model to simulate metal forming processes where there is a possibility of localized straining.

Such a simulation offers many challenges which should be systematically overcome to

minimize user intervention and experience. For example, these simulations often lead to severe mesh distortions and inadequate representation of the contact boundary for sharp edges in the worktools. The arbitrary Lagrangian-Eulerian (ALE) kinematic description has been successfully implemented in analysis of large deformation in solids [1, 2, 3, 4] to avoid these difficulties. In this description, the finite element mesh is decoupled from the underlying material, thereby creating a flexible mesh which can have a motion different from the material. The ALE description is used to overcome some of the problems encountered with a pure Lagrangian or a pure Eulerian type of mesh. Applications of the ALE description in metal forming problems have been examined by Ghosh et.al. [3, 4, 5], Huetink et. al. [2], Liu et. al. [6] among others.

Despite the flexibility of the finite element mesh in the ALE description, additional degrees of freedom introduced can pose difficulties while simulating complex problems. Controlling the motion of an ALE mesh requires a keen knowledge on the deformation process, and can adversely affect the simulation if improperly specified. Lack of knowledge on the sensitivity of solutions to the grid configuration can deteriorate the quality of solutions. Obstacles in the ALE method can be surpassed by combining with grid adaptation methods as a tool for reducing element distortions incurred through improper nodal positioning during deformation. The r-method of node relocation driven by element distortion is consequently coupled with the ALE description. This method has been applied to large deformation problems by Kikuchi and Torigaki [7] to reduce interpolation error.

Strain localization occur over very narrow regions in comparison with the overall dimensions of the workpiece. Since most constitutive relations are local in nature, the finite element predictions are extremely mesh sensitive. Consequently for many meshes with no apriori knowledge of localized regions, a simulation may not be capable to capture this phenomenon due to lack of appropriate resolution. A coarse mesh may completely miss the localized behavior in deformation. Various computational methods have evolved for simulating problems of strain localization without having to use extremely high resolution in the overall mesh. Important contributions among these include coupled finite element-spectral methods by Belytschko et. al. [23, 24], assumed stress based finite element by Atluri et al [25], [26], finite element with embedded localization zones and the enhanced strain elements by Simo and Armero [27, 28].

Adaptive finite element techniques have evolved to optimize the overall computational effort and provide a measure of reliability through error indicators. An important feature of the adaptive method is to use computed results a-posteriori for improving the quality of the solution. Various methods such as h-method of mesh refinement [8, 11, 12, 14], and p-method of mesh enrichment [15, 16] and r-method of node relocation [17] have been proposed. Of all methods the combined h-p method adaptation have been proven to be very effective for a wide class of problems with localization such as shock wave propagation and strain localization etc [20, 19, 13]. Fish et. al. [21, 22], have proposed a powerful adaptive multi-level mesh superposition method called the *s-method*. This method increases the resolution of the finite element analysis by superimposition of multiple levels of hierarchical elements in local

regions of high solution gradients. Fish and his coworkers have applied this method for a wide variety of problems, including linear elastic analysis of homogeneous and heterogeneous materials, laminated composites, and problems with cracks.

In this paper, the r-adapted ALE mesh is combined with multilevel s-adaptation to simulate metal forming problems featuring large elastic-plastic deformation with strain localization. Though the global mesh is ALE, the s-adapted mesh is made to follow the material. The material yield function is that for porous ductile materials, originally proposed by Gurson [31] and subsequently modified by Tvergaard [34, 36]. A perturbed Lagrangian formulation is executed for normal contact between workpiece and worktools.

## 5.2 Governing Equations

### 5.2.1 Basic equations in the ALE model

The arbitrary Lagrangian-Eulerian description introduces a reference configuration, consisting of a set of unconstrained grid points that undergo arbitrary spatial motion. Each point in this reference configuration is unambiguously represented by an invariant set of three independent coordinates  $\chi_i$ . The motion of points in the reference frame is denoted by the set of spatial coordinates  $x_i$ , and is expressed as arbitrary continuous functions of  $\chi_i$  and time  $t$ . The continuity and momentum equations in this description are respectively written as:

$$\frac{\partial(\rho J)}{\partial t}|_x + J \frac{\partial}{\partial x_i} (\rho(V_i - W_i)) = 0 \quad (5.1)$$

$$b_i + \frac{\partial \sigma_{ji}}{\partial x_j} = \rho \frac{\partial V_i}{\partial t}|_x + \rho(V_j - W_j) \frac{\partial V_i}{\partial x_j} \quad (5.2)$$

where  $\mathbf{W}$  refers to the velocity of a representative grid point,  $\mathbf{V}$  is the velocity of the material point coinciding with the grid at time  $t$ ,  $\sigma_{ij}$  is the Cauchy stress tensor,  $\rho$  is the density,  $b_i$  is the body force per unit volume and  $J$  is the Jacobian. Evaluation of process variables at nodal points in an ALE description requires an additional relation for updating variable values from material points to grid points. This equation correlates time derivatives of a material variable in fixed material coordinates to that in fixed referential coordinates. Thus, if  $\beta$  is a time dependent material variable, rates in the two coordinate systems are related as:

$$\frac{\partial \beta}{\partial t}|_x = \frac{\partial \beta}{\partial t}|_X + (W_k - V_k) \frac{\partial \beta}{\partial x_k} \quad (5.3)$$

where  $(\frac{\partial}{\partial t})|_x$  and  $(\frac{\partial}{\partial t})|_X$  refer to material and referential time derivatives respectively.

### 5.2.2 Constitutive Model

Material parameters play a very important role in the development of localized shear bands when subjected to quasi-static loading conditions. Localization has been proven to occur with features such as yield surface curvature [34], vertex effects [35], alignment of preferred

slip direction [40] and internal damage accumulation such as void volume fraction [34] etc. Since the metal forming simulations considered in this study are conducted under quasi-static conditions, a constitutive model featuring void nucleation, growth and coalescence is adopted. This model has been developed for porous ductile materials by Gurson [31] for void growth, and subsequently modified by researchers like Tvergaard [34, 36], Tvergaard and Needleman [35] etc for void growth and coalescence. Void nucleation model in this research is based on the model of Needleman and Rice [39]. Hom and McMeeking [37] have shown that the Gurson-Tvergaard model compares very well with complete 3-D finite element predictions for uniaxial tension, hydrostatic tension, and pure shear stress fields.

In this model an approximate yield condition is postulated in the form

$$\Phi(\sigma_{ij}, \sigma_f, f) = \frac{\sigma_e^2}{\sigma_f^2} + 2 f^* q_1 \cosh\left\{\frac{q_2 \sigma_{kk}}{2 \sigma_f}\right\} - (1 + q_3 f^{*2}) = 0 \quad (5.4)$$

where  $\sigma_e$  is the macroscopic effective stress,  $\sigma_f$  is the equivalent tensile flow stress representing actual microscopic stress state in the matrix material,  $\sigma_{kk}$  is the hydrostatic stress and  $f$  is the void volume fraction. The control function  $f^*$  is defined in terms of  $f$  as

$$\begin{aligned} f^*(f) &= f & \text{for } f \leq f_C \\ &= f_C + \frac{f_U^* - f_C}{f_F - f_C} (f_F - f_C) & \text{for } f > f_C \end{aligned}$$

where  $f_C$  is a critical value of void volume fraction ( $\sim 0.15$ ),  $f_U$  is the ultimate value of void volume fraction at fracture ( $\sim 0.25$ ), and  $f_U^* = f(f_F) = \frac{1}{q_1}$  is the volume fraction at which the material loses its stress carrying capacity [39]. The parameters  $q_1$ ,  $q_2$  and  $q_3$  are chosen to be 1.5, 1.0 and 2.25 respectively in this study as suggested in [33, 36]. The rate of evolution of  $f$  is taken to be

$$\dot{f} = \dot{f}_{growth} + \dot{f}_{nucleation} = (1 - f) D_{kk}^p + A \dot{\sigma}_f + B \frac{\sigma_{kk}}{3} \quad (5.5)$$

Void nucleation parameters  $A$  and  $B$ , can be obtained for cases like plastic strain controlled, stress controlled or both, as suggested in [39]. In this work only plastic strain controlled nucleation is considered for which

$$A = \left( \frac{1}{E_t} - \frac{1}{E} \right) \frac{f_N}{s \sqrt{2\Pi}} e^{-\frac{1}{2} \left( \frac{\epsilon_f^P - \epsilon_N}{s} \right)^2} \quad \text{and} \quad B = 0 \quad (5.6)$$

In equation (5.6),  $E_t$  corresponds to the elastic-plastic tangent modulus,  $f_N$  is the volume fraction of void nucleating particles,  $\epsilon_N$  is the mean nucleation strain and  $s$  is the corresponding standard deviation. Based on [32], values  $f_N = 0.04$ ,  $s = 0.1$  and  $\epsilon_N = 0.3$  are used in this study. The plastic part of the macroscopic rate of deformation tensor  $D_{ij}^P$  is obtained by normality rule as

$$D_{ij}^P = \Lambda \frac{\partial \Phi}{\partial \sigma_{ij}} \quad (5.7)$$

An additional assumption that the rate of equivalent work in matrix material equals the macroscopic work is made as:

$$\sigma_{ij} D_{ij}^p = (1 - f) \sigma_f \dot{\epsilon}_f^p \quad (5.8)$$

Finally, the rate independent elastic-plastic equation is formulated in a rotated Lagrangian system from considerations of stress-rate objectivity as explained in [3, 4] and is expressed as

$$\dot{t}_{ij} = E_{ijkl}(d_{kl} - d_{kl}^P) \quad (5.9)$$

where  $\dot{t}_{ij}$  is material derivative of a rotated Cauchy stress tensor  $t_{ij}$ , obtained by rotation of the Cauchy stress tensor  $\sigma_{ij}$  through  $R_{ij}$  which is derived from the polar decomposition of the deformation gradient tensor.  $d_{ij}$  is the corresponding rotated rate of deformation tensor, and  $E_{ijkl}$  is a fourth order elasticity tensor. Numerical integration of the elasto-plastic constitutive equations described above, is carried out using a technique based on the backward Euler integration rule, proposed by Aravas [38].

### 5.2.3 Contact Formulation

Only normal contact is considered in this study. The perturbed Lagrangian formulation ( PLF ) [41] is implemented to incorporate non-penetration constraint on the contact surface. This method combines the advantages of Lagrange multiplier method and the penalty function method to improve convergence and reduce the dependence on penalty parameter. It introduces a regularization of the Lagrange multiplier terms by a penalty term to a modified form of the potential energy as:

$$\Pi_\epsilon = \Pi_{pe} + \int_{\Gamma^c} \lambda \langle g \rangle d\Gamma - \frac{1}{2\epsilon} \int_{\Gamma^c} \lambda^2 d\Gamma \quad (5.10)$$

where  $\Pi_{pe}$  is the strain energy of the deforming body,  $\lambda$  is the Lagrange multiplier,  $g$  is a gap function representing distance between contacting surfaces and  $\Gamma^c$  is the contact surface.  $\epsilon$  is an arbitrary positive parameter and  $\langle \rangle$  is the MacCaulay operator. Equation ( 5.10 ) approaches the Lagrange multiplier method as  $\epsilon$  tends to infinity. The contact pressure is assumed to be constant in each contact segment, yielding

$$\lambda_s = \frac{\epsilon}{2}(g_1 + g_2) \quad (5.11)$$

Here  $g_1$  and  $g_2$  are the gaps at the edges of the contact segment as shown in figure 5.1. This results in an averaged form of the non-penetration constraint (  $g > 0$  ) for each contact segment.

During the deformation process, when two surfaces come in contact as shown in figure 5.1, the following steps are implemented to incorporate the contact condition (5.11).

1. Drop a perpendicular from node (B) of surface 1 onto segment (ab) of surface 2 and identify the intersection (f).
2. Similarly drop a perpendicular from node (b) on surface 2 onto segment (BC) of surface 1 and identify the intersection (F).

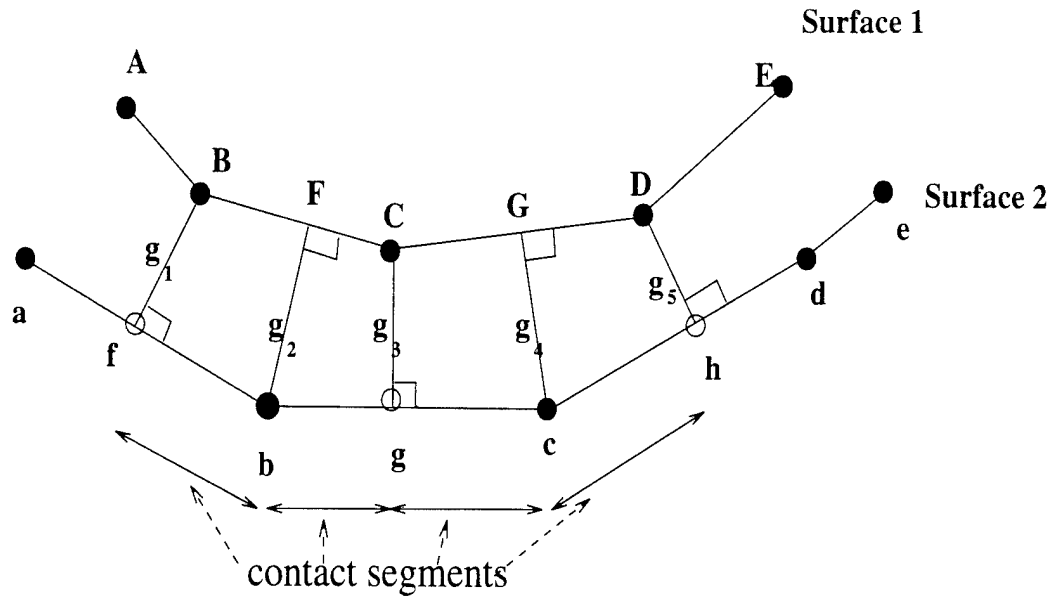


Figure 5.1: Discretization of the contact interface into contact segments.

Contact segments for surface 2 are  $fb$ ,  $bg$ ,  $gc$ ,  $ch$ , etc. The corresponding contact segments for surface 1 are  $BF$ ,  $FC$ ,  $CG$ ,  $GD$  etc. The gap functions  $g_1, g_2 \dots$  are shown in figure 5.1 from which contact pressure on each segment is evaluated.

### 5.3 Node Relocation (R-Adaptation)

In order to reduce element distortion during complex large deformation of the workpiece in metal forming problems, the r-method of node relocation is coupled with the flexible ALE description. In this method, the motion of ALE nodal points is guided by parameters determined from an element distortion criterion, based on an inverse mapping algorithm as suggested in [42].

For isoparametric QUAD4 elements, a measure of distortion can be the included angle  $\theta$  between the adjacent edges. However in some cases, the isoparametric transformation resulting from overall element distortion is not proper, even though  $\theta$  is less than  $180^\circ$ . This can be averted by choosing to represent distortion through an inverse mapping as suggested in [42]. The assumption in this technique is that the number of iterations required for convergence of the inverse mapping process from  $(x, y)$  to  $(\xi, \eta)$  coordinates in equation (5.12) characterizes element distortion.

$$\begin{Bmatrix} \xi \\ \eta \end{Bmatrix} = \begin{bmatrix} \sum_i x_i \xi_i & \sum_i x_i \eta_i \\ \sum_i y_i \xi_i & \sum_i y_i \eta_i \end{bmatrix}^{-1} \begin{Bmatrix} 4x - \sum_i x_i(1 + \xi_i \eta_i \xi \eta) \\ 4y - \sum_i y_i(1 + \xi_i \eta_i \xi \eta) \end{Bmatrix} \quad (5.12)$$

where  $x_i, y_i$  and  $\xi_i, \eta_i$  are node coordinates in the physical and master domains respectively for QUAD4 elements with bilinear shape functions. Equation (5.12) is solved iteratively for

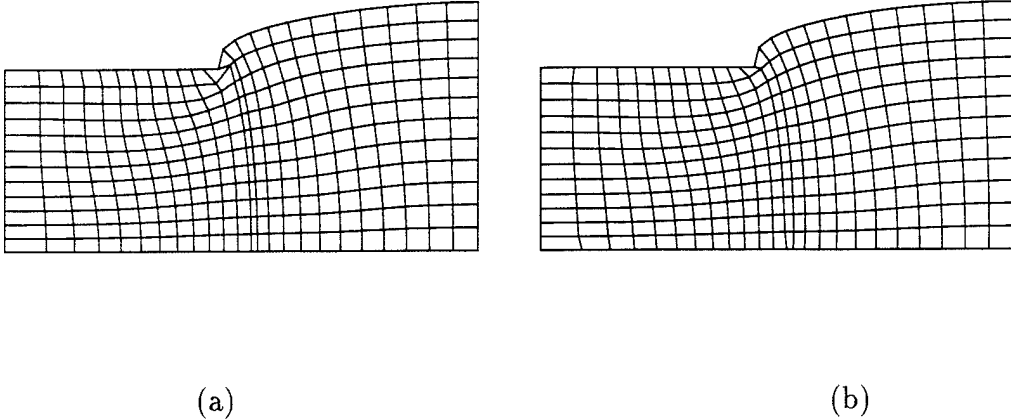


Figure 5.2: Backward extrusion at 15% deformation (a) without node relocation (b) with node relocation.

$(\xi, \eta)$ . Node relocation is enforced with an ALE node if the difference between two consecutive absolute values of  $\xi$  or  $\eta$  exceeds 1% after 20 iterations.

A weighted averaging formula is then used to determine the new node location as

$$x = \frac{\sum_{k=1}^n \frac{1}{J_k} x_k}{\sum_{k=1}^n \frac{1}{J_k}}, \quad y = \frac{\sum_{k=1}^n \frac{1}{J_k} y_k}{\sum_{k=1}^n \frac{1}{J_k}} \quad (5.13)$$

where  $n$  is the total number of surrounding elements sharing the node to be relocated and  $x_k, y_k$  are the centroidal coordinates of the neighboring element  $k$ .  $J_k$  is the Jacobian in element  $k$  at the node to be relocated, whose inverse is used as a weighting function. This is seen to be more effective than relocation based on mean of centroidal coordinates, suggested in [42], because it adds the influence of the inverse Jacobian to the relocation.

The effect of this r-adaptation with ALE nodes are seen in a backward extrusion simulation illustrated in figure 5.2. In this problem the ALE node at the punch edge is made to follow this edge with progress of deformation. Existence of Lagrangian nodes in the region around the corner ALE node, gives rise to element distortion which are easily overcome by this node relocation scheme.

## 5.4 Adaptive Mesh Superposition With S-Method

The multi-level mesh superimposition method termed as the s-method, proposed by Fish [21, 22], has the potential of increasing local resolution in the solution by overlaying a portion of a finite element mesh with a locally enriched mesh. Such regions may be only a very small part of an element, and subsequent levels of enrichment may be added based on errors

indicators at existing levels. This method is implemented to predict regions of localized deformation in metal forming simulations by combining the global-local methodologies in critical regions with the feedback approach of adaptive techniques. Level 0 corresponds to the global mesh and levels 1,2 etc. correspond to the higher levels of adapted domain. The extent of adapted domains at each level (1,2 ..) decrease with the increase in level number. Additionally higher level (1,2,..) meshes at each level may grow or diminish with deformation. The level 0 mesh in this study can be ALE, while the higher level adapted meshes are necessarily Lagrangian to depict material localization. Consequently the higher level meshes may convect through the level 0 mesh.

S-adaptation in this study is initiated when unacceptable local errors or steep solution gradients are identified in a existing level mesh. Only 1 level of s-adapataion is explained in the ensuing discussion. Figure 5.3 shows global (level 0) and local (level 1) meshes, where  $\Omega$  is the domain of the global mesh with a boundary  $\Gamma$ .  $\Omega^L (\subset \Omega)$  corresponds to the locally enriched region discretized into a local mesh, and  $\Gamma^{GL}$  is the interface between the global and local domains such that  $\Gamma^{GL} \cap \Gamma = 0$ . The solution in the entire domain is obtained by superimposing incremental displacements ( $\Delta\mathbf{u}$ ) from the global mesh onto a local displacement field ( $\Delta\mathbf{u}^L$ ) defined on  $\Omega^L$  within an increment. The resulting kinematic relations in the incremental analysis are

$$\Delta\mathbf{u} = \begin{cases} \Delta\mathbf{u}^G + \Delta\mathbf{u}^L & \text{on } \Omega^L \subset \Omega \\ \Delta\mathbf{u}^G & \text{on } \Omega^G, \Omega^G \subset \Omega, \Omega^G \cap \Omega^L = 0 \end{cases}$$

where

$$\Delta\mathbf{u}^L = 0 \quad \text{on } \Omega^G \quad (5.14)$$

$$\Delta\mathbf{u}^L = 0 \quad \text{on } \Gamma^{GL} \quad (5.15)$$

and

$$\Delta\mathbf{u}^G + \Delta\mathbf{u}^L = \Delta\mathbf{u}^P \quad \text{on } \Gamma^u \quad (5.16)$$

where  $\Gamma^u$  is the prescribed displacement boundary. In this analysis, the displacement boundary conditions is considered to be accommodated by the global mesh, leaving  $\Delta\mathbf{u}^L = 0$  on  $\Gamma^u$ . The global and local incremental displacement fields are discretized using standard  $C^0$  continuous shape functions

$$\Delta u_i^G = N_A^G \Delta u_{iA}^G \quad (5.17)$$

$$\Delta u_k^L = N_A^L \Delta u_{kA}^L \quad (5.18)$$

where  $\Delta u_{iA}^G$  and  $\Delta u_{kA}^L$  are nodal displacement increments. The compatibility condition ( 5.15), is enforced by the relation

$$\Delta u_{kA}^L = 0 \quad \text{on } \Gamma^{GL} \quad (5.19)$$

### 5.4.1 Finite element formulations for global local analysis

For a quasi-static process using a backward Euler time integration scheme, the principle of virtual work is written in the final grid configuration in the  $n$ -th increment as

$$\int_{\Omega_{n+1}} \sigma_{ij} \frac{\partial \delta u_i}{\partial x_j} d\Omega = \int_{\Omega_{n+1}} b_i \delta u_i d\Omega + \int_{\Gamma_{n+1}} t_i \delta u_i d\Gamma \quad (5.20)$$

The equation of virtual work is solved for the displacements and consequently the stresses, using an iteration algorithm. For this purpose, it is convenient to represent equation ( 5.20) as a scalar valued function  $G$  in terms of global-local variables of the form

$$\begin{aligned} G(\Delta \mathbf{u}, \delta \mathbf{u}) &= \int_{\Omega_{n+1}^G} \sigma_{ij} (\mathbf{u}_n + \Delta \mathbf{u}^G) \frac{\partial \delta u_i^G}{\partial x_j} d\Omega + \int_{\Omega_{n+1}^L} \sigma_{ij} (\mathbf{u}_n + \Delta \mathbf{u}^G + \Delta \mathbf{u}^L) \frac{\partial \delta (u_i^G + u_i^L)}{\partial x_j} d\Omega \\ &- \int_{\Omega_{n+1}^G} b_i \delta u_i^G d\Omega - \int_{\Omega_{n+1}^L} b_i \delta (u_i^G + u_i^L) d\Omega \\ &- \int_{\Gamma_{n+1}^G} t_i \delta u_i^G d\Gamma - \int_{\Gamma_{n+1}^L} t_i \delta (u_i^G + u_i^L) d\Gamma \\ &= \int_{\Omega_{n+1}} \sigma_{ij} (\mathbf{u}_n + \Delta \mathbf{u}^G + \Delta \mathbf{u}^L) \frac{\partial \delta u_i^G}{\partial x_j} d\Omega + \int_{\Omega_{n+1}^L} \sigma_{ij} (\mathbf{u}_n + \Delta \mathbf{u}^G + \Delta \mathbf{u}^L) \frac{\partial \delta u_i^L}{\partial x_j} d\Omega \\ &- \int_{\Omega_{n+1}} b_i \delta u_i^G d\Omega - \int_{\Omega_{n+1}^L} b_i \delta u_i^L d\Omega \\ &- \int_{\Gamma_{n+1}} t_i \delta u_i^G d\Gamma - \int_{\Gamma_{n+1}^L} t_i \delta u_i^L d\Gamma \end{aligned} \quad (5.21)$$

Consistent linearization by obtaining the directional derivative of  $G$  in equation ( 5.21) along incremental displacement vector  $\Delta \mathbf{u}$ , is required to set up the tangent stiffness matrix. The quasi-Newton family of update algorithms, such as BFGS or Broyden's algorithms requiring a first approximation to the stiffness, are employed for solving the equation ( 5.21). These methods iteratively update the stiffness matrix to provide a secant approximation to the stiffness matrix. The equations once assembled has the following structure

$$\begin{bmatrix} [K]^G & [K]^C \\ [K]^C & [K]^L \end{bmatrix} \begin{Bmatrix} \Delta u^G \\ \Delta u^L \end{Bmatrix} = \begin{Bmatrix} \Delta F^G \\ \Delta F^L \end{Bmatrix} \quad (5.22)$$

where

$$[K]^G = \int_{\Omega_{n+1}} \frac{\partial N_j^G}{\partial x_i} \frac{\partial \sigma_{ij}}{\partial \epsilon_{lk}} \frac{\partial N_k^G}{\partial x_l} d\Omega$$

$$[K]^C = \int_{\Omega_{n+1}^L} \frac{\partial N_j^G}{\partial x_i} \frac{\partial \sigma_{ij}}{\partial \epsilon_{lk}} \frac{\partial N_k^L}{\partial x_l} d\Omega$$

$$[K]^L = \int_{\Omega_{n+1}^L} \frac{\partial N_j^L}{\partial x_i} \frac{\partial \sigma_{ij}}{\partial \epsilon_{lk}} \frac{\partial N_k^L}{\partial x_l} d\Omega$$

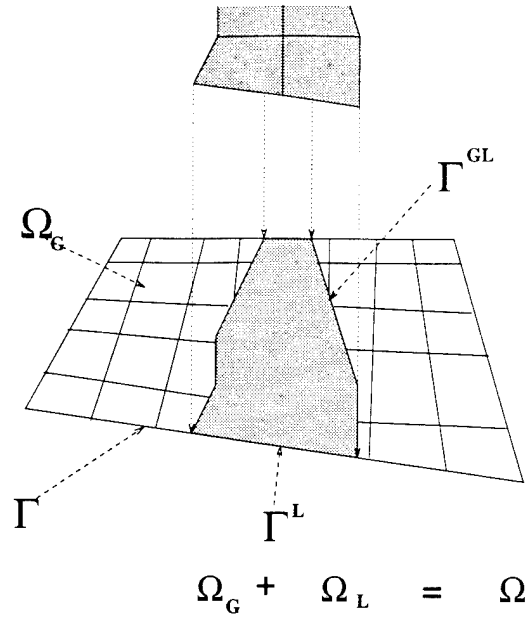


Figure 5.3: An example of the original mesh and the superimposed patch of higher-order element.

$$\{\Delta F^G\} = \int_{\Omega_{n+1}} b_i N_i^G d\Omega + \int_{\Gamma_{n+1}} t_i N_i^G d\Gamma - \int_{\Omega_{n+1}} \sigma_{ij} (\mathbf{u}_n + \Delta \mathbf{u}^G + \Delta \mathbf{u}^L) \frac{\partial N_i^G}{\partial x_j} d\Omega$$

$$\{\Delta F^L\} = \int_{\Omega_{n+1}^L} b_i N_i^L d\Omega + \int_{\Gamma_{n+1}^L} t_i N_i^L d\Gamma - \int_{\Omega_{n+1}^L} \sigma_{ij} (\mathbf{u}_n + \Delta \mathbf{u}^G + \Delta \mathbf{u}^L) \frac{\partial N_i^L}{\partial x_j} d\Omega$$

The hierarchical structure in the stiffness matrix is realized in equation ( 5.22).

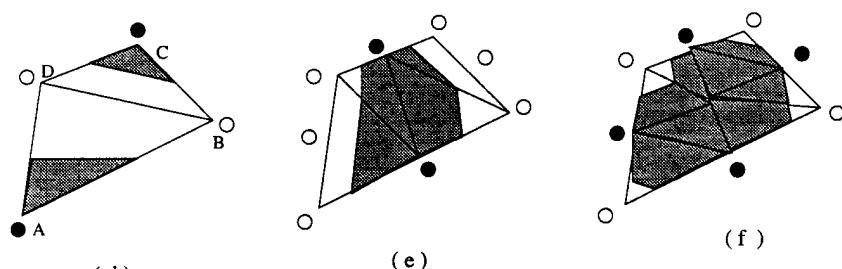
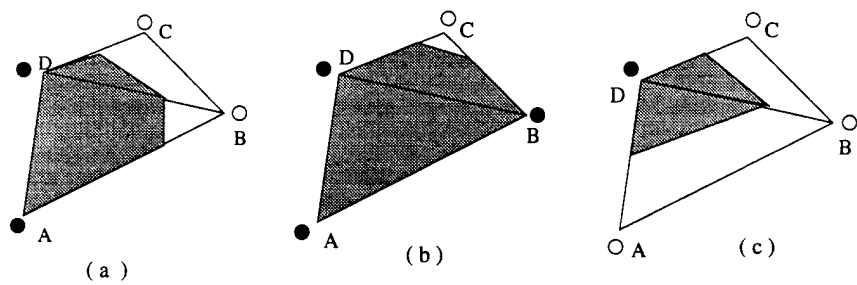
#### *Hierarchical Shape Functions for s-adapted domain*

Level 0 mesh is created using bilinear QUAD4 shape functions, while higher level meshes use hierarchical shape functions. In this paper two levels of s-adaptation is considered using upto fourth order hierarchical shape functions. Higher order hierarchical shape functions are developed as a tensor product of integrals of Legendre polynomials. The  $j$ -th order hierarchical shape functions in one dimension are generated in the following fashion:

$$\phi_j(\xi) = \sqrt{\frac{j+1}{2}} \int_{-1}^{\xi} P_{j-1}(x) dx \quad (5.23)$$

where  $P_j$  is the Legendre polynomial of order  $(j)$ . Detailed discussion on the development of hierarchical shape functions are presented in [29, 22].

The shape functions used in two dimensions can be separated into a set of nodal, side and internal shape functions. These are dependent on whether the set corresponds to Lagrangian or Serendipity families. The space spanned by the hierarchical shape functions for



○ Node with  $\eta$  value below the cutoff

● Node with  $\eta$  value above the cutoff

Figure 5.4: Various possibilities in constructing s-adapted subregions in an element.

any order of interpolation is the same as that spanned by Lagrangian shape functions for the same order. Two additional issues are systematically addressed in the construction of hierarchical shape functions. They are: (i) the set of shape functions be geometrically isotropic, i.e., stays the same irrespective of orientation of the local coordinate system, and (ii) compatibility of displacement modes arising from odd order hierarchical interpolation functions belonging to adjacent elements along a common edge, are systematically addressed. This has been described in details in [30]. In this work, level 1 mesh is modeled with quadratic hierarchical shape functions and level 2 mesh is modeled with cubic or quartic hierarchical shape functions.

#### 5.4.2 Construction of superimposed domains

Generation of superimposed element patches require a criteria for dissecting global elements, and elements at subsequent levels. This is done by a method based on the gradients of equivalent plastic strains defined as  $\nabla \epsilon^{ep} = \sqrt{(\frac{\partial \epsilon^{ep}}{\partial x})^2 + (\frac{\partial \epsilon^{ep}}{\partial y})^2}$ . It gives a strong indication of regions of localized straining in large deformation problems. The following steps are sequentially implemented in constructing the s-adapted domain.

- Using the superconvergent patch recovery technique suggested in [9, 10], gradients of the equivalent plastic strain  $\nabla \epsilon^{ep}$  are evaluated at element nodal points. A parameter  $\eta$  defined in equation (5.24) is evaluated at each node.

$$\eta = \frac{\nabla \epsilon^{ep} - (\nabla \epsilon^{ep})_{minimum}}{(\nabla \epsilon^{ep})_{maximum} - (\nabla \epsilon^{ep})_{minimum}} \quad (5.24)$$

where  $(\nabla \epsilon^{ep})_{minimum}$  and  $(\nabla \epsilon^{ep})_{maximum}$  are the minimum and maximum values of the gradient at all nodal points in  $\Omega$ .

- A cutoff value,  $\eta_{cutoff}$  is specified, based on the desired levels. In general a value  $\eta_{cutoff} = 0.5$  is prescribed in this work. Any node having a value greater than  $\eta_{cutoff}$  is overlaid with superimposed elements.
- Every quadrilateral element in the global mesh is subdivided into two triangles. This eliminates the possibility of generating polygons with more than four sides.
- If both the nodes on a particular element edge are above  $\eta_{cutoff}$ , both are selected as nodes for the superimposed element, e.g. edge AD in figure 5.4(a). If neither of the nodes on the element edge is above  $\eta_{cutoff}$ , no points are selected from that element edge (edge BC in figure 5.4(a)). If one of the nodes is above  $\eta_{cutoff}$  and the other is below (edge AB in figure 5.4(a)), a linear interpolation is used to determine the location of the new node in the s-domain. The linear interpolation is used only when adapting from level 0 to level 1.
- When s-adapting from level 1 to level 2, the above procedure is modified to incorporate the quadratic variation of state variables along element boundaries. In this case,  $\eta$  values are determined for midside nodes in addition to the corner nodes. If  $\eta$  for all

the mid side nodes are greater than  $\eta_{cutoff}$ , but for corner nodes are less than  $\eta_{cutoff}$ , then a level 1 element is subdivided into 4 quadrilaterals as shown in figure 5.4(e). If  $\eta$  for only two opposite mid side nodes is greater than  $\eta_{cutoff}$ , but  $\eta$  for other nodes are less than  $\eta_{cutoff}$ , then the level 1 element is subdivided into 2 quadrilaterals as shown in figure 5.4(f).

- If the mesh generation procedure creates two adjacent triangular elements sharing a common edge, as shown in figure 5.4(c), a single condensed quadrilateral is formed ensuring that the included angles are all less than  $180^\circ$ .

In metal forming simulations, zones of strain concentration may move considerably and new zones of high strains appear with deformation. Consequently it is necessary to change the extent of superimposed domain at a given level, together with the addition of new levels throughout the process of deformation.

#### 5.4.3 Aspects of Numerical Integration

Numerical integration of the local terms  $[K^L]$  and coupling terms  $[K^C]$  in the stiffness matrix (equation (5.22)) is performed using the conventional Gauss quadrature on the superimposed domain. For example, corresponding to a quadratic hierarchical element, terms in  $[K^L]$  are approximately of order 4 and consequently  $3 \times 3$  Gauss integration rule is used for  $[K^L]$  and  $[K^C]$ . The global terms  $[K^G]$  are integrated using  $[\bar{B}]$  based selective reduced integration. During the evaluation of stresses in  $[K^C]$  and  $[K^L]$  at integration points like C of the hierarchical element, and  $[K^G]$  at integration points like A of the global element (figure 5.5), the incremental strain contribution from the superimposed incremental displacement field and the global displacement field are added.

### 5.5 Numerical Examples

Numerical examples using the techniques developed in this paper are divided into two sets. The first two problems are aimed at testing and validating the effectiveness of the numerical model with s-adaptation. Two metal forming examples are then conducted using the r-s adapted ALE model. The material used for all examples is ASTM-A514 steel with the following properties:

Youngs modulus  $E = 210.0 \times 10^9$  MPa, Poisson ratio  $\nu = 0.30$  and initial yield stress  $\sigma_0 = 6.93 \times 10^8$  MPa. The initial void volume fraction is  $f_0 = 0$ , the ultimate void volume fraction is  $f_U = 2/3$  and the critical void volume fraction is  $f_C = 0.15$ . Plastic strain controlled void nucleation criteria is used for which  $f_N = 0.04$ ,  $s = 0.1$  and  $\epsilon_N = 0.3$ , as suggested by Tvergaard [32]. The parameters in the Gurson-Tvergaard yield function in equation (5.4) are taken to be  $q_1 = 1.5$ ,  $q_2 = 1.0$  and  $q_3 = 2.25$ . The uniaxial *true stress* ( $\sigma$ ) – *logarithmic strain* ( $\epsilon$ ) relation is expressed using a power law as:

$$\epsilon = (\sigma_0/E)(\sigma/\sigma_0)^n \quad (5.25)$$

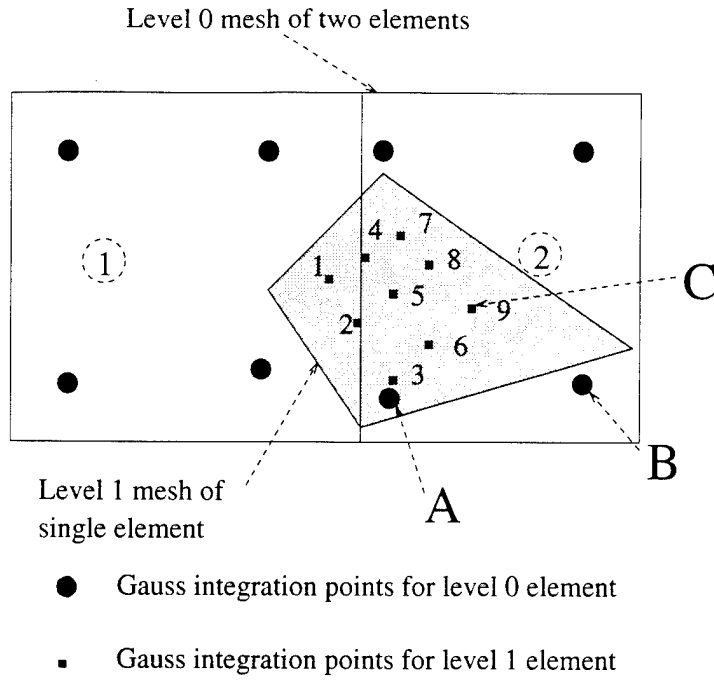


Figure 5.5: Numerical integration scheme.

where the exponent  $n$  is assigned a value 10.

### 5.5.1 Plane strain tension test with surface imperfection

In this example a plane strain tension test of a plate with surface imperfection is analyzed. This example has been solved using an extremely refined mesh by Tvergaard [32] and Heinlein [43]. Figure 5.6 shows the entire plate and the region considered for finite element modeling. The plate is pulled in the lateral tension by applying displacement increments to a maximum of 40% engineering strain. An imperfection is assumed as a geometric surface wave in the form of a cosine function, given in figure 5.6, with an amplitude  $\delta/l = 0.005$ ,  $h = 7$  mm, and  $l = 1$  mm.

The simulation is executed using a coarse mesh and a refined mesh of 495 and 1936 QUAD4 elements respectively. Figure 5.7 shows the deformation patterns in the refined mesh with increasing values of average logarithmic strain  $\epsilon_a$ . It is observed that deviations from uniform straining are increasingly prominent with increased straining. The mesh shows pronounced localized deformation at strain levels of 0.336. Figure 5.8 shows the contour plots of equivalent plastic strain and void volume fraction at  $\epsilon_a = 0.336$ . The localized plastic strain and void volume fraction in the bands are clearly observed in this figure. The corresponding deformation patterns and contour plots for the coarse mesh are depicted in figures 5.9 and 5.10 respectively. The mesh does not indicate any sign of localized deformation, and the contour plots are very diffused with no localization of values. Comparison of figures

5.8 and 5.10 clearly indicate that the peak values of  $\epsilon^{ep}$  and  $f$  are grossly under-represented with the coarse mesh. Mesh sensitivity of the localization phenomenon with the constitutive models is apparent in this problem.

To overcome limitations of the coarse mesh in representing localization, a 2 – *level* s-adaptation is activated. The global mesh (level 0) of 495 elements is superimposed with level 1 (grey) and level 2 (black) adapted regions, as illustrated in figures 5.11. The simulation adaptively superimposes the first level (level 1) of hierarchical quadratic elements at  $\epsilon_a = 0.182$ , at which the parameter  $\eta$  exceeds 0.50 (equation (5.24)). It is important that the superposition process is started before the localization process begins, failing which the values of localized strains will be significantly lower. Level 2 domain of quartic hierarchical elements is superimposed at  $\epsilon_a = 0.2231$ , at which  $\eta$  exceeds 0.70. It can be seen that level 2 region is significantly narrower than the level 1 region indicating convergence to the localized bands. The corresponding contour plots at  $\epsilon_a = 0.336$  are shown in figure 5.12. A comparison of figures 5.8 and 5.12 shows that the results of coarse mesh with s-adaptation are in very good agreement with those for the highly refined mesh. Though the localized band with refined mesh is narrower than that with level 2 s-adaptation, it is expected that subsequent levels can reduce the discrepancy. In figure 5.13, a plot of the maximum principal logarithmic strain at a point A as a function of increasing average strain  $\epsilon_a$  is shown. Results obtained with the refined mesh, coarse mesh, coarse mesh with s-adaptation are compared in this plot. The same results are also generated using ABAQUS with the same refined mesh. It is seen that s-adaptation can drastically reduce the error incurred with a coarse mesh alone, especially at higher values of  $\epsilon_a$ , thereby producing acceptable results in comparison with refined models.

### 5.5.2 Tension test of a notched specimen

In this example a notched tensile bar under plane strain uniaxial stress conditions is analyzed as shown in figure 5.14(a). The specimen is pulled to a maximum of 6% engineering strain in the vertical direction. Only the upper right quarter of the problem is modeled from symmetry considerations. The problem is simulated using a coarse mesh of 450 QUAD4 elements, a refined mesh of 1800 Quad4 elements as shown in figure 5.14(b), and a coarse mesh with s-adaptation shown in figure 5.16. Figure 5.14(b) shows the refined mesh configuration at 6% deformation, for which the contour plots of equivalent plastic strain and void volume fraction are depicted in figure 5.15. Figure 5.16 shows the deformed mesh configurations with level 1(grey) and level 2(black) s-adaptations at 3.2% and 6% strains respectively, corresponding to  $\eta > 0.5$ . Contour plots are depicted in figure 5.17. From figures 5.17 and 5.15, it is seen that the peak values of equivalent plastic strain and void volume fraction with s-adapted coarse mesh are within 4% and 10% of the refined mesh predictions. This is as opposed to 24% and 46% difference with the coarse mesh alone. The evolution of equivalent stress at point A (figure 5.14(a)) is plotted as a function of % elongation in figure 5.18(a). This plot shows that though the stress concentration initially increases with strain, it drops off quickly to very low values with development of localized straining near the notch. The corresponding plot (figure 5.18(b)) of void volume fraction shows a significant increase in the local void

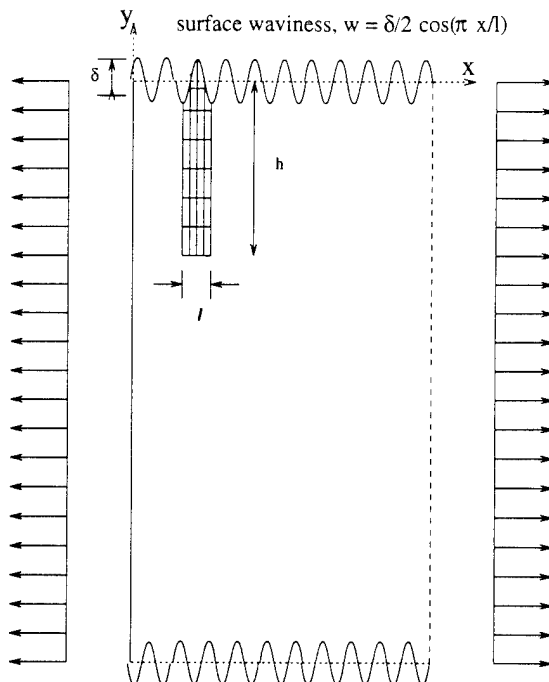


Figure 5.6: Plane strain tension test of a surface region with imperfection

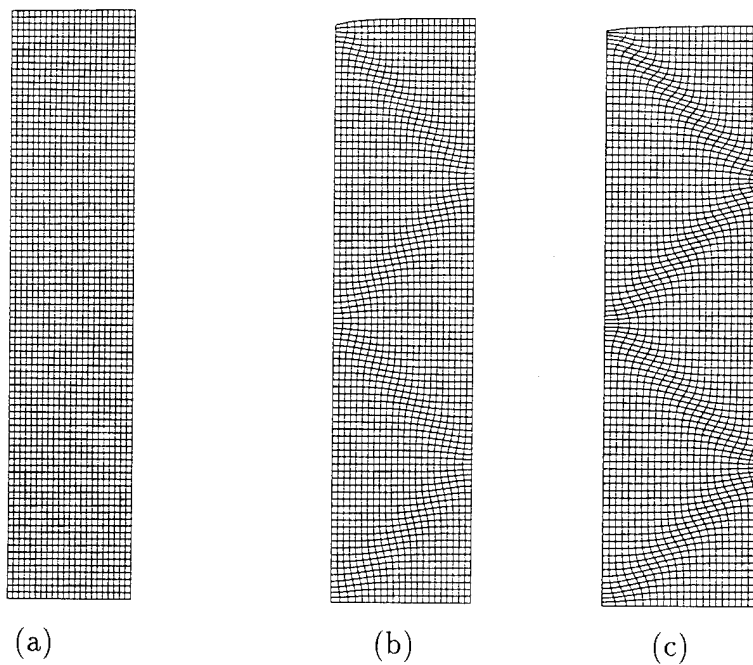


Figure 5.7: Refined mesh configurations at average strain levels of (a) 0.216 (b) 0.277 (c) 0.336

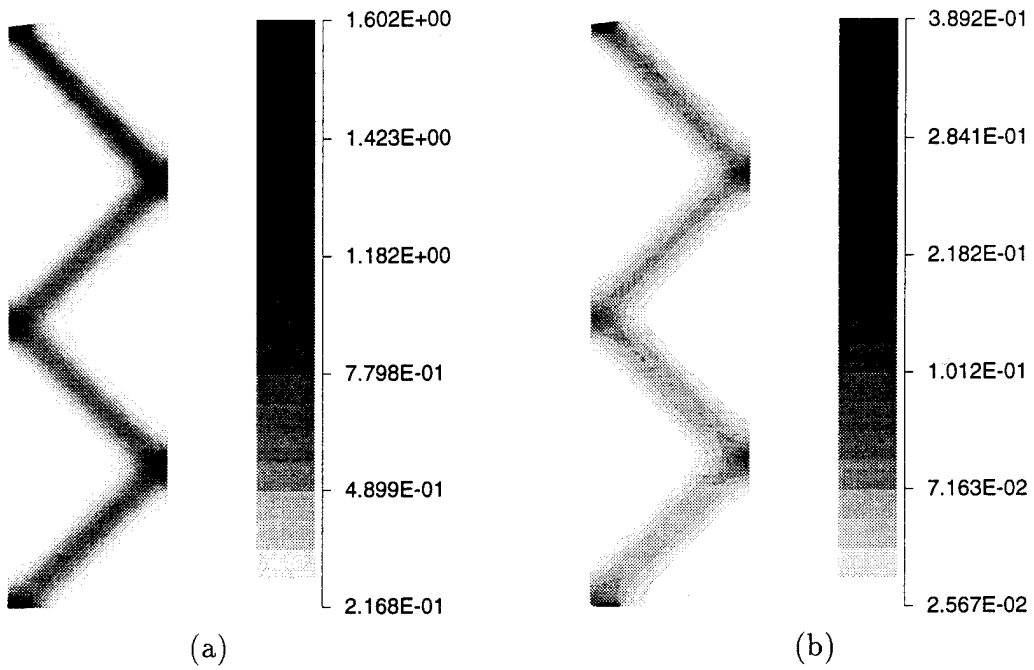


Figure 5.8: Contour plots for (a) equivalent plastic strain and (b) void volume fraction at average strain of 0.336

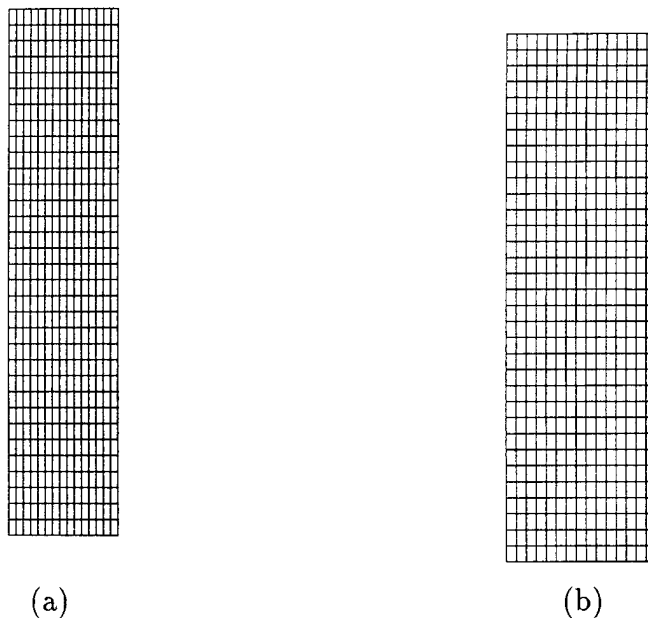


Figure 5.9: Coarse mesh configurations at average strain levels of (a) 0.216 (b) 0.336

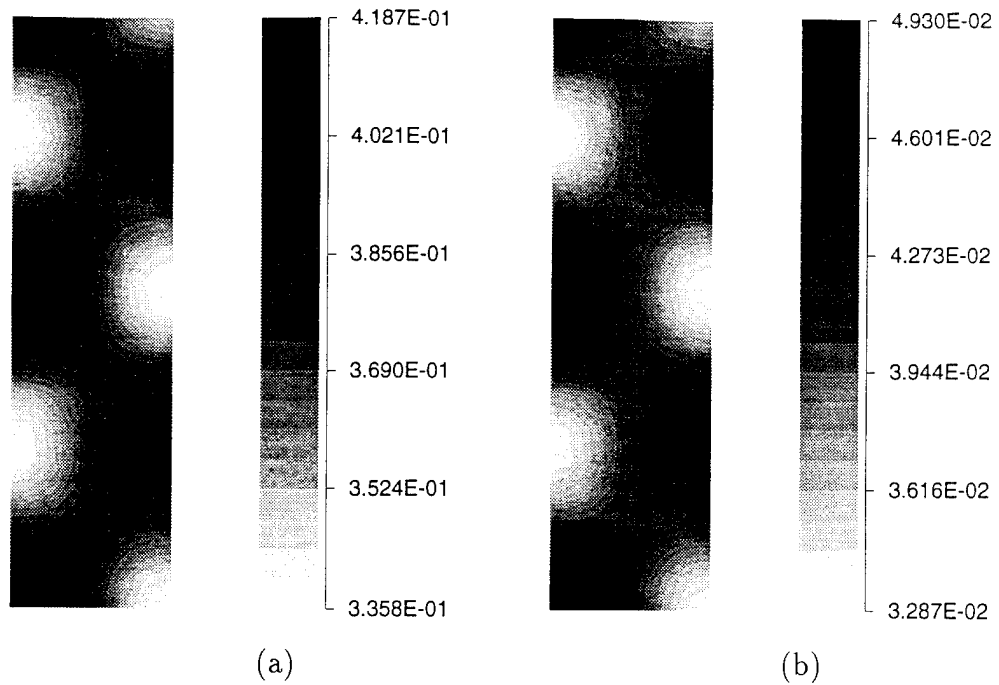


Figure 5.10: Contour plots for (a) equivalent plastic strain and (b) void volume fraction at average strain of 0.336

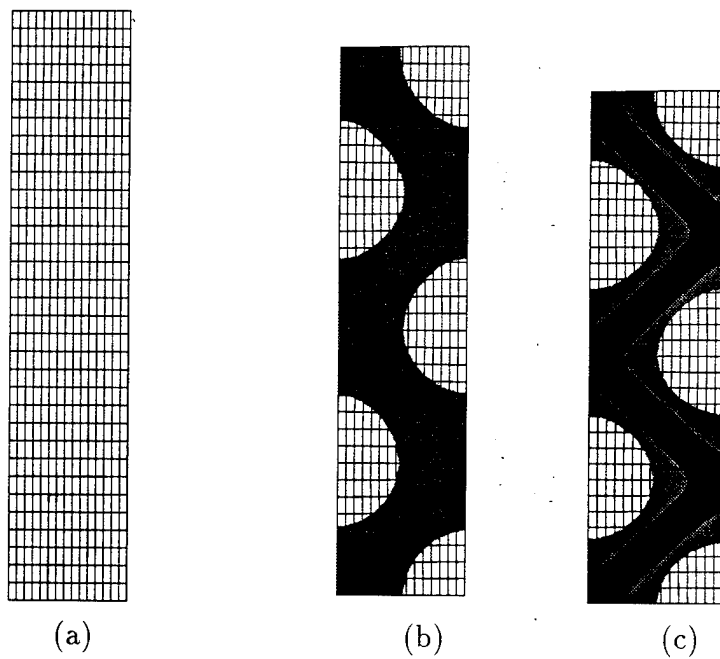


Figure 5.11: Coarse mesh configurations with s-adaptation. (a) initial global mesh (b) with level 1 of quadratic elements, at average strain of 0.221 (c) with level 2 of quartic elements, and level 1 of quadratic elements, at an average strain of 0.336

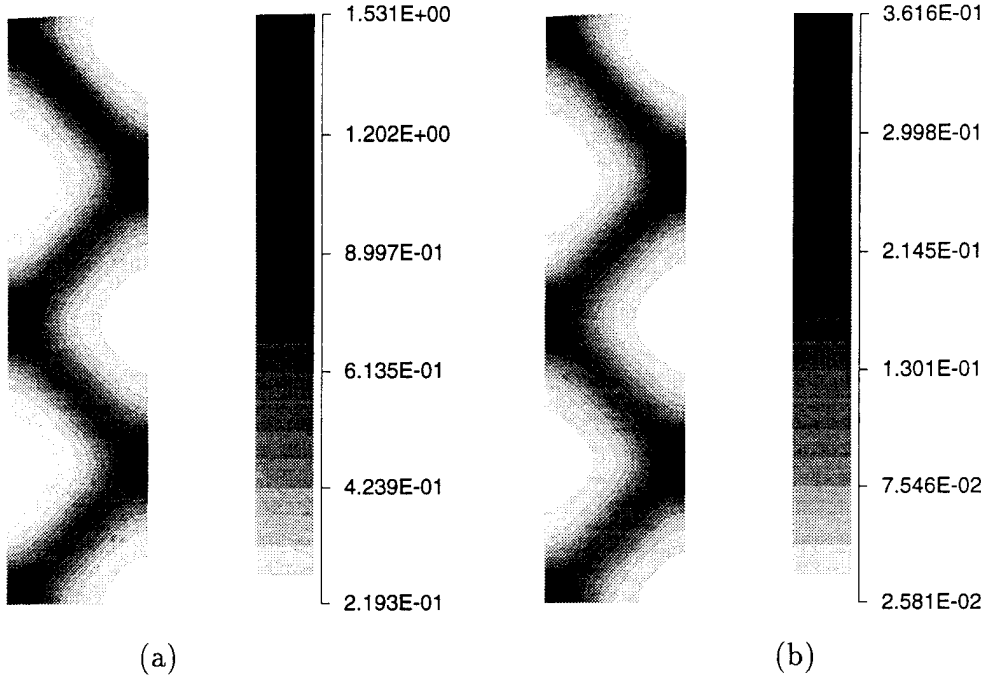


Figure 5.12: Contour plots for (a) equivalent plastic strain and (b) void volume fraction at average strain of 0.336

volume at A.

### 5.5.3 Metal forming examples

Plane strain analysis is carried out for two metal forming problems. Each of the problems are solved using the ALE mesh with r-adaptation at three different resolutions viz. (a) coarse mesh, (b) coarse mesh with s-adaptation and (c) refined mesh. Only normal contact is assumed in these simulations.

#### Backward Extrusion

In this problem, a rigid square punch is made to back extrude a rectangular billet inside a rigid die as shown in figure 5.19. The advantage of the ALE description for surface nodes that contact at the edges of the punch, is realized in this example, since the Lagrangian description would lead to severe compromises in accuracy [3, 5]. The punch is moving vertically down at a speed of 50 cm/sec for 0.026 seconds. Faces DA, AB and CD are contact surfaces on the rigid punch, EF and GH are contact faces on the die. Only the right half of the problem is modeled because of the symmetry. The effect of r-adaptation in this problem is discussed in section 3. If all the nodes under the punch are ALE nodes, which have no relative motion with respective points on the punch, serious mesh distortion can ensue as shown in figure 5.20. Even r-adaptation scheme cannot avert this problem, since elements become excessively elongated. This is overcome with by a special scheme as follows.

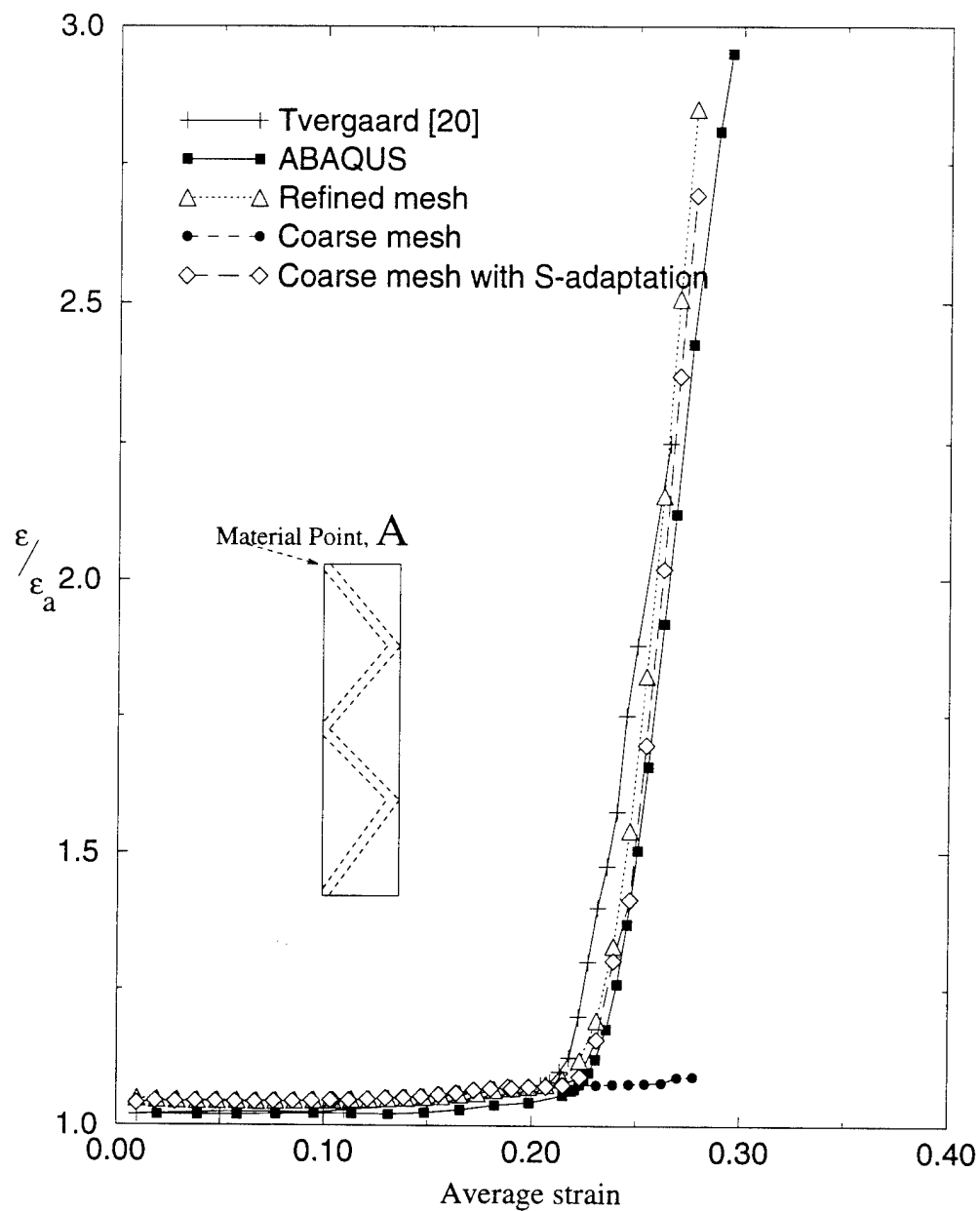


Figure 5.13: Maximum principal logarithmic strain,  $\epsilon$ , at a material point A vs average strain,  $\epsilon_a$ .

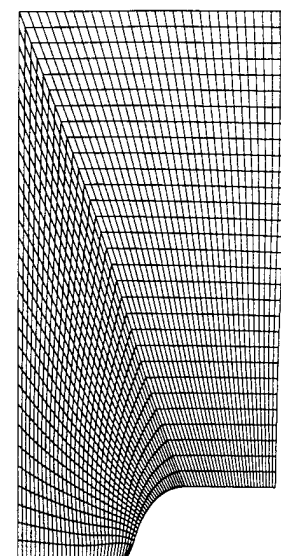
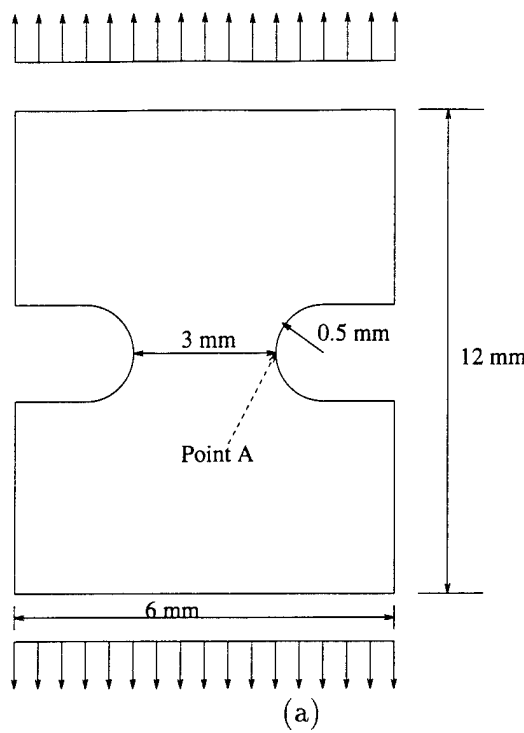


Figure 5.14: (a) Notched tension specimen (b) Refined mesh configuration at 6% elongation

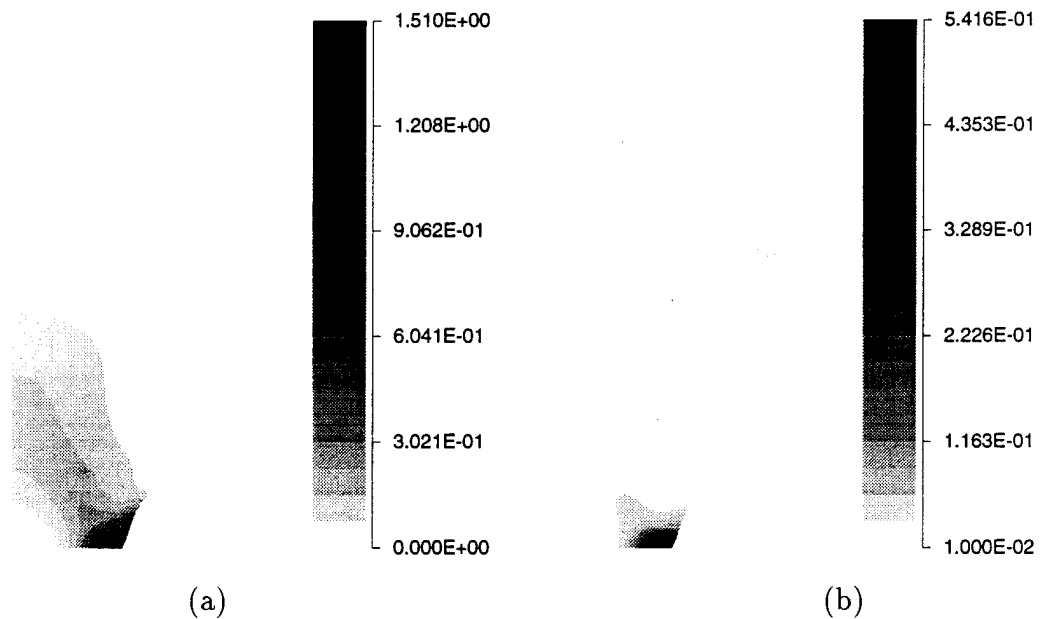


Figure 5.15: Contour plots for (a) equivalent plastic strain and (b) void volume fraction at 6.0% elongation for the refined mesh

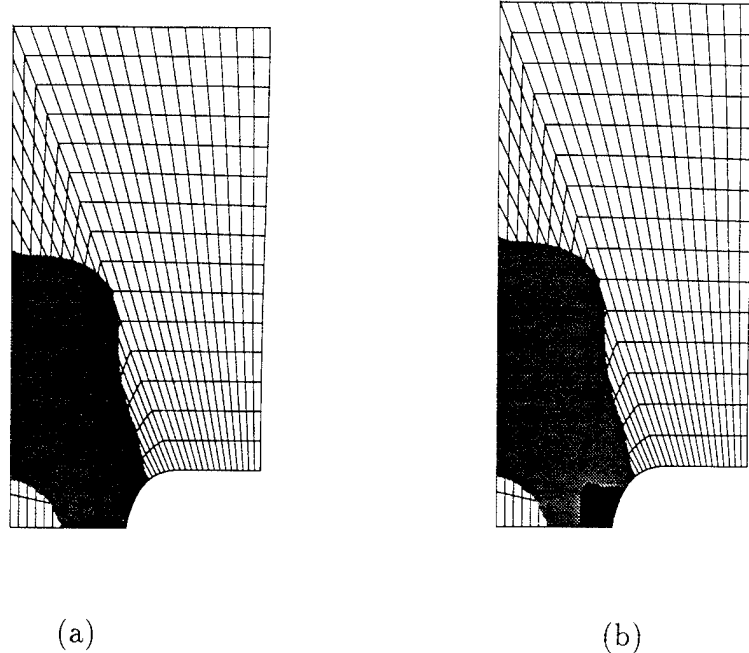


Figure 5.16: Coarse mesh configurations with s-adaptation (a) with level 1 of quadratic elements at 3.2% elongation (b) with level 2 of cubic elements, and level 1 of quadratic elements, at 6.0 % elongation

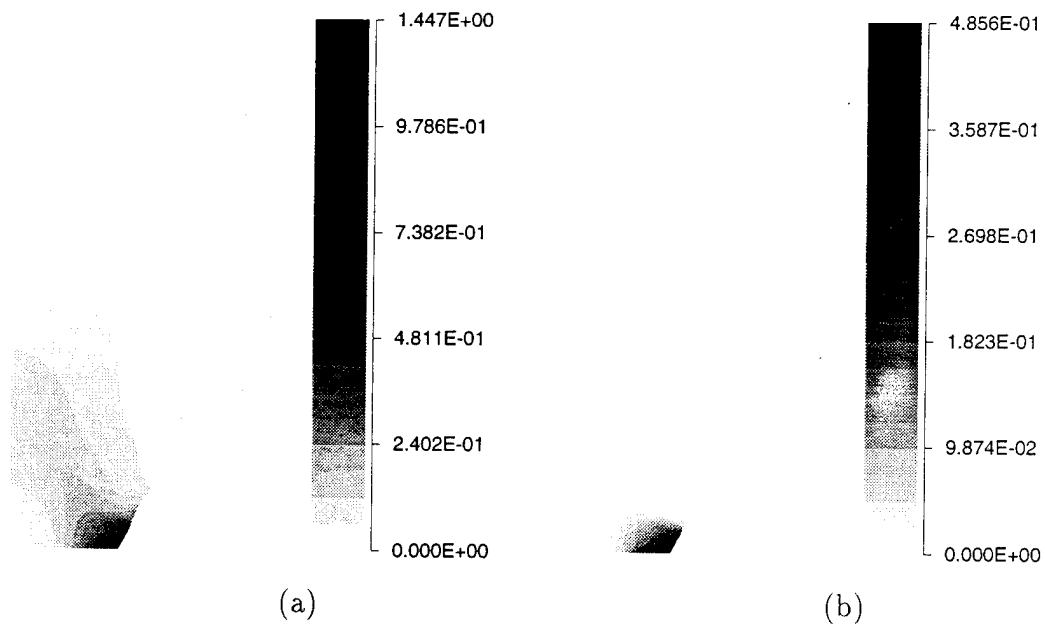
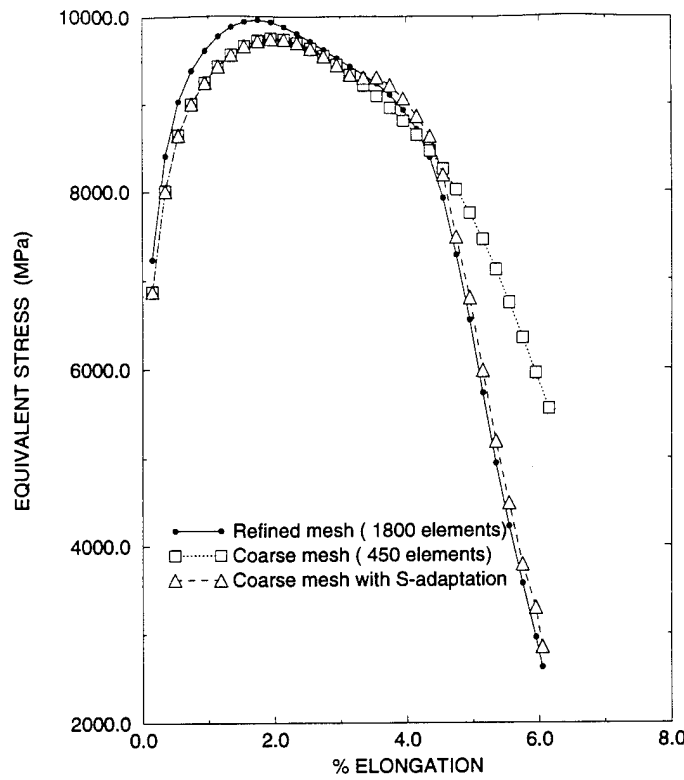
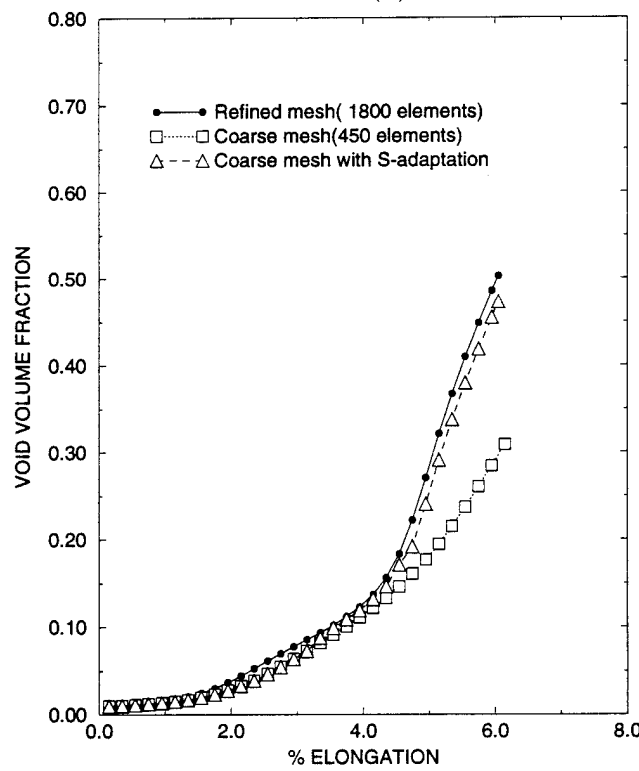


Figure 5.17: Contour plots for (a) equivalent plastic strain and (b) void volume fraction at 6.0 % elongation for the coarse mesh with s-adaptation.



(a)



(b)

Figure 5.18: Evolution of (a) equivalent stress and (b) void volume fraction at A.

- All nodes under the punch are initially Lagrangian (move with the material), with the exception of an ALE corner node.
- As the adjacent Lagrangian node approaches the corner node, the latter is released and made a Lagrangian node. The adjacent node is now moved to the corner and made ALE.
- The above steps are repeated throughout the simulation and r-adaptation is used to smoothen the transition between and Lagrangian nodes.

Figure 5.21 illustrate the results of simulation using a refined mesh with 1500 ALE elements. The corresponding results by a coarse mesh simulation with s-adaptation are shown in figure 5.22. Level 1 of quadratic superimposed elements (grey) is started at 20% deformation under the punch. With the progress of deformation, regions of intense straining grows and changes, and consequently the s-adapted level 1 region extends. It is important to note that the superimposed s-domain may convect through the level 0 ALE mesh, as can be seen in figure 5.22(b). Level 2 mesh superposition begins at 40% deformation. The superimposed mesh domain in figure 5.22(b) gives an indication of localized straining under the punch, starting at the corner. Contour plots of equivalent plastic strain and void volume fraction in figure 5.22(c) and (d) exhibit good agreement with refined mesh predictions. Figure 5.23(a) show the contact stress distribution under the punch at 65% deformation, while figure 5.23(b) presents the load-displacement diagram for the back extrusion problem.

### Ironing

In this last example, a rigid prismatic punch is used to form a thin walled hollow cup by ironing as shown in figure 5.24. The punch moves vertically down at a speed of 50 cm/sec for a total simulation time is 0.2 seconds. Faces AB, BC, CD and DE are contact surfaces on the rigid punch, FG and HI are contact faces on the die as shown. The top face of the workpiece is roller supported to imitate the effect of friction. Figure 5.25(a) and (b) show the initial and final refined mesh (1500 QUAD4 elements) configurations corresponding to a punch travel of 7.5 cm (75% of the initial height). Contour plots of equivalent plastic strain and void volume fraction at the final stage are depicted in figures 5.25(c) and (d) respectively. Similar figures for the coarse mesh simulation (450 QUAD4 elements) with s-adaptation are shown in 5.26. Level 1 (grey) superimposition with quadratic hierarchical elements is initiated when the punch travel is 1.5 cm, for  $\eta > 0.5$ . As seen in figure 5.26(b), level 1 superimposed domain grows with deformation in the form of a band. Level 2 (black) superimposed cubic hierarchical elements are introduced when the punch travel is 5 cm.

## 5.6 Conclusions

This work entails two types of adaptations in simulating large deformation metal forming problems. They are (a) the r-method of node relocation for maintaining mesh and mod-

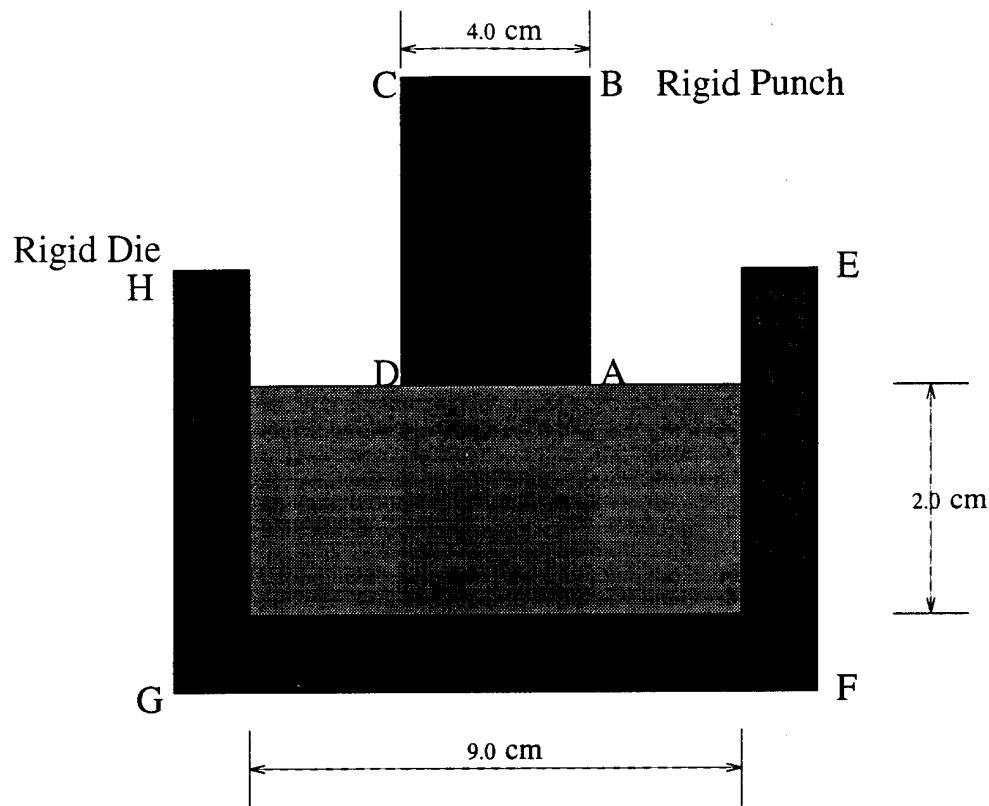


Figure 5.19: Schematic view of the backward extrusion problem.

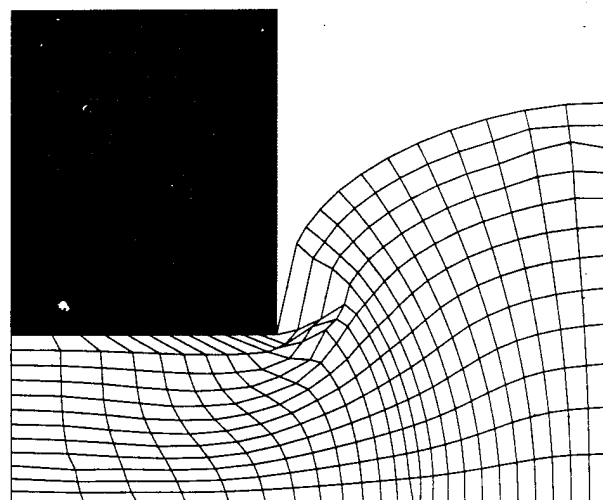


Figure 5.20: Backward extrusion at 40% deformation with node relocation and ALE nodes on contact surface which are not released.

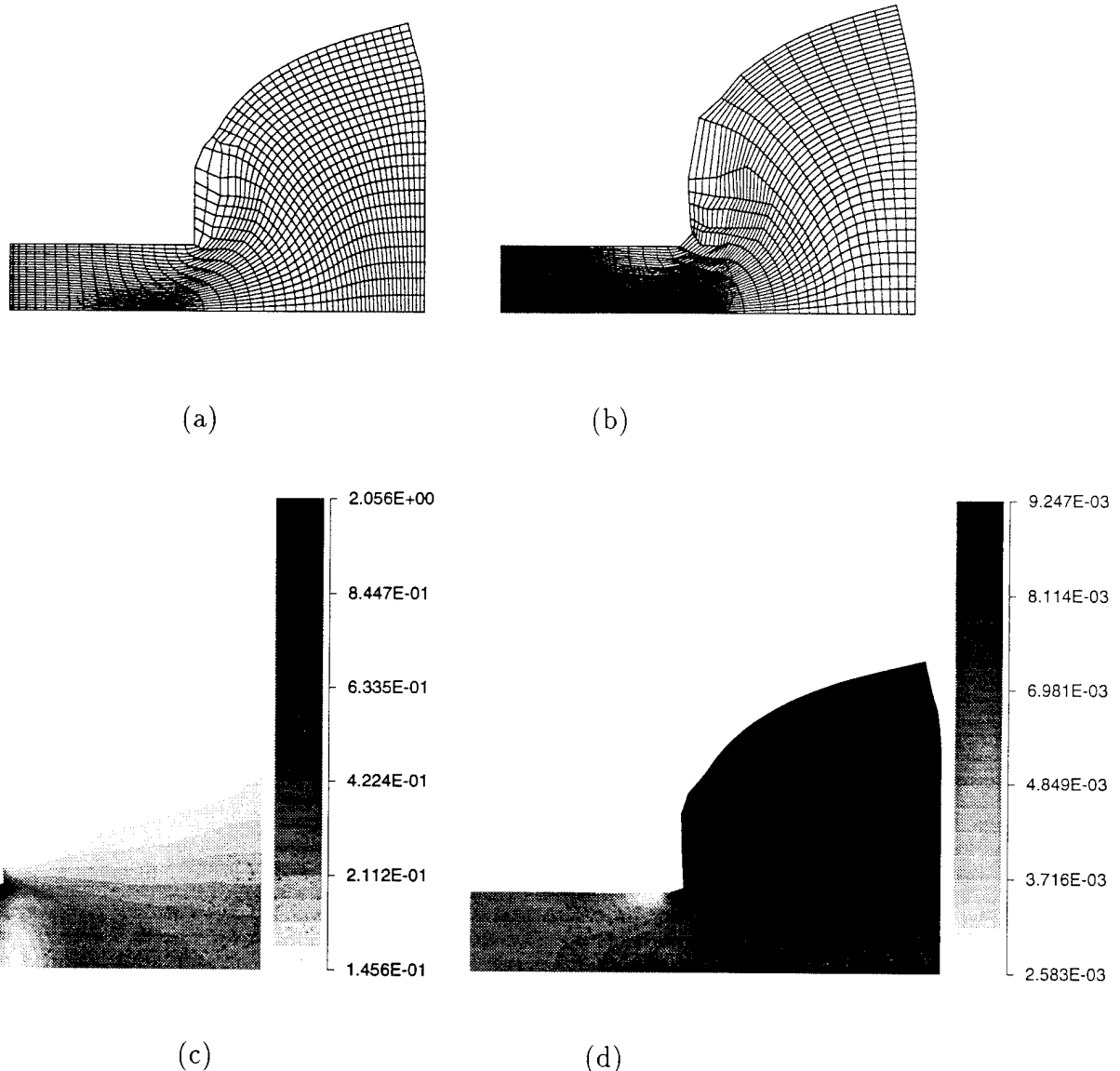
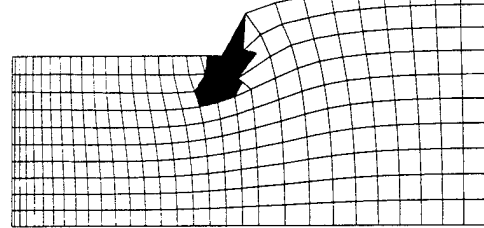
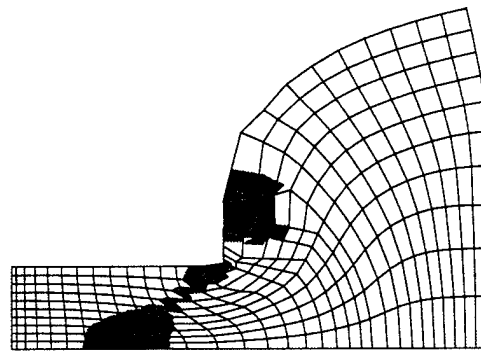


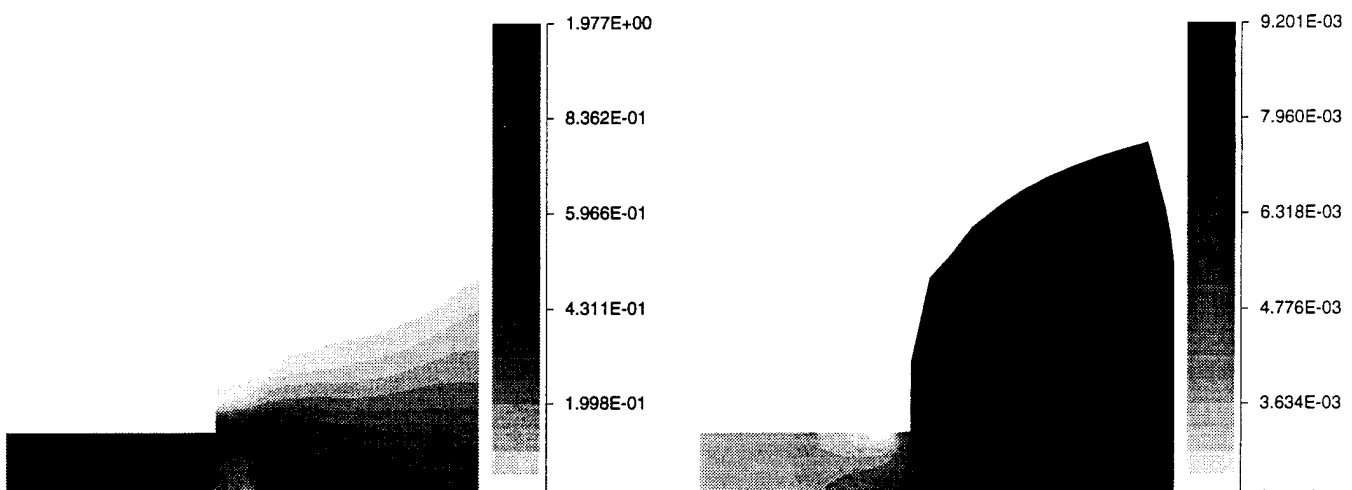
Figure 5.21: Backward extrusion results at 65% deformation under the punch (a) refined mesh configuration (b) material mesh configuration (c) equivalent plastic strain contours and (d) void volume fraction contours



(a)



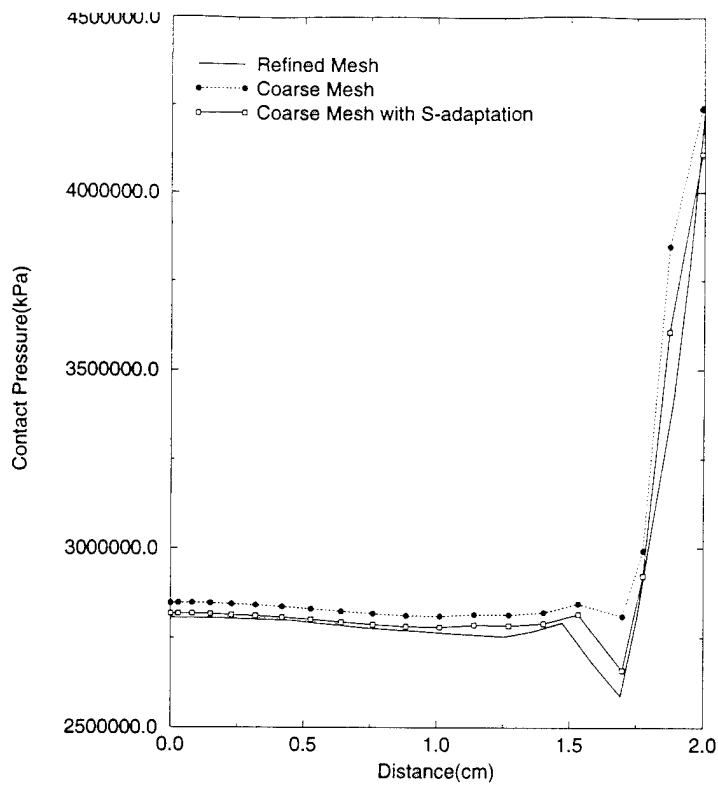
(b)



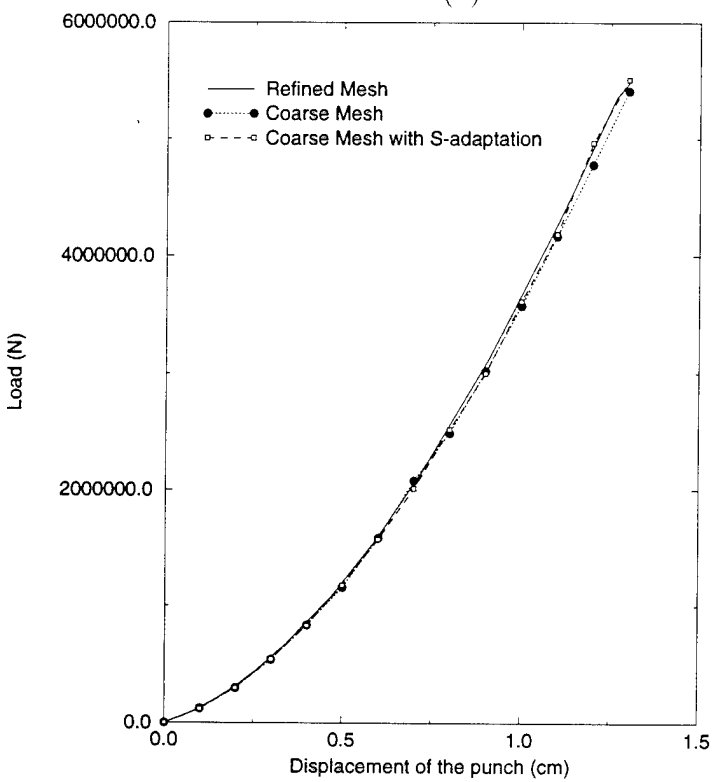
(c)

(d)

Figure 5.22: Coarse mesh configuration with s-adaptation (a) at 20% deformation (b) at 65% deformation. Contour plots at 65% deformation for (c) equivalent plastic strain and (d) void volume fraction



(a)



(b)

Figure 5.23: (a) Normal stress distribution along the contact region at 65% deformation and (b) Load-displacement for back extrusion.

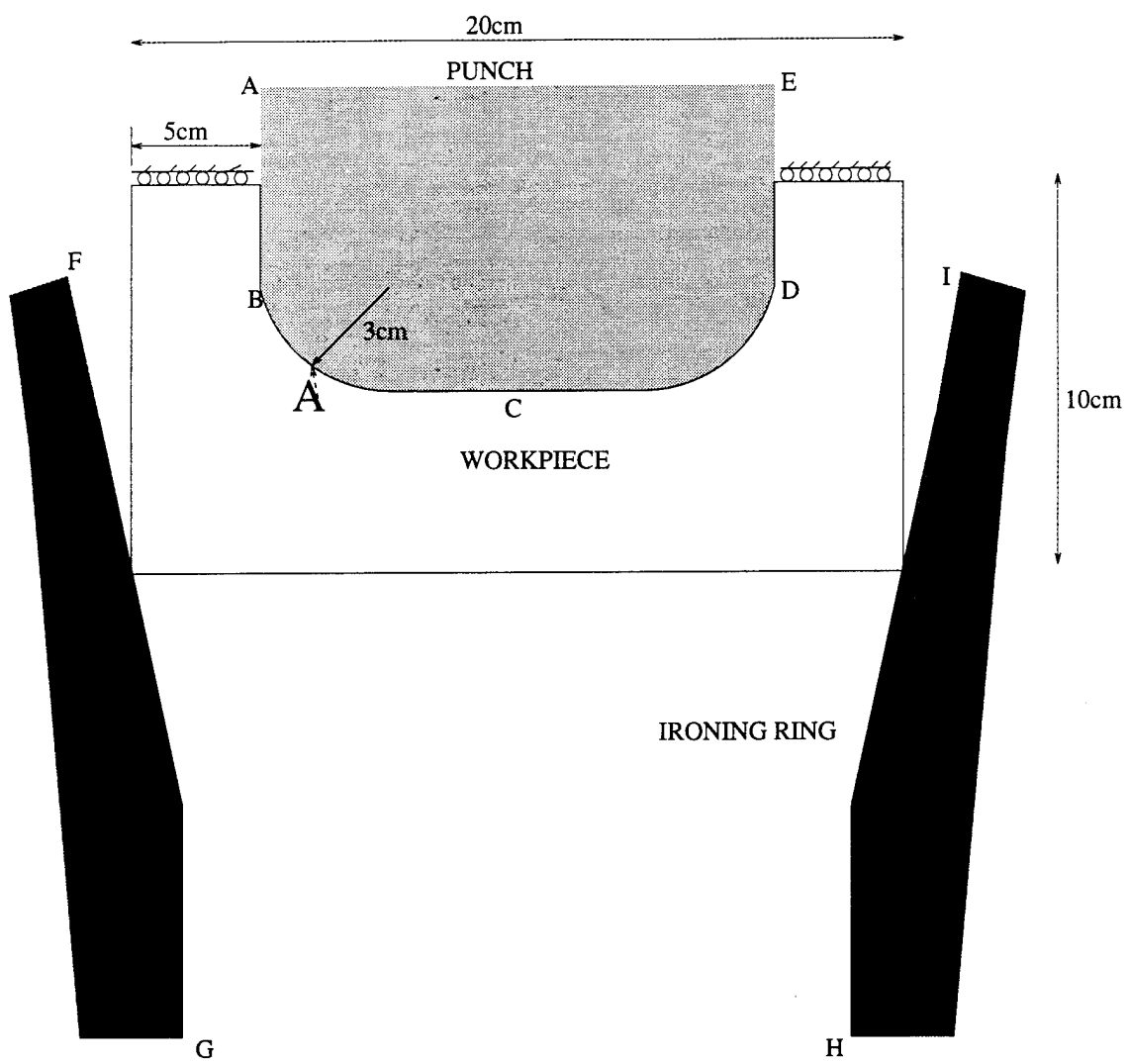
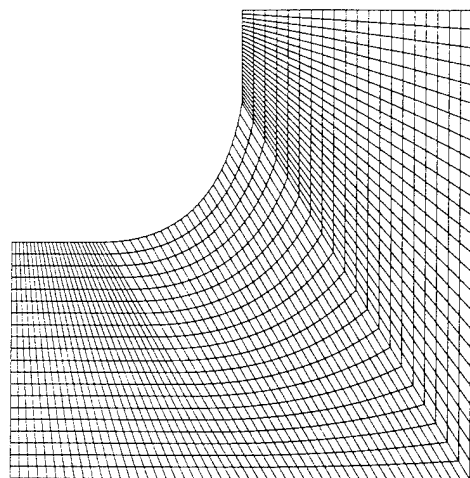
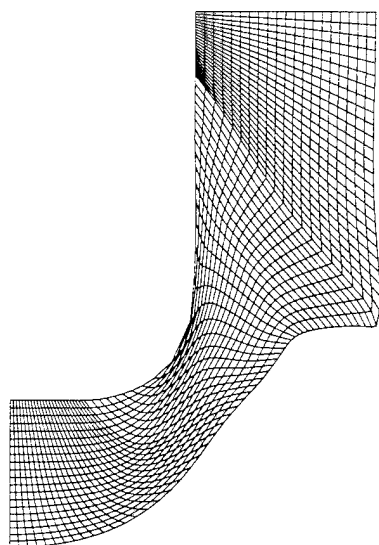


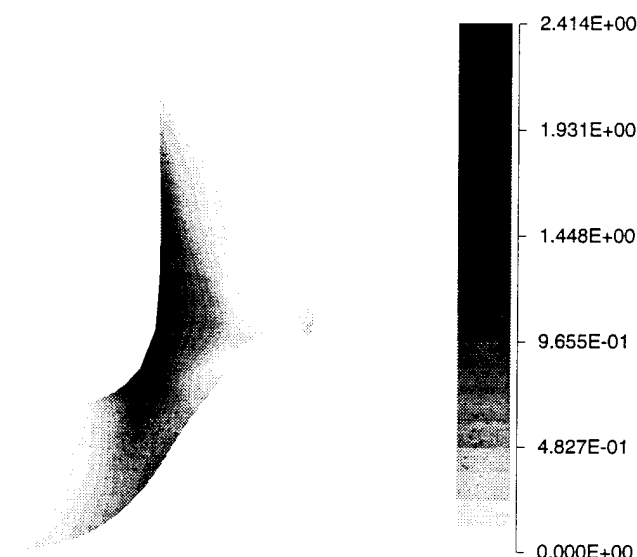
Figure 5.24: Schematic view of the ironing process.



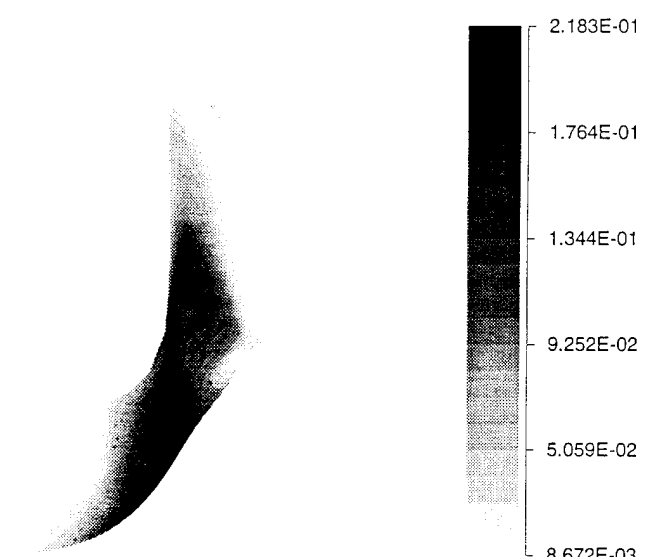
(a)



(b)



(c)



(d)

Figure 5.25: Refined mesh configurations (a) initially (b) at 75% deformation. Contour plots at 75% deformation for (c) equivalent plastic strains and (d) void volume fraction

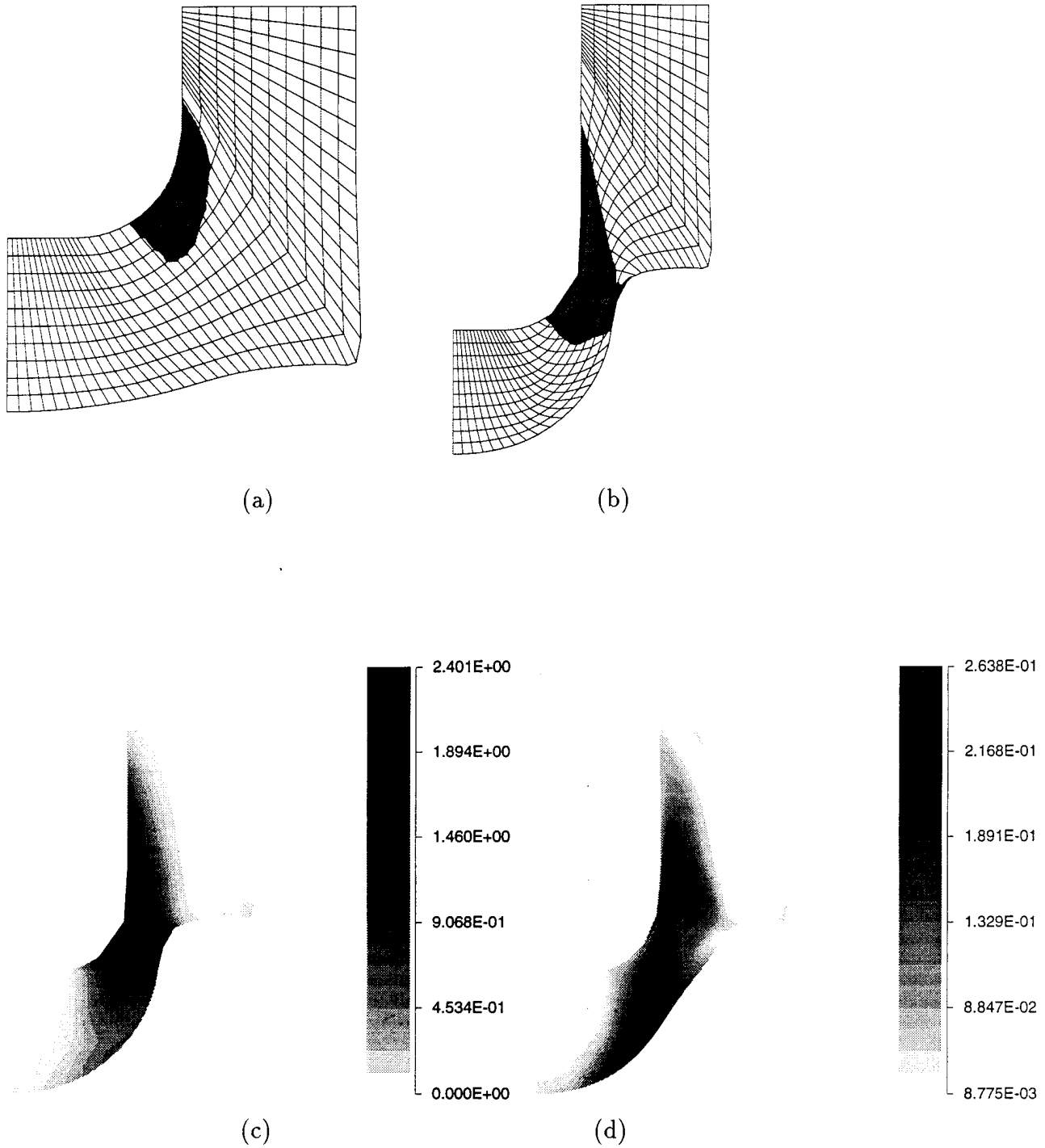


Figure 5.26: Coarse mesh configuration with s-adaptation (a) at 15% deformation (b) at 75% deformation. Contour plots at 75% deformation for (c) equivalent plastic strain and (d) void volume fraction

eling quality, and (b) a multi-level mesh superposition based s-adaptation for increasing the accuracy of local predictions. R-adaptation in conjunction with the ALE kinematic description, is very effective in removing element distortions and better representation of the contact boundary. For metal forming problems, this helps in executing the simulation to fairly high degrees of deformation without mesh collapse. The resolution of a global finite element mesh is increased locally by s-adaptation through superimposition of hierarchical elements in regions of high solution gradients. Strain localization occurs over very narrow regions in comparison with the overall dimensions and the prediction of localized bands is mesh sensitive. For meshes which are not refined, the simulation is incapable of capturing any strain localization phenomenon at all. Here the s-adaptation is particularly important since localization zones are *a priori* unknown. S-adaptation in this study helped capture localized deformations by superimposing level 1 of quadratic hierarchical elements and level 2 of cubic or quartic hierarchical elements. Subsequent levels can zoom in on the localized process. Accuracy of the solution is considerably improved with s-adaptation in all problems considered in this study.

# Bibliography

- [1] W.K. Liu, T. Belytschko and H. Chang, 'An arbitrary Lagrangian Eulerian finite element method for path dependent materials', *Comp. Methods in Appl. Mech. Eng.*, **58**, 227-245 (1986).
- [2] J. Huetink, J. van der Lught and P. T. Vreeke, 'A mixed Euler-Lagrangian finite element method for simulation of thermo-mechanical processes', in J. L. Chenot and E. Onate (eds.), *Modelling of Metal Forming Processes*, Kluwer Academic Publishers, 57-64, (1988).
- [3] S. Ghosh, and N. Kikuchi, 'An Arbitrary Lagrangian Eulerian finite element method for large deformation analysis of elastic-viscoplastic solids', *Comp. Methods in Appl. Mech. Eng.*, **86**, 127-188 (1991).
- [4] S. Ghosh, 'Finite element simulation of some extrusion processes using the arbitrary Lagrangian-Eulerian description', *ASM J. Mater. Shaping Tech.*, **8**: 1, 53-64 (1990).
- [5] S. Ghosh, 'Arbitrary Lagrangian-Eulerian finite element analysis of large deformation in contacting bodies', *Int. J. Num. Methods Eng.*, **33**, 1891-1925 (1992).
- [6] Y-K. Hu and W. K. Liu, 'ALE finite element formulation for ring rolling analysis', *Int. J. Num. Methods Eng.*, **33**, 1217-1246 (1992).
- [7] N. Kikuchi and T. Torigaki, 'Advances in inelastic analysis', AMD-**88** PED-**28**, ASME, 309-331 (1988).
- [8] J. Z. Zhu and O. C. Zienkiewicz, 'Adaptive techniques in the finite element method', *Comm. Appl. Numer. Methods*, **4**, 197-204 (1988).
- [9] O. C. Zienkiewicz and J. Z. Zhu. 'The superconvergent patch recovery and a posteriori error estimates. part 1 : The recovery technique.', *Int. J. Num. Methods Eng.*, **33**, 1331-1364, (1992).
- [10] O. C. Zienkiewicz and J. Z. Zhu. 'The superconvergent patch recovery and a posteriori error estimates. part 2 : Error estimates and adaptivity', *Int. J. Num. Methods Eng.*, **33**, 1365-1382, (1992).
- [11] G. F. Carey, 'A mesh-refinement scheme for finite element computations', *Comp. Methods in Appl. Mech. Eng.*, **7**, 93-105 (1976).

- [12] R. J. Melosh and P. V. Marcal, 'An energy basis for mesh refinement of structural continua', *Int. J. Num. Methods Eng.*, **11**(7), 1083-1092 (1977).
- [13] B. Guo and I. Babuska, 'The h-p version of the finite element method. Part 1: The basic approximation results. Part 2: General results and applications', *Comp. Mech.*, **1**, 21-41, 203-226 (1986).
- [14] L. Demkowicz, Ph. Devloo and J. T. Oden, 'On an h type mesh refinement strategy based on a minimization of interpolation error', *Comp. Methods in Appl. Mech. Eng.*, **3**, 67-89 (1985).
- [15] B. A. Szabo, P. K. Basu and M. P. Rossow, 'Adaptive finite element analysis based on the p-convergence, Research in computerized structural analysis and synthesis', *NASA Conference Publication 2059*, 43-50 (1978).
- [16] I. Babuska and M. Suri, 201z'The p- and h-p version of the finite element method, An overview,' *Comp. Methods in Appl. Mech. Eng.*, **80**, 15-20 (1990).
- [17] A. R. Diaz, N. Kikuchi and J. Taylor, 'A method of grid optimization for finite element methods', *Comp. Methods in Appl. Mech. Eng.*, **41**, 29-45 (1983).
- [18] L. Demkowicz, J. T. Oden, W. Rachowicz and O. Hardy, 'Toward a universal h-p finite element strategy, Part 1. Data structure and constrained approximation', *Comp. Methods in Appl. Mech. Eng.*, **77**, 79-112 (1989).
- [19] I. Babuska, 'The p and h-p version of the finite element method. The state of art', in R. Vought Ed., *Proceedings of finite element method workshop*, Springer (1987).
- [20] O. C. Zienkiewicz, J. Z. Zhu and N. G. Gong, 'Effective and practical h-p version adaptive analysis procedures for the finite element methods', *Int. J. Num. Methods Eng.*, **28**, 879-891 (1989).
- [21] J. Fish, 'The s-version of the finite element method', *Comp. Struct.*, **43**, 539-547 (1992).
- [22] S. I. Markolefas, 'Adaptive superposition method for linear elasticity problems', M. S thesis, Rensselaer Polytechnic Institute, Troy, NY (1992).
- [23] T. Belytschko, J. Fish, and B. E. Englemann, ' A finite element with embedded localization zones', *Comp. Meth. Appl. Mech. Eng.*, **70**, 59-89, (1988).
- [24] T. Belytschko, J. Fish, and A. Bayliss, 'The spectral overlay on the finite element solutions with high gradients', *Comp. Meth. Appl. Mech. Eng.*, **81**, 71-89, (1990).
- [25] W. Seki, 'Analysis of strain localization, using assumed stress hybrid elements' , Ph.D Thesis, Georgia Institute of Technology, Atlanta, (1994).
- [26] W. Seki and S. N. Atluri, 'Analysis of strain localization in strain-softening hyperelastic materials, using assumed stress hybrid elements', *Comp. Mech.*, **14** (6), 549-585 , (1994).

- [27] J. C. Simo, F. Armero and R. L. Taylor, 'Improved versions of assumed enhanced strain tri-linear elements for 3D finite deformation problems', *Comp. Meth. Appl. Mech. Eng.*, **110**, 359-382 (1993).
- [28] J. C. Simo and F. Armero, 'Geometrically nonlinear enhanced mixed finite element methods and the method of incompatible modes', *Int. J. Numer. Meth. Eng.*, **33**, 1413-1449, (1992).
- [29] B. A. Szabo and I. Babuska, 'Finite Element Analysis', John Wiley & Sons Inc. (1991).
- [30] R. Suresh, 'R-S adapted arbitrary Lagrangian Eulerian finite element method for metal forming problems with strain localization', M. S. thesis, The Ohio State University, Columbus, Ohio (1995).
- [31] A. L. Gurson, 'Continuum theory of ductile rupture by void nucleation and growth: Part I - Yield criteria and flow rules for porous ductile materials', *J. Eng. Mat. Tech.*, **99**, 2-15 (1977).
- [32] V. Tvergaard, 'Influence of void nucleation on ductile shear fracture at a free surface', *J. Mech. Phys. Solids*, **30**(6), 399-425, (1982).
- [33] V. Tvergaard, 'Influence of voids on shear band instabilities under plane strain conditions', *Int. J. Fract. Mech.*, **17**, 389-407 (1981).
- [34] V. Tvergaard, 'Effect of yield surface curvature and void nucleation on plastic flow localization', *J. Mech. Phys. Solids*, **35**, 43-60 (1987).
- [35] V. Tvergaard, A. Needleman and K. K. Lo, 'Flow localization in the plane strain tensile test', *J. Mech. Phys. Solids*, **29**, 115-142 (1981).
- [36] V. Tvergaard, 'Material failure by void growth to coalescence', *Adv. Appl. Mech.*, **27**, 83-151 (1990).
- [37] C. L. Hom and R. M. McMeeking, 'Void growth in elastic-plastic materials', *J. Appl. Mech.*, ASME, **56**, 309-321 (1989).
- [38] N. Aravas, 'On the numerical integration of a class of pressure-dependent plasticity models', *Int. J. Num. Meth. Eng.*, **24**, 1395-1416 , (1987).
- [39] A. Needleman and J. R. Rice, 'Limits to ductility set by plastic flow localization', in D. P. Koistinen et al (eds), *Mechanics of Sheet Metal Forming*, Plenum Press, New York, (1978).
- [40] R. J. Asaro and A. Needleman, 'Flow localization in strain hardening crystalline solids', *Scripta Metall.*, **18**, 429-446 (1984).
- [41] J. C. Simo, P. Wriggers and R. L. Taylor, 'A Perturbed Lagrangian formulation for the finite element solution of contact problems', *Comp. Meth. Appl. Mech. Eng.*, **50**, 163-180 (1985).

- [42] H. T. Y. Yang, M. W. Heinstein and J. M. Shih, 'Adaptive 2D finite element simulation of metal forming processes', *Int. J. Num. Meth. Eng.*, **28**, 1407-1428 (1989).
- [43] M. W. Heinstein and H. T. Y. Yang, 'Plane strain finite element simulation of shear band formation during metal forming', *Int. J. Num. Meth. Eng.*, **33**, 719-737 (1992).

## Chapter 6

# An Arbitrary Lagrangian-Eulerian Finite Element Model for Heat Transfer Analysis of Solidification Processes

### Summary

In this work, a heat transfer analysis for solidification problems has been conducted to evaluate the temperature field and the location of the phase change interface. An arbitrary Lagrangian-Eulerian kinematic description has been utilized in the finite element formulation for imparting flexibility to the motion of the nodes in model. By detaching the nodal points from the underlying material, nodes can be monitored to follow the evolving front while maintaining shapes of the elements. Special numerical techniques to smoothen the deforming front and to avoid continuous remeshing are introduced. Numerical examples have been solved to establish the validity of the present model and its strength.

### 6.1 Introduction

Accurate modeling of various solidification processes is of prime interest to the casting industry for enhancing the quality of castings and reducing the number of rejects. In depth process analysis enables an engineer to understand the effects of temperature history and gradients, solid-liquid interface motion, fluid velocity etc. on the evolution of void and porosity distribution, shrinkage and microstructure of solidified body. Design and control of various process parameters can then be exercised to optimize these variables in order to obtain the desired shape, size and thermophysical properties of the finished product. A rigorous thermal analysis of various solidification processes entails a coupling of fluid flow, heat transfer and motion of the phase transition zone. Consideration should be given to various interacting factors such as:

- a. Transient behavior of the resulting temperature field.
- b. Apriori unknown motion of the irregular phase change interface.
- c. Effects of convection in the liquid pool.

A number of exact and approximate analytical studies have been published on the solution of moving boundary problems with applications in solidification or melting, and a cogent review has been presented by Crank [1]. Notable among these methods are the heat balance integral methods by Goodman [2], embedding methods by Boley [3] and Greens function methods by Hansen and Hougaard [4]. Although mathematically elegant, these analytical methods have essentially been limited to one dimensional problems with over-simplified boundary conditions and material properties. Realistic problems are seldom unidirectional with simple features, and hence, cannot be handled by these methods. A number of numerical techniques have been consequently developed for solving multi-dimensional heat transfer problems with phase change. Among them, the finite difference method was the first to gain popularity with researchers for its simplicity in dealing with partial differential equations. A comprehensive analysis of various finite difference methods that have evolved in solidification analysis has been presented by Crank [5]. Among the important contributions in this area are the works of Lazaridis [6], Shamsunder and Sparrow [7], Wilson et.al. [8] etc. However, this method lacks the generality for treating practical problems, especially when complicated geometries and boundary conditions are involved. The last decade has seen an increasing trend towards the development of the finite element method for heat transfer problems because of its effectiveness with arbitrary shaped domains and complex boundary conditions. A classification of different techniques based on the finite element method is presented in Crank [1]. A major challenge in the analysis of phase change problems is the accurate representation of continuously moving solid-liquid interfaces, for which velocity and heat transfer conditions have to be met. Based on the procedure for treating the release of latent heat of solidification at these interfaces, the methods have been traditionally categorized into two classes, namely the fixed grid or moving grid methods.

In the class of fixed domain finite element analysis, the enthalpy method has been extensively used because of its relative ease of implementation in computer codes. In this method, the thermal properties in the solid and liquid phases and the identification of the phase change interface are all unified through the introduction of a discontinuous enthalpy function  $H(T)$ , where  $T$  is the temperature field. Such an implicit representation of the latent heat release conditions inherently reduces the burden of continuous tracking of the solidification front and solving separate equations for each phase. Among the large volume of published research on the enthalpy formulation in finite difference or finite element methods are the innovative works of Crowley [9], Comini et. al. [10], Voller and Cross [11], Shamsunder and Sparrow [7], Samands et. al. [12] and Salcudean et. al. [13]. Although the enthalpy finite element formulation enjoys good convergence rates to the weak solution of the boundary value problems, they suffer from some limitations especially in modeling isothermal solidification as discussed by Bell [14] and Voller and Cross [15]. These methods do not explicitly account for the sharp discontinuities and mechanical boundary conditions

at the interface. Hence, the accuracy of the solution deteriorates in the vicinity of the interfaces. Mesh refinement and introduction of interfacial control volumes have been proposed in [15] for accuracy enhancement, but have resulted in rapid decline in the efficiency of the numerical analysis.

The moving grid finite element methods use front tracking techniques to follow the discrete phase change interface continuously, and the latent heat release is treated as a moving boundary condition. In these methods, the energy equations are written in terms of temperature as the dependent variable. In general, it is accepted that the moving grid finite element methods are more accurate in predicting the motion of the interface and the temperature gradients across it. Various methods like deforming grids, variable or coordinate transformation, introduction of special algorithms near the phase change interface etc. have been experimented with. In order to trace the free boundary of the phase interface, Bonnerot and Jamet [16] have used a space-time formulation, to allow for a change of nodal positions with time. Yoo and Rubinsky [17] have solved a static heat transfer problem followed by internal boundary relocation, based on the solution of energy balance on the phase change interface. Miller [18] has implemented principles of error minimization to move elements in Stefan problems. Significant contributions to the finite element analysis of moving boundary problems have been made by Lynch, O'Neill and coworkers [19, 20, 21, 22, 23]. Lynch and Gray [19] have developed a general Galerkin finite element formulation to automatically account for continuous mesh deformation in solving shallow water wave problems. In their papers [20,21] Lynch and O'Neill have incorporated implicit time dependence in the element interpolation functions for solving parabolic problems with phase change. The finite element mesh is allowed to deform continuously for conforming with the evolving solid-liquid interface. Through the introduction of a deforming/growing numerical coordinate system, the motion of nodal points is explicitly accounted for in the weak form of the governing equations. No loss of energy is therefore encountered while updating variables, during mesh changes in every time step. This makes it a more attractive method compared to the static methods using remeshing (e.g. [17]), in terms of efficiency and accuracy. Equivalence between various approaches viz. weighted residual, coordinate transformation, space- time elements [16] and error minimization [18], in formulating deforming grid finite element analysis has been established in a comprehensive paper by Lynch [22]. Ensuing shortcomings of the deforming grid formulation from excessive mesh distortion were surpassed in a paper by Albert and O'Neill [23], where they monitored the motion of the grid by transfinite mapping techniques.

The present work introduces an arbitrary Lagrangian-Eulerian (ALE) kinematic description in the finite element method for heat transfer analysis of problems involving phase change. This formulation treats the finite element mesh as a reference frame which may be moving with an arbitrary velocity in the laboratory system. Thus it combines the advantages of pure Lagrangian and Eulerian systems into one description. The ALE formulation was introduced in the finite element method by Donea [24] and Belytschko [25, 26] for modeling fluid-structure interaction. In these problems, the fluid was treated with ALE formulation and the solid with pure Lagrangian formulation. Liu and coworkers [27] have extended this formulation for three dimensional liquid storage systems. Recently, the ALE description

has been successfully implemented in nonlinear solid mechanics problems by Liu, Belytschko and coworkers [28,29], Ghosh and coworkers [30,31,33] and Haber [32] for modeling large deformation. These numerical models have been particularly effective in overcoming some of the major shortcomings of pure Lagrangian and Eulerian formulations in metal forming simulations [31,33], such as excessive distortion of elements or improper representation of contact boundary conditions.

Though the arbitrary Lagrangian-Eulerian finite element method has some obvious similarities with the deforming finite element formulation [22], especially with respect to the development involving coordinate transformation, it is perceived of as being a more general and flexible system that can be used for a wide variety of applications. Since this formulation invokes conservations laws of mechanics with respect to an arbitrarily moving reference system, the notion of independent grid motion is fundamentally incorporated into the finite element analysis. With this formulation, different parts of the computational domain can be represented using different kinematic descriptions. For example, in a solidification problem involving fluid convection, pure Eulerian nodes can model the fluid domain, pure Lagrangian nodes can represent the evolving solid domain and a set of ALE nodes can follow the moving phase change front within the same computational mesh. It is this inherent flexibility that makes the ALE formulation an attractive candidate for this class of problems. In this work, a heat transfer analysis of solidification problems using this method has therefore been pursued.

## 6.2 Governing Equations In Arbitrary Lagrangian-Eulerian Description

The arbitrary Lagrangian-Eulerian description introduces a reference configuration which consists of grid points in arbitrary spatial motion. Each point of this reference configuration is unambiguously identified by an invariant set of three independent coordinates  $\chi_i$ . Concurrently, the material coordinate system is represented by an invariant set of coordinates  $X_i$  attached to a material point and the spatial coordinate denoting the location of each point in space is given by  $x_i$ . The motion of grid and material points can then be expressed as continuous function of time  $t$  and  $\chi_i$  and  $X_i$  respectively as :

$$x_i = \phi_i(\chi_j, t) \quad (6.1)$$

$$x_i = \hat{\phi}_i(X_j, t) \quad (6.2)$$

where  $\phi_i$  and  $\hat{\phi}_i$  are mapping functions with nonvanishing Jacobians. The material time derivative of any time dependent physical quantity  $\beta$  may then be related to the referential time derivative by the relation

$$\frac{\partial \beta}{\partial t}|_x = \frac{\partial \beta}{\partial t}|_X + (W_k - V_k) \frac{\partial \beta}{\partial x_k} \quad (6.3)$$

where  $\frac{\partial}{\partial t}|_X$  is the material time derivative and  $\frac{\partial}{\partial t}|_X$  is the referential time derivative. In equation (6.3)  $V_i [= \frac{\partial x_i}{\partial t}]_X$  is the material velocity and  $W_i [= \frac{\partial x_i}{\partial t}]_x$  is the grid velocity.

Using the above relations, material conservation laws with respect to an arbitrary reference system may be expressed as :

Continuity:

$$\frac{\partial(\rho J)}{\partial t}|_x + J \frac{\partial}{\partial x_i} (\rho(V_i - W_i)) = 0 \quad (6.4)$$

Momentum:

$$\rho G_i + \frac{\partial \sigma_{ji}}{\partial x_j} = \rho \frac{\partial V_i}{\partial t}|_x + \rho(V_j - W_j) \frac{\partial V_i}{\partial x_j} \quad (6.5)$$

Energy:

$$\rho \frac{\partial \hat{u}}{\partial t}|_x + \rho(V_j - W_j) \frac{\partial \hat{u}}{\partial x_j} = \sigma_{ji} D_{ji} - \frac{\partial q_i}{\partial x_i} + f \quad (6.6)$$

where  $\rho$  refers to the material density,  $\sigma_{ij}$  is the Cauchy stress tensor,  $G_i$  is the body force per unit mass,  $\hat{u}$  is the specific internal energy,  $q_i$  is the heat flow vector,  $D_{ij}$  is the rate of deformation tensor and  $f$  is the rate of heat addition by a source. Expressing the specific internal energy function as :

$$\hat{u} = C_p(\theta - \theta_{ref}) \quad (6.7)$$

where  $C_p$  is the specific heat at constant pressure,  $\theta$  is the absolute temperature and  $\theta_{ref}$  is a reference temperature. Incorporating the Fourier's law of heat conduction, the energy balance equation (6.6) may be restated as :

$$\rho C_p \frac{\partial \theta}{\partial t}|_x + \rho C_p(V_j - W_j) \frac{\partial \theta}{\partial x_j} = \sigma_{ji} D_{ji} + \frac{\partial}{\partial x_i} (k_{ij} \frac{\partial \theta}{\partial x_j}) + f \quad (6.8)$$

where  $k_{ij}$  is the thermal conductivity. The convection terms containing the relative velocity ( $V_i - W_i$ ) in equations 5.4, 5.5 and 5.8, control the nature of pointwise description in the finite element model. Thus, when  $\mathbf{W}$  is set to zero, the description becomes locally Eulerian while it is Lagrangian in the event that  $\mathbf{W} = \mathbf{V}$  at a point. The energy balance equation in the solid domain  $\Omega_s(t)$  is obtained from equation (6.8) by substituting  $(C_p)_s$ ,  $(k_{ij})_s$  and  $\rho_s$  for specific heat, thermal conductivity and density in the solid and that in the liquid domain  $\Omega_l(t)$  is obtained by substituting the respective liquid properties  $(C_p)_l$ ,  $(k_{ij})_l$  and  $\rho_l$ . The boundary of the solid domain is assumed to be the combination of two basic conditions i.e.  $\Gamma(t)$  is  $\Gamma_1(t) \cup \Gamma_2(t)$  and may be delineated as

$$\theta(\mathbf{x}, t) = \theta_g(\mathbf{x}, t) \quad \forall \mathbf{x} \text{ on } \Gamma_1(t)$$

and

$$k_{ij} \frac{\partial \theta}{\partial x_j} n_i = q_n(\mathbf{x}, t) \quad \forall \mathbf{x} \text{ on } \Gamma_2(t) \quad (6.9)$$

where  $n_i$  corresponds to the outer unit normal on the boundary. The initial domain is assumed to be comprised wholly of the liquid domain i.e.

$$\Omega_s(t=0) = 0 \quad \Omega_l(t=0) = \Omega_o \quad (6.10)$$

where  $\Omega_o$  is prescribed. The initial temperature in the liquid is assumed to be specified everywhere as

$$\theta(\mathbf{x}, 0) = \theta_l(\mathbf{x}) \quad \forall \mathbf{x} \text{ on } \Omega_l(t = 0) \quad (6.11)$$

The Stefan condition on the solidification front, which governs the a-priori unknown motion of the phase change interface is expressed as

$$(k_{ij} \frac{\partial \theta}{\partial x_j} n_i)_s - (k_{ij} \frac{\partial \theta}{\partial x_j} n_i)_l = \rho L \frac{\partial \mathbf{s}}{\partial t} \cdot \mathbf{n} \quad (6.12)$$

where  $\mathbf{n}$  denotes the latent heat of fusion,  $\mathbf{s}(t)$  refers to the location of the solidification front and  $\mathbf{n}$  is the unit normal on the interface  $\Gamma_{S-L}$  pointing into the liquid. Additionally, the isothermal conditions are assumed on the solidification front, i.e.

$$\theta(\mathbf{x}, t) = \theta_m \quad \forall \mathbf{x} \text{ on } \Gamma_{S-L}(t) \quad (6.13)$$

where  $\theta_m$  is the melting temperature. On account of the unknown motion of the phase change interface, equation (6.12) renders the problem nonlinear, even if the material properties are temperature independent. Temperature fields, position and velocity of the interface with the progress of time are now the solution variables of the problem.

### 6.3 Finite Element Formulations For Heat Transfer Analysis

Since this work deals with heat transfer analysis only, the weak forms of the mass and energy balance equations will only be considered here. Such weak forms are obtained by taking the product of (6.4) and (6.6) with appropriate weighting functions and integrating over the current grid configuration. However, in the finite element analysis of time dependent problems, emphasis is placed on the proper time integration scheme and hence the selection of appropriate configuration for integration. The commonly used family of one step algorithms using one parameter, has been utilized in this analysis. The stability behavior of commonly used algorithms, namely the generalized trapezoidal family or the generalized mid-point family have shown that, both the one ( $\alpha$ ) parameter algorithms yield unconditional stability for  $\alpha \geq \frac{1}{2}$  in the case of linear problems [34, 36]. However, as pointed out by Hughes [35, 36], the trapezoidal family gives unconditional stability for  $\alpha = 1$  for nonlinear heat conduction problems whereas it is second order accurate for  $\alpha = \frac{1}{2}$ . On the other hand, the mid-point is unconditionally stable for  $\alpha \geq \frac{1}{2}$  and second order accurate for  $\alpha = \frac{1}{2}$  for nonlinear heat conduction problems. Consequently, this method of integration has been invoked in the integration of the governing equations in the Lagrangian-Eulerian formulation. The weak form of the energy balance equation is written in an intermediate grid configuration  $\Omega(t_{n+\alpha})$  as :

$$\begin{aligned} & \int_{\Omega(t_{n+\alpha})} \rho C_p \frac{\partial \theta}{\partial t} |_{\mathbf{x}} \bar{\theta} d\Omega + \int_{\Omega(t_{n+\alpha})} \rho C_p (V_j - W_j) \frac{\partial \theta}{\partial x_j} \bar{\theta} d\Omega - \int_{\Omega(t_{n+\alpha})} k_{ij} \frac{\partial \theta}{\partial x_j} \frac{\partial \bar{\theta}}{\partial x_i} d\Omega \\ &= \int_{\Omega(t_{n+\alpha})} \sigma_{ji} D_{ji} \bar{\theta} d\Omega + \int_{\Omega(t_{n+\alpha})} f \bar{\theta} d\Omega + \int_{\Gamma(t_{n+\alpha})} q_n \bar{\theta} d\Gamma \end{aligned} \quad (6.14)$$

where all variables are at the intermediate configuration corresponding to time  $t_{n+\alpha}$  with the position of a grid point being interpolated as

$$\mathbf{x}^{n+\alpha} = (1 - \alpha)\mathbf{x}^n + \alpha\mathbf{x}^{n+1} \quad \text{for } 0 \leq \alpha \leq 1 \quad (6.15)$$

To establish an unambiguous connection between the Lagrangian and the referential system, a condition that the material boundary never leaves the grid domain may be imposed i.e.

$$(\mathbf{V} - \mathbf{W}) \cdot \mathbf{n} = 0 \quad (6.16)$$

where  $\mathbf{n}$  corresponds to the outward normal on the boundary. The first term on the right hand side of equation (6.14) corresponds to heat generation due to mechanical coupling and has been neglected in this analysis. The different variables are evaluated at  $t_{n+\alpha}$  by interpolating between their values at two consecutive equilibrium states at time  $t_n$  and  $t_{n+1}$  as :

$$\beta^{n+\alpha} = (1 - \alpha)\beta^n + \alpha\beta^{n+1} \quad (6.17)$$

where  $\beta$  is a typical material variable and  $\alpha$  is the interpolation parameter. To evaluate the value of a material variable in the grid configuration at time  $t_{n+\alpha}$ , the increment of the variable  $\Delta^g\beta$  at a fixed grid point is equated to that at a fixed material point  $\Delta^m\beta$  using generalized midpoint integration as

$$\Delta^g\beta = \Delta^m\beta + \Delta t (W_k^{n+\alpha} - V_k^{n+\alpha}) \frac{\partial\beta}{\partial x_k^{n+\alpha}} \quad (6.18)$$

Substituting equations (6.17) and (6.18) in equation (6.14) for the time derivative and increment of temperature, the energy balance equation takes the form

$$\begin{aligned} \int_{\Omega(t_{n+\alpha})} \left\{ \frac{1}{\Delta t} \rho C_p \Delta^g \theta \bar{\theta} + \alpha [\rho C_p (V_j - W_j) \frac{\partial \Delta^g \theta}{\partial x_j} \bar{\theta} + k_{ij} \frac{\partial \Delta^g \theta}{\partial x_j} \frac{\partial \bar{\theta}}{\partial x_i}] \right\} d\Omega = & \int_{\Omega(t_{n+\alpha})} f \bar{\theta} d\Omega + \\ \int_{\Gamma(t_{n+\alpha})} q_n \bar{\theta} d\Gamma - \int_{\Omega(t_{n+\alpha})} [\rho C_p (V_j - W_j) \frac{\partial \theta^n}{\partial x_j} \bar{\theta} + k_{ij} \frac{\partial \theta^n}{\partial x_j} \frac{\partial \bar{\theta}}{\partial x_i}] d\Omega & \end{aligned} \quad (6.19)$$

*Remark 1.* The heat flow vector on the second boundary  $\Gamma_2(t)$  may be assumed to be a combination of flux due to convection between the environment and the body and radiation from the environment. In the event that these conditions or the temperature are specified on the material, the boundary nodes may be made Lagrangian.

*Remark 2.* As opposed to Lagrangian formulation, the ALE description requires continuous evaluation of density at nodal points because of mass advection through each element. The midstep value of density can be evaluated directly by solving the weak form of the continuity equation (6.4) with the application of the constraint condition (6.16).

$$\int_{\Omega(t_{n+\alpha})} \frac{\partial \theta}{\partial t} |_x \bar{\rho} d\Omega = \int_{\Omega(t_{n+\alpha})} \rho (V_j - W_j) \frac{\partial \bar{\rho}}{\partial x_j} d\Omega - \int_{\Omega(t_{n+\alpha})} \rho \frac{\partial W_i}{\partial x_i} \bar{\rho} d\Omega \quad (6.20)$$

Equation (6.20) is solved for  $[\frac{\partial \rho}{\partial t}]^{n+\alpha}$ , from which the density at an intermediate step may be obtained as :

$$\rho^{n+\alpha} = \rho^n + \alpha \Delta t \left( \frac{\partial \rho}{\partial t} \right)^{n+\alpha} \quad (6.21)$$

Nevertheless, in this work, density has been assumed to be the same everywhere in the domain and thus is independent of temperature. Thus the above continuity equation has not been solved in the numerical examples performed here. The grid domain in the intermediate configuration is discretized into a set of bilinear isoparametric finite elements with shape functions  $N_\gamma(\mathbf{x})$  are defined in each element. Defining the temperature field and the weighting functions in each element as

$$\begin{aligned} \theta(\mathbf{x}, t) &= \theta_\gamma(t) N_\gamma(\mathbf{x}) \\ \bar{\theta}(\mathbf{x}, t) &= \bar{\theta}_\gamma(t) N_\gamma(\mathbf{x}) \end{aligned} \quad (6.22)$$

the Galerkin matrix form of the energy balance equation takes the form

$$\left( \sum_{E_e} C_{ab} + \alpha \sum_{E_e} K_{ab}^1 + \alpha \sum_{E_e} K_{ab}^2 \right) \Delta^g \theta_b = \sum_{E_e} f_a - \left( \sum_{E_e} K_{ab}^1 + \sum_{E_e} K_{ab}^2 \right) \theta_b^n \quad (6.23)$$

where  $\Delta^g \theta_b$  is the nodal temperature increment,  $E_e$  is the total number of domain elements and  $E_e^\Gamma$  is the number of elements on the second boundary. In equation (6.23), the configuration of the domain  $\Omega(t_{n+\alpha})$  is not known apriori and hence an iterative solution procedure is warranted.

### 6.3.1 Movement of the phase change interface

The motion of the solid-liquid interface is governed by equation (6.12) which may be solved for obtaining the normal velocity of the front at each point. However, this is not possible in the finite element analysis involving a discretized phase change boundary, and hence, a weaker integral form of the Stefan condition as proposed by Lynch [22] and Albert and O'Neill [23] has been adopted in this work. Multiplying the Stefan condition (6.12) by a virtual temperature  $\bar{\theta}$  and integrating over the solid-liquid boundary  $\Gamma_{s-l}^{n+\alpha}$ , in the intermediate configuration, the resulting weak form becomes

$$\int_{\Gamma_{s-l}^{n+\alpha}} \rho L \frac{\partial s_i}{\partial t} n_i \bar{\theta} d\Gamma = \int_{\Gamma_{s-l}^{n+\alpha}} \left\{ (k_{ij})_s \frac{\partial \theta_s}{\partial x_j} - (k_{ij})_l \frac{\partial \theta_l}{\partial x_j} \right\} n_i \bar{\theta} d\Gamma \quad (6.24)$$

Discretizing the solidifying front into  $E_{s-l}$  two-node linear finite elements and interpolating the velocity  $\frac{\partial s_i}{\partial t}$  and virtual temperature  $\bar{\theta}$  as

$$\begin{aligned} \frac{\partial s_i}{\partial t} &= \left( \frac{\partial s_i}{\partial t} \right)_\gamma M_\gamma(\mathbf{x}) \\ \bar{\theta} &= \bar{\theta}_\gamma(t) M_\gamma(\mathbf{x}) \end{aligned} \quad (6.25)$$

where  $M_\alpha$  are linear interpolation functions, the discretized equation takes the form

$$\sum_{E_{s-l}} \left( \int_{\Gamma_{s-l}^{n+\alpha}} \rho L n_i M_\alpha M_\beta d\Gamma \right) \left( \frac{\partial s_i}{\partial t} \right)_\beta = \sum_{E_{s-l}} \int_{\Gamma_{s-l}^{n+\alpha}} \left\{ (k_{ij})_s \frac{\partial \theta_s}{\partial x_j} - (k_{ij})_l \frac{\partial \theta_l}{\partial x_j} \right\} n_i M_\alpha d\Gamma \quad (6.26)$$

In the ALE formulation, the velocity of nodes on the front are made to coincide with the phase change velocity, given by  $\frac{\partial s_i}{\partial t}$ . Equation (28) specifies only the normal component of velocity of the moving front at nodal points, and hence, the tangential component is not restricted. Thus the tangential components of nodal velocities may be specified by the user according to the requirements of the problem especially with respect to element geometry. For example, the tangential component may be prescribed to avoid non-convex elements or element entanglement at the solid-liquid front. Equations (6.23) and (6.26), together with the specified tangential node velocities at the front are then solved simultaneously.

## 6.4 Numerical Implementation

In this section, a few of the salient features of the solution procedure have been highlighted.

### 6.4.1 Iteration Scheme

As mentioned in section 3, heat transfer analysis of the solidification process involves the iterative solution of the energy balance equation (6.23) and Stefan condition (6.26) simultaneously to yield the resulting temperature field and the location of the phase change interface. The quasi-Newton family of iterative solvers, e.g. the Broyden or BFGS update formulae (Matthies and Strang [39]) have been

implemented in this work for solution of the system of nonlinear equations. These update methods require line search algorithms and are superlinearly convergent to the solution. The steps involved in the iteration process are now outlined.

Applying the finite element approximations in the discretized domain, a linearized form of the energy balance equation (6.23) may be written for the  $i$ -th iteration step as

$${}^{t_{n+\alpha}}[\mathbf{K}]^{(i)}\Delta\Theta = {}^{t+\alpha\Delta t}\mathbf{R} - {}^{t+\alpha\Delta t}\mathbf{F}^{(i)} \quad (6.27)$$

where  $\Delta\Theta = \Delta^g\Theta^i - \Delta^g\Theta^{i-1}$  refers to the correction in the incremental grid point temperature in the intermediate configuration. The column  ${}^{t+\alpha\Delta t}\mathbf{R}$  in the right hand side of equation (6.27) corresponds to the external load i.e. the right hand side of equation (6.23), while the column  ${}^{t+\alpha\Delta t}\mathbf{F}^{(i)}$  is the internal load corresponding to the left hand side of (6.23).

- a) With an initial guess for  $\Delta\Theta$  and the intermediate configuration  $\Omega_{n+\alpha}$ , a starting stiffness matrix  ${}^{t+\alpha\Delta t}[\mathbf{K}]^{(0)}$  and right hand vector  ${}^{t+\alpha\Delta t}\mathbf{R} - {}^{t+\alpha\Delta t}\mathbf{F}^{(i)}$  is calculated.
- b) An incremental vector, defining the direction of the actual incremental solution vector is then obtained as

$$\Theta' = {}^{t_{n+\alpha}}[\mathbf{K}^{(i-1)}]^{-1}({}^{t+\alpha\Delta t}\mathbf{R} - {}^{t+\alpha\Delta t}\mathbf{F}^{(i)}) \quad (6.28)$$

- c) A line search is performed in the direction of to satisfy equilibrium by varying a scalar parameter  $s (0 \leq s \leq 1)$  given as

$$\Delta^g\Theta^i = \Delta^g\Theta^{i-1} + s\Theta' \quad (6.29)$$

to make the projection of the off balance loads in the direction of  $\Theta'$  approximately zero. The corresponding temperature field in the mid-step configuration is given by

$$\Theta^{n+\alpha} = \Theta^n + \alpha \Delta^g \Theta^i \quad (6.30)$$

d) Substituting the mid-step temperature field  $\Theta^{n+\alpha}$  in the discretized form of the Stefan condition (6.26) and adding input regarding the tangential components of grid velocities at the front, a global matrix equation is established. This equation (6.31) is now solved for grid velocities at the solid-liquid interface as :

$$\dot{\mathbf{S}} = [(\mathbf{K}^{s-l})^i]^{-1} \{ \mathbf{F}^{s-l} \}^i \quad (6.31)$$

where  $\dot{\mathbf{S}}$  corresponds to the mid-step velocity of the interface,  $[(\mathbf{K}^{s-l})^i]$  is the stiffness matrix and  $\{ \mathbf{F}^{s-l} \}^i$  corresponds to the load vector in the  $n + \alpha$  th configuration for the i-th iteration. It is to be noted that  $[(\mathbf{K}^{s-l})^i]$  and  $\{ \mathbf{F}^{s-l} \}^i$  should be updated at each iteration step, because of the changing values of the unit normal  $\mathbf{n}^{n+\alpha}$  at the front and intermediate temperatures  $\Theta^{n+\alpha}$ . The location of the phase change interface is now updated to the subsequent intermediate configuration by the relation :

$$\mathbf{S}^{n+\alpha} = \mathbf{S}^n + \dot{\mathbf{S}}^{n+\alpha} \Delta t \quad (6.32)$$

The right hand side of equation (6.27), corresponding to the out of balance loads, is now recalculated based on the new values of temperatures, intermediate configuration and velocities.

e) A convergence check is done at the end of each iteration based on temperatures, out of balance loads and energy. Divergence of the solution results when the out of balance loads exceed their initial value, and at this point a stiffness matrix reformation is performed.

#### 6.4.2 Evaluation of Normals to the Interface

Accurate evaluation of normals and tangents to the solidifying front is critical for better quality of numerical results in the discrete problem. Non-smoothness in the discretized front can lead to abrupt changes in the direction of the normal at the same nodal point, corresponding to two neighboring elements. This in turn, results in distinctly different temperature gradients at nodal points and adversely affects thenodal velocities. A local smoothing technique is therefore suggested to reduce mismatches in the normal at locations, where the physical boundary is expected to be smooth. This method establishes higher order elements from the data available for two-node line elements, that are elsewhere used in the computations.

Consider a 2-node line element , corresponding to the boundary of a QUAD4 plane element. The coordinates are interpolated by using a linear interpolation function in a natural coordinate system ( $-1 \leq s \leq 1$ ) as:

$$\mathbf{x}_h(s) = \mathbf{x}(-1) \frac{1}{2}(1-s) + \mathbf{x}(1) \frac{1}{2}(1+s) \quad (6.33)$$

Using a Taylor series expansion in the neighborhood of  $\mathbf{x}(s)$  and retaining upto quadratic terms, the coordinates of the interface points near  $\mathbf{x}(s)$  may be approximated as :

$$\mathbf{x}(s^0) = \mathbf{x}(s) + (s^0 - s) \frac{\partial \mathbf{x}}{\partial s}(s^0 - s) + \frac{1}{2}(s^0 - s)^2 \frac{\partial^2 \mathbf{x}}{\partial s^2} \quad (6.34)$$

Substituting equation (6.33) in (6.34) yields an interpolation, that accounts for quadratic terms and is smoother than (6.33).

$$\mathbf{x}(s) = \mathbf{x}_h(s) + \frac{1}{2}(s^2 - 1) \frac{\partial^2 \mathbf{x}}{\partial s^2} \quad (6.35)$$

The second derivative in equation (37) is evaluated by using a method of weighted averages from values in neighboring elements. Due to its quadratic nature, equation (37) can be considered to represent the 3-node quadrilateral line elements and the coordinates of a third point at  $s = 0$  can be computed from it. The slope to the interface and hence the normal vectors are then computed at any point from interpolation based on the three nodal points as:

$$\frac{\partial \mathbf{x}}{\partial s} = \sum_{\alpha=1..3} \mathbf{x}^\alpha \frac{\partial M^\alpha}{\partial s} \quad (6.36)$$

#### 6.4.3 Introduction of a Pseudo Domain for Discretization

A solidification problem involves an internal solid-liquid boundary which is continuously evolving with time. In the ALE formulation, a set of nodes is placed on the moving front at the start of simulation and is made to adhere to it throughout the process. This calls for a continuous rediscretization of the computational domain, resulting in changing the degrees of freedom and element connectivity of the finite element model. For example, if the domain initially consists of the liquid only, elements should be added as the solidifying front forms and moves through the liquid. To avoid the burden of having to update the degrees of freedom, element connectivity and hence the order of the stiffness matrix and load vectors , a pseudo-domain is introduced adjacent to the solidifying front as shown in figure 1. This domain is discretized along with the physical domain, to yield a combined number of elements which remain unchanged throughout the simulation. A few special assumptions are imposed on this part of the finite element model as follows.

- i) The specific heat capacity  $C_p$  is zero, i.e. this domain is always in a steady state condition.
- ii) If the boundary  $\Gamma_{actual}$  is of the second type, i.e. the heat flux normal to the boundary is specified, then a heat flux should be specified on the pseudo boundary  $\Gamma_{pseudo}$ . This is done according to the assumption that the normal heat flux through the pseudo boundary  $\Gamma_{pseudo}$  at any time  $t$ , is equal to the heat flux through the adjacent physical boundary, or

$$\int_{\Gamma_{pseudo}} q_i n_i d\Gamma = \int_{\Gamma_{actual}} q_i n_i d\Gamma \quad (6.37)$$

The other sides of the pseudo-domain are insulated.

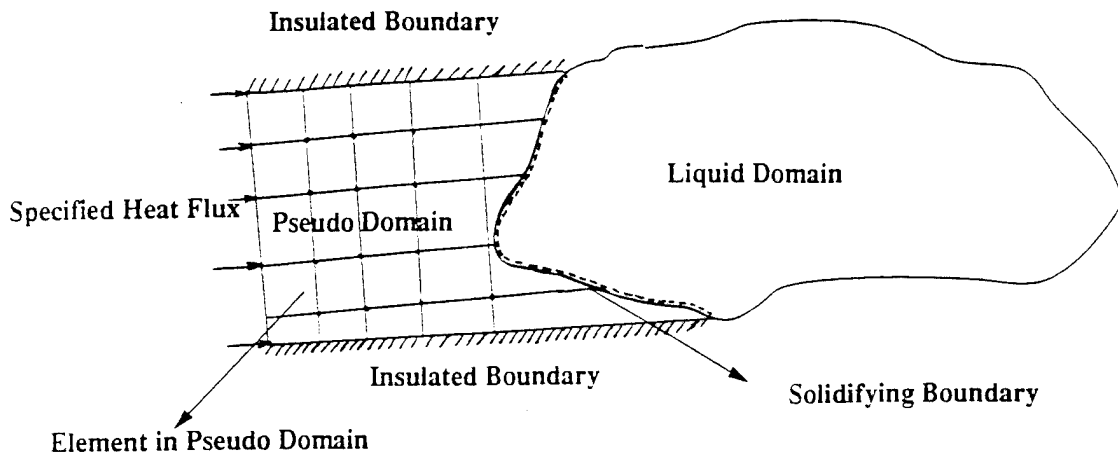


Figure 6.1: Introduction of the pseudo domain

- iii) If temperature conditions are prescribed on the actual boundary, from which solidification initiates, additional efforts are needed. First of all, the prescribed boundary temperatures are imposed on the common boundary. Secondly, heat flux at the nodes of the common boundary are calculated from adjacent element temperatures in the physical domain. This heat flow vector is then prescribed on the pseudo-boundary  $\Gamma_{pseudo}$  according to equation (6.37).
- iv) The boundary of the pseudo-domain coincides with the that of the physical domain approximately along the part from which solidification takes place.
- v) Nodes from the pseudo-domain continuously move into the physical domain by virtue of the ALE formulation to maintain well behaved elements in the physical domain. Since the pseudo-domain is merely a node bank, element shapes in this region is not important.

## 6.5 Numerical Examples

A two-dimensional program has been developed with QUAD4 domain elements and 2- node line elements on the solid-liquid interface. The value of  $\alpha$  for intermediate configuration has been chosen to be  $1/2$ . The results of the program have been compared with all the heat transfer results presented in Zabaras [38]. Finally a simplified form of a continuous casting process has been simulated. In the numerical examples, it has been assumed that the liquid domain is maintained at a uniform temperature corresponding to the melting temperature and there are no convection effects in the liquid. Consequently, only the solid domain has been modeled.

In accordance with the data presented in [38], the following thermal properties have been assumed for the material (Aluminum, in this case) for all the problems. They are  
 $K_s = 0.0548 \text{ kcal/ms. } ^\circ\text{C}$  (Conductivity of solid)  
 $K_l = 0.0548 \text{ kcal/ms. } ^\circ\text{C}$  (Conductivity of liquid)

$$(C_p)_s = 0.2526 \text{ kcal/kg} \cdot {}^\circ\text{C} \text{ (Specific heat of solid)}$$

$$(C_p)_l = 0.2526 \text{ kcal/kg} \cdot {}^\circ\text{C} \text{ (Specific heat of liquid)}$$

$$L = 94.44 \text{ kcal/kg} \text{ (Latent heat of fusion)}$$

$$\rho = 2650 \text{ kg/m}^3 \text{ (Density of solid/liquid)}$$

$$\theta_I = 660 \text{ } {}^\circ\text{C} \text{ (Initial liquid temperature)}$$

$$\theta_m = 660 \text{ } {}^\circ\text{C} \text{ (Melting temperature)}$$

Furthermore, as suggested in [38], a temperature condition has been specified at the cooling boundary as:

$$\theta_o(t) = \theta_a(t) + (\theta_m(t)\theta_a(t))e^{-Rt} \quad (6.38)$$

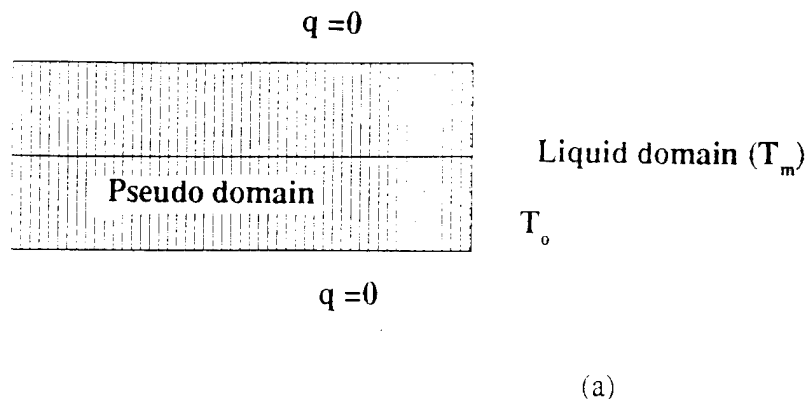
where  $\theta_a(t)$  corresponds to the ambient temperature and  $R$  is a cooling parameter.

### 6.5.1 An one-dimensional problem

A one dimensional solidification problem, for which the initial domain and discretization is shown in figure 2(a), is solved with the boundary conditions specified. In equation (6.38),  $R$  is assumed to have a value of  $0.023 \text{ s}^{-1}$  and two different cases have been solved with the ambient temperature  $\theta_a(t)$  taking a value of  $300 \text{ } {}^\circ\text{C}$  and  $51.7 \text{ } {}^\circ\text{C}$  respectively. The actual domain is initially made up entirely of liquid, and 102 QUAD4 elements are packed into the pseudo-domain as shown. As solidification begins, the nodes on the right hand face of the model move with the front. The set of nodes behind the front are moved to replace the former set, so as to retain the actual boundary with temperature boundary conditions. Following this, ALE nodes are admitted periodically into the physical domain and moved to avoid elongated elements. Figure 2(b) shows the discrete solidified domain and the temperature distribution for  $\theta_a(t) = 300 \text{ } {}^\circ\text{C}$ . The motion of the solid-liquid interface as a function of time has been plotted in figure 3 (a). The solidification front has a greater velocity for the lower ambient temperature, as can be physically predicted. Figures 3(b) and 4 are plots of temperatures at three different locations for the two different ambient temperatures. Excellent agreement is obtained for all these results with those predicted by Zabaras [38].

### 6.5.2 Solidification of a Cylindrical Body

Solidification of a cylindrical body is considered in this two dimensional example. An ambient temperature  $\theta_a(t) = 500 \text{ } {}^\circ\text{C}$  is prescribed along the circumference of a circular section of radius 18 mm and  $R = 0.1 \text{ s}^{-1}$ . The simulation is executed for 8.32 seconds at which time the solidification is almost complete. Figure 5(a) shows the initial discretization of the pseudo-domain with 240 elements. Only a quarter of the problem has been considered because of symmetry with appropriate boundary conditions indicated on figure 5(a). Figures 5(b) and 5(c) show the mesh domain and the temperature in the solidifying medium, at times 4.0 secs and 8.32 secs respectively. The total number of elements in the pseudo and physical domains remain the same at all times. The results of this problem are plotted and compared with those given in [38]. Figure 6 (a) is a plot of the front movement as a function of time while in figure 6(b), the temperature histories at different radii are depicted. Except for a slight deviation near the completion of solidification, the front radius in figure 6(a) matches



(a)

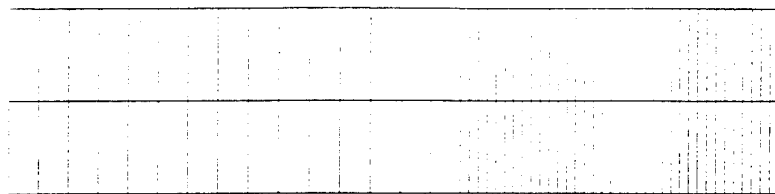


Figure 6.2: (a) Initial domain (b) final domain at time  $t = 300$  s  $\theta_a(t) = 300$   $^{\circ}\text{C}$

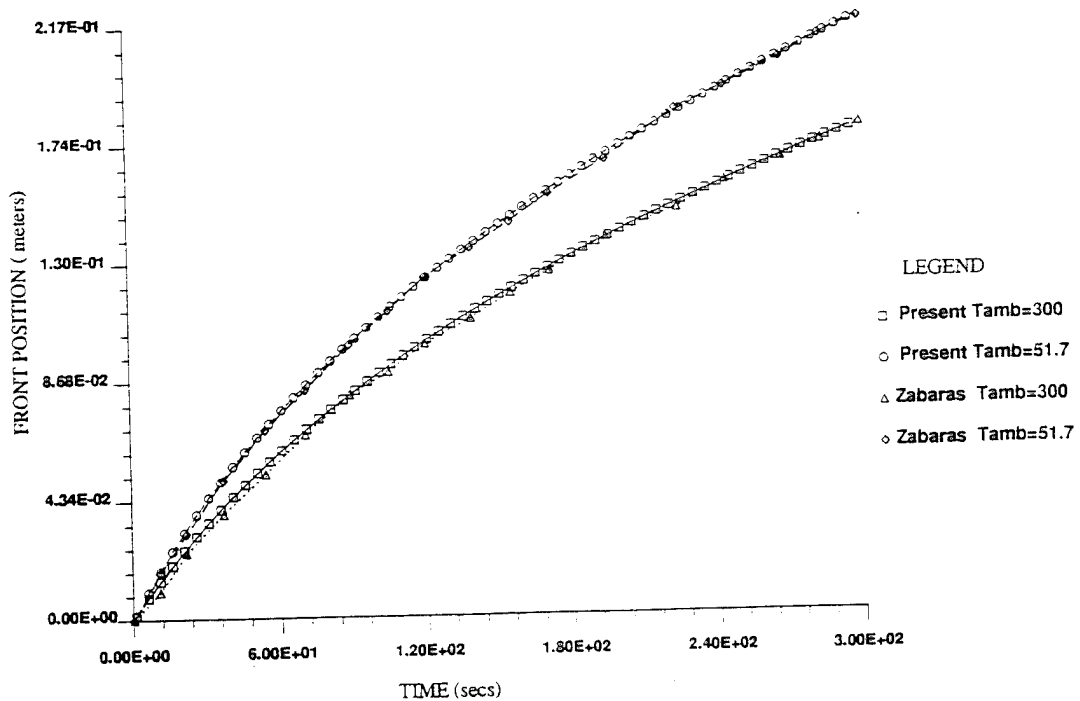
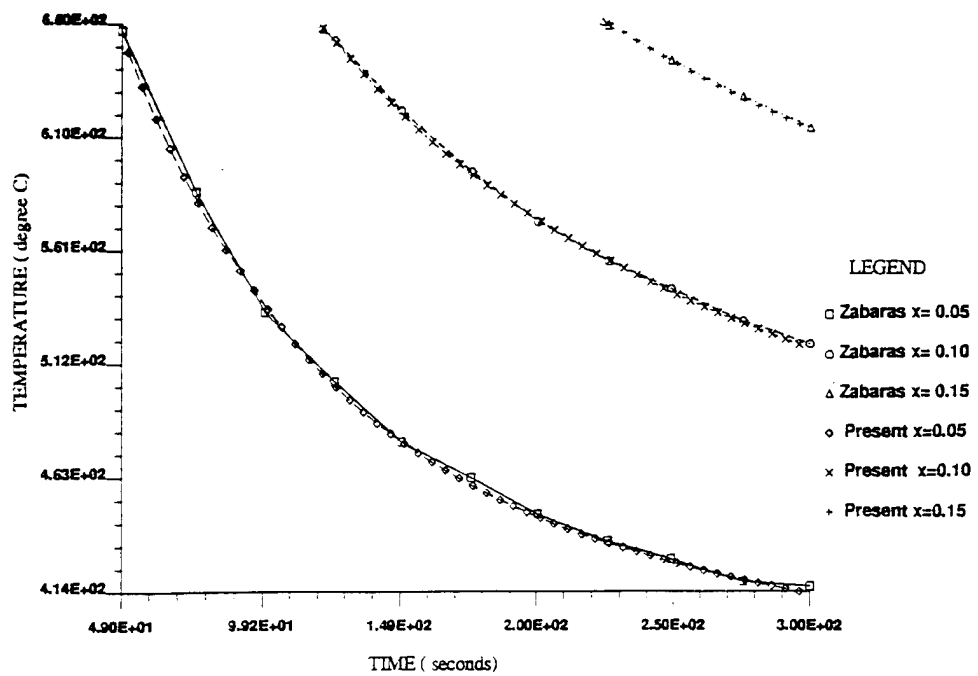
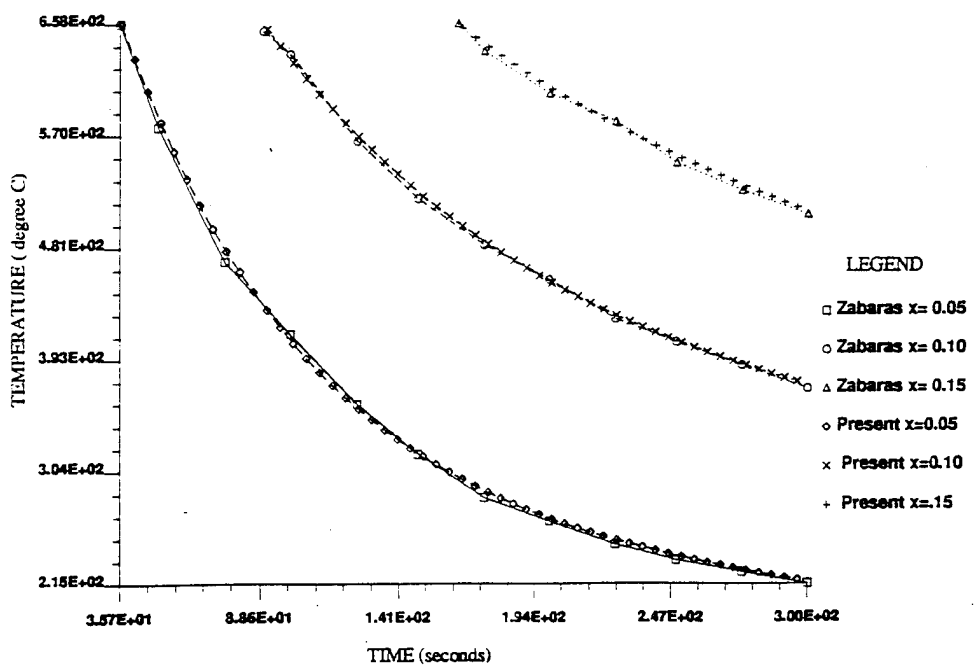


Figure 6.3: (a) Position of the front for  $\theta_a(t) = 51.7$   $^{\circ}\text{C}$  and  $\theta_a(t) = 300$   $^{\circ}\text{C}$



(a)



(b)

Figure 6.4: (a) Temperature variation at different locations with time  $\theta_a(t) = 300$  °C and (b)  $\theta_a(t) = 51.7$  °C in unidirectional solidification

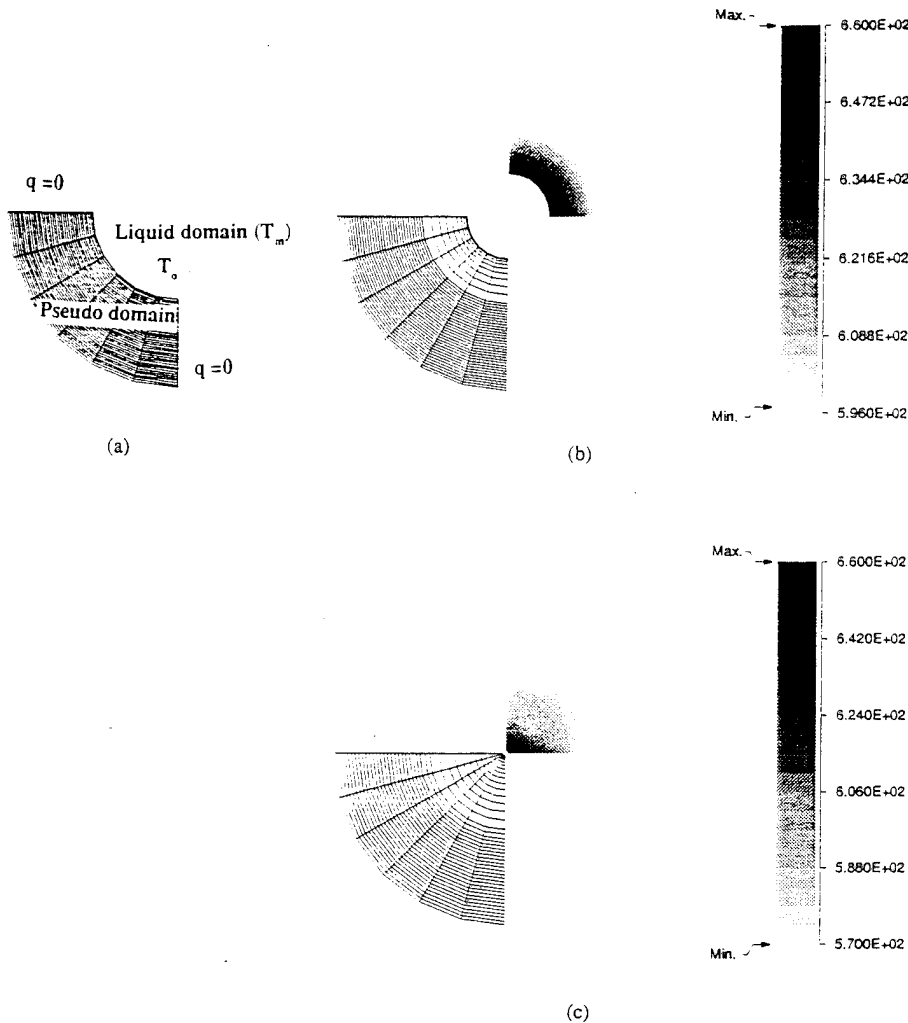
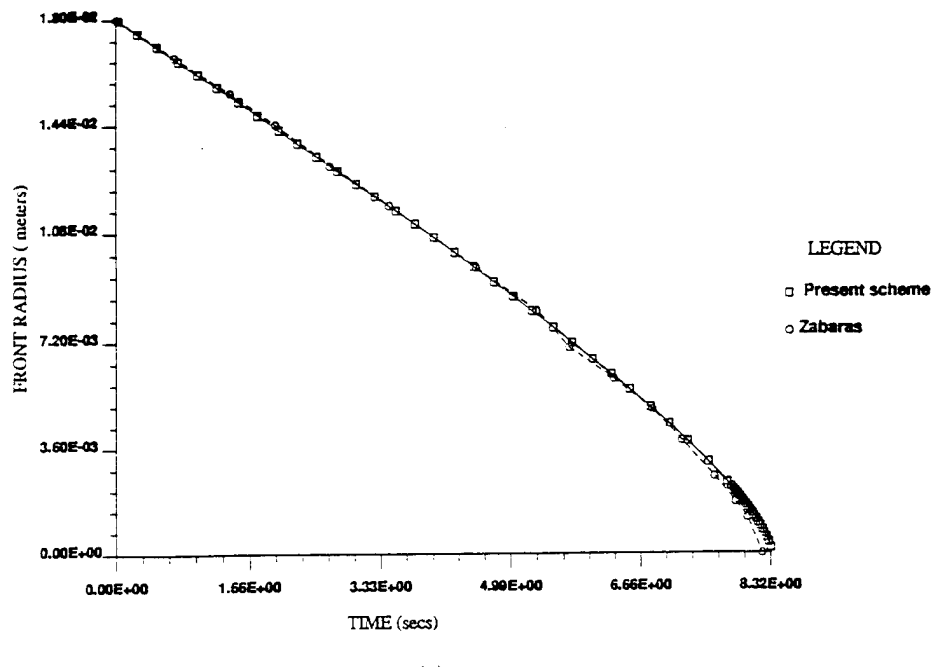


Figure 6.5: (a) Initial discretization of the pseudo-domain (b) mesh configuration and temperature distribution for time  $t=4s$ , and (c)  $t= 8.32$  s in cylindrical problem

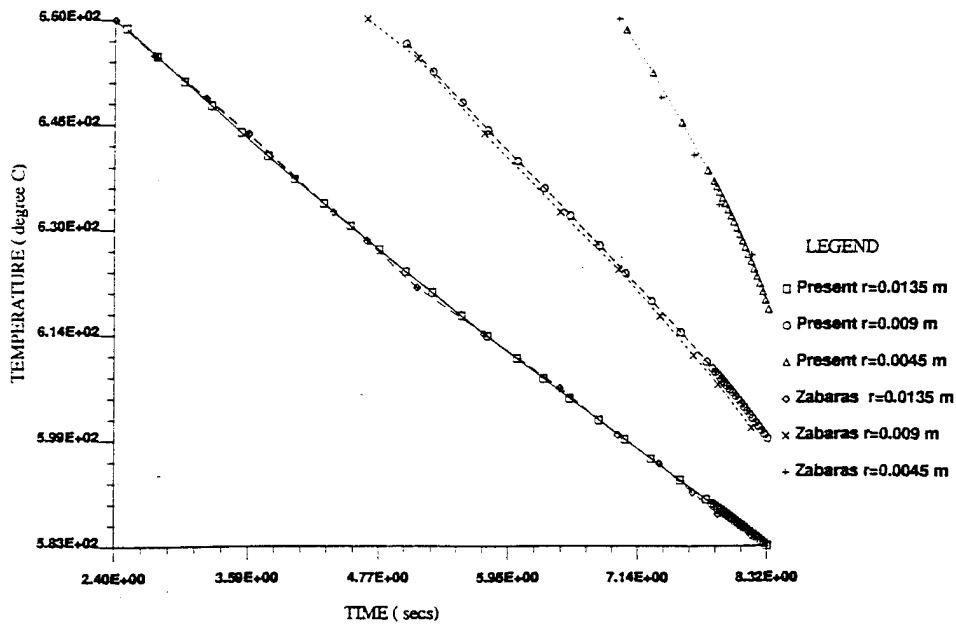
with Zabaras' results very well. Also the temperature profiles are in good agreement at different radial locations.

### 6.5.3 Solidification of a Square Region

A 40mm x 40mm square liquid domain with a specified ambient temperature  $\theta_a(t) = 500$  °C on its boundary is now simulated for solidification. As before, only a quarter of the square region is analyzed because of symmetry and appropriate boundary conditions are used. As in the previous example, the value of  $R$  is chosen to be  $0.1$   $s^{-1}$ . The process is simulated for 10.4 seconds for solidification to be nearly complete. Figure 7(a) shows the discretization of the pseudo-domain into 166 QUAD4 elements with specified boundary conditions. Figures 7(b) and 7(c) show the combined mesh configurations and temperature distributions in the solidifying medium at 5.0 secs and 10.4 secs respectively. It may be observed, that towards the end of simulation, almost all the elements in the pseudo-domain have moved to the



(a)



(b)

Figure 6.6: (a) Radial location of the front versus time (b) temperature history at various radial locations in cylindrical solidification

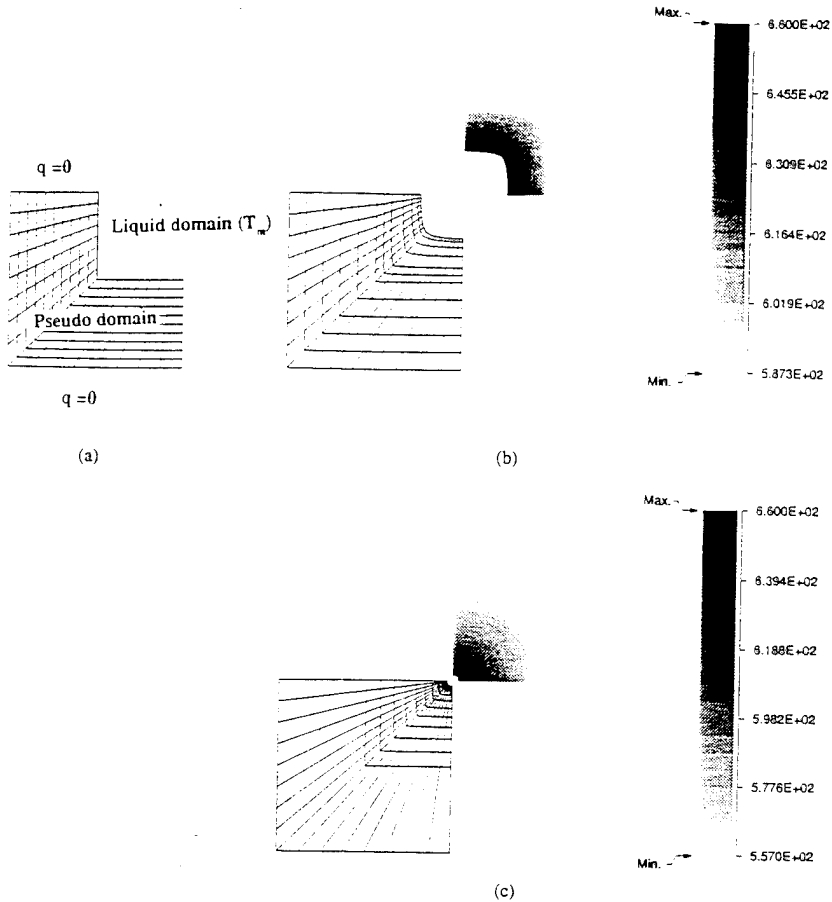


Figure 6.7: (a) Initial discretization of the pseudo-domain (b) mesh configuration and temperature distribution for time  $t=5$  s, and (c)  $t= 10.4$  s in square problem

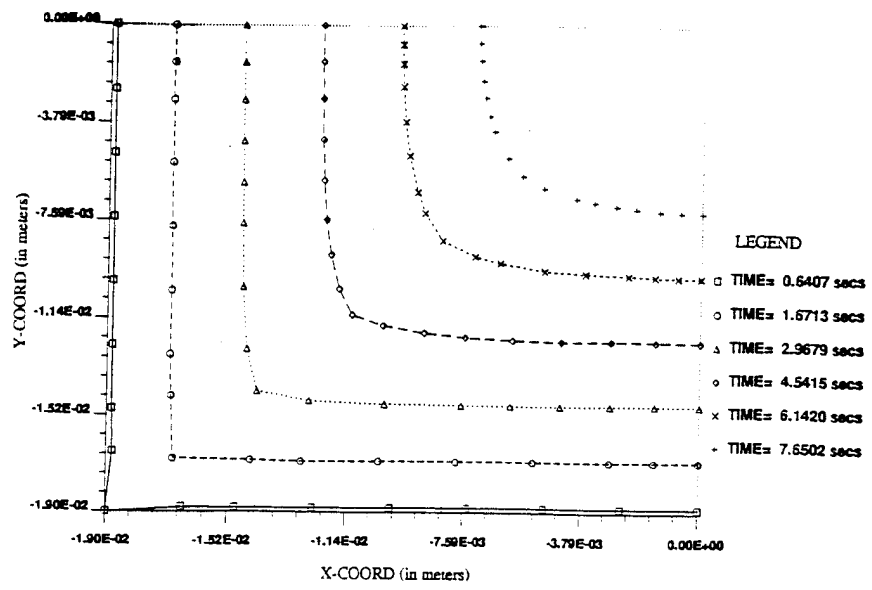
physical domain. Figure 8(a) shows a plot of the x- and y- coordinates of the front at various times in the solidification process. In figure 8(b), the temperature histories at two different locations are found to agree well with the results of Zabaras [38].

#### 6.5.4 Simplified Example of a Continuous Casting Process

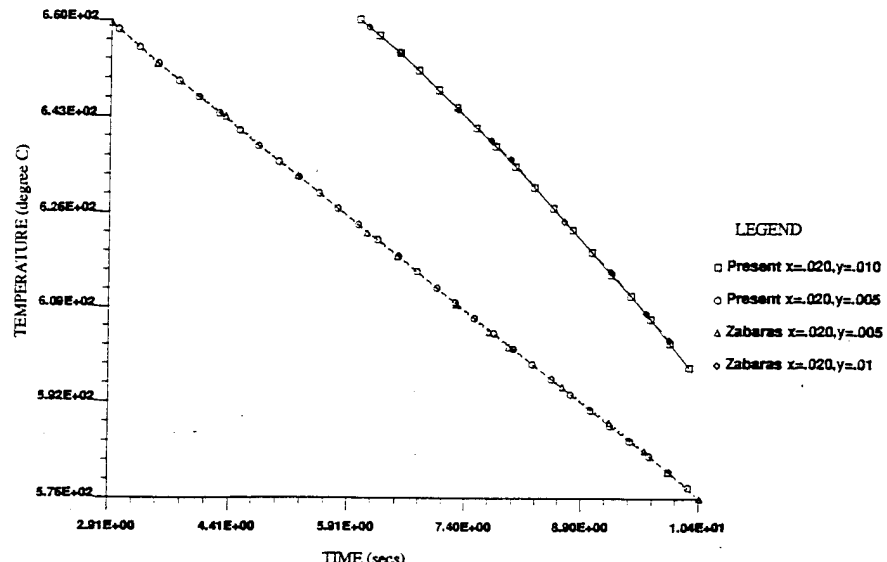
In this final example, a simplified model for two-dimensional continuous strip casting has been simulated. As illustrated in figure 9(a), the liquid is assumed to move from left to right with a horizontal velocity of 10 mm/sec. The top surface of the liquid is in contact with water and accordingly the heat flux across this boundary is assumed to be given as

$$k \frac{\partial \theta}{\partial n} = -k_o(\theta - \theta_{water}) \quad (6.39)$$

where  $k_o$  is a convection coefficient = 5 kcal/  $m^2$  sec  $^{\circ}C$  and  $\theta_{water} = 30$   $^{\circ}C$ . The right surface representing the free end of the solid is assumed to be in contact with a medium with very



(a)



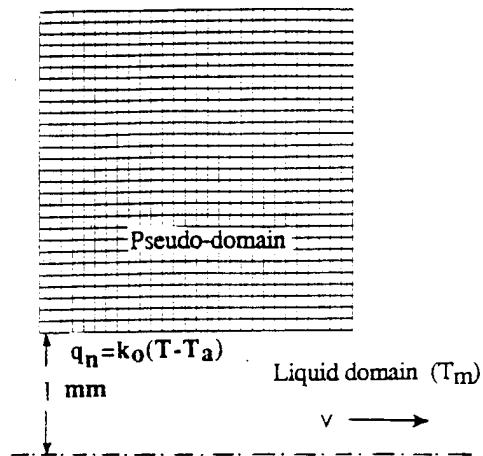
(b)

Figure 6.8: (a) Location of the front versus time (b) temperature history at various locations in square solidification

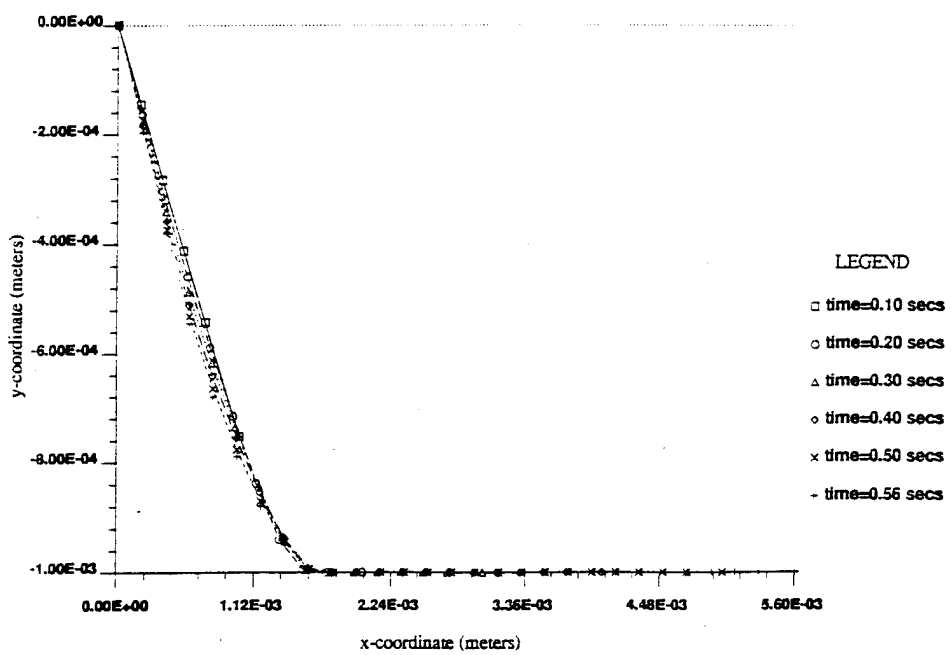
low convection coefficient and hence the heat flux across this boundary is set to zero. The convection boundary condition (6.39) is directly applied to the actual boundary at all times. The nodes that are completely within the pseudo-domain are apriori set and maintained at a specified temperature. The center-line or line of symmetry is at a distance 1 mm from the top surface of the liquid. Various steps of the solidification are depicted in figure 10 . The pseudo-domain has been excluded from these figures for better understanding of the actual domain. Nodes at the top boundary of the liquid domain are at rest in each time step, i.e. these are Eulerian nodes . However, as the front progresses, nodes from the pseudo-domain move down to replace the previous set of nodes on this boundary. The latter set of nodes now move into the solidified region. All nodes in the solidified region are ALE nodes and have the flexibility to be moved independent of the material. The horizontal component of velocity  $W_x$  , for nodes on the right hand boundary of the solidified region are maintained at the material velocity. The vertical component of velocities  $W_y$ , for ALE nodes in the solidified domain including the solid-liquid boundary, are adjusted so as to get a uniform spacing, shown in figures 17 and 18. On the interface, the horizontal node velocities are determined from the normal velocity  $W_n$ , horizontal velocity  $W_x$  and the direction cosines of the local tangent . When the front reaches the center-line, the vertical component of velocities are set to zero. Also the temperature boundary conditions are changed to zero heat flux conditions. Figure 10 shows the mesh movement and temperature contours at various stages of simulation upto 0.56 secs, during which time the solidified region has a length of 5.6 mm. Figure 9(b) depicts the x- and y- coordinates of the front as a function of time.

## 6.6 Conclusions

In this work an arbitrary Lagrangian-Eulerian finite element method has been implemented for solving the heat transfer problem in simulation of solidification processes. The flexibility imparted by introducing an arbitrary reference frame, is favorably used in monitoring the solid-fluid interface as well as in maintaining well behaved elements in the solidified region. Through the introduction of a pseudo-domain , continuous addition of nodes to the solidifying body has been avoided. Comparison of the results with some of the previously reported results in [38] shows excellent agreement. A simplified form of continuous casting that was solved with this algorithm yields expected nature of results. Overall the ALE finite element method shows promise for this class of problems and is expected to be used for realistic simulations in future.



(a)



(b)

Figure 6.9: (a) Initial discretization with boundary conditions (b) progression of the front for various times in continuous casting

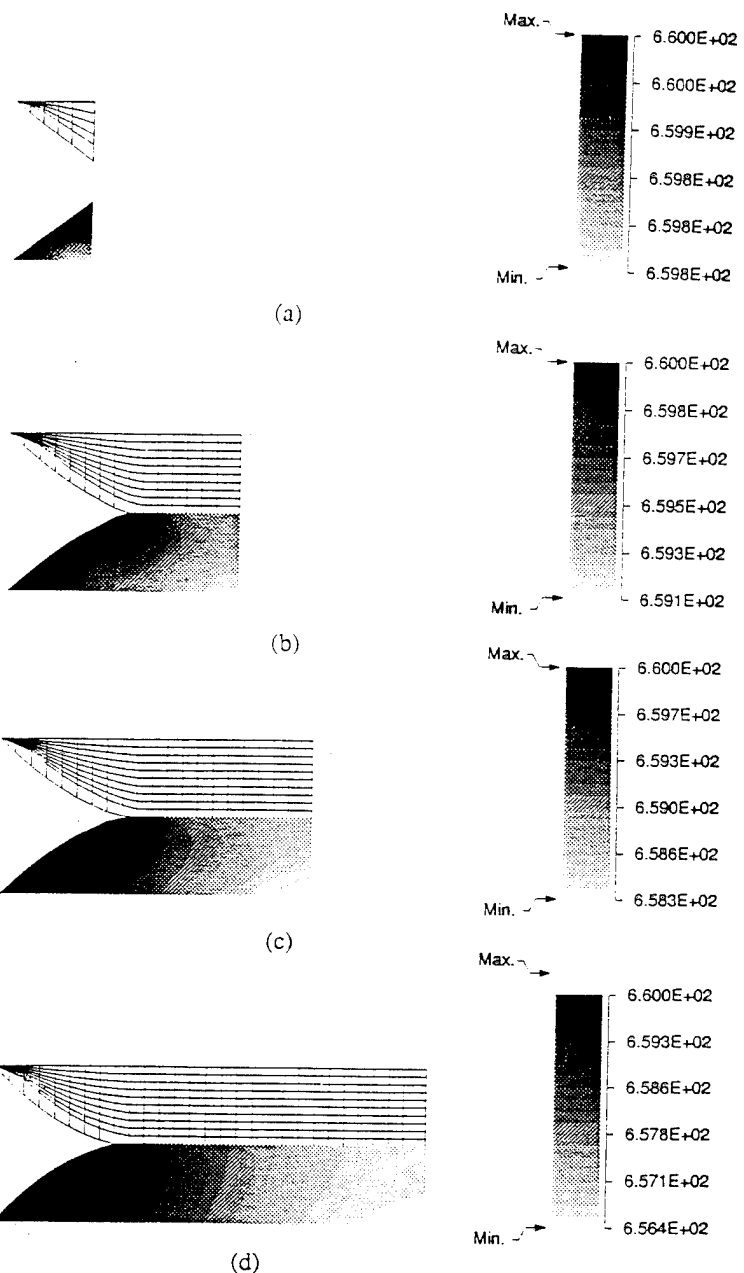


Figure 6.10: (a) Mesh configuration and temperature distributions of continuous casting at (a) 0.1 s (b) 0.3 s, (c) 0.4 s and (d) 0.56 s

# Bibliography

- [1] J. Crank, How to deal with moving boundaries in thermal problems, in Lewis, Morgan and Zienkiewicz (eds), Numerical Methods in Heat Transfer, John Wiley and Sons, 177-200, (1981).
- [2] T.R. Goodman, The heat balance integral - Further considerations and refinements, *J. Heat Transfer, Trans. ASME (C)*, Vol. 83, 83-86, 1961.
- [3] B.A. Boley, A method of heat conduction analysis of melting and solidification, *J. Math. Phys.*, Vol. 40, 300-313, 1961.
- [4] E. Hansen and P. Hougaard, On a moving boundary problem from biomechanics, *J. Inst. Math. Applic.*, Vol. 13, 385-398, 1974.
- [5] J. Crank, Finite difference methods, in J.R. Ockendon and W.R. Hodgkins (eds), Moving boundary problems in heat flow and diffusion, Clarendon Press, Oxford, 1975.
- [6] A. Lazaridis, A numerical solution of the multi-dimensional solidification (or melting) problems, *Int. J. Heat Mass Transfer*, Vol. 13, 1459-1477, 1970.
- [7] N. Shamsunder and E.M. Sparrow, Analysis of multidimensional conduction phase via the enthalpy method, *Jour. of Heat Transfer*, Vol. 97, 333-340, 1975.
- [8] D.G. Wilson, A.D. Solomon and P.J. Boggs, Moving boundary problems, Academic press, New York, 1978.
- [9] A.B. Crowley, Numerical solution of Stefan problems, *Int. J. Heat Mass Transfer*, Vol. 21, 215-219, 1978.
- [10] G. Comini, S. Del Guidice, R.W. Lewis and O.C. Zienkiewicz, Finite element solutions of nonlinear heat conduction problems with special reference to phase change, *Int. J. Num. Meth. Engng.*, Vol. 8, 613-624, 1974.
- [11] V.R. Voller and M. Cross, "Use of the enthalpy method in the solution of Stefan problems", Numerical Methods in Thermal Problems, Lewis, Johnson and Smith (eds), Vol. 3, Pineridge Press, 91-101, 1983.
- [12] M. Samands, K. Morgan and R.W. Lewis, Finite element modeling of solidification in sand castings employing an explicit-implicit algorithm, *Appl. Math. Modeling*, Vol. 9, 170-174, 1985.

- [13] M. Salcudean, V. Costescu and Ardeleanu, Contributions to the study of ingot solidification, cooling and heating phenomena by mathematical modelling, *Rev. Roum. Sci. Tech. Met.*, Vol. 17, 39-49, 1972.
- [14] G. Bell, On the performance of the enthalpy method, *Int. J. Heat Mass Transfer*, Vol. 25 (4), 587-589, 1982.
- [15] V. Voller and M. Cross, Accurate solutions of moving boundary problems using the enthalpy method, *Int. J. Heat Mass Tranfer*, Vol. 24, 545-556, 1980.
- [16] R. Bonnerot and P. Janet, Numerical computation of the free boundary for the two dimensional Stefan problem by space-time finite elements, *J. Comp. Physics*, Vol. 25, 163-181, 1977.
- [17] J. Yoo and B. Rubinsky, A finite element method for the study of solidification processes in the presence of natural convection, *Int. J. Num. Meth. in Engng.*, Vol. 23, 1785-1805, 1986.
- [18] K. Miller, Alternate modes to control the nodes in the moving finite element method, in *Adaptive Computational Methods for Partial Differential Equations*, SIAM, Philadelphia, 1983.
- [19] D.R. Lynch and W.G. Gray, Finite element simulation of flow in deforming regions, *J. Comp. Physics*, Vol. 36, 135-153, 1980.
- [20] D.R. Lynch and K. O'Neill, Continuously deforming finite elements for the solution of parabolic problems with and without phase change, *Int. J. Num. Meth. in Engng.*, Vol. 17, 81-96, 1981.
- [21] K. O'Neill and D.R. Lynch, "A finite element solution for freezing problems using a continuously deforming coordinate system", in R. Lewis, K. Morgan and O.C. Zienkiewicz (eds.), *Numerical Methods in Heat Transfer*, , Wiley London, 1981.
- [22] D.R. Lynch, Unified approach to simulation on deforming elements with application to phase change problems, *J. Comp. Physics*, Vol. 47, 387-411, 1982.
- [23] M.R. Albert and K. O'Neill, Moving boundary-moving mesh analysis of phase change using finite elements with transfinite mappings, *Int. J. Num. Meth. Engng.*, Vol. 23, 591-607, 1986.
- [24] J. Donea, "Arbitrary Lagrangian-Eulerian finite element methods", in T. Belytschko and T.J.R. Hughes (eds.), *Computational Methods for Transient Analysis*, , 473-516, North Holland, Amsterdam 1983.
- [25] T. Belytschko, J.M. Kennedy and D.F. Schoeberle, Quasi-Eulerian finite element formulation for fluid-structure interaction, *ASME J. Pressure Vessel Technol.*, Vol. 102, 62-69, 1980.

- [26] T. Belytschko and J.M. Kennedy, Computer models for subassembly simulation, Nuclear Engng. Design, Vol. 49, 17-38, 1978.
- [27] W.K. Liu and J. Gvildys, Fluid-structure interaction of tanks with an eccentric core barrel, Comp. Meth. Appl. Mech. and Engng., Vol. 58, 51-57, 1986.
- [28] W.K. Liu, T. Belytschko and H. Chang, An arbitrary Lagrangian-Eulerian finite element method for path dependent materials, Comp. Meth. Appl. Mech. and Engng., Vol. 58, 227-245, 1986.
- [29] W.K. Liu, H. Chang J.S. Chen and T. Belytschko, Arbitrary Lagrangian- Eulerian Petrov-Galerkin finite elements for nonlinear continua, Comp. Meth. Appl. Mech. Engng., Vol. 68, 259-310, 1988.
- [30] S. Ghosh and N. Kikuchi, An arbitrary Lagrangian-Eulerian finite element method for large deformation analysis of elastic-viscoplastic solids, Comp. Meth. in Appl. Mech. and Engng., Vol. 86, 127-188, 1991.
- [31] S. Ghosh, Arbitrary Lagrangian-Eulerian finite element analysis of large deformation in contacting bodies, Int. J. Num. Meth. Engng., (in press) 1992.
- [32] R.B. Haber, A mixed Eulerian-Lagrangian displacement model for large deformation analysis in solid mechanics, Comp. Meth. Appl. Mech. Engng., Vol. 43, 277-292, 1984.
- [33] S. Ghosh, Finite element simulation of some extrusion processes using the arbitrary Lagrangian-Eulerian description, J. Mat. Shaping. Tech., Vol. 8, 53- 64, 1990.
- [34] T.J.R. Hughes and T. Belytschko, A precis of developments in computational methods for transient analysis, J. Appl. Mech., Vol. 50, 1033-1041, 1983.
- [35] T.J. R. Hughes, "Unconditionally stable algorithms for nonlinear heat conduction", Comp. Meth. App. Mech. and Engng., Vol. 10, 135-139, 1977.
- [36] T.J. R. Hughes, "Analysis of transient algorithms with particular reference to stability behavior", in T. Belytschko and T.J.R. Hughes (eds), Computational Methods for Transient Analysis, Vol. 1, North-Holland, 1983.
- [37] M. Heinlien, S. Mukherjee and O. Richmond, A boundary element method analysis of temperature fields and stresses during solidification, Acta Mech., Vol. 59, 59-81, 1986.
- [38] N. Zabaras, Y. Ruan and O. Richmond, Front tracking thermomechanical model for hypoelastic-viscoplastic behavior in a solidifying body, Comp. Meth. Appl. Mech. and Engng., Vol. 81, 333-364, 1990.
- [39] H. Matthies and G. Strang, The solution of nonlinear finite element equations, Int. J. Num. Meth. Engng., Vol. 14 (11), 1613-1626, 1979.

## Chapter 7

# List of Participating Scientific Personnel

1. **Somnath Ghosh**, Principal Investigator, Associate professor of Applied Mechanics, The Ohio State University.
2. **Suresh Moorthy**, Graduate Research Associate and Ph.D. Candidate in Applied Mechanics.  
Ph.D. Expected in July 1996.
3. **Suresh Raju**, Graduate Research Associate and M.S. student in Mechanical Engineering.  
M.S. Completed in September 1995.
4. **Yunshan Liu**, Graduate Research Associate and M.S. student in Engineering Mechanics.  
M.S. Completed in December 1993.
5. **Rajesh Parameswaran**, Graduate Research Associate and Ph.D. student in Applied Mechanics.  
Has taken leave of absence to work in industry after six quarters of GRA.